UNIVERSITY OF CRETE

DEPARTMENT OF PHYSICS

PhD THESIS

Ultra-luminous X-ray sources and X-ray luminosity scaling relations in nearby galaxies

Konstantina Anastasopoulou

Advisor: *Associate Professor* Andreas Zezas - University of Crete

UNIVERSITY OF CRETE
DEPARTMENT OF PHYSICS

PhD THESIS

DOCTOR OF PHILOSOPHY
OF
- ASTROPHYSICS -

Defended by
KONSTANTINA ANASTASOPOULOU

Ultra-luminous X-ray sources and X-ray luminosity scaling relations in nearby galaxies

COMMITTEE

Associate Professor	Zezas Andreas	-	UNIVERSITY OF CRETE
Associate Professor	Pavlidou Vasiliki	-	UNIVERSITY OF CRETE
Research Director	Reig Pablo	-	INSTITUTE OF ASTROPHYSICS, FORTH
Professor	Charmandaris Vasileios	-	UNIVERSITY OF CRETE
Professor	Papadakis Iossif	-	UNIVERSITY OF CRETE
Professor Emeritus	Kylafis Nikolaos	-	UNIVERSITY OF CRETE
Senior Researcher	Georgakakis Antonios	-	NATIONAL OBSERVATORY OF ATHENS

Date of the defense:
18/12/2019

Περὶληψη

Τα διπλά αστρικά συστήματα εκπομπής ακτίνων X και οι υπέρλαμπρες πηγές ακτίνων X αποτελούν την κύρια πηγή ακτινοβολίας X υψηλών ενεργειών (>2keV) από γαλαξίες που παρουσιάζουν αστρογένεση. Σχέσεις κλίμακας μεταξύ της λαμπρότητας του πληθυσμού των διπλών συστημάτων εκπομπής ακτίνων X με τον ρυθμό αστρογένεσης ή/και την συνολική αστρική μάζα των γαλαξιών, έχουν χρησιμεύσει ως ένα σημαντικό εργαλείο για τη μέτρηση της περιεκτικότητας κοντινών γαλαξιών σε διπλά συστήματα εκπομπής ακτίνων X. Επιπλέον, τέτοιες σχέσεις έχουν χρησιμοποιηθεί για την εκτίμηση των παραμέτρων θεωρητικών μοντέλων που αφορούν τον σχηματισμό και την εξέλιξη διπλών αστρικών συστημάτων εκπομπής ακτίνων X.

Στη παρούσα διδακτορική διατριβή, εξετάζουμε εάν οι σχέσεις κλίμακας λαμπρότητας ακτίνων X είναι αντιπροσωπευτικές για ένα γενικό δείγμα γαλαξιών στο κοντινό Σύμπαν, ανεξάρτητα από τα ιδιαίτερα χαρακτηριστικά του (π.χ. ρυθμό αστρογένεσης και αστρική μάζα). Αρχικά χρησιμοποιούμε δεδομένα του δορυφόρου *Chandra* και εξετάζουμε αυτές τις σχέσεις για τα διπλά συστήματα εκπομπής ακτίνων X σε έναν γαλαξία με ιδιαίτερα υψηλό ρυθμό αστρογένεσης, τον Arp 299. Στη συνέχεια διερευνούμε την εγκυρότητά τους σε υποπεριοχές των γαλαξιών NGC 3310 και NGC 2276 που είναι πλούσιοι σε υπέρλαμπρες πηγές ακτίνων X.

Τέλος, αναλύουμε δεδομένα για το μεγαλύτερο έως τώρα δείγμα γαλαξιών (650 αντικείμενα) που παρουσιάζουν αστρογένεση και έχουν παρατηρηθεί στις ακτίνες X με βάση το αρχείο δεδομένων του δορυφόρου *XMM-Newton*. Αυτό το δείγμα προέρχεται από ένα πλήρες δείγμα γαλαξιών που βρίσκονται σε αποστάσεις έως 200 Mpc και καλύπτει όλο το εύρος ρυθμών αστρογένεσης και αστρικής μάζας γαλαξιών που παρατηρείται στο κοντινό Σύμπαν. Μετράμε τις σχέσεις κλίμακας λαμπρότητας ακτίνων X με τον ρυθμό αστρογένεσης και την συνολική αστρική μάζα των γαλαξιών καθώς και τη διασπορά τους. Διαπιστώνουμε ότι η σχέση της λαμπρότητας στις ακτίνες X με τον ρυθμό αστρογένεσης είναι υπογραμμική. Αυτό οφείλεται στη συνεισφορά υπέρλαμπρων πηγών ακτίνων X ή/και διπλών συστημάτων εκπομπής ακτίνων X χαμηλής μάζας σε γαλαξίες με μικρή τιμή του ρυθμού αστρογένεσης. Παρ΄ όλα αυτά, η σχέση μεταξύ της λαμπρότητας στις ακτίνες X με τον ρυθμό αστρογένεσης και την αστρική μάζα, συμφωνεί, αλλά με μεγαλύτερη διασπορά, συγκριτικά με σχέσεις που έχουν βρεθεί για μικρότερα δείγματα γαλαξιών. Η μεγαλύτερη διασπορά οφείλεται στη πληθώρα διαφορετικών τύπων γαλαξιών (π.χ. διαφορετικές ηλικίες αστρικών πληθυσμών και περιεκτικότητες σε μέταλλα) που καλύπτονται από το δείγμα μας σε σύγκριση με προηγούμενες μελέτες μικρότερης κλίμακας.

Abstract

X-ray binaries (XRB) and their most extreme manifestation Ultra-luminous X-ray sources (ULXs), are the dominant source of the hard X-ray emission in star-forming galaxies. X-ray scaling relations between the luminosity of the XRB population, the star-formation rate (SFR), and stellar mass (M_*) have served as an important tool for measuring the XRB component of any galaxy in the local Universe. Moreover, they have been used to set observational constrains to the population synthesis models of XRBs and their formation and evolution parameters.

In this thesis, we have striven to answer the question of whether these correlations are universal and representative of galaxies in the local Universe irrelevant of their conditions (e.g. SFR, M_*). For this reason we test the scaling relations of XRBs on one of the most extreme, highly star-forming galaxies Arp 299 and explore their validity at sub-galactic scales for the ULX-rich galaxies NGC 3310 and NGC 2276 using *Chandra* data.

Moreover, using the *XMM-Newton* archive we build the largest X-ray sample of bona-fide normal galaxies observed in the X-ray band (650 objects). This sample is drawn from a complete sample of galaxies within 200Mpc and it encompasses the full range of SFR and M_* observed in the local Universe. With this sample of local star-forming galaxies, we measure the XRB-SFR, XRB-M_* scaling relations, and their *intrinsic* scatter. We find that the X-ray luminosity-SFR scaling relation for the full sample of normal local galaxies is sub-linear. This is most likely the result of contribution from ULX-hosting galaxies and/or LMXBs in the low SFR regime. On the other hand the X-ray luminosity-SFR-M_* scaling relation, is consistent with the relations reported for smaller samples, but with larger intrinsic scatter. The increased scatter is interpreted as the result of the wider range of different types of galaxies (i.e. stellar population ages, metallicity) covered by the full sample in comparison to the previous smaller scale surveys.

To my parents

Acknowledgements

First and foremost, I would like to thank my advisor Prof. Andreas Zezas for his guidance, support, and patience throughout the years of my PhD. I would also like to thank him for always being there, especially at moments when his help was really needed.

I would like to thank the Max Planck Institute for Extraterrestrial Physics for hosting me during the six months of the ERASMUS trainee-ship program. Special thanks also to Dr. Frank Haberl for the scientific guidance and counsel during my visit. I would also like to thank the Center for Astrophysics, Harvard & Smithsonian for hosting me the last nine months of my PhD as well as my colleagues for the great conversations at the HEAD lounge during that time.

Special thanks to the Prof. P.E. Christopoulou for the constant support since my Bachelor studies, as well as to the Professors of Astrophysics of the University of Crete for creating a great working environment. Special thanks to the Skinakas observatory personnel, A. Steiakaki, T. Kougentakis, G. Paterakis, and M. Palaiologou, for the technical assistance and the amazing time we had these last five years at the Skinakas office.

Many thanks to the Post-Docs and fellow PhD students who have passed through the University of Crete: G. Liodakis, A. Maragkoudakis, I. Leonidaki, K. Kouroumpatzakis, G. Maravelias, K. Kovlakas, P. Sell, J. Andrews, D. Blinov, I. Psaradaki, A. Psychogios, P. Bonfini, for the useful discussions, help whenever needed, and for the wonderful time in Heraklion.

I more than thankful to my colleague and good friend Maria Kopsacheili for always being there and putting up with me every single day. Special thanks for their continuous support, since our Bachelor studies, to my good friends, Theodora, Voula, Efi, and Gogo. Many thanks also to Lina, Katerina, Giannis, Georgia, and Nikos, for the moments we shared fighting for a different and better society.

Last but not least, I will always be grateful to my family, Loukas, Chara, Th. Maria, and especially to my parents, Mitsos and Olga, for making me love astronomy as a kid, and for their immense support all these years.

Contents

List of Figures

List of Tables

1
Introduction

1.1 The beginning of X-ray astronomy

It was 1895, when Wilhelm C. Röntgen discovered in his laboratory, in Würzburg, Germany, a new form of radiation. This radiation could penetrate paper, wood, aluminium but was stopped from heavier elements and also showed the shadow of his bones in his hand. Röntgen named this unknown radiation 'X-rays' (also called today Röntgen radiation), which had immediate application in the medical world, and gave him the first Nobel Prize in Physics in 1901.

Today, more than 120 years since the discovery of X-rays, X-ray Astronomy has become a major branch of Astronomy. However, it is interesting how astronomers at the beginning of the 20th century were very sceptical about the existence of objects capable of generating detectable amount of high-energy radiation. That would require astrophysical objects that have temperatures of millions of degrees, which was in contrast with the temperature of thousands of degrees observed on the surface of stars.

Since X-rays cannot penetrate Earth's atmosphere, they can only be detected above the atmosphere. This was made possible for the first time using rockets available from World War II. These studies (mainly from the U.S. Naval Research Laboratory; Herbert Friedman) revealed that the Sun was a powerful source of X-ray radiation, but also discouraged astronomers since more distant objects would need to be up to 10^{11} times more luminous than the Sun in order to be detected.

It was in 1962 that a group at the American Science and Engineering, led by Riccardo Giacconi, detected the first powerful cosmic X-ray source: Sco X-1 (Giacconi *et al.*, 1962) which was the first Galactic X-ray binary (XRB) ever to be observed. This initial discovery led to the identification of more X-ray sources in the early 60s, forcing astronomers to think of new cosmic objects, astrophysical processes, and methods of energy production. Since then, X-ray Astrophysics evolved rapidly, and in the 70s the first satellite mission *Uhuru* (NASA, PI: Giacconi) was launched, with numerous others following up to now (e.g. *EXOSAT*, *Einstein*, *ROSAT*, *Rossi XTE*, *BeppoSAX*, *Chandra*, *XMM-Newton*, *Swift*, *Suzaku*, *eROSITA*) which have transformed the landscape of Astrophysics.

1.2 Populations of X-ray binaries

The first X-ray survey of the sky (*Uhuru*), showed that the most common luminous X-ray sources in our Galaxy are XRBs. With the beginning of imaging X-ray astronomy and the *Einstein* mission, many XRBs have been detected in a number of nearby galaxies (e.g. Fabbiano, 1989). With following missions (*ROSAT*, *ASCA*, *XMM-Newton*) and the exquisite angular resolution of Chandra (0.5 arcsecond), populations of luminous point-like sources have been detected even in more distant galaxies (>50 Mpc) (for a review see: Fabbiano, 2006, Fig 1.1) providing a more complete picture of the X-ray content of galaxies.

Today we know that the X-ray emission of normal galaxies (i.e. galaxies not hosting an Active galactic Nucleus (AGN)), is dominated by the collective emission of their XRB populations at energies $\gtrsim$2 keV and by a hot gaseous component at energies $\lesssim$2 keV (for a review see Fabbiano (2006)). In the case of an AGN, the emission is produced by accretion of material onto the super-massive black hole in its centre, and it generally outshines the emission produced by the rest of the galaxy unless the luminosity of the AGN is very low ($< 10^{39}\ ergs^{-1}$), or if it is obscured.

In this work we mostly focus on the XRB population of star-forming galaxies. XRBs are binary systems composed of a stellar remnant and a companion star. The stellar remnant is either a black hole (BH), a neutron star (NS), or a white dwarf (WD). The X-rays are produced by the gravitational accretion of material from the atmosphere of the companion star (also referred to as donor or secondary) onto the compact object (primary). Depending on the mass of the stellar companion the XRBs are divided in high-mass XRBs ($M \gtrsim 10M_{\odot}$; HMXBs), and low-mass XRBs ($M \lesssim 3M_{\odot}$; LMXBs).

Two main forms of mass transfer mechanisms are responsible for powering the X-ray

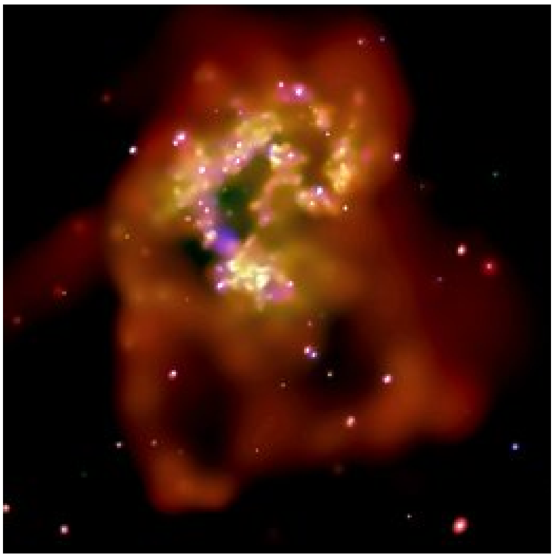

Figure 1.1: *Chandra* X-ray image of the Antennae galaxy - Smoothed color Chandra image of the Antennae galaxies. With red, green, and blue colours we see the low, medium, and high energy X-rays. It is clear that point sources (XRBs) dominate at medium and hard energies while we see in red and low energies the diffuse hot gas of the galaxy. Credit:NASA/CXC/SAO/Fabbiano *et al.* (2003)

source: i) through a stellar wind, and ii) through Roche-lobe overflow (Fig. 1.2). Mass transfer through a stellar wind is commonly seen in HMXBs, where the companion is an O or B type star which emits a powerful stellar wind driven by radiation pressure. A fraction of the stellar wind is intercepted by the compact object and it is eventually accreted. The accretion luminosity in this case, depends on the wind mass loss rate, its velocity, and the compact object mass.

Accretion through Roche-lobe overflow takes place when the companion star has evolved to fill its Roche lobe (surface of equal gravity), and its transferring material through the inner Lagrangian point. Because of its angular momentum, the matter forms an accretion disc around the compact object and friction converts part of the gravitational energy into thermal energy which is radiated in the X-ray band. This mechanism is seen in LMXBs, where the companion star is of low mass and therefore it will not have a strong stellar wind, but also in some of the HMXBs where the companion star is a super-giant star. The accretion through Roche-lobe overflow is the most efficient among the two mechanisms resulting generally in more luminous sources.

Since HMXBs are associated with early-type stars they follow the evolution of the companion star and they are short-lived systems (up to a few million years) representing

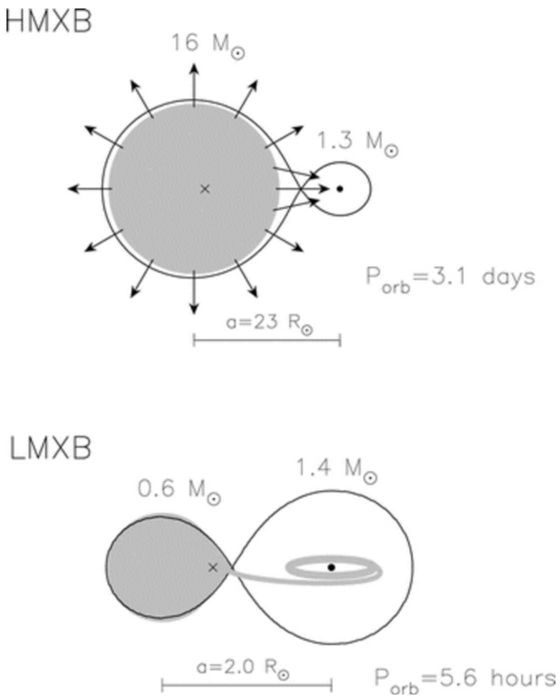

Figure 1.2: Schematic representation of the two mass transfer mechanisms in XRBs: - wind accretion (taking place in HMXBs) and Roche lobe overflow (taking place in LMXBs but also in HMXBs with evolved donors).

younger stellar populations. As a result they are often found in star-forming galaxies or on the spiral arms of spiral galaxies. On the other hand, LMXBs represent older stellar populations and they have generally longer lifetimes ($\sim 10^9 yrs$). Therefore, they are usually found in elliptical galaxies or galaxy bulges. They are also found in Globular Clusters, or in galactic halos. Fig 1.3 shows the distribution of HMXBs, and LMXBs in the Milky way. The former trace young stellar populations, while the latter trace old stellar populations.

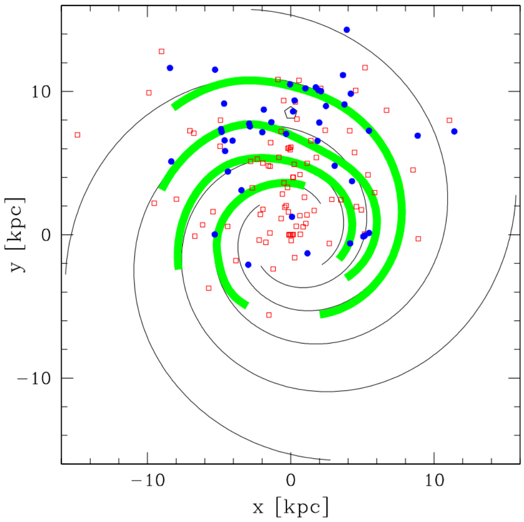

Figure 1.3: Distribution of XRBs in the Galaxy. - Face-on view of the distribution of XRBs in the Milky Way (Grimm *et al.*, 2002). HMXBs (blue filled circles) are located on the spiral arms, in the plane of the Galaxy and LMXBs (red open circles) which are older are located in the Galactic Bulge.

The most extreme manifestation of XRBs are the so-called Ultra-luminous X-ray sources (ULXs). ULXs are off-nuclear sources that have luminosities $L(0.3 - 10.0\, keV) > 10^{39}\ erg\ s^{-1}$ which exceed the Eddington luminosity of a typical stellar-mass black hole or a neutron star, requiring very high accretion rates. In some cases ULXs are so bright that they can dominate the X-ray output of the entire galaxy like in the case of the galaxy M 82. In general ULXs are more abundant in low metallicity galaxies (e.g. Douna *et al.*, 2015; Prestwich *et al.*, 2013) and are found in large numbers in merging and star-forming galaxies (e.g. Anastasopoulou *et al.*, 2016; Swartz *et al.*, 2011).

Two main models have been proposed to explain what powers their high luminosities. The first model assumes accretion onto an intermediate-mass black hole (IMBH).

IMBHs consist a hypothetical third class of objects with masses ($\sim 10^2 - 10^5$ $M_\odot$), ranging between those of stellar mass BHs and super-massive BHs. This range of masses allows for ULX luminosities without exceeding the Eddington limit. However, there is very little observational evidence for their existence (e.g. Kaaret *et al.*, 2017). In addition, it is not clear either how such black holes can form an X-ray binary system.

The second model is that of super-Eddington accretion onto a stellar-mass BH or a NS XRB (e.g. Kaaret *et al.*, 2017; King, 2002, 2009; Wiktorowicz *et al.*, 2015, 2017). In this case the accretion takes place via a slim or thick accretion disk which forms a funnel around the compact object. For example Narayan *et al.* (2017) presenting relativistic magneto-hydrodynamic simulations of super-Eddington accretion on a $10M_\odot$ BH find that such accretion disks can reproduce the main empirical spectra observed in ULXs, and produce luminosities that exceed $L > 10^{40}$ $erg\ s^{-1}$. The model of the super-Eddington accretion with beamed emission, has become the generally most accepted model to explain the ULX nature, especially after the discovery of pulsar ULXs (M 82 X-2; being the first example of this class Bachetti *et al.*, 2014).

1.3 Correlations with multi-wavelength data

The study of individual sources in nearby (<20Mpc) galaxies has been very important to understand the properties of XRB populations. Equally important in this aspect has been the study of the integrated emission of samples of galaxies, that are more distant or observed with lower resolution instruments. Therefore, XRB populations can be studied in a variety of different environments than is possible for the small volume for which we can detect resolved XRB populations. In this way, we can interpret the XRB emission in the context of stellar populations (e.g. star-formation rate (SFR), stellar mass (M_*)) of a galaxy.

The first sample of galaxies ever observed with *Einstein* (for reviews see: Fabbiano, 1989, 1995) has shown that the integrated X-ray luminosity of galaxies hosting old stellar populations (morphological types E and S0) scaled with their optical luminosity (i.e. the stellar population). In spiral galaxies which host younger stellar populations, their X-ray luminosity scaled with their far-IR emission (i.e. star-forming activity). Several other studies, using *ROSAT*, *BeppoSAX*, and *ASCA* data, have confirmed the correlation between the luminosity of the XRB populations and the SFR in star-forming galaxies (e.g. Ranalli *et al.*, 2003; Read & Ponman, 2001).

But it was with the exquisite spatial resolution of *Chandra* and the high effective area of XMM-Newton that the deepest samples of XRBs have been acquired in nearby

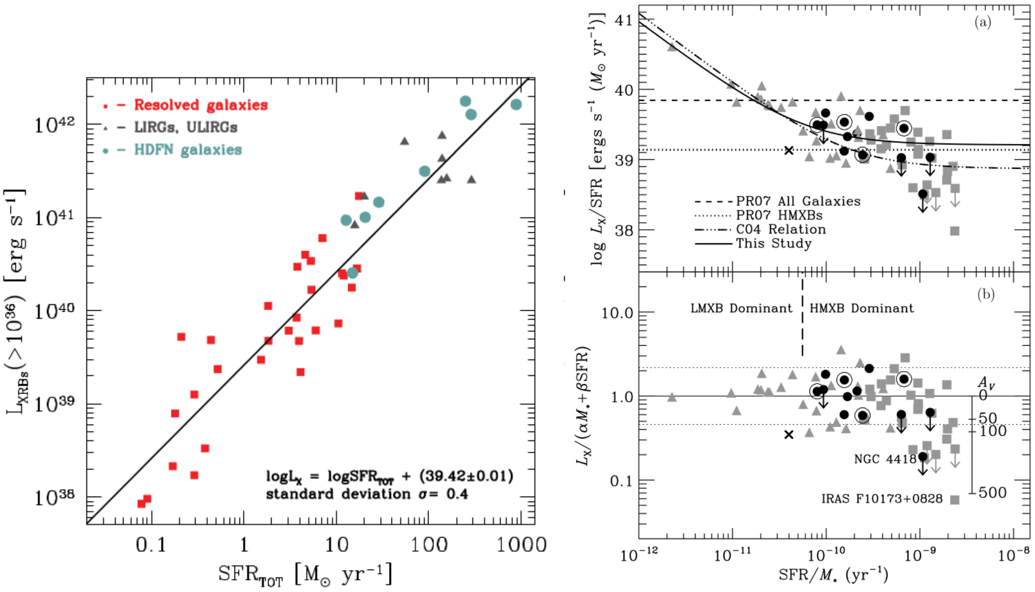

Figure 1.4: Left: Lx(HMXBs)/SFR scaling relation from Mineo *et al.* (2012a); Right: Lx/SFR-sSFR scaling relation from Lehmer *et al.* (2010).

galaxies. *Chandra* studies of nearby star-forming galaxies have confirmed that the X-ray emission of the young XRBs (i.e. HMXB population) scales with the SFR of the galaxy (Lx(HMXBs)-SFR scaling relation), while the X-ray emission of the old XRBs (i.e. LMXB population) scales with the stellar mass (Lx(LMXBs)-M_*) scaling relation) of the galaxy (e.g. Gilfanov, 2004; Grimm *et al.*, 2003; Lehmer *et al.*, 2010, 2014; Mineo *et al.*, 2012a). For example Mineo *et al.* (2012a) (Fig 1.4; left panel) studied the HMXB populations in 29 nearby star-forming galaxies and calculated a linear correlation of $L_X \approx 2.6 \times 10^{39} \times SFR$ with a rather large dispersion of rms ∼0.4 dex. Similar scaling relations have been reported for the number of ULXs (e.g. Fig. 1.5; Mapelli *et al.*, 2010). On the other hand, Lehmer *et al.* (2010) (Fig 1.4; right panel) studied 17 luminous infrared galaxies, and provided a more physical scaling relation of the form $Lx = \alpha M + \beta SFR$, with $\alpha = (9.05 \pm 0.37) \times 10^{28} ergs^{-1} M^{-1}$, and $\beta = (1.62 \pm 0.22) \times 10^{39} ergs^{-1} (Myr^{-1})^{-1}$). This scaling accounts for the X-ray emission from both HMXBs and LMXBs, assuming they scale linearly with SFR and M_* respectively. They found that this correlation has less scatter of about ≈0.1-0.2 dex, than the Lx-SFR correlation. These results indicate, that HMXBs dominate the galaxy-wide X-ray emission for galaxies with SFR/M $\gtrsim 5.9 \times 10^{-11} yr^{-1}$.

Moreover the scaling relations have been found to depend on other physical parameters of the galaxy like the age and the metallicity. For a number of powerful star-forming galaxies the Lx(HMXBs)-SFR scaling relations are elevated for lower metallicities (e.g. Basu-Zych *et al.*, 2013a; Brorby *et al.*, 2014). This is also consistent with studies of ULXs, showing larger number of ULXs per SFR in lower metallicity galaxies (Fig 1.5; Brorby *et al.* (2014); Douna *et al.* (2015); Mapelli *et al.* (2010)).

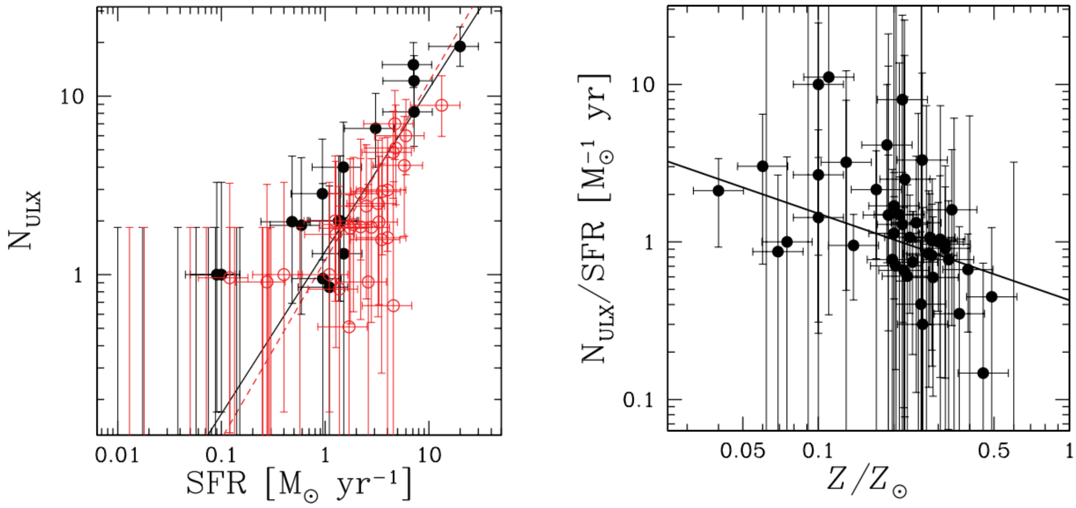

Figure 1.5: Left: Number of ULXs versus the SFR. Galaxies with metallicity $\leq 0.2\ Z_\odot$ are shown with filled black circles and galaxies with metallicity $\geq 0.2\ Z_\odot$ are shown with open red circles. Right: Number of ULXs normalised with the SFR versus metallicity (Mapelli *et al.*, 2010).

Studies of nearby early type galaxies (Boroson *et al.*, 2011; Lehmer *et al.*, 2014; Zhang *et al.*, 2012) have shown that there is a dependence of the Lx(LMXBs)-M_* relation with the stellar age: older galaxies tend to have more LMXBs than younger galaxies, which is explained by the evolution of the LMXB population with time. Evolution of the scaling relation with redshift have also been identified (e.g. Aird *et al.*, 2017; Basu-Zych *et al.*, 2013b; Fornasini *et al.*, 2018; Lehmer *et al.*, 2016; Mineo *et al.*, 2014). This is probably a result of the decrease in mean stellar age and metallicity with look-back time. Indeed this has been confirmed by Fornasini *et al.* (2019) who found direct evidence connecting the redshift evolution of Lx-SFR and the metallicity of HMXBs. These dependences of the scaling relations with metallicity, age, and redshift are also in agreement with theoretical expectations from XRB population synthesis models (Fig. 1.6; e.g. Fragos *et al.*, 2013; Linden *et al.*, 2010; Wiktorowicz *et al.*, 2015).

]]>

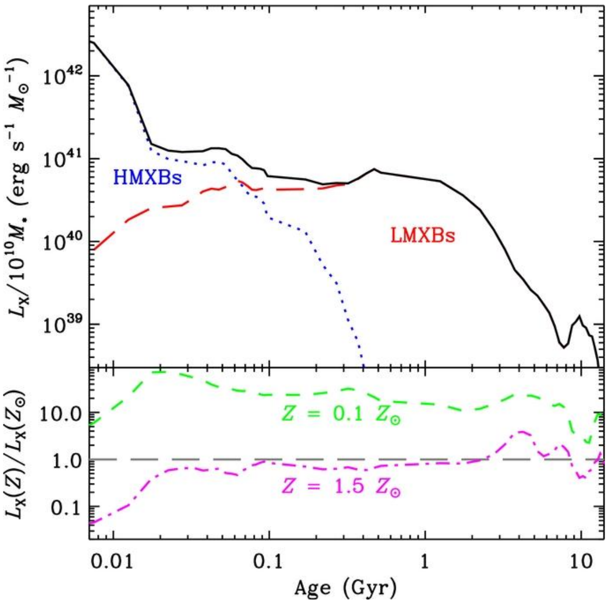

Figure 1.6: Top panel: Evolution of an XRB population as function of age, and for solar metallicity. Bottom panel: evolution of the same XRB population for sub-solar and super-solar metallicies compared to solar (Fragos *et al.*, 2013).

1.4 Motivation

Such scaling relations are important because they provide insights for the connection of the X-ray output of galaxies with the stellar populations which are responsible for it. In addition, they give a reference for investigations of the study of the evolution of the X-ray emission in high-z star-forming galaxies. Therefore, the scaling relations for HMXBs and LMXBs provided a metric to measure XRB formation and evolution parameters by directly comparing theoretical models with observed XRB populations.

The populations and integrated X-ray luminosity of XRBs, depend strongly on the parameters that drive their formation and evolution (e.g. Fragos *et al.*, 2013; Tzanavaris *et al.*, 2013). For example, Tzanavaris *et al.* (2013), compared the integrated luminosity from theoretical X-ray luminosity functions of LMXBs and HMXBs calculated for different XRBs formation parameters to the measured scaling relations in the local Universe. They found that the scaling relations were consistent with the expectation from the XRB formation model that best reproduced the observed X-ray luminosity function of resolved sources. Similarly, Lehmer *et al.* (2010) and Basu-Zych *et al.* (2013a) compared these models with scaling relations in local and higher-z galaxies and were able to discriminate between different XRB formation and evolution models. Therefore, in these research efforts we are interested in the study of X-ray source populations in nearby galaxies, in an effort to better understand and constrain their association with physical parameters of the host galaxies.

Since scaling relations are based on local galaxies with star formation rates up to ~ 20 $M_\odot$/yr (e.g. Lehmer *et al.*, 2010; Mineo *et al.*, 2012a), and there is some evidence for evolution of these scaling relations with SFR (Basu-Zych *et al.*, 2013a; Mineo *et al.*, 2014), it is important to examine their validity in the most extreme cases. For this reason in Chapter 2 we present the detailed analysis of Chandra data of one of the most powerful star-forming, ULX-rich galaxies in the local Universe, Arp 299. In order to explore the effect of local variations of the stellar populations on these correlations, in Chapter 3, we analyse Chandra data of two nearby star-forming galaxies which have been found to host large number of ULXs, NGC 3310 and NGC 2276 (e.g. Lehmer *et al.*, 2015; Wolter *et al.*, 2011, 2015). These two galaxies due to their proximity, local variations of star-forming activity, and large number of X-ray sources, are excellent laboratories for studying the validity of the general relations between X-ray binaries and star-forming activity to galaxies with large numbers of ULXs, even at sub-galactic scales.

However, since all studies of general scaling relations between X-ray luminosity and stellar populations (SFR, M_*) so far have been based on small samples of galaxies (couple dozen), we want to examine how representative these scaling relations are for the majority of galaxies in the local Universe. In Chapter 4 we measure the scaling relations between the luminosity of the X-ray binary populations and the physical properties (SFR and M_*) of the host galaxy. Our sample contains 650 local galaxies observed by *XMM-Newton*, yielding the largest X-ray sample in the local Universe and covering 4 orders of magnitude in SFR and M_*. We quantify the scaling relations and also we evaluate the amount of scatter, for the most representative sample in the local Universe.

2

A deep *Chandra* observation of the interacting star-forming galaxy Arp 299

2.1 Introduction

X-ray emission of galaxies is key for understanding compact object populations and accreting binaries and in particular their most extreme manifestation the so-called Ultra-Luminous X-ray sources (ULXs; defined as off-nuclear point sources that have luminosities $L_{(0.1-10.0 \text{ keV})} > 10^{39}$ erg s^{-1}). In particular, high star-formation rate galaxies often host large populations of ULXs (e.g. Swartz *et al.*, 2011). As such they are useful for studying the population, demographics, and scaling relations of ULXs with galaxy parameters. Since scaling relations are based on local galaxies with star formation rates (SFR) up to a few (~ 20) $M_{\odot}$/yr (e.g. Lehmer *et al.*, 2010; Mineo *et al.*, 2012a), and there is some evidence for evolution of these scaling relations with SFR (Basu-Zych *et al.*, 2013a; Mineo *et al.*, 2014), examining if a local highly star-forming galaxy verifies these relations is an important test of their applicability to the most extreme star forming galaxies and is informative for their use as analogues of high-z galaxies.

Arp 299 is one of the most powerful star-forming galaxies in the local Universe (44Mpc; Heckman *et al.*, 1999) belonging to the class of Luminous Infrared Galaxies (LIRGs; Sanders & Mirabel, 1996) with a total infrared luminosity of $L_{\rm IR} = 5.16 \times 10^{11} L_{\odot}$

(Charmandaris *et al.*, 2002). It consists of two galaxies in an advanced merging state separated by ∼22". The western galaxy is referred to as NGC 3690 (or B) and it is believed to host an AGN (Ballo *et al.*, 2004; Della Ceca *et al.*, 2002; Ptak *et al.*, 2015; Zezas *et al.*, 2003). The eastern galaxy is referred to as IC 694 (or A) and the overlapping region as C and C' (following the nomenclature of Hibbard & Yun, 1999).

Due to its proximity and intense star forming activity Arp 299 has been studied extensively in all wavelengths. Optical and infrared observations have shown that Arp 299 is dominated by widespread star formation taking place in the two nuclei and in the overlapping area with typical ages of ∼ 15Myrs (Alonso-Herrero *et al.*, 2000). Results in the mid infrared show that most of the star-forming regions are deeply embedded into dust (Charmandaris *et al.*, 2002). Recent *Spitzer*/IRS results are now showing that the integrated mid-infrared spectrum of Arp 299 exhibits a remarkable similarity with those of high-z Ultra Luminous Infrared Galaxies (ULIRGs) albeit its lower luminosity and possibly higher metallicity. This suggests that it may represent a local example of the star-forming processes occurring at high-z (Alonso-Herrero *et al.*, 2009).

In the X-ray regime Arp 299 is the second most luminous galaxy in the local Universe ($\lesssim$ 50 Mpc) with a luminosity of L(0.1 − 10.0 keV) = 4×10^{41}ergs s^{-1} (Heckman *et al.*, 1999; Zezas *et al.*, 1998). A short 24 ks *Chandra* observation obtained in 2001 showed that Arp 299 hosts 16 ULXs, one of the richest galaxies in the local Universe, although the short exposure allowed to probe only a fraction of the overall population (Zezas *et al.*, 2003). Luangtip *et al.* (2015) studied a sample of 17 nearby LIRGs (including Arp 299) and found a general deficit in their number of ULXs per unit SFR compared to the rate in nearby normal star-forming galaxies from Swartz *et al.* (2011). This result is also supported by Smith *et al.* (2012) who found that the total number of ULXs in LIRGs (including Arp 299) normalised to their far-infrared luminosity is deficient in comparison to the ULX rates found for spiral galaxies. They argue that metallicity may have some influence on ULX numbers but the main reason for this deficit is high columns of gas and dust that obscure these ULXs from our view. If this trend holds for galaxies experiencing intense starbursts, it will have important implication for understanding the X-ray output of high-z galaxies.

Furthermore *BeppoSAX* revealed for the first time the existence of a deeply buried ($N_H \sim 2.5 \times 10^{24} cm^{-2}$) AGN with a luminosity of $L_{0.5-100\ keV} \simeq 1.9 \times 10^{43} erg\ s^{-1}$ (Della Ceca *et al.*, 2002). *Chandra* and *XMM-Newton* observations confirmed the existence of a strongly absorbed AGN and located it in the nucleus of NGC 3690 while there is evidence that the second nucleus IC 694 might also host an AGN of lower luminosity (Alonso-Herrero *et al.*, 2013; Ballo *et al.*, 2004; Iwasawa *et al.*, 2009; Pérez-Torres *et al.*, 2010; Zezas *et al.*, 2003). Recent results of simultaneous observations with *NuSTAR* and *Chandra* (including *Chandra* data presented in this paper) confirmed the existence of an AGN in NGC 3690 constrained its total X-ray luminosity to $L(10-30 \text{ keV}) \sim 1.2 \times 10^{43} \text{ergs}^{-1}$ and its obscuring column density to $N_{\rm H} \sim 4 \times 10^{24} \text{cm}^{-2}$. It also showed that any AGN in IC 694 must be heavily obscured or have a much lower luminosity than that in NGC 3690 (Ptak *et al.*, 2015).

In this paper we analyse data from a deep *Chandra* observation of Arp 299 ($\simeq$ 90 ks) which allow us to further explore the nature of the X-ray source population in this interesting system. In particular we are able to study the entire population of ULXs by reaching a detection limit of 4×10^{38} erg s^{-1} and to explore the contribution of the AGN to the energetics of the galaxy. Arp 299 is possibly an analogue of actively star-forming galaxies at higher redshifts (Alonso-Herrero *et al.*, 2009). Therefore studying its hot gaseous and X-ray binary components and energetics with this deep *Chandra* high resolution observation and their scaling with its star-forming activity we can have useful insights of the nature of the high-z normal galaxies detected in medium and high depth surveys where a detailed analysis of the sources is not possible.

The structure of the paper is as follows: In section 3.2 we describe the observation, the data analysis and our results. We discuss our results in section 4.5 and in section 4.6 we summarize our findings. All errors from spectral analysis correspond to the 90% confidence interval unless otherwise stated.

2.2 Observation and Data Analysis

Chandra (Weisskopf *et al.*, 2000) observed Arp 299 with the ACIS-S camera (Garmire, 1997) for a total of 90.37 ks. The observation was split in two segments due to scheduling constraints: a 38.49 ks exposure performed on the 12th of March 2013 (OBSID 15619) and a second exposure of 51.88 ks performed on the 13th of March 2013 (OBSID 15077). The data analysis was performed with the CIAO software version 4.7 and CALDB version 4.6.5. To apply the latest calibration data we reprocessed the Level-1 events files using the *acis_process_events* tool. We then created the Level-2 events files using the *dmcopy* tool to filter for bad grades and status bits (keeping only grades=0, 2, 3, 4, 6 and status=0). We checked for background flares during our observation and we found that the background level is fairly constant.

Since the two observations are almost contiguous, and they are performed at the same ROLL angle and pointing, we created an events file for the merged exposure.

Using the *reprojec_obsid* tool we first reprojected the two Level-2 files to a common tangent point and then we combined them to create the merged Level-2 events file. The scientific analysis was performed on these three files.

We created images as well as exposure maps in the broad (0.5-7.0 keV), soft (0.5-1.2 keV), medium (1.2-2.0 keV), and hard (2.0-7.0 keV) bands using the *fluximage* tool for the reprojected files and the *flux_obs* tool for the merged one. We additionally normalized all the exposure maps to the exposure of a reference pixel at approximately the centre of the galaxy.

We adaptively smoothed these images using the *csmooth* CIAO tool with a Gaussian convolution kernel, and applying a minimum and maximum signal-to-noise ratio of 3 and 5 respectively. A "true colour image" consisting of the soft (red), medium (green), and hard (blue) smoothed images for the merged observation is shown in Fig. 2.1. From this image we see a population of discrete sources (§3.2.1) and extended soft diffuse emission of the galaxy.

2.2.1 Source Detection

We used the *wavdetect* tool (Freeman *et al.*, 2001) to detect discrete sources. We searched in the broad (0.5-7.0 keV), soft (0.5-1.2 keV), medium (1.2-2.0 keV), and hard band (2.0-7.0 keV) images of the reprojected individual observation segments, as well as, the merged dataset for sources on scales of 2, 4, 8, and 16 pixels. We then cross-correlated the source lists created in all bands of the individual and the merged observations. We visually inspected the final source list in order to make sure that no individual sources were excluded. We found in total 42 sources within the D25 region of the galaxy (RC3; Corwin *et al.*, 1994; de Vaucouleurs *et al.*, 1991).

In order to calculate the photometric parameters of the sources, we manually defined a source aperture based on the merged observation. We took care to include as many of the source counts as possible and at the same time to avoid contamination from nearby sources and background. The minimum aperture radius of ($\sim 1''$) which encompasses at least 90% of the encircled energy at 1.49 keV of an on-axis point source for the ACIS-S camera was satisfied by the mean aperture radius of our sources which is $\sim 1.3''$. The background was defined as an annulus around each source with inner radius about 1-2 pixel larger than the source aperture in order to avoid contamination by the wings of the source PSF and outer radius large enough ($\sim$ 2-5$''$) to obtain good count statistics to perform photometry and to avoid contamination from nearby sources.

We used the *dmextract* tool to perform the photometry on the 42 sources in the merged and individual exposures for the broad, hard, medium, and soft bands. In more

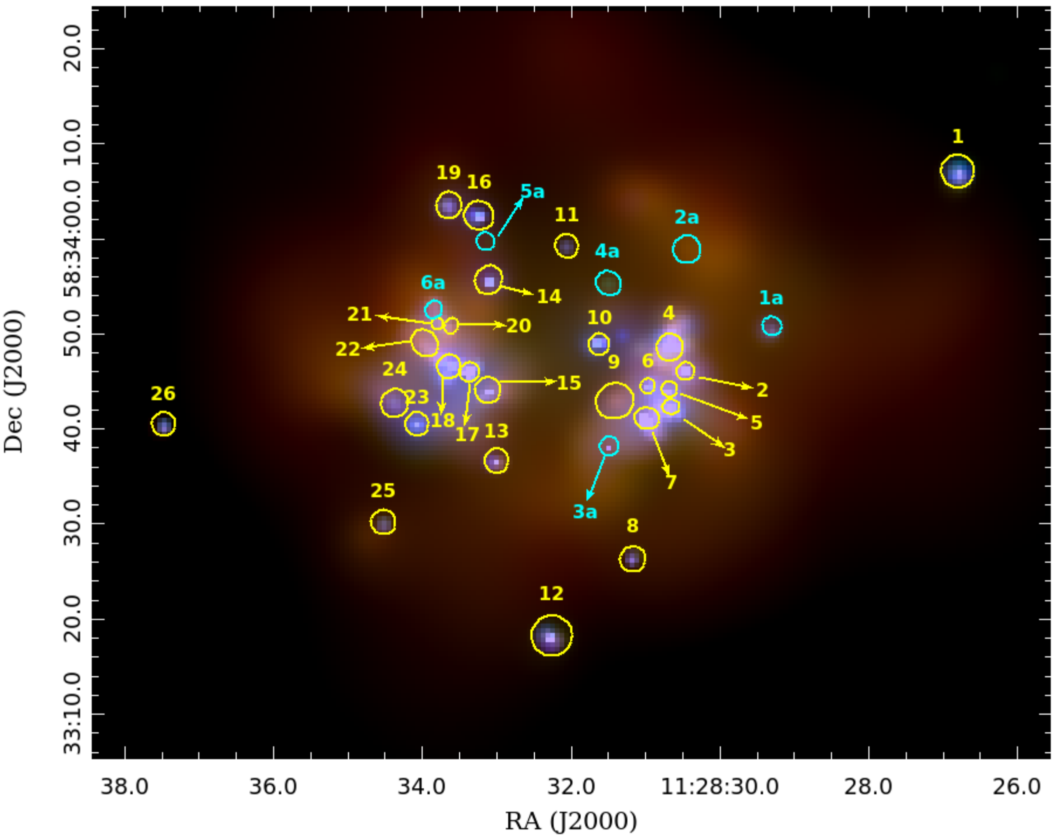

Figure 2.1: Smoothed colour image of Arp 299 -An adaptively smoothed true colour image of Arp 299 from the merged observation. We show with red colour the soft band (0.5-1.2 keV), with green colour the medium band (1.2-2.0 keV), and with blue the hard band (2.0-7.0 keV). Overlaid are the 26 sources with SNR > 3.0 (yellow circles) as well as the 6 detections (1a to 6a; cyan circles) with 2.0 <SNR< 3.0 that are noted as possible sources.

Table 2.1: Properties of the discrete sources in the broad band (0.5 – 7.0 keV).

Src	RA	Dec	Net counts	Bkg	S/N	r_1	r_2	Src ID	Notes
ID	h m s	$^{\circ}$ $'$ $''$	±error			$''$	$''$	(Z03)	
(1)	(2)	(3)	(4)	(5)	(6)	(7)	(8)	(9)	(10)
1	11:28:26.8	+58:34:07	135.3 ± 12.9	4.7	10.1	1.74	1.73	1	ULX
2	11:28:30.4	+58:33:46	430.8 ± 25.3	115.2	15.9	0.93	0.94	-	ULX
3	11:28:30.6	+58:33:42	336.2 ± 28.7	260.7	10.9	0.92	0.77	4?	ext (hard)
4	11:28:30.7	+58:33:48	583.0 ± 37.8	372.0	15.4	1.43	1.39	2	C; ext (hard)
5	11:28:30.7	+58:33:44	206.2 ± 19.8	84.8	9.9	0.82	0.82	3	ext (hard)
6	11:28:31.0	+58:33:44	140.5 ± 16.7	80.5	7.5	0.73	0.80	5	ULX
7	11:28:31.0	+58:33:41	892.5 ± 37.3	264.4	22.8	1.31	1.11	6	AGN; B1; ext
8	11:28:31.2	+58:33:26	35.2 ± 7.5	5.8	4.2	1.33	1.36	7	
9	11:28:31.4	+58:33:43	72.2 ± 24.5	172.7	3.3	2.00	1.85	-	ULX
10	11:28:31.6	+58:33:49	221.3 ± 16.9	23.6	12.5	1.08	1.13	8	ULX; C”
11	11:28:32.0	+58:33:59	23.2 ± 6.8	6.8	3.0	1.27	1.18	-	
12	11:28:32.2	+58:33:18	198.2 ± 15.6	12.8	12.2	2.11	2.15	9	ULX
13	11:28:33.0	+58:33:37	70.3 ± 11.1	24.6	5.7	1.23	1.30	10	ULX
14	11:28:33.1	+58:33:56	195.0 ± 16.6	30.0	11.2	1.40	1.54	11	ULX
15	11:28:33.1	+58:33:44	147.6 ± 19.3	99.4	7.4	1.36	1.34	12	ULX
16	11:28:33.2	+58:34:02	213.7 ± 16.4	8.2	13.0	1.57	1.47	13	ULX
17	11:28:33.3	+58:33:45	559.9 ± 28.1	109.0	19.1	1.04	0.99	14	ULX
18	11:28:33.6	+58:33:46	423.3 ± 36.9	294.6	12.7	1.28	1.20	16	A; ext (hard)
19	11:28:33.6	+58:34:03	56.7 ± 10.3	17.3	5.1	1.31	1.41	-	ULX;variable[a]
20	11:28:33.6	+58:33:51	43.3 ± 12.1	58.7	3.0	0.85	0.71	15	ext
21	11:28:33.8	+58:33:51	45.3 ± 11.5	40.6	3.6	0.67	-	15	
22	11:28:34.0	+58:33:49	132.1 ± 25.4	238.8	5.0	1.54	1.27	-	blob; ext (hard)
23	11:28:34.1	+58:33:40	133.1 ± 15.0	45.8	8.1	1.21	1.23	17	ULX
24	11:28:34.4	+58:33:43	50.0 ± 12.8	61.9	3.4	1.40	1.51	-	ext (hard)
25	11:28:34.5	+58:33:30	26.5 ± 7.0	7.4	3.3	1.29	1.28	-	
26	11:28:37.5	+58:33:40	35.6 ± 7.2	1.4	4.7	1.21	1.23	18	ULX

Column 1: The source identification number, Columns 2 and 3: Sky coordinates, Column 4: Net source counts and corresponding error counts, Columns 5 and 6: The background source counts and the signal to noise ratio of each source, Columns 7 and 8: The two ellipse major and minor radius for the source apertures, Column 9: The corresponding source identifier from Zezas *et al.* (2003), Column 10: Comments on variability, extension, and name sources from previous works. Sources that are point-like ULXs are also reported in this column.

---

[a] See §2.6.

detail we ran *dmextract* on the images and normalized exposure maps for the discrete sources and on the background image. The errors on the number of counts were calculated following the Gehrels approximation (Gehrels, 1986). We calculated the signal to noise ratio (SNR) of each source as $\mathrm{SNR} = \mathrm{S}/\sqrt{(1+\sqrt{0.75+\mathrm{T}})^2 + (1+\sqrt{0.75+\mathrm{B}})^2}$ where S are the net source counts, T the total counts, and B the estimated background counts for each source rescaled to the source area. We consider as significant detections and therefore present in this paper the results for the 26 sources that have $\mathrm{SNR} \geq 3.0$. We also present six detections (1a-6a) that exceeded $\mathrm{SNR} = 2.0$ as possible sources.

The photometry for the 26 sources obtained from the merged events file is presented in Table 2.1 for the broad band. Column (1) gives the source number, Columns (2) and (3) give the sky coordinates, Column (4) gives the net source counts and the corresponding error counts. The background source counts and the signal to noise ratio of each source are presented in columns (5) and (6). Columns (7) and (8) give the ellipse major and minor radius for the source apertures. Column (9) gives the corresponding source identifier from Zezas *et al.* (2003), and Column (10) presents comments about each source such as variability, extension, and names from previous works. The same information for the hard, medium, and soft bands is presented in the Appendix (Table 2.8). The description of columns is the same as for columns (1)-(6) of Table 2.1. Columns (7)-(10) of Table 2.1 are exactly the same and thus not included. The properties of the 6 lower significance detections (1a to 6a), that are noted as possible sources, are presented in the Appendix (Table 2.9).

The location of 26 discrete sources as well as the 6 lower significance detections (1a to 6a) is shown on the “true colour image” of Fig. 2.1.

In Fig. 2.2 we overlay the location of the discrete sources on a multi-band image consisting of HST images in the F814W (814 nm; green) and F435W (435 nm; blue) and a *Spitzer* IRAC band 4 (8 μm; red) non-stellar image. The IRAC non stellar image in particular was produced by subtracting a scaled 3.6 μm image from the 8 μm in order to remove the stellar emission (Brassington *et al.*, 2015). The above filters give a picture of the distribution of the old, young, and obscured young stellar populations respectively (Fig. 2.2). We see that the vast majority of the sources are located within the main body of the galaxy and particularly its most actively star-forming regions.

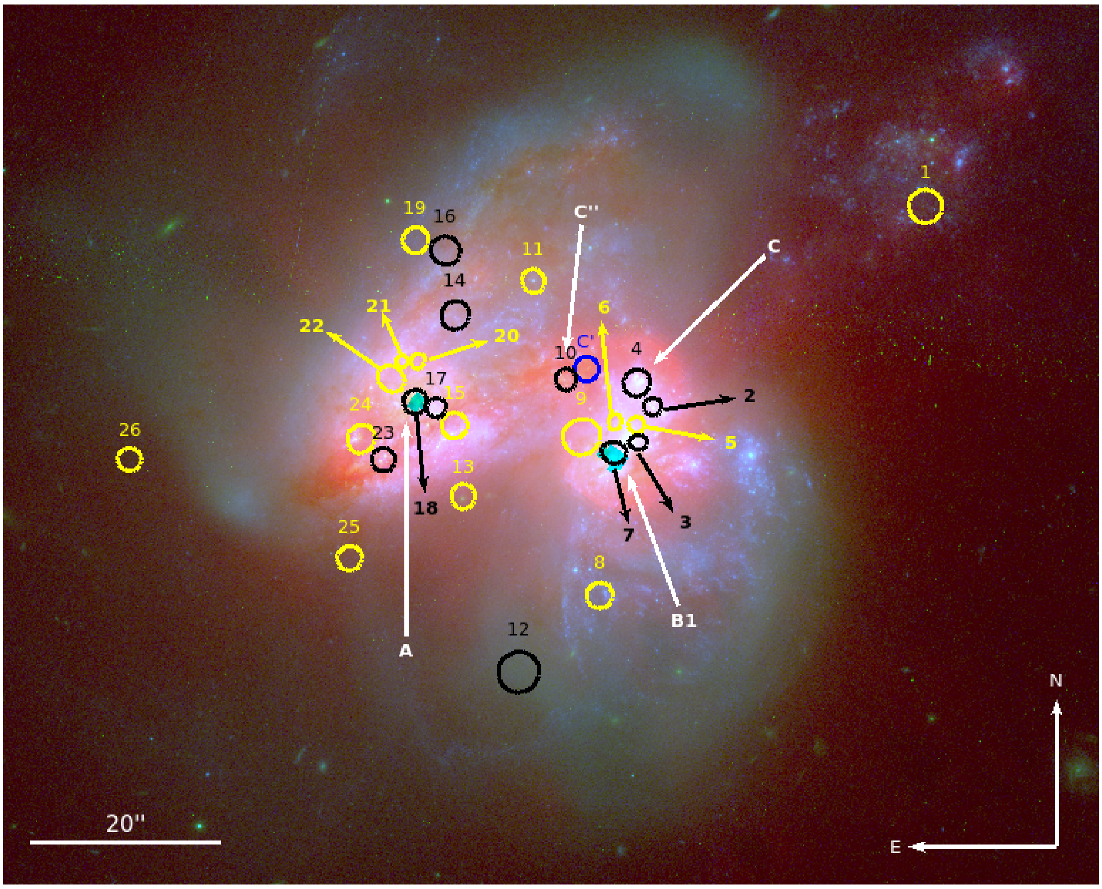

Figure 2.2: Colour image of Arp 299 -Colour image of Arp 299. Composed of a F814W (814 nm; green), F435W (435 nm; blue) HST images and IRAC band 4 (8 μm; red; saturated at the nuclei) non stellar image (see text). The X-ray sources with luminosities L(0.1 − 10.0 keV) $> 5 \times 10^{39}$ erg s^{-1} are shown with black circles, while lower luminosity sources (L(0.1 − 10.0 keV) $< 5 \times 10^{39}$ erg s^{-1}) are shown with yellow circles. With white arrows we show the additional names of our sources Src 18 (A), Src 7 (B1), Src 4 (C), Src 10 (C"); C' is unidentified in our observation and is presented here with a blue circle.

2.2.2 Spectral Analysis

We extracted source and background spectra of the discrete sources using the *specextract* tool. Since the two observations are taken with the same orientation, and within 13 hours of each other, we decided to extract the spectra from the merged events file [1] . This is supported by the fact that the spectral parameters of the sources are consistent between the two observations, while all but one source do not show any variability between the observations (§3.2.5). We supplied *specextract* a stack of the two reprojected events files and a stack of their corresponding auxiliary files, and we ran it with *combine=yes*. This produced the correctly summed Pulse Height Amplitude (PHA) file, spatially weighted Auxiliary Response File (ARF) and Redistribution Matrix File (RMF). As a final step we grouped the resulting spectra to have at least 20 total counts per spectral bin using the *dmgroup* tool to allow for χ^2 fitting.

We fitted the grouped spectra using the XSPEC v12.8.2 software (Arnaud, 1996). We ignored events with energies above 8.0 keV and below 0.4 keV since they are dominated by the background. The spectral fitting was performed only for the 20 sources with more than about $\approx$50 net counts (i.e 3 or more spectral bins). In all but four cases a single power-law model which is generally used to fit the spectra of X-ray binaries (XRBs) with photoelectric absorption gave satisfactory fits. For these sources the photon indices range from $\Gamma = 0.9$ to $\Gamma = 3.9$, consistent with those of XRBs, and the hydrogen column density is typically greater than the Galactic ($\sim 9.5 \times 10^{19}\mathrm{cm}^{-2}$; using the Colden tool[2]).

The spectra of sources 9 and 22 were too noisy after subtracting their local background. Since we extract the background from areas surrounding each source, this indicates that these two sources are local enhancements in the diffuse emission and their spectra are similar to the spectra of their surrounding regions. Therefore, in order to obtain a picture of the physical properties of these regions we extracted background from an area outside the galaxy and we model the diffuse emission with a thermal plasma component.

For Src 9 an absorbed power-law plus a thermal plasma model gave a good fit while for Src 22 a reasonable fit was given by an absorbed thermal plasma model. Source 9 could be a diffuse emission region but the existence of a power-law component suggests that one or more X-ray binaries are embedded in this region. We consider Src 22 a diffuse emission region as its spectrum is well fitted with only a thermal plasma component. The detailed results for the fitted parameters of the 20 sources are reported

---

[1] `http://cxc.harvard.edu/ciao/caveats/merged_events.html`

[2] `http://cxc.harvard.edu/toolkit/colden.jsp`

in Table 2.2.

2.2.3 Hardness ratios

Hardness ratios or X-ray colours are a useful tool for deriving the spectral properties of faint sources. We calculated X-ray colours for all sources; in this way we estimate the spectral parameters for the sources with less than 50 counts while for the brighter sources we can have a direct comparison of the spectral parameters calculated from the X-ray colours and the spectral fits. X-ray colours are defined as $C_1 \equiv \log_{10}(S/M)$, $C_2 \equiv \log_{10}(M/H)$, $C_3 \equiv \log_{10}(S/H)$ where S, M, and H are the net counts in the soft (0.5-1.2 keV), medium (1.2-2.0 keV), and hard (2.0-7.0 keV) bands. In our analysis we use X-ray colours instead of the hardness ratios, since they are better behaved in terms of their error distribution (Park *et al.*, 2006). We calculated the X-ray colours and their uncertainties for the 26 sources, using the BEHR code (Park *et al.*, 2006) which evaluates their posterior probability distribution and provides reliable estimates and confidence limits even when either or both soft and hard counts are very low. The resulting X-ray colours and their corresponding 90% confidence intervals, are presented in Table 2.2.

In order to estimate the spectral parameters of the X-ray sources we created grids on plots involving two different X-ray colours and placed our sources on them. The grids were calculated by simulating absorbed power-law spectra. Fig. 2.3 shows our sources on the grid of the $C_2 - C_1$ plot. We see that while the majority of the sources fall on the grid and particularly the region corresponding to $\Gamma \sim 1.5 - 2.5$ and $N_H < 0.85 \times 10^{22}\mathrm{cm}^{-2}$, there are 5 sources (9, 20, 21, 22, and 24) that fall outside the grid indicating sources with either too low absorption or too steep photon index. For three of them (9, 22, and 24) we have X-ray spectra; two are well fitted with a soft thermal-plasma model (Src 22) or a power-law component combined with a thermal plasma (Src 9), which would increase the intensity of their soft band and shift the C_1 colour to higher values. Source 24 has very large errors in both C_1 and C_2 colours, and particularly C_1 which is most closely related to the column density N_H. Therefore we decided to fix its N_H to the Galactic line-of-sight value. For the rest of the sources we estimate their spectral parameters based on their location on the grid and we present these estimates in Table 2.2. In Table 2.2 we do not include the results of the colours based analysis for sources 7, 9, 18, and 22 which have more complex spectra. For sources 20 and 21 that we cannot estimate their spectral parameters based on their X-ray colours we adopt in our following analysis $\Gamma = 1.7$ and the hydrogen column density at the galactic value $N_H = 9.5 \times 10^{19}\mathrm{cm}^{-2}$ (Table 2.2). This is consistent with

Table 2.2: Spectral parameters based on spectra and X-ray colours of the discrete sources.

	Spectral analysis				X-ray colours				
Src ID (1)	Γ (2)	kT keV (3)	N_H 10^{22}cm^{-2} (4)	χ^2 (dof) (5)	C_1 (6)	C_2 (7)	C_3 (8)	Γ_{col} (9)	N_{Hcol} 10^{22}cm^{-2} (10)
1	$2.19^{+0.89}_{-0.63}$	-	$0.86^{+0.88}_{-0.45}$	2.6 (4)	$-0.50^{+0.20}_{-0.20}$	$-0.02^{+0.13}_{-0.13}$	$-0.52^{+0.20}_{-0.20}$	2.0	0.6
2	$1.86^{+0.36}_{-0.32}$	-	$0.23^{+0.19}_{-0.16}$	22.3 (21)	$-0.12^{+0.11}_{-0.11}$	$-0.00^{+0.09}_{-0.09}$	$-0.12^{+0.11}_{-0.11}$	1.6	0.13
3	$3.20^{+0.78}_{-0.66}$	-	$2.33^{+0.87}_{-0.70}$	29.1 (24)	$-1.62^{+0.92}_{-1.48}$	$-0.22^{+0.12}_{-0.12}$	$-1.84^{+0.91}_{-1.47}$	3.5	3.0
4	$2.76^{+0.60}_{-0.50}$	-	$0.27^{+0.17}_{-0.15}$	37.7 (37)	$0.00^{+0.10}_{-0.10}$	$0.31^{+0.12}_{-0.12}$	$0.32^{+0.13}_{-0.12}$	2.7	0.25
5	$2.67^{+1.06}_{-0.89}$	-	$0.88^{+0.83}_{-0.68}$	7.8 (9)	$-0.49^{+0.23}_{-0.26}$	$0.12^{+0.14}_{-0.14}$	$-0.36^{+0.24}_{-0.27}$	2.6	0.8
6	$3.92^{+1.69}_{-1.17}$	-	$2.89^{+1.97}_{-1.28}$	7.4 (8)	$-1.49^{+0.97}_{-1.50}$	$-0.21^{+0.17}_{-0.16}$	$-1.70^{+0.95}_{-1.49}$	3.2	2.5
7 [a]	$1.02^{+0.66}_{-0.75}$	$0.52^{+0.09}_{-0.18}$	$1.02^{+0.22}_{-0.27}$	52.53 (41)	$-0.24^{+0.09}_{-0.09}$	$-0.10^{+0.06}_{-0.06}$	$-0.34^{+0.09}_{-0.08}$	-	-
			$127.0^{+51.9}_{-61.9}$[b]						
8	-	-	-	-	$-0.39^{+0.46}_{-0.56}$	$0.15^{+0.29}_{-0.28}$	$-0.24^{+0.50}_{-0.56}$	2.6	0.6
9	$2.73^{+0.97}_{-1.72}$	$0.46^{+0.52}_{-0.16}$	$0.51^{+0.16}_{-0.27}$	13.9 (7)	$0.76^{+1.15}_{-0.72}$	$0.28^{+1.86}_{-1.82}$	$1.07^{+1.42}_{-0.82}$	-	-
10	$1.21^{+0.88}_{-0.35}$	-	$0.06^{+0.91}_{-0.06}$	10.8 (7)	$-0.77^{+0.26}_{-0.28}$	$-0.16^{+0.11}_{-0.11}$	$-0.92^{+0.25}_{-0.28}$	1.9	1.0
11	-	-	-	-	$-0.52^{+0.75}_{-1.19}$	$0.07^{+0.39}_{-0.40}$	$-0.45^{+0.77}_{-1.19}$	2.5	0.8
12	$1.91^{+0.78}_{-0.67}$	-	$0.40^{+0.40}_{-0.32}$	4.3 (6)	$-0.26^{+0.14}_{-0.14}$	$0.11^{+0.12}_{-0.12}$	$-0.14^{+0.15}_{-0.15}$	2.2	0.40
13	$1.98^{+1.02}_{-0.69}$	-	$0.14^{+0.41}_{-0.14}$	0.5 (2)	$0.00^{+0.27}_{-0.27}$	$0.10^{+0.26}_{-0.25}$	$0.10^{+0.28}_{-0.28}$	1.7	0.07
14	$1.72^{+0.84}_{-0.73}$	-	$0.53^{+0.63}_{-0.48}$	3.0 (6)	$-0.36^{+0.20}_{-0.22}$	$-0.07^{+0.12}_{-0.12}$	$-0.44^{+0.20}_{-0.22}$	1.6	0.4
15	$2.67^{+2.01}_{-1.32}$	-	$0.96^{+1.36}_{-0.82}$	11.9 (8)	$-0.57^{+0.42}_{-0.60}$	$0.18^{+0.18}_{-0.18}$	$-0.40^{+0.44}_{-0.62}$	3.0	1.0
16	$2.53^{+0.85}_{-0.74}$	-	$1.28^{+0.68}_{-0.53}$	6.2 (6)	$-0.55^{+0.20}_{-0.21}$	$-0.08^{+0.11}_{-0.10}$	$-0.62^{+0.20}_{-0.21}$	1.8	0.6
17	$1.69^{+0.31}_{-0.28}$	-	$0.25^{+0.16}_{-0.14}$	27.7 (28)	$-0.25^{+0.09}_{-0.09}$	$0.01^{+0.08}_{-0.08}$	$-0.24^{+0.09}_{-0.09}$	1.8	0.3
18	$0.93^{+0.70}_{-0.60}$	-	$1.87^{+1.47}_{-1.00}$	40.10 (31)	$-1.46^{+1.01}_{-1.55}$	$-0.67^{+0.19}_{-0.20}$	$-2.13^{+0.98}_{-1.50}$	-	-
19	$1.02^{+0.92}_{-0.47}$	-	$0.01^{+0.42}_{-0.01}$	1.8 (1)	$-0.43^{+0.56}_{-0.88}$	$-0.12^{+0.23}_{-0.24}$	$-0.55^{+0.54}_{-0.87}$	1.5	0.45
20	-	-	-	-	$0.33^{+0.84}_{-0.68}$	$0.19^{+0.68}_{-0.86}$	$0.52^{+0.54}_{-0.54}$	-	-
21	-	-	-	-	$-1.09^{+0.88}_{-1.45}$	$0.46^{+0.40}_{-0.35}$	$-0.61^{+1.01}_{-1.61}$	-	-
22	-	$0.63^{+0.17}_{-0.07}$	$0.62^{+0.08}_{-0.08}$	33.6 (16)	$0.47^{+0.41}_{-0.34}$	$1.30^{+1.72}_{-1.11}$	$1.79^{+1.53}_{-0.99}$	-	-
23	$2.02^{+0.53}_{-0.54}$	-	2.05	2.9 (5)	$-0.84^{+0.63}_{-1.13}$	$-0.36^{+0.17}_{-0.18}$	$-1.21^{+0.60}_{-1.11}$	1.3	1.0
24	$2.69^{+3.89}_{-1.91}$	-	0.0095[c]	1.1 (4)	$-0.19^{+1.52}_{-1.81}$	$-0.62^{+0.58}_{-1.02}$	$-0.83^{+0.74}_{-1.34}$	-	-
25	-	-	-	-	$-0.12^{+0.41}_{-0.47}$	$0.37^{+0.46}_{-0.44}$	$0.24^{+0.58}_{-0.56}$	3.2	0.45
26	-	-	-	-	$-0.16^{+0.32}_{-0.32}$	$-0.05^{+0.28}_{-0.28}$	$-0.21^{+0.31}_{-0.32}$	1.4	0.13

Column 1: Source identification number, Column 2: Photon index values from spectral fitting and corresponding errors, Column 3: Thermal plasma model temperatures, Column 4: Line-of-sight hydrogen column density, Column 5: Chi-square of the spectral fit and degrees of freedom (d.o.f), Columns 6, 7, and 8: X-ray colours, and their corresponding uncertainties, defined as $C_1 = \log_{10}(S/M)$, $C_2 = \log_{10}(M/H)$, $C_3 = \log_{10}(S/H)$ where S, M, and H are the net counts in the soft (0.5-1.2 keV), medium (1.2-2.0 keV), and hard (2.0-7.0 keV) bands (see text for details). Columns 9 and 10: Photon index Γ_{col} and hydrogen column density N_{Hcol} based on the X-ray colours

---

[a] The spectral model contains also a Gaussian line with $E_l = 6.30 \pm 0.03$ keV with $\sigma = 0.018^{+0.093}_{-0.018}$ keV and EW $= 0.72 \pm 0.01$ keV.

[b] Equivalent hydrogen column density of partial covering fraction absorption with covering fraction 95%.

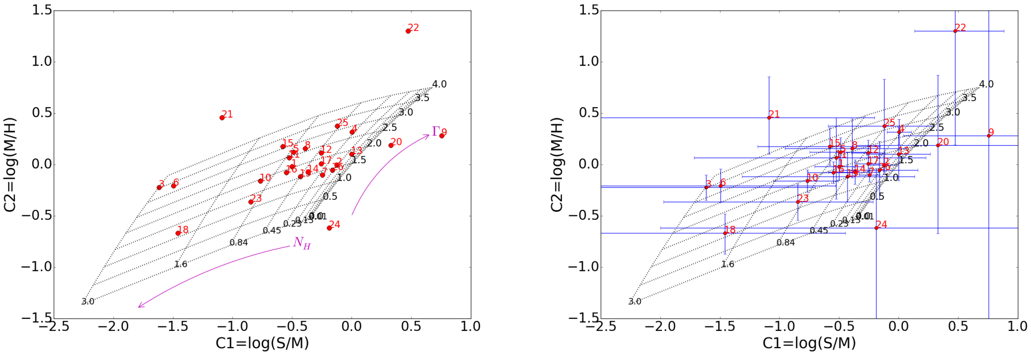

Figure 2.3: (Left panel) $C_2 \equiv \log_{10}(M/H)$ versus $C_1 \equiv \log_{10}(S/M)$ X-ray colour. Overlaid is the grid of different hydrogen column densities (in units of 10^{22} cm^{-2}) and photon indices assuming a simple absorbed power-law model . With the red filled circles we plot our sources and with the magenta arrows we show the direction of increasing hydrogen column density and photon index. (Right panel) Same as top panel but showing the corresponding errors for each source with blue bars.

the X-ray colour of Src 20 (Fig. 2.3), while Src 21 appears to have somewhat softer colours.

We checked the accuracy of the spectral parameters, calculated based on their X-ray colours, by comparing them with those calculated from the spectral fit (see Table 2.2) and we found that they agree well within their errors (Fig. 2.4 and 2.5). For the four sources (7, 9, 18, and 22) which were not fitted with a single absorbed power-law model as well as for the sources not falling on the grid (sources 20, 21, and 24) we cannot make this comparison.

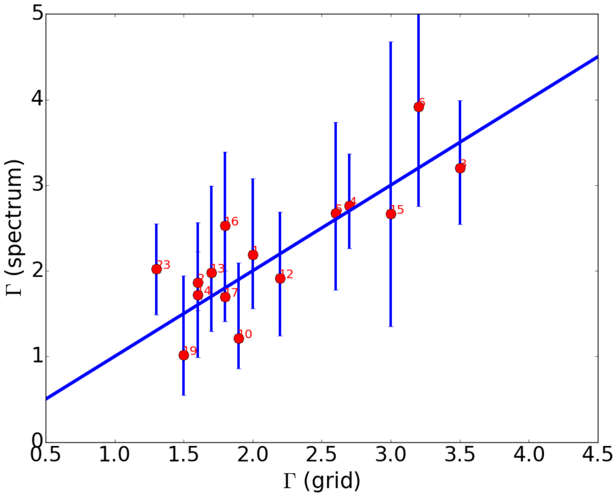

Figure 2.4: Colour versus spectroscopic photon index -Photon index calculated from the spectral analysis versus photon index calculated from the X-ray colours for our sources with spectra fitted with a simple absorbed power-law model. The errors from the spectral fit are shown with blue bars. The blue solid line is the 1:1 line.

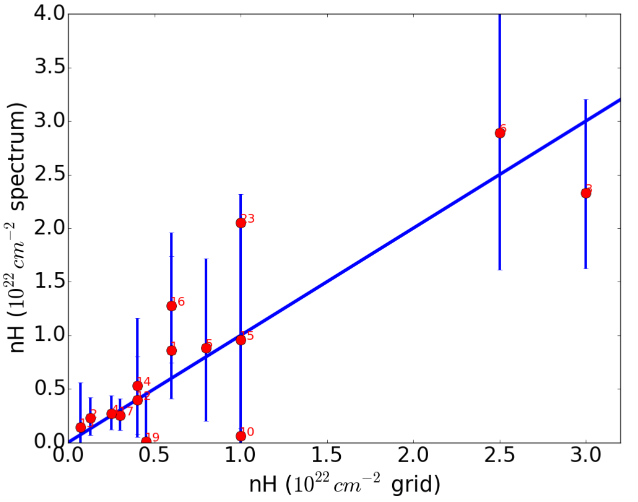

Figure 2.5: Colour versus spectroscopic hydrogen column density -Hydrogen column density calculated from the spectral analysis versus hydrogen column density calculated from the X-ray colours for our sources with spectra fitted with a simple absorbed power-law model. The errors from the spectral fit are shown with blue bars. The blue solid line is the 1:1 line.

2.2.4 Variability

We searched for variability with the *glvary* tool applied on the two reprojected events files. This tool uses the Gregory-Loredo algorithm (Gregory & Loredo, 1992). First we ran the *dither_region* tool which creates a normalized effective area file to be used with *glvary*. The latter accounts for the fraction of the total exposure that a source falls on bad pixels or goes off the detector. For our sample the fractional area was always 1 meaning that the source was always within good detector pixels. This ensures that any measured time variation is intrinsic and not due to the combination of the dither motion of the spacecraft and the pixel-to-pixel variation in the detector effective area. Then *glvary* assigns a variability index that takes values from 0 to 10, with the value of 0 indicating a definitely not variable source and values from 6 to 10 indicating a definitely variable source.

The results of the *glvary* tool did not identify any variable source for observation OBSID 15619 with the majority of the sources being definitely not variable (variability index=0) and some considered not variable and probably not variable (variability index=1 or 2).

For OBSID 15077 we found that only one source showed evidence for variability: Source 19 presented a variability index of 8 indicating that it is definitely a variable source. Inspecting its lightcurve one can see a dramatic reduction in the observed counts by about a factor of 6 in the second half of the observation. Also we explored its long-term variability by analysing data from the first observation of Arp 299 (OBSID 1641), and OBSID 15619. We calculated its broad-band observed flux ($0.1 - 10.0$ keV) based on spectra extracted from each observation and the best-fit parameters we calculated from the merged observation. In the case of OBSID 15077 we split the observation into two segments at the time when the counts decreased. Source 19 was not detected in the first observation of Arp 299 (Zezas *et al.*, 2003). Nonetheless we can use BEHR (Park *et al.*, 2006) to calculate the 90% confidence interval upper limit on the broad-band intensity of the source even though it is not formally detected in any band.

In Fig. 2.6 we present the broad band flux ($0.1 - 10.0$ keV) of source 19 versus the date of observation. We can see that the observations 15619 and 15077a do not show major differences as their fluxes agree within the errors but there is a difference with both the first observation performed in 2001 and the second half of OBSID 15077 by at least a factor of 4.

Furthermore we examined the long-term variability of all sources that were also detected at Zezas *et al.* (2003). We found 6 variable sources that differed in luminosity by a factor of 3 or more; namely the sources 6, 7, 10, 14, 17, and 18.

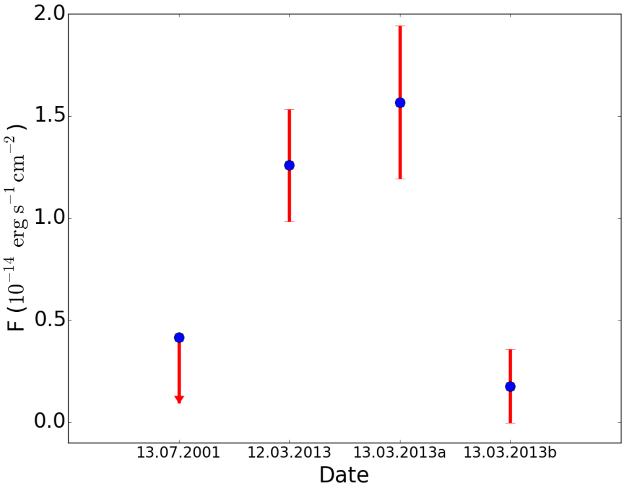

Figure 2.6: Variability of Src 19 -Observed flux in the broad band (0.1 – 10.0 keV) versus date of observation for source 19. The corresponding errors are shown with red bars.

2.2.5 Extended sources

The relatively large distance of Arp 299 make it subject to possible confusion effects. Therefore, we used the *srcextent* tool[1] to determine if our sample contains extended sources. The *srcextent* tool calculates the sizes and associated errors of a list of sources using the Mexican Hat Optimization (MHO) algorithm (C., 2007). A PSF is used as input to *srcextent* for more reliable results. For this purpose we used ChaRT (Carter *et al.*, 2003) to simulate the PSF and converted the output set of rays into a pseudo-events file by projecting the rays onto the detector-plane using MARX v.5.01.1 (Davis *et al.*, 2012). This analysis resulted in nine extended sources in the broad band (0.1 – 10 keV) at the 90% confidence level. Namely the sources 3, 4, 5, 7, 20, 21, 22, 24, and 28. Sources 3, 4, 5, 18, 22, and 24 are extended in the (2.0 – 8.0 keV) band as well, following the same analysis.

2.2.6 Fluxes and Luminosities of the discrete sources.

The calculation of the flux for the 20 sources that had spectral fitting parameters (see Table 2.2) was done with the XSPEC package. The errors were calculated by

---

[1] `http://cxc.harvard.edu/ciao/threads/srcextent/`

propagating the count errors and taking into account the count-rate to flux conversion given the specific model for each source. In order to see how much is the effect of the spectral uncertainties in the measured flux, we used the *flux* command with the *error* option which accounts for spectral uncertainties in the flux calculation. The errors are estimated by drawing parameter values from their best-fit distribution and calculating the flux for each set of draws. Then the resulting fluxes are ordered and the central 90% percent is selected to give the error range. This method increases the errors on average by a factor of 2.

The fluxes for the 6 remaining sources were calculated also using the *flux* command but this time the spectral parameters were fixed to the values determined based on their X-ray colours (Table 2.2). Flux uncertainties are then simply calculated by propagating the count-rate errors reported in Table 2.1. The resulting observed and absorption corrected luminosities in the broad $(0.1-10.0$ keV), soft $(0.1-2.0$ keV), and hard $(2.0-10.0$ keV) bands are presented in Table 2.3.

We find that 22 sources (20 of which are off-nuclear) have luminosities above 10^{39} erg s^{-1}, (i.e the ULX limit) reaching observed luminosities of 4.8×10^{40} erg s^{-1} $(0.1-10$ keV). Our sample also includes 4 sources below the ULX limit, with the faintest source at 4.0×10^{38} erg s^{-1} $(0.1-10$ keV).

2.2.7 Integrated X-ray emission of the galaxy

We extracted the integrated spectrum of the galaxy encompassed within its D25 area (RC3; Corwin *et al.*, 1994; de Vaucouleurs *et al.*, 1991). The background spectrum was determined from a source-free area outside the D25 area using the *specextract* tool. Based on previous observations of this galaxy (Zezas *et al.*, 2003) which indicate the presence of X-ray binaries together with a hot gaseous component, we obtained the best-fit ($\chi^2_\nu/\mathrm{dof} = 331.88/294$) with a model consisting of an absorbed thermal plasma component and a power-law plus a second thermal component, both seen through an additional absorber. The first absorption component was fixed to the Galactic line-of-sight value. We also added a Gaussian line to account for a line-like feature at 1.3 keV which significantly improves the fit without affecting the values of any other model parameters (Fig 3.9). Therefore the full model in XSPEC was: `phabs(gaussian+apec+phabs(apec+ powerlaw))`.

The best-fit parameters are $\Gamma = 1.67^{+0.11}_{-0.12}$, $\mathrm{N_{H_1}} = 9.5\times10^{19}$ $\mathrm{cm^{-2}}$, $\mathrm{N_{H_2}} = (0.55^{+0.06}_{-0.07})$ $\times10^{22}$ cm^{-2}, $\mathrm{kT_1} = 0.32\pm0.01$ keV and $\mathrm{kT_2} = 0.83^{+0.04}_{-0.03}$ keV (Table 2.4). These results are consistent with studies of the integrated X-ray spectra of other star-forming galaxies (e.g. Cappi *et al.*, 1999; Moran *et al.*, 1999; Pereira-Santaella *et al.*, 2011; Zezas *et al.*,

Table 2.3: Observed and absorption-corrected fluxes and luminosities.

Src ID (1)	$fx^{obs}(f_x^{corr})$ (0.1 – 10.0 keV) 10^{-14} erg s^{-1} cm^{-2} (2)	$fx^{obs}(f_x^{corr})$ (0.1 – 2.0 keV) 10^{-14} erg s^{-1} cm^{-2} (3)	$fx^{obs}(f_x^{corr})$ (2.0 – 10.0 keV) 10^{-14} erg s^{-1} cm^{-2} (4)	$L_x^{obs}(L_x^{corr})$ (0.1 – 10.0 keV) 10^{39} erg s^{-1} (5)	$L_x^{obs}(L_x^{corr})$ (0.1 – 2.0 keV) 10^{39} erg s^{-1} (6)	$L_x^{obs}(L_x^{corr})$ (2.0 – 10.0 keV) 10^{39} erg s^{-1} (7)
1∗	1.6 ±0.1 (5.6)	0.3±0.1 (4.2)	1.3 ±0.2 (1.4)	3.7 ±0.3 (13.0)	0.7±0.1 (9.7)	3.0 ±0.4 (3.3)
2∗	4.7 ±0.3 (8.12)	1.4±0.1 (4.7)	3.4 ±0.3 (3.4)	10.9±0.6 (18.8)	3.2±0.2 (10.8)	7.8 ±0.7 (8.0)
3	4.8 ±0.4 (240.9)	0.8±0.1 (235.3)	4.0 ±0.4 (5.6)	11.1±0.9 (558.0)	1.9±0.3 (544.9)	9.2 ±0.9 (13.0)
4	4.4 ±0.3 (27.8)	2.4±0.2 (25.7)	2.0 ±0.3 (2.0)	10.2±0.7 (64.5)	5.6±0.4 (59.7)	4.6 ±0.7 (4.8)
5	2.0 ±0.2 (17.6)	0.6±0.1 (16.0)	1.45±0.2 (1.6)	4.7 ±0.4 (40.9)	1.3±0.2 (37.1)	3.4 ±0.5 (3.8)
6∗	1.7 ±0.2 (747.7)	0.3±0.1 (745.4)	1.4 ±0.2 (2.2)	4.0 ±0.5 (1732.0)	0.8±0.2 (1726.0)	3.2 ±0.4 (5.3)
7	27.5±0.9 (66.4)	2.2±0.1 (40.0)	25.3±1.2 (26.4)	63.8±2.1 (153.8)	5.0±0.3 (92.7)	58.8±2.7 (61.1)
8	0.3 ±0.1 (1.02)	0.1±0.1 (0.7)	0.2 ±0.1 (0.2)	0.7 ±0.2 (2.3)	0.2±0.1 (1.8)	0.5 ±0.2 (0.5)
9∗	1.4 ±0.1 (10.9)	1.0±0.1 (10.5)	0.4 ±0.1 (0.4)	3.3 ±0.1 (25.3)	2.3±0.1 (24.3)	0.9 ±0.1 (1.0)
10∗	4.2 ±0.3 (4.6)	0.8±0.1 (1.2)	3.4 ±0.3 (3.4)	9.8 ±0.7 (10.7)	1.9±0.2 (2.8)	7.9 ±0.8 (7.9)
11	0.2 ±0.1 (0.7)	0.1±0.1 (0.5)	0.2 ±0.1 (0.2)	0.6 ±0.1 (1.7)	0.1±0.1 (1.3)	0.4 ±0.2 (0.4)
12∗	2.2 ±0.2 (4.46)	0.5±0.1 (2.7)	1.7 ±0.2 (1.8)	5.2 ±0.4 (10.3)	1.2±0.1 (6.2)	3.9 ±0.6 (4.1)
13∗	0.7 ±0.1 (1.24)	0.3±0.1 (0.8)	0.4 ±0.1 (0.4)	1.6 ±0.2 (2.9)	0.6±0.1 (1.8)	1.0 ±0.3 (1.0)
14∗	2.7 ±0.2 (4.8)	0.5±0.1 (2.4)	2.3 ±0.3 (2.4)	6.4 ±0.5 (11.0)	1.1±0.1 (5.5)	5.3 ±0.6 (5.5)
15∗	1.4 ±0.2 (12.6)	0.4±0.1 (11.4)	1.0 ±0.2 (1.2)	3.3 ±0.4 (29.3)	0.9±0.1 (26.5)	2.4 ±0.5 (2.7)
16∗	2.4 ±0.2 (18.1)	0.5±0.1 (15.8)	2.0 ±0.2 (2.3)	5.7 ±0.4 (42.0)	1.1±0.1 (36.7)	4.6 ±0.5 (5.4)
17∗	7.3 ±0.4 (11.1)	1.7±0.1 (5.4)	5.6 ±0.5 (5.7)	16.9±0.8 (25.8)	4.0±0.3 (12.5)	12.9±1.1 (13.2)
18	13. ±1.2 (18.0)	0.3±0.1 (3.2)	13.2±0.9 (14.7)	31.4±2.7 (41.7)	0.8±0.2 (7.4)	30.6±2.3 (34.2)
19∗	1.0 ±0.2 (1.1)	0.2±0.1 (0.2)	0.9 ±0.2 (0.9)	2.5 ±0.4 (2.6)	0.5±0.1 (0.5)	2.1 ±0.5 (2.1)
20	0.5 ±0.1 (0.5)	0.2±0.1 (0.2)	0.2 ±0.1 (0.2)	1.2 ±0.3 (1.2)	0.5±0.2 (0.6)	0.4 ±0.2 (0.4)
21	0.5 ±0.1 (0.5)	0.2±0.1 (0.2)	0.3 ±0.1 (0.3)	1.2 ±0.3 (1.2)	0.5±0.1 (0.5)	0.7 ±0.3 (0.7)
22	1.8 ±0.1 (13.7)	1.6±0.1 (13.4)	0.2 ±0.1 (0.2)	4.2 ±0.2 (31.8)	3.7±0.2 (31.2)	0.5 ±0.1 (0.5)
23∗	2.4 ±0.3 (8.12)	0.2±0.1 (5.4)	2.3 ±0.3 (2.7)	5.6 ±0.6 (18.8)	0.4±0.1 (12.5)	5.2 ±0.7 (6.4)
24	0.7 ±0.2 (10.5)	0.1±0.1 (9.6)	0.7 ±0.1 (0.9)	1.6 ±0.4 (24.4)	0.1±0.1 (22.2)	1.5 ±0.3 (2.2)
25	0.1 ±0.1 (0.9)	0.1±0.1 (0.9)	0.1 ±0.1 (0.1)	0.4 ±0.1 (2.2)	0.2±0.1 (2.0)	0.2 ±0.1 (0.2)
26∗	0.5 ±0.1 (0.6)	0.1±0.1 (0.2)	0.4 ±0.1 (0.4)	1.3 ±0.3 (1.4)	0.3±0.1 (0.4)	1.0 ±0.3 (1.0)

Column 1: The source identification number, ULXs are denoted with ∗; Columns 2, 3, and 4: Fluxes in the broad, soft, and hard bands respectively; Columns 5, 6, and 7: Luminosities in the broad, soft, and hard bands respectively.

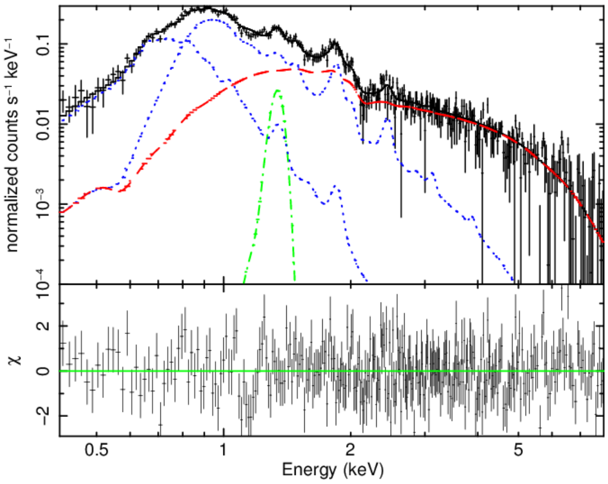

Figure 2.7: Integrated X-ray spectrum of Arp 299. - (Top panel) The integrated X-ray spectrum of Arp 299, along with the best-fit folded model consisting of: An absorbed power-law component (dashed red line), two apec components (dotted blue lines), and a Gaussian line (dashed-dotted green line). (Bottom panel) The fit residuals in terms of sigmas with error bars of size 1σ.

1998).

The results of the absorbed, corrected for the Galactic absorption, and unabsorbed luminosities in the broad ($0.1 - 10.0$ keV), soft ($0.1 - 2.0$ keV), and hard ($2.0 - 10.0$ keV) bands are shown in Table 3.11.

2.2.7.1 Luminosity of X-ray binaries and ULXs

X-ray binaries are the dominant component of X-ray emission of galaxies above 2 keV (e.g. Fabbiano, 2003; Lira *et al.*, 2002). We measure the integrated emission of both resolved and unresolved XRBs in Arp 299 by extracting the integrated spectrum of the galaxy, excluding Src 7 which corresponds to the AGN in NGC 3690 (§2.2.8). We fitted this spectrum, with a model consisting of an absorbed thermal plasma component and a power-law plus a second thermal component, both seen through an additional absorber (full model in XSPEC: `phabs(apec+phabs(apec+ powerlaw))`; $\chi^2 = 302.11/282$). The power-law component is then attributed to the total population of X-ray binaries which may be embedded in a star-forming region, hence requiring an additional absorption. In this way we account not only for the discrete X-ray sources but also for the unresolved X-ray binaries. The best-fit parameters for this fit are presented in 2.4 (second row) and the corresponding absorbed and unabsorbed luminosities in Table 3.11.

As mentioned previously ULXs are off-nuclear point sources that have luminosities $L_{(0.1-10.0\ \mathrm{keV})} > 10^{39}$ erg s^{-1}. In our sample we found 20 off-nuclear sources that fulfil the criterion and belong to the ULX class. In these we do not include Src 22 which had a soft thermal plasma spectrum that is inconsistent with an X-ray binary. If we account only for the point sources in the broad-band our sample reduces to 14 ULXs (denoted with an asterisk in Table 2.3).

Given the distance of Arp 299 we expect that this observation suffers from source confusion which affects the number of observed sources. In order to avoid this complication our analysis focuses on the total luminosity of ULXs which is not affected by source confusion. When we discuss the source numbers, we give results for the total ULX sample (20 sources), as well as for the more conservative choice of point-like objects (14 sources).

We calculated the total flux of the 20 and 14 ULXs by extracting a spectrum from a region consisting of all their apertures and using a background spectrum from a source-free area outside the D25 area. A model consisting of an absorbed power-law and a thermal-plasma model with variable abundances gave an acceptable fit but with significant residuals in the $1.0 - 2.0$ keV range (Model in XSPEC: `phabs(vapec+po)`). Therefore, we also used an absorbed thermal-plasma (with variable abundances) and a disk blackbody model (Makishima *et al.*, 1986; Mitsuda *et al.*, 1984) which has been successfully used to model the spectra of ULXs (Gladstone *et al.*, 2009; Rana *et al.*, 2015) (Model in XSPEC: `phabs(vapec+diskbb)`). The best-fit parameters for both models are shown in Table 2.4 and they are in good agreement with fits to the *XMM-Newton* spectra of nearby ULXs Gladstone *et al.* (2009).

In order to measure the integrated luminosity of the ULXs, we used the second model (`phabs(vapec+diskbb)`) because it gave a marginally better fit and accounted only for the *diskbb* component. The thermal component is interpreted as the contribution of the diffuse emission of the galaxy which could not be subtracted completely by the background spectrum. This is supported by the fact that the abundance of Fe is in agreement with that of the diffuse emission (see §3.2.6.2). The integrated absorbed and unabsorbed luminosities of the combined 20 and the combined 14 ULXs are reported in Table 3.11.

2.2.7.2 Luminosity of the diffuse emission

The diffuse emission of star-forming galaxies shows evidence for a hot thermal gaseous component often associated with a galactic scale superwind (e.g. Strickland & Stevens,

Table 2.4: Spectral fitting parameters of integrated spectrum of galaxy, binaries, ULXs, and diffuse emission

	Power-law			Thermal plasma			Disk blackbody		
Region	N_H	Γ	Norm[a]	kT	Z	Norm[b]	Tin	Norm[c]	
	10^{22} cm^{-2}			keV	$(\times Z_\odot)$		keV		χ^2/dof
Total galaxy[d]	$0.55^{+0.06}_{-0.07}$	$1.67^{+0.11}_{-0.12}$	$26.33^{+4.03}_{-3.94}$	0.32 ± 0.01	-	13.4 ± 1.0	-	-	331.88/294
				$0.83^{+0.04}_{-0.03}$		70.1 ± 14.0			
Total galaxy (no AGN)[e]	0.55 ± 0.06	$1.80^{+0.12}_{-0.13}$	$27.17^{+4.38}_{-4.45}$	0.32 ± 0.01	-	13.4 ± 1.0	-	-	302.11/282
				0.84 ± 0.03		67.3 ± 14.3			
All ULXs (20)	$0.27^{+0.05}_{-0.07}$	-	-	$0.62^{+0.14}_{-0.11}$	$0.18^{+0.08}_{-0.06}$ (Fe)	$11.0^{+3.8}_{-3.5}$	$1.42^{+0.11}_{-0.09}$	$6.6^{+2.0}_{-1.6}$	160.75/164
	$0.50^{+0.12}_{-0.08}$	$2.04^{+0.12}_{-0.10}$	$18.1^{+3.0}_{-2.2}$	$0.31^{+0.08}_{-0.06}$	$0.71^{+0.53}_{-0.30}$ (Fe)	$19.2^{+28.1}_{-10.6}$	-	-	176.00/164
Point-like ULXs (14)	$0.23^{+0.12}_{-0.06}$	-	-	$0.54^{+0.14}_{-0.15}$	$0.19^{+0.21}_{-0.09}$ (Fe)	$4.1^{+4.0}_{-2.2}$	$1.51^{+0.13}_{-0.14}$	$3.4^{+1.67}_{-0.9}$	121.60/131
	0.55 ± 0.14	$1.95^{+0.11}_{-0.12}$	$10.9^{+1.7}_{-1.6}$	$0.24^{+0.06}_{-0.04}$	1.00 (Fe)	$20.0^{+47.2}_{-15.2}$	-	-	130.08/132
Diffuse emission	7.45 ± 0.02	$1.52^{+0.21}_{-0.24}$	$7.0^{+2.0}_{-1.8}$	0.72 ± 0.03	$1.24^{+0.34}_{-0.29}$ (Ne)	$49.0^{+7.8}_{-7.4}$	-	-	201.44/210
					$1.14^{+0.25}_{-0.20}$ (Mg)				
					$0.26^{+0.04}_{-0.03}$ (Fe)				

---

[a] Normalization of power-law component in units of 10^{-5} photons keV^{-1} cm^{-2} s^{-1} at 1 keV.

[b] Normalization of thermal plasma component in units of 10^{-5} photons keV^{-1} cm^{-2} s^{-1} at 1 keV.

[c] Normalization of disk black body component in units of 10^{-3} photons keV^{-1} cm^{-2} s^{-1} at 1 keV.

[d] Also includes a component to account for the Galactic line-of-sight absorption ($N_H = 9.5 \times 10^{19} cm^{-2}$).

[e] Also includes a component to account for the Galactic line-of-sight absorption ($N_H = 9.5 \times 10^{19} cm^{-2}$).

2000). Arp 299 is not an exception as seen from fits to its integrated X-ray spectrum (§3.2.6). Furthermore, optical observations of Arp 299 show evidence for a galactic-scale wind (Heckman *et al.*, 1999). A plume in the west of NGC 3690 (Fig. 2.8) extending beyond the optical outline of the galaxy would be associated with such a superwind.

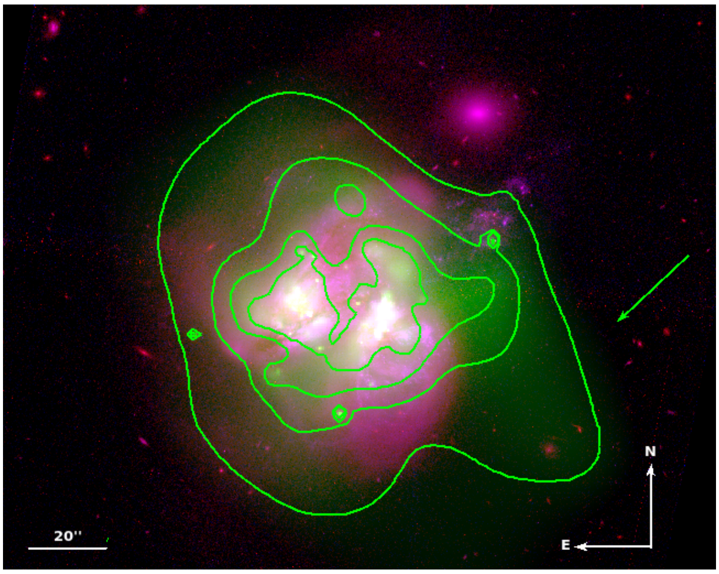

Figure 2.8: Evidence for a superwind in Arp 299 -Composite colour image of Arp 299 where the soft smoothed image at $0.1 - 1.2$ keV is the green colour and red and blue colours are the F814W (814 nm) and F435W (435 nm) images from *HST*. The contours outline the distribution of the diffuse X-ray emission and the green arrow indicates the location of the plume in the west of the galaxy.

In order to measure the luminosity of the diffuse soft $(0.1 - 2.0$ keV) and hard $(2.0 - 10.0$ keV) X-ray emission of Arp 299, we created "swiss cheese" images in each of the two bands after removing the regions corresponding to the 25 detected X-ray sources. To obtain a picture of its spectral parameters we extracted a spectrum from the D25 region of the galaxy (also excluding the discrete X-ray sources) and a background spectrum from a source-free area outside the D25 area using the *specextract* tool. The spectrum was fitted with an absorbed power-law model (to account for unresolved X-ray binaries) plus a thermal plasma model with variable abundances. We also added a second photoelectric absorption component fixed to the line-of-sight Galactic absorption (model in XSPEC: `phabs(phabs(po+vapec))`). The abundances of Ne, Mg, and, Fe were left free to vary. For the other elements we adopted solar abundances. We tried to thaw the oxygen and silicon elements but since there was no improvement in the fit, and their resulting values were close to the solar, we adopted a solar value for these

Table 2.5: Luminosities of the integrated spectrum of the total galaxy, X-ray binaries, ULXs, and the diffuse emission

N	$\mathrm{L_x^{obs}(L_x^{corr})}$ (0.1 − 10.0 keV) 10^{40} erg s^{-1}	$\mathrm{L_x^{obs}(L_x^{corr})}$ (0.1 − 2.0 keV) 10^{40} erg s^{-1}	$\mathrm{L_x^{obs}(L_x^{corr})}$ (2.0 − 10.0 keV) 10^{40} erg s^{-1}	$\mathrm{L_x^{obs}(L_x^{corr})}$ (0.5 − 8.0 keV) 10^{40} erg s^{-1}
Total galaxy[a]	49.0 ± 0.4	23.0 ± 0.2	26.0 ± 0.6	42.1 ± 0.3
	$(51.0 \pm 0.4\ \vert 120.0 \pm 0.8)$	$(23.0 \pm 0.2\ \vert 92.0 \pm 0.8)$	$(27.0 \pm 0.6\ \vert 28.0 \pm 0.6)$	$(42.7 \pm 0.3\ \vert 89.8 \pm 0.6)$
Binaries[b]	25.0±0.2 (48.0 ± 0.4)	4.5±0.4 (26.2 ± 2.3)	21.0±0.8 (21.8 ± 0.8)	21.7±0.2 (32.4 ± 0.3)
ULXs20	10.4±0.1 (13.1 ± 0.1)	2.6±0.4 (5.1 ± 0.8)	7.8±0.2 (8.1 ± 0.2)	10.0±0.1 (11.9 ± 0.1)
ULXs14	7.1±0.1 (8.8 ± 0.1)	1.7±0.4 (3.2 ± 0.7)	5.4±0.1 (5.5 ± 0.1)	6.8±0.1 (7.9 ± 0.1)
Diffuse emission	22.1±0.2 (24.2 ± 0.2)	15.0±0.2 (17.0 ± 0.2)	7.1±0.7 (7.2 ± 0.7)	19.7 ±0.2 (20.6 ± 0.2)

---

[a] The displayed luminosities for Apr 299 are given in the form $\mathrm{L_x^{obs}(L_{xGal}^{corr}|L_x^{corr})}$ where the $\mathrm{L_x^{obs}}$ is the observed luminosity, $\mathrm{L_{xGal}^{corr}}$ is the luminosity corrected only for the Galactic line-of-sight absorption, and $\mathrm{L_x^{corr}}$ is the unabsorbed luminosity.

[b] Includes also emission from unresolved sources.

elements as well. The best-fit parameters for this model ($\chi^2_\nu/\mathrm{dof} = 201.44/210$) and their corresponding errors at the 90% confidence level are shown in Table 2.4.

Since this spectrum does not account for the diffuse emission that lies within the excised source regions we cannot directly compute the flux and therefore the luminosity of the diffuse emission of Arp 299. For this reason we created an image of the diffuse emission by interpolating the pixel values in the source regions with values from annular regions surrounding them, using the *dmfilth* tool. These annular regions were the same as those used as background regions in the spectral analysis. Then we measured the total diffuse emission intensity within the D25 region of the galaxy. Using the spectral model and making the implicit assumption that the spectrum in the source regions is on average the same as in the rest of the galaxy, we calculated the flux and the corresponding luminosity of the diffuse emission in the soft and hard bands by rescaling the model-predicted fluxes by the ratio of the counts in the interpolated image and the swiss-cheese image in each band.

The absorbed as well as the corrected luminosities for both absorption components are reported in Table 3.11. Correcting for the Galactic line-of-sight absorption essentially makes no difference in the absorption-corrected luminosity.

2.2.8 Nucleus of NGC 3690

The NGC 3690 nucleus has been extensively studied in the X-ray regime. The fist observational evidence of a heavily obscured AGN existing in Arp 299 was revealed with *Beppo-SAX* (Della Ceca *et al.*, 2002). *Chandra* and *XMM-Newton*, as well as recent results from simultaneous observations with *NuSTAR* and *Chandra*, confirmed the existence of an AGN in NGC 3690 with the detection of a strong 6.4 keV line (Ballo *et al.*, 2004; Ptak *et al.*, 2015; Zezas *et al.*, 2003). With the excellent spatial resolution and this deep exposure of *Chandra* we are able to individually study the nucleus of NGC 3690 and its contribution in the X-ray output of Arp 299. Therefore we extracted the spectrum of Src 7 (nucleus of NGC 3690, B1) from the same region and using the same background as in our photometric analysis (§3.2.1).

We first tried a simple model consisting of an absorbed power-law, a Gaussian line and a thermal plasma component (model in XSPEC: `phabs(apec+po+gaussian)`). The best-fit parameters ($\chi^2_\nu/\mathrm{dof} = 60.92/43$) and their corresponding uncertainties are: $\mathrm{N_H} = (1.15 \pm 0.18) \times 10^{22}\mathrm{cm}^{-2}$ for the hydrogen column density and $\Gamma = 0.19^{+0.60}_{-0.70}$ for the photon index of the power-law component. The thermal plasma model has a temperature of $\mathrm{kT} = 0.55^{+0.11}_{-0.10}$ keV and the Gaussian line energy is $\mathrm{E_l} = 6.33 \pm 0.04$ keV with $\sigma = 0.10^{+0.09}_{-0.10}$ keV.

We notice that Γ is very flat indicative of a heavily obscured AGN. Therefore we try a model appropriate for heavily obscured AGN (e.g. Iwasawa *et al.*, 2009). This model consisted of a power-law plus a Gaussian line at 6.4 keV seen through a partial covering absorber (Fig. 2.9) and a thermal-plasma component. All the components were absorbed by photoelectric absorption (model in XSPEC: `phabs(apec+pcfabs (po+gaussian))`). The adopted model corresponds to a physical picture where the emission of a deeply embedded AGN, and possibly some X-ray binaries (which we cannot isolate from the AGN), escapes and is later absorbed by another concentration of cold gas.

We obtained a very good fit ($\chi^2_\nu/\mathrm{dof} = 52.53/41$) where the best-fit parameters and their corresponding uncertainties (also shown in Table 2.2) are: $\mathrm{N_H} = (1.02^{+0.22}_{-0.27}) \times 10^{22} cm^{-2}$ for the hydrogen column density of the overall photoelectric absorption component, while for the HI column density and covering fraction the of the partial covering absorber we have $\mathrm{N_{H_{fr}}} = (127.0^{+51.9}_{-61.9}) \times 10^{22}\ \mathrm{cm}^{-2}$ and f = 0.95 (i.e. 5% of the emission escapes the first absorber). The photon index of the power-law component is $\Gamma = 1.02^{+0.66}_{-0.75}$. The still flat photon index originates probably from the fact that we are not recovering the intrinsic power-law spectrum because of the limited band of *Chandra*.

The thermal plasma model has a temperature of $kT = 0.52^{+0.09}_{-0.18}$ keV. The Gaussian line energy is $E_l = 6.30 \pm 0.03$ keV with $\sigma = 0.018^{+0.093}_{-0.018}$ keV and an equivalent width of $EW = 0.72 \pm 0.01$ keV. These results are consistent with the *NuSTAR* spectral fits (Ptak *et al.*, 2015) apart from the power-law photon index which in our case is much flatter than in the *NuSTAR* fits. This is understandable given the much narrower energy range of *Chandra*.

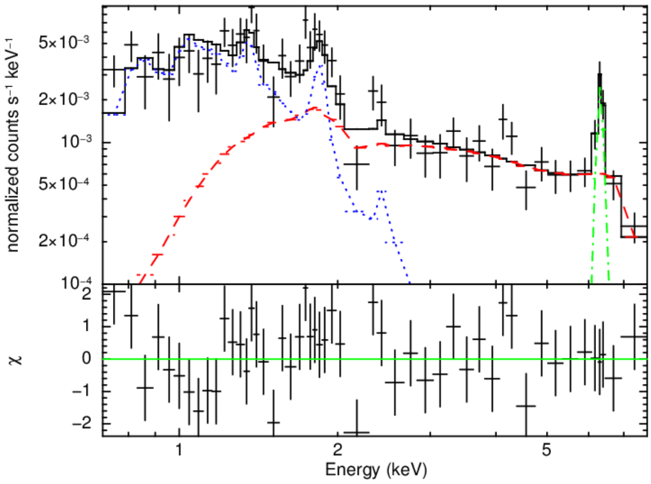

Figure 2.9: X-ray spectrum of the nucleus of NGC 3690 -(Top panel) The X-ray spectrum of the nucleus of NGC 3690 (Src 7), along with the best-fit folded model consisting of: An absorbed power-law component (dashed red line), a thermal plasma component (dotted blue line), and a Gaussian line (dashed-dotted green line). (Bottom panel) The fit residuals in terms of sigmas with error bars of size 1σ.

Table 2.6 shows the observed and absorption corrected luminosity of the AGN. We note here that with the *Chandra* data we do not recover the intrinsic AGN and therefore the luminosities we measure are only a lower limit. Nonetheless they are very useful for constraining its contribution in the observed total X-ray output of Arp 299 in the *Chandra* band. Rows 1, 2, and 3 present the absorbed luminosity, the unabsorbed luminosity corrected only for the Galactic column density, and the total unabsorbed luminosity for the broad, soft, and hard bands. Row 4 presents the AGN unabsorbed luminosity not accounting for the thermal-plasma emission in the same bands. This luminosity can give us an idea of the emission of the AGN. In all cases we cannot disentangle contamination from X-ray binaries within the AGN aperture. However the large X-ray luminosity (even if not corrected for absorption) suggests that the measured

Table 2.6: AGN luminosities

Ltype	L (0.1 – 10.0 keV) 10^{39} erg s^{-1}	L (0.1 – 2.0 keV) 10^{39} erg s^{-1}	L (2.0 – 10.0 keV) 10^{39} erg s^{-1}
absorbed	63.8±2.1	5.0±0.3	58.8±2.7
Galactic corrected[a]	153.8±5.1	92.7 ±5.5	61.1±2.8
unabsorbed[b]	759.7±24.3	211.8±12.7	547.9±25.1
AGN unabsorbed[c]	672.3 ±22.1	125.3 ±7.5	547.0±25.1

---

[a] Corrected luminosity for the Galactic line-of-sight.

[b] Corrected luminosity for both photoelectric absorption components.

[c] Corrected luminosity for both photoelectric absorption and for thermal plasma components.

emission is dominated by the AGN.

The AGN contributes to 13.1% of the total absorbed luminosity of Arp 299 in the broad band (0.1 – 10.0 keV), 2.3% in the soft band (0.1 – 2.0 keV), and 22.1% in the hard band (2.0 – 10.0 keV). Correcting the spectrum for the photoelectric absorption (`phabs`) the contributions are 12.7% in the broad, 10.0% in the soft and 21.7% in the hard band. When correcting for the second absorption (`pcfabs`) the hard X-ray luminosity of the AGN is larger than the hard X-ray luminosity of the whole galaxy. This result may seem at odds but can be explained by the fact that the contribution of the AGN in the integrated spectrum of the galaxy is only 22%. As a result we cannot recover the AGN spectral parameters from the integrated galaxy spectrum. Furthermore, the inferred AGN luminosity is strongly model dependent on its spectral parameters, which have rather large uncertainties. Nonetheless, the AGN has only minor contribution to the observed X-ray output of the system, but it may dominate its energetics.

2.2.9 Nucleus of IC 694

The nucleus of IC 694 (Arp 299-A) has also been studied extensively and its nature is still debated. Zezas *et al.* (2003) with a relatively short exposure claimed that the IC 694 can be explained with a significant number of high-mass X-ray binaries (HMXBs; 5×10^5 O-type stars) although the presence of a relatively weak, mildly obscured, AGN cannot be excluded. *Chandra* and *XMM-Newton* observations detected ionized Fe-K emission in IC 694. Part of it may come from an AGN although significant contribution may be accounted to star formation (Ballo *et al.*, 2004). Evidence of an AGN in IC 694 based on the existence of a strong flat spectrum radio source is presented in Pérez-Torres *et al.* (2010). Alonso-Herrero *et al.* (2013) also supported the existence of both a more obscured and much less luminous AGN than in NGC 3690 by modelling its mid-infrared spectrum. Ptak *et al.* (2015) with a simultaneous observation of *Chandra* and *NuSTAR* showed that the lack of significant emission above 10 keV suggests that any AGN must be highly obscured or have a much lower luminosity than that of NGC 3690. In general the observed He-like Fe-Kα emission line and the lack of a 6.4 keV Fe-Kα line makes the presence of an AGN inconclusive. For example several nearby LIRGs/ULIRGS with no apparent AGN signatures, show strong ionized Fe-line (Iwasawa *et al.*, 2005, 2009), which can be accounted for by thermal emission originating from a starburst (e.g. Strickland & Heckman, 2009).

With the spatial resolution and high S/N of the *Chandra* observation considered here we can locate the source of the Fe-K line and separate the nuclear (possible AGN) from the circumnuclear (XRBs) hard component.

Therefore we extracted the spectrum of the nucleus of IC 694 (Src 18) from the same annulus and using the same background as in the photometric analysis (§3.2.1; Table 2.1). Src 18 was strongly contaminated from the local background (see Fig. 2.10) in the soft band. In order to assess the effect of the background in our analysis we also tried to model the spectrum using a background region outside the D25 area of the galaxy. As expected the errors in the soft (< 1.5 keV) part of the spectrum were significantly smaller. Apart from that no significant change in the shape of the spectrum was noticed. Therefore we decided to use the local background of the source.

We obtained a good fit with an absorbed power-law model ($\chi^2_\nu/\mathrm{dof} = 40.10/31$). The best-fit spectral parameters for all models are shown in Table 2.7. However, because there is a hint for an emission line at $\sim 6.0 - 7.0$ keV we introduced a Gaussian line in our model (model in XSPEC: `phabs(po+gaussian)`).

If we model it as an unresolved line its centre is at $6.60^{+0.10}_{-0.05}$ keV which is consistent to an ionized Fe-Kα line. The inclusion of the Gaussian line improves the fit, but at a non-statistically significant level, and it makes the photon index slightly steeper (~ 1.50) with respect to $\Gamma \sim 0.93$. As a result the absorption corrected flux in the broad and soft bands change by 30% and 140% respectively (the hard flux is effectively the same). These results still do not give any evidence for either a weak, relatively obscured AGN, or a buried AGN. Either case is consistent with the non-detection of a 6.4 keV Fe-Kα line. On the other hand, a 6.7 keV line from highly ionized iron could be produced by a high temperature thermal plasma associated with intense star-forming activity confined in the nuclear region of IC 694.

Table 2.7: Nucleus of IC 694 spectral fitting parameters

model	N_H 10^{22} cm^{-2}	Γ	Norm[a]	E keV	Norm[b]	σ keV	EW keV	χ^2/dof
phabs(po+gaussian)	$3.62^{+2.80}_{-1.70}$	$2.10^{+1.30}_{-0.93}$	$5.49^{+32.17}_{-3.97}$	$6.57^{+5.3}_{-0.29}$	$3.40^{+18.90}_{-1.70}$	$0.55^{+2.95}_{-0.23}$	3.11	28.47/28
phabs(po+gaussian)	$2.72^{+2.00}_{-1.32}$	$1.50^{+0.88}_{-0.74}$	$2.37^{+6.98}_{-1.62}$	$6.60^{+0.10}_{-0.05}$	1.64 ± 1.02	0.02^{c}	1.19	33.01/29
phabs po	$1.87^{+1.47}_{-1.00}$	$0.93^{+0.70}_{-0.60}$	$1.02^{+2.02}_{-0.62}$	-	-	-	-	40.10/31

---

[a] Normalization of power-law in units of 10^{-5} photons keV^{-1} cm^{-2} s^{-1} at 1 keV.

[b] Normalization of Gaussian line in units of 10^{-6} photons keV^{-1} cm^{-2} s^{-1}.

[c] This parameter is frozen.

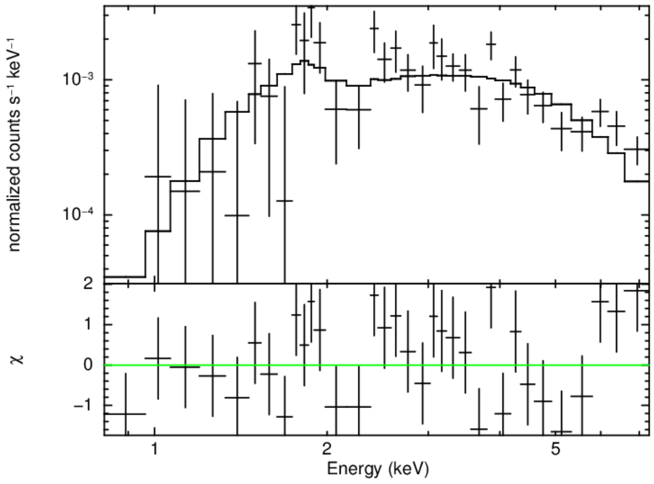

Figure 2.10: X-ray spectrum of the nucleus of IC 694 -(Top panel) The X-ray spectrum of the nucleus of IC 694 (Src 18), along with the best-fit folded model consisting of an absorbed power-law component. (Bottom panel) The fit residuals in terms of sigmas with error bars of size 1σ.

2.3 DISCUSSION

In the previous sections we presented the results from the analysis of the discrete sources (photometry, spectral, timing analysis), as well as the spectral properties of the integrated galactic emission. In this section we discuss these results in the context of the star-forming of the star-forming activity in Arp 299. We examine the contribution of the XRBs, ULXs, and the diffuse emission to the integrated luminosity of the Arp 299. We discuss the nature of the discrete sources and the implication of our results for studies of very high SFR galaxies.

2.3.1 Multiwavelength comparison

To further explore the nature of the discrete sources we used Fig. 2.2 where we combined HST images in the F814W (814 nm; green) and F435W (435 nm; blue) and IRAC band 4 (8 μm; red) non-stellar image. We see that the majority of the sources are located in the most actively star-forming regions with very few sources located outside the main body of the galaxy, indicating that they are HMXBs.

We can further explore this assertion by looking at the ages of the star-forming episodes in the regions of our sources. The ages of the nucleus of IC 694 (A) and the overlap region (C-C'), based on the ratio of mid infrared lines, are > 7 Myr and $4-7$ Myr respectively, with complex C-C' considered to be the youngest region of Arp 299 (Alonso-Herrero *et al.*, 2009). This association indicates that Src 18 (Nucleus of IC 694; A), Src 7 (nucleus of NGC 3690; B1), Src 4 (C), and Src 10 (C") are young HMXBs; region C' is not associated with any discrete X-ray source (Fig. 2.2). Complex C is identified as Src 4 in our sample which is a ULX with $\mathrm{L}(0.1-10.0~\mathrm{keV}) = 1.03\times10^{40}~erg~s^{-1}$. Since this is the youngest region in the galaxy, and ULXs are related to young stellar populations, such a high luminosity would be justified by a very young HMXB. Such a young X-ray binary would be expected to have a very massive black hole fed by a donor star with a strong stellar wind especially at the relatively high metalicity of Arp 299 giving rise to high X-ray luminosity.

In addition we constructed a map of specific star formation rate (sSFR; defined as the SFR per unit stellar mass) of Arp 299. We used images in the 8 μm and 3.6 μm obtained from the *Spitzer* IRAC camera provided by Brassington *et al.* (2015). We transformed the 8 μm non-stellar image to SFR map using the relation :

$$\mathrm{SFR}_{8\mu\mathrm{m}}(\mathrm{M}_\odot~\mathrm{yr}^{-1}) = \frac{\nu\mathrm{L}_\nu[8\mu\mathrm{m}]}{1.57\times10^9\mathrm{L}_\odot} \tag{2.1}$$

(Wu *et al.*, 2005) and the 3.6 μm image to a mass map using the relation:

$$\log \frac{\mathrm{M}}{\mathrm{M}_{\odot}} = (-0.79 \pm 0.03) + (1.19 \pm 0.01) \times \log \frac{\mathrm{L}(3.6\mu\mathrm{m})}{\mathrm{L}_{\odot}} \tag{2.2}$$

(Zhu *et al.*, 2010). We therefore computed that the total D25 sSFR of the galaxy is sSFR $= 1.54 \times 10^{-10}\mathrm{yr}^{-1}$. Lehmer *et al.* (2010) suggest a limit in sSFR of $5.9 \times 10^{-11}\ yr^{-1}$, above which the X-ray source population are dominated by HMXBs. Since the integrated sSFR of Arp 299 as well as the sSFR at the location of the X-ray sources are above this limit, we can conclude that all the sources we have detected are HMXBs. This is in good agreement with the maximum number of LMXBs expected in our sample, less than 2 sources, based on the XLF for LMXBs of Lehmer *et al.* (2014), and stellar mass calculated from the K-band luminosity of the galaxy.

Furthermore, we wanted to see if a correlation between sSFR and the youngest most massive stars exists in Arp 299. In this case we could use this correlation to identify which sources are younger and possibly hosting more massive donor stars by inspecting the sSFR map of the galaxy. We used a map of [NeIII]/[NeII], which is a tracer of the most massive stars present in a galaxy (Alonso-Herrero *et al.*, 2009). Comparison of this map with the sSFR map of the galaxy did not show any correlation between the [NeIII]/[NeII] ratio and the sSFR at the general region of the X-ray sources. The fact that we do not see a correlation most probably implies that the highest values of the [NeIII]/[NeII] ratio could correspond to deeply embedded areas of the galaxy, since these mid-infrared lines are less affected by absorption, than the shorter wavelengths used to trace the SFR and stellar mass.

2.3.2 The Star-formation rate

In order to study the link between X-ray binaries, the hot gas of the galaxy, and its star-forming activity we calculate the total star formation rate (SFR) of Arp 299 by adopting two different methods. Based on *IRAS* flux densities and using the relation of Helou *et al.* (1988) we find that the total infrared luminosity is $\mathrm{L}_{(8-1000\ \mu\mathrm{m})} = 5.9 \times 10^{11}\ \mathrm{L}_{\odot}$ and then using the calibration of Kennicutt & Evans (2012) we find a $\mathrm{SFR}_{\mathrm{IR}} = 88.89$ $M_{\odot}\ yr^{-1}$. Since the total infrared luminosity includes the contribution of the AGN, the SFR estimated this way should be treated as an upper limit to the total SFR of the galaxy.

We have also calculated the SFR from the polycyclic aromatic hydrocarbon (PAH) emission, which is a reasonably good SFR indicator (Shipley *et al.*, 2016; Wu *et al.*, 2005), using an IRAC 8μm non stellar image (Brassington *et al.*, 2015) and the calibration relation of Wu *et al.* (2005). This gives $\mathrm{SFR}_{8\mu\mathrm{m}} = 33.06\ \mathrm{M}_{\odot}\ \mathrm{yr}^{-1}$. The image

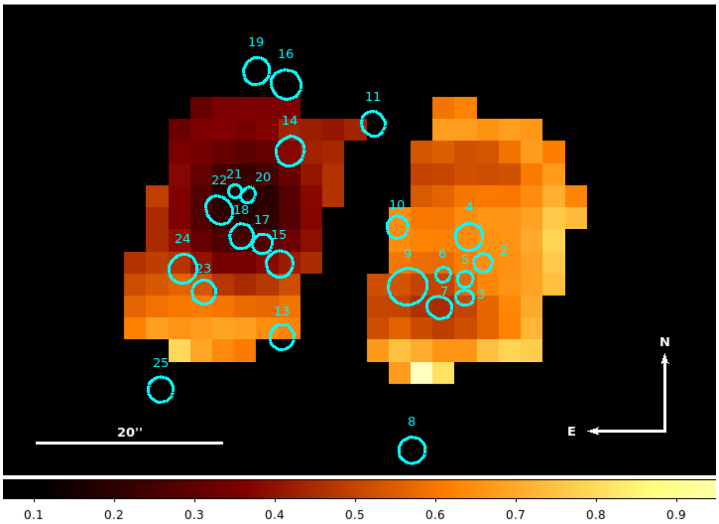

Figure 2.11: Line ratio map of Arp 299. -A [NeIII] 15.56 μm/[NeII] 12.8 μm line ratio map of Arp 299 (Alonso-Herrero *et al.*, 2009). The X-ray sources are overlaid with cyan ellipses. Lighter colours indicate higher [NeIII]/[NeII] ratios indicating younger star-forming regions (see text for details).

was saturated at the nuclei and knowing that the 8μm PAHs emission is suppressed in AGN (Lutz *et al.*, 1998) we consider this as lower limit.

2.3.3 Nature of the X-ray sources

Based on analysis presented in section 3.2.6.1 the total luminosity (0.1 – 10 keV) of the X-ray binaries based on their power-law component is 2.5×10^{40} erg s^{-1} (absorbed) and 48.0×10^{40} erg s^{-1} (unabsorbed). From the results in Table 3.11 we find that the contribution of binaries to the absorbed luminosity of Arp 299 is 52% in the broad band, 21% in the soft band, and 77% in the hard band, while their contribution to the unabsorbed luminosity is 39% in the broad band, 28% in the soft band and 77% in the hard band.

We can also compare the number of X-ray sources using their scaling relation $\mathrm{N_{XRB}}(> 10^{38}) = 3.22 \times \mathrm{SFR}$ (Mineo *et al.*, 2012a). Although our observation does not reach luminosities all the way down to 10^{38} erg s^{-1} due to incompleteness, we can still have an idea of the number of XRBs. According to the integrated SFR of the galaxy (§2.3.2) we would expect to observe between 4 to 11 times more XRBs than we do, depending on the SFR adopted.

Given the much higher SFR of Arp 299 compared to the population of nearby galaxies we wish to test whether Arp 299 verifies the scaling relations between XRB X-ray luminosities and SFR observed for other galaxies. For that reason we used the linear relation $L^{XRBS}_{0.5-8.0keV}(ergs^{-1}) = 2.61 \times 10^{39} SFR(M_{\odot}yr^{-1})$ (Mineo *et al.*, 2012a) between the integrated luminosity of HMXBs and SFR which is based on a sample of 29 nearby star-forming galaxies. The scatter of this relation is 0.43 dex. Measuring the total luminosity of the XRBs of Arp 299 (Table 3.11) in the same energy range we find $L_{XRBS(0.5-8.0keV)} = 2.17 \times 10^{41}$ erg s^{-1}. In Fig. 2.12 we plot the X-ray luminosity of XRBs in the sample of galaxies used by Mineo *et al.* (2012a) against their SFR, along with their best-fit linear relation. In the same plot we show Arp 299 (red points depending on the SFR indicator used). We see that Arp 299 verifies the relation within the 1 σ scatter using both of the calculated SFRs.

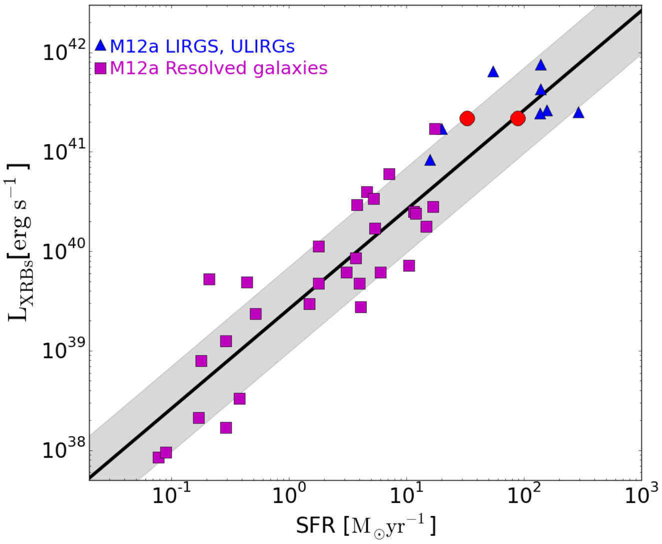

Figure 2.12: Lx-SFR scaling relation -$L_X - SFR$ relation for a sample of 29 nearby galaxies LIRGS and ULIRGS, the best-fit solid line and the 1σ scatter indicated by the grey area (Mineo *et al.*, 2012a, M12a). We show the position of Arp 299 on the diagram with two red circles corresponding to the higher and lower SFR we calculated. For Arp 299 we show the Lx of the power-law which traces the XRBs.

We also calculated the expected luminosity of the ULXs again in the (0.5 − 8.0 keV) band from the XLF of Mineo *et al.* (2012a) and found a luminosity of $L_{ULXs} = (2.3 \pm 0.4) \times 10^{41}$ *erg s*$^{-1}$ based on the total infrared SFR, and $L_{ULXs} = (8.5 \pm 0.2) \times 10^{40}$ erg s^{-1} based on the PAH 8μm SFR. The errors in the luminosities were calculated by propagating the errors from the XLF. We find that the observed integrated luminosities of

ULXs in the $0.5 - 8.0$ keV band agree with those expected from the general HMXB XLF within 2.5σ if we use the $\mathrm{SFR_{IR}} = 88.89\ \mathrm{M_\odot\ yr^{-1}}$ and under 1σ if we use the $\mathrm{SFR}_{8\mu\mathrm{m}} = 33.06\ \mathrm{M_\odot\ yr^{-1}}$.

From the same general HMXB XLF we calculated that the expected number of ULXs per unit of SFR is $N_{ULX}^{XLF}/SFR\ (M_\odot\ yr^{-1}) = 0.66$. In the case of Arp 299, given the total population of 20 ULXs we find a much lower ratio of 0.23 assuming the IR-based SFR, and a ratio of 0.60 assuming the 8 μm PHAs-based SFR. The same results for the 14 point-like ULXs are 0.16 and 0.42 for the IR-SFR and the PHA-SFR respectively.

If we now compare with the number of ULXs expected from the work of Swartz *et al.* (2011) ($(N_{ULX}^{XLF}/SFR\ (M_\odot\ yr^{-1}) = 2.0)$) the deficit is even larger since the values for Arp 299 are 0.16 to 0.60 (depending on SFR and number of ULXs chosen). We would expect 65-178 ULXs in our observation depending on the SFR chosen.

These results indicate a marginally statistically significant deficit in the number of ULXs in Arp 299: 0.5-1.3σ comparing with the XLF of Mineo *et al.* (2012a), and $> 2.5 - 3\sigma$ with respect to with the ULX SFR calibration of Swartz *et al.* (2011) ($(N_{ULX}^{XLF}/SFR\ (M_\odot\ yr^{-1}) = 2.0)$). Since this effect in Arp299 (but also other LIRGs) has been discussed extensively in the literature, we discuss its origin in the light of the deeper observations presented in this work.

The same deficit is reported by Luangtip *et al.* (2015) who studied a sample of 17 nearby LIRGs (including Arp 299). Although they found 8-9 ULXs for Arp299, based on the first much shallower *Chandra* exposure and the exclusion of sources very close to the nuclei, the deficit remains when we include the new detections. This result is also supported by Smith *et al.* (2012) where the total population number of ULXs in LIRGs (including Arp 299) compared to the far-infrared luminosity is deficient in comparison to the values found in spiral galaxies. Luangtip *et al.* (2015) discuss that metallicity may have some influence on ULX numbers (Basu-Zych *et al.*, 2013a,b; Brorby *et al.*, 2014; Linden *et al.*, 2010; Mapelli *et al.*, 2011; Prestwich *et al.*, 2013) but they argue that the main reason for this deficit is high columns of gas and dust that obscure these ULXs from our view.

But can high columns of dust and gas be the main reason for this deficit of ULXs in Arp 299? The X-ray luminosity of HMXBs we observe agrees with the one we would expect and follows the existing scaling relation by Mineo *et al.* (2012a) (Fig. 2.12) which strongly suggests that we are not missing any X-ray emission from sources in heavily obscured areas of the galaxy. If high obscuration was present we would also expect a deficit in the observed X-ray luminosity, or in other words a lower ratio between the observed ULX X-ray luminosity and that expected from the scaling relation with SFR, since the SFR is based on the 8μm luminosity which is less affected by the extinction. Therefore, Arp 299 would be below the line indicating the Mineo *et al.* (2012a) relation in Fig. 2.12, which is not the case as it falls on the fitting line for the IR-SFR and above it for the 8 μm SFR. Checking area A (Src 18), one of the areas with the greatest absorption ($A_v = 34$ mag; Alonso-Herrero *et al.*, 2009), and using the relation $N_H = 1.9 \times 10^{21} A_v$ (Zombeck, 2006) we find an expected H_I column density of $N_H = 6.46 \times 10^{22}$ cm^{-2} which agrees within the errors with our observed value $3.62^{+2.80}_{-1.70} \times 10^{22}$ cm^{-2}. This indicates that the region where most of the HMXBs are expected to be produced is hidden only behind moderate absorbing columns, which would influence the detectability of only the faintest sources, and certainly not their integrated emission.

Can metallicity be a reason of this deficit? Recent studies have shown that the numbers of ULXs could be suppressed in high metallicity environments (Basu-Zych *et al.*, 2013a,b; Brorby *et al.*, 2014; Linden *et al.*, 2010; Mapelli *et al.*, 2011; Prestwich *et al.*, 2013). Luangtip *et al.* (2015) based on the results of Prestwich *et al.* (2013) argued that metallicity on its own could not be a sufficient reason for this deficit. According to Douna *et al.* (2015) HMXBs are typically 10 times more numerous per unit of SFR in low-metalicity galaxies ($12 + \log(O/H) < 8.0$). In Arp 299 where $12 + \log(O/H) = 8.80$ (Relaño *et al.*, 2007) the metallicity could play a role in the deficit of sources but the existing trends (Douna *et al.*, 2015) have significant scatter and therefore do not allow us to draw any definite conclusions.

In Arp 299 there is a clear deficit in the number of HMXBs as well as in the number of ULXs but no deficiency in their total observed luminosity compared to that expected from scaling relations. We argue that this is the result of source confusion owing to the large distance of the galaxy (44 Mpc). At this distance the typical scale of star-forming region ($\lesssim 0.5$ kpc) corresponds to 2.5″ hindering the detection of individual discrete sources especially in the most active star-forming regions. HST data show that star-forming regions have angular scales of $0.5 - 1.0''$ which are easily confused with the 0.5″ *Chandra* beam. Therefore, given that the total luminosity of the HMXBs is consistent with that expected from the scaling relation, and accounting for the large distance of Arp 299, we attribute this deficit mainly to confusion effects. Such effects may also explain the deficit of ULXs in other (U)LIRGs, which are generally in larger distances than Arp 299.

2.3.4 Diffuse emission

Based on analysis presented in section 3.2.6.2 we found that the luminosity of the diffuse emission in the soft ($0.1-2.0$ keV) band is 1.5×10^{41} (absorbed), 1.7×10^{41} (unabsorbed), and in the hard ($2.0-10.0$ keV) band is 7.1×10^{40} (absorbed), and 7.2×10^{40} (unabsorbed). From the results presented in Table 3.11 we see that the contribution of the soft, diffuse, emission to the total soft X-ray luminosity of the galaxy is 70% (absorbed), 17% (corrected for the Galactic absorption), and 18% (totally unabsorbed). The contribution of the hard diffuse emission to the total hard luminosity of the galaxy is 26% (absorbed) and 25% (corrected for the Galactic absorption and the totally unabsorbed).

The parameters of the thermal emission such as the temperature ($\mathrm{kT} = 0.72\pm0.03$ keV; Table 2.4) are consistent within the errors with results found in other star-forming galaxies (e.g. Antennae, M101 Baldi *et al.*, 2006a; Fabbiano *et al.*, 2003; Kuntz & Snowden, 2010; Mineo *et al.*, 2012b). The elemental abundances are generally expected to be solar or subsolar in starburst galaxies or ULIRGs (e.g. Huo *et al.*, 2004; Strickland *et al.*, 2002, 2004). The abundance of Fe is consistent ($0.26^{+0.04}_{-0.03}$) with this result. The abundances of Ne and Mg are super solar ($1.24^{+0.34}_{-0.29}$ and $1.14^{+0.25}_{-0.20}$) but consistent with solar within the uncertainties. Subsolar values of Fe and especially the high values of [Mg/Fe] and [Ne/Fe] ratios indicate enrichment of the ISM by Type II supernovae (Baldi *et al.*, 2006b). This is expected given its strong recent star forming activity which would result in an enhanced type II supernova rate.

Mineo *et al.* (2012b) have reported scaling relations of the total diffuse emission from star-forming galaxies and their SFR. Arp 299 is an extreme star-forming galaxy with a high star-formation rate similar to that witnessed in higher redshift galaxies. Therefore it is instructive to see if it follows this general scaling relation derived from more moderate systems. We used the correlations of Mineo *et al.* (2012b) involving (a): the luminosity of the diffuse emission in the $0.5-2.0$ keV band versus SFR, and (b): the luminosity of the thermal component in the $0.3-10.0$ keV band. The measured luminosities for the diffuse and thermal plasma components of Arp 299 are $\mathrm{L}^{\mathrm{dif}}_{0.5-2.0\ \mathrm{keV}} = 1.44\times10^{41}$ erg s^{-1} and $\mathrm{L}^{\mathrm{thermal}}_{0.3-10.0\ \mathrm{keV}} = 1.89\times10^{41}$ erg s^{-1}. In Fig 2.13 and 2.14 we plot the scaling relation of Mineo *et al.* (2012b) along with the values for Arp 299.

As we see from these Figures Arp 299 even though has a SFR 2-4 times higher than the most actively star-forming system used in the scaling relation it does not deviate from the general trend. Such deviation would be expected, for example in the case of

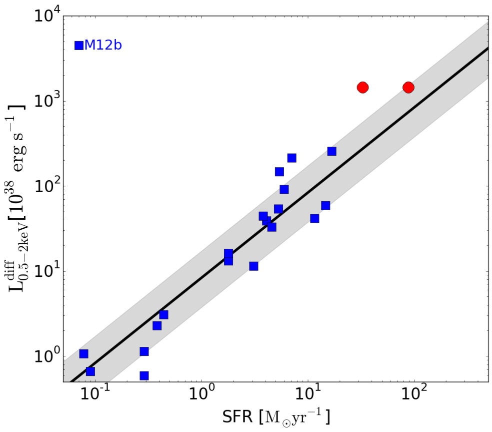

Figure 2.13: Ldiffuse-SFR scaling relation. -Unabsorbed (corrected for the galactic column density) luminosity of the diffuse emission in the $0.5 - 2.0$ keV band versus SFR for a sample of 21 galaxies, the best-fit solid line, and the 1σ scatter indicated by the grey area (Mineo *et al.*, 2012b, M12b). We show the position of Arp 299 with the red circles for the two SFRs calculated.

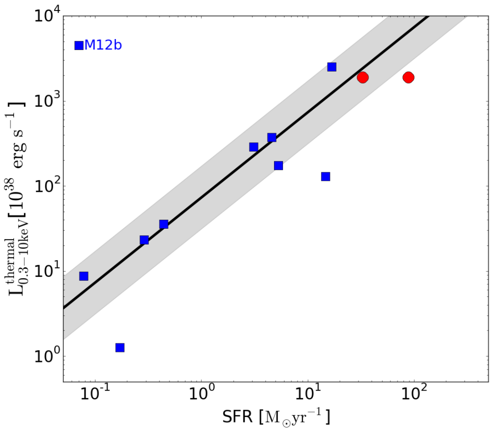

Figure 2.14: Lapec-SFR scaling relation. -Unabsorbed luminosity of the thermal component of the diffuse emission in the $0.3 - 10.0$ keV band versus SFR for a sample of 21 galaxies and the best-fit solid line, and the 1σ scatter indicated by grey area (Mineo *et al.*, 2012b, M12b). We show the position of Arp 299 with the red circles for the two SFRs calculated.

strong superwinds which would drive significant amount of hot gas outside the galaxy (Strickland & Stevens, 2000). In fact Arp 299 has a very high supernova rate (e.g. Kankare *et al.*, 2014; Ulvestad, 2009) which would drive such an outflow. As discussed in §3.2.6.2 there is evidence of a plume extending beyond the optical body of the galaxy in the west of NGC 3690 (Fig. 2.8), suggestive of such an outflow. However, this is not a full-scale superwind as seen in other galaxies (e.g. M82; Fabbiano, 1988; Stevens *et al.*, 2003; Strickland & Heckman, 2009; Strickland *et al.*, 1997; Watson *et al.*, 1984). This could be the result of either the young age of star-formation in Arp 299 or its much larger mass compared to that of the dwarf galaxies typically exceeding large scale outflows.

2.4 SUMMARY

We have analysed a deep 90 ks *Chandra* ACIS-S observation of the interacting star-forming galaxy Arp 299 (NGC 3690/IC 694) and found in total 25 discrete sources and a diffuse emission component. We have found, in agreement with previous studies (Fabbiano, 2003; Lira *et al.*, 2002), that the discrete sources dominate the hard X-ray emission of the galaxy above 2.0 keV whereas the diffuse emission component contributes to the soft emission of the galaxy below 2.0 keV.

We verify the presence of an AGN in the nucleus of NGC 3690 by observing its prominent Fe-Kα line. However, its contribution to the overall hard emission of the galaxy is quite small ($\sim$ 20%). For the nucleus of IC 694 we have only a hint of the ionized Fe-Kα line which could arise from hot thermal gas in this intensively star-forming region. The lack of a neutral iron line does not let us to conclude the existence of an AGN.

We have reported 23 off-nuclear sources, 20 of which exceed the ULX limit. Fourteen of them are point-like sources and therefore considered ULXs. We argued that these sources are young HMXBs based on their association with regions of active, on-going star-formation.

We reported a deficit in the number of HMXBs and ULXs versus the SFR according to the expecting number from the XLF of Mineo *et al.* (2012a) and the calibration of the ULX/SFR of Swartz *et al.* (2011). We attributed the main cause of this deficit to confusion of sources since we observed the expected emission of the HMXBs and ULXs.

These results show that although Arp 299 is a local extreme star-forming galaxy, its observed hard X-ray luminosity per unit SFR is very similar to that of higher-z galaxies (e.g. Basu-Zych *et al.*, 2013a; Mineo *et al.*, 2014). This indicated that Arp 299 is an excellent analogue of the X-ray luminous higher-z objects detected in the deep X-ray surveys.

2.5 Tables

Table 2.8: Properties of the discrete sources in the hard, medium and soft bands.

Src[a]	Net counts(hard)	Bkg	S/N	Net counts(medium)	Bkg	S/N	Net counts(soft)	Bkg	S/N
ID	±error			±error			±error		
(1)	(2)	(3)	(4)	(5)	(6)	(7)	(8)	(9)	(10)
1	59.8 ± 8.9	1.1	6.5	57.3 ± 8.5	1.6	6.3	18.1 ± 5.6	1.9	2.9
2	157.0 ± 14.4	15.9	10.0	156.2 ± 15.6	40.8	9.3	117.5 ± 15.1	58.5	7.0
3	210.4 ± 20.5	101.0	9.6	126.2 ± 18.2	100.7	6.5	-0.5 ± 10.9	58.5	-0.0
4	113.0 ± 16.6	60.0	6.7	234.0 ± 24.6	153.0	9.5	236.0 ± 24.9	159.0	9.4
5	74.4 ± 11.7	21.6	6.0	98.6 ± 13.4	30.4	7.0	33.2 ± 10.6	32.8	2.9
6	87.5 ± 11.8	22.5	6.7	54.5 ± 10.7	29.5	4.5	-1.5 ± 7.0	28.5	-0.1
7	398.0 ± 24.0	80.0	15.0	315.2 ± 23.0	103.7	13.0	179.2 ± 18.7	80.7	9.0
8	11.5 ± 4.6	0.5	2.2	16.5 ± 5.2	0.5	2.9	7.2 ± 4.6	4.7	1.3
9	5.4 ± 9.6	21.5	0.6	11.2 ± 15.1	64.8	0.8	55.6 ± 18.4	86.4	3.3
10	121.9 ± 12.5	8.05	9.3	84.5 ± 10.9	9.5	7.3	14.8 ± 5.9	6.2	2.2
11	8.9 ± 4.4	1.0	1.8	10.4 ± 4.7	1.6	2.0	3.8 ± 4.3	4.2	0.7
12	65.7 ± 9.4	3.3	6.6	85.2 ± 10.4	1.8	8.0	47.3 ± 8.6	7.7	5.0
13	19.9 ± 6.1	4.1	2.9	25.1 ± 6.9	6.8	3.3	25.3 ± 7.6	13.7	2.9
14	88.0 ± 10.6	2.0	8.1	74.3 ± 10.3	6.7	6.9	32.7 ± 9.2	21.3	3.2
15	50.1 ± 10.8	22.8	4.4	75.2 ± 12.7	30.8	5.7	22.2 ± 11.6	45.8	1.8
16	102.9 ± 11.4	1.0	8.9	86.0 ± 10.6	1.0	8.1	24.8 ± 7.6	6.2	3.3
17	215.8 ± 17.8	41.1	11.0	221.1 ± 18.4	49.8	11.4	122.9 ± 13.5	18.1	8.8
18	354.3 ± 26.2	90.6	14.0	77.6 ± 22.0	121.3	4.0	-8.7 ± 16.6	82.7	-0.6
19	27.0 ± 6.7	2.0	3.8	20.7 ± 6.3	3.3	3.1	9.0 ± 6.4	12.0	1.2
20	6.9 ± 4.1	1.1	1.5	12.1 ± 7.2	18.8	1.4	24.2 ± 9.8	38.8	2.1
21	11.7 ± 5.7	5.3	1.8	32.0 ± 8.0	10.0	3.7	1.7 ± 7.5	25.3	0.2
22	-4.5 ± 8.8	31.4	-0.5	35.8 ± 14.5	73.1	2.4	100.7 ± 20.1	134.2	4.9
23	87.9 ± 11.5	16.0	7.1	38.4 ± 8.9	16.6	3.9	6.7 ± 6.1	13.3	0.9
24	33.8 ± 7.8	7.1	4.0	9.9 ± 7.5	22.0	1.1	6.2 ± 8.3	32.8	0.6
25	5.2 ± 3.6	0.8	1.2	11.9 ± 4.7	1.0	2.3	9.4 ± 5.0	5.5	1.5
26	14.3 ± 5.0	0.6	2.6	12.6 ± 4.7	0.4	2.4	8.6 ± 4.1	0.4	1.9

---

[a] Column 1: The source identification number, Columns 2, 5, and 8: Net source counts and corresponding error counts in the hard ($2.0 - 7.0$ keV), medium ($1.2 - 2.0$ keV), and soft ($0.5 - 1.2$ keV) bands respectively, Columns 3, 4, 6, 7, 9 and 10: The background source counts and the signal to noise ratio of each source and hard, medium and soft bands respectively.

Table 2.9: Properties of lower significant detections (2.0 < SNR < 3.0) in the broad band (0.5 – 7.0 keV).

Src[a] ID (1)	RA h m s (2)	Dec ° ′ ″ (3)	Net counts ±error (4)	Bkg (5)	S/N (6)	r_1 ″ (7)	r_2 ″ (8)
1a	11:28:29.3	+58:33:50.8	24.0 ± 7.5	12.0	2.8	0.96	1.02
2a	11:28:30.4	+58:33:58.8	33.1 ± 10.5	33.9	2.9	1.45	1.45
3a	11:28:31.5	+58:33:38.1	34.4 ± 11.2	42.6	2.8	1.00	0.96
4a	11:28:31.5	+58:33:55.2	21.3 ± 7.5	16.6	2.4	1.37	1.22
5a	11:28:33.1	+58:33:59.7	16.5 ± 6.1	6.5	2.4	0.95	1.22
6a	11:28:33.8	+58:33:52.5	39.5 ± 13.5	63.5	2.7	0.85	0.97

---

[a] Column 1: The source identification number, Columns 2 and 3: Sky coordinates, Column 4: Net source counts and corresponding error counts, Columns 5 and 6: The background source counts and the signal to noise ratio of each source, Columns 7 and 8: The two ellipse major and minor radius for the source apertures.

3

Do sub-galactic regions follow the galaxy-wide X-ray scaling relations? The example of NGC 3310 and NGC 2276

3.1 Introduction

Ultra luminous X-ray sources are off-nuclear sources that have luminosities L(0.3−10.0 keV) $> 10^{39}\ erg\ s^{-1}$. This generally exceeds the Eddington luminosity of a typical stellar-mass black hole and therefore it indicates very high accretion rates. The most generally accepted model to explain the nature of ULXs is that of super-Eddington accretion (with possibly mild beaming) onto a stellar-mass black hole or a neutron star (NS) X-ray binary (XRB) (e.g. Kaaret *et al.*, 2017; King, 2009, and references therein). Other models include accretion onto an intermediate-mass black hole (IMBH) although with very little observational evidence (e.g. Kaaret *et al.*, 2017). In general ULXs are more abundant in low metallicity galaxies (e.g. Douna *et al.*, 2015; Prestwich *et al.*, 2013) and are found in large numbers in merging and star-forming galaxies (e.g. Anastasopoulou *et al.*, 2016; Swartz *et al.*, 2011).

Two star-forming galaxies which have been found to host large number of ULXs are NGC 3310 and NGC 2276 (e.g. Lehmer *et al.*, 2015; Wolter *et al.*, 2011, 2015).

They are relatively nearby, at distances of 22 Mpc for NGC 3310 and at 41 Mpc for NGC 2276. These distances are based on the latest cosmology (Collaboration, 2018, $H_o = 67.4$ km s^{-1} Mpc^{-1}, $\Omega_M = 0.32$, and $\Omega_\Lambda = 0.68$) using the Virgo infall corrected redshift. For both galaxies the available redshift-independent distances, are based on the Tully-Fischer relation, which given their disturbed morphology and signs of interaction (described in the next paragraph) are not reliable.

Both galaxies exhibit unique morphologies. NGC 3310, which is among the most luminous star-forming galaxies in the local Universe, shows a disturbed morphology, which is possibly the result of a recent merger (~30 Myr ago; de Grijs *et al.*, 2003b; Elmegreen *et al.*, 2002) with a low metallicity dwarf galaxy which triggered a circumnuclear star forming ring of about 20 arcsec. The galaxy also shows two distinct spiral arms, one on the north and one on the south. NGC 2276, which is a member of the loose group NGC 2300 displays also a uniquely disturbed morphology, where the west side of the galaxy is being compressed as it moves supersonically (900 km s^{-1}) through the NGC 2300 intra-group medium (IGM; Rasmussen *et al.*, 2006).

In the X-rays, NGC 3310 showed evidence for the existence of an active galactic nucleus (AGN) based on the presence of an FeKα line in *Chandra* spectra of the nucleus Tzanavaris & Georgantopoulos (2007). However this is not supported by any other AGN indicator (e.g. optical lines, Ho *et al.*, 1997). Lehmer *et al.* (2015) combined simultaneous *Chandra* and *NuSTAR* observations of the galaxy and found an excess of X-ray emission per unit SFR in the 6-30 keV band compared to other lower sSFR (specific SFR=SFR per stellar mass) star-forming galaxies. This was interpreted as the result of the over-abundance of ULXs in NGC 3310 compared to typical galaxies. They argue that this excess of ULXs is most likely explained by the relatively low metallicity of the young stellar population in this galaxy. *HST* optical observations have identified hundreds of star clusters (Elmegreen *et al.*, 2002) younger than 10 Myr and with masses of 10^4-$10^5 M_\odot$ for the largest clumps, as well as, 17 candidate super star clusters, mainly in the innermost southern spiral arm. Furthermore de Grijs *et al.* (2003a,b) using the same data, found that the age and metallicity distributions of the clusters in and outside the circumnuclear ring in NGC 3310 are statistically indistinguishable, although there is a clear and significant excess of higher mass clusters in the ring compared to the non-ring cluster sample. Miralles-Caballero *et al.* (2014a) using data from the PPAK Integral Field Spectroscopy (IFS) Nearby Galaxies Survey (PINGS) found a rather flat gas-phase abundance gradient for about a hundred HII regions located on the disk and the spiral arms. This indicates that the minor merger event had a substantial impact on metal mixing in the galaxy, resulting in uniform metallicity across the galaxy.

Miralles-Caballero *et al.* (2014b) studied the Wolf-Rayet population of NGC 3310 by spatially resolving 18 star-forming knots with typical sizes of 200-300 pc in the disc of the galaxy hosting a substantial population of Wolf-Rayet stars, which assuming metallicity-dependent luminosities results to an integrated number of more than 4000.

NGC 2276 has been extensively studied in the X-rays. *Chandra* observations have shown that it hosts 16 ULXs (Wolter *et al.*, 2011, 2015). Its diffuse X-ray morphology shows several similarities to its optical morphology with the shock-like feature along the west side and a faint tail to the east side of NGC 2276 (Rasmussen *et al.*, 2006; Wolter *et al.*, 2015) and has temperatures of kT $\sim 0.3-0.8$ keV and luminosities of L$(0.3-2.0$ keV$)$ = 1.9-18.0 $\times 10^{39}$ erg s^{-1} for the main body and the faint tail of the galaxy. Wolter *et al.* (2015) using hydrodynamic simulations found that, though the periapsis passage of NGC 2276 and NGC 2300 $\sim$ 85 Myr ago helped to produce tidal arms and thicken the gaseous disk, these effects are marginal compared to the effects from ram-pressure and viscous stripping of the galaxy by the IGM. In the optical, the galaxy contains numerous HII regions (e.g. Davis *et al.*, 1997; Hodge & Kennicutt, 1983) and supernovæ (e.g. Dimai *et al.*, 2005; Iskudaryan & Shakhbazyan, 1967). Furthermore Mezcua *et al.* (2015) analysing quasi-simultaneous *Chandra* X-ray observations and European VLBI Network radio observations, report an IMBH candidate (NGC2276-3c) of 5×10^{4}M$_{\odot}$ associated with a *Chandra* source with L$(0.3-10.0\,$keV$) = 5.5\times10^{39}$erg s^{-1}.

These two galaxies due to their proximity, unique morphology and large number of X-ray sources, are excellent laboratories for studying the connection of XRBs and ULXs with galaxy parameters like the SFR and the stellar mass, even at sub-galactic scales. An investigation of the ULX population in the interacting pair NGC 2207/IC 2163 Mineo *et al.* (2013, 2014) showed that at sub-galactic scales the number of ULXs and their luminosity scales with SFR in a similar way as in galaxy-wide scales. However, they do find tentative evidence for a dependence of the number (and possibly the luminosity) of ULXs on the FIR to UV luminosity ratio, a proxy for the age of the stellar populations and dust extinction. However it is unclear if this trend is the result of local variations of the ULX population stemming from local variations of the star formation history, or it is the result of stochastic sampling of the X-ray binary luminosity function.

In this paper we use the available high quality data for NGC 3310 and NGC 2276 in order to address two questions: (a) the validity of the general relations between X-ray binaries and star-forming activity (e.g. Lehmer *et al.*, 2010; Mineo *et al.*, 2012a) to galaxies with large numbers of ULXs, and (b) the validity of these galaxy-wide scaling relations to sub-galactic scales. The structure of the paper is as follows: in section 3.2 we describe the observation, the data analysis and present our results. We discuss our results in section 4.5 and in section 4.6 we summarize our findings. All errors correspond to the 90% confidence interval unless otherwise stated.

3.2 Observation and Data Analysis

In this work we use observations obtained with the ACIS-S camera (Garmire, 1997) on board the *Chandra* X-ray observatory (Weisskopf *et al.*, 2000) for the galaxies NGC 3310 and NGC 2276. The observations for NGC 3310 were performed on January 15th 2003 (OBSID 2939; 47.16 ks) and October 22nd 2016 (OBSID 19891; 35.84 ks). A much shorter observation (10 ks; OBSID 16025) performed on the 11th of June 2014 is not included in our analysis since it will complicate the analysis without improving the statistics. The observations for NGC 2276 were performed on June 23rd 2004 (OBSID 4968; 45.57 ks) and May 14th 2013 (OBSID 15648; 24.74 ks). Although detailed analysis of the first observation of NGC 2276 has already been presented (Rasmussen *et al.*, 2006; Wolter *et al.*, 2011, 2015), we re-analyse the data for consistency and to incorporate all available data sets.

In our analysis we followed the same procedures described in Anastasopoulou *et al.* (2016). We used the CIAO data analysis suite version 4.8 and CALDB version 4.7.0 for the analysis of the data. We first applied the latest calibration data (using the *acis_process_events* tool) by reprocessing the Level-1 event files and then by filtering for bad grades and status bits (using the *dmcopy* tool) we created the Level-2 events files. We kept only grades=0, 2, 3, 4, 6 and status=0. The net exposure times after the removal of background flares are for NGC 3310 : 46.67 ks (OBSID 2939) and 35.84 ks (OBSID 19891) and for NGC 2276 : 44.29 ks (OBSID 4968) and 21.15 ks (OBSID 15648).

We used the *fluximage* tool on the events-2 files with *binsize=1.0* for each OBSID for the creation of the images and the exposure maps in the broad (0.5-7.0 keV), soft (0.5-1.2 keV), medium (1.2-2.0 keV), and hard (2.0-7.0 keV) bands. We also created images (using the *merge_obs* tool) for the co-added exposure based on the two observations for each galaxy. Additionally, we created sub-pixel resolution images (*binsize=0.2*) in order to look at small-scale structures which helps to distinguish sources in crowded areas of the galaxies. In order to measure the relative variation of the effective area in different regions of each image, we normalized all the exposure maps to the exposure of a reference pixel at approximately the centre of the galaxy (c.f. Zezas *et al.*, 2006).

Finally we used the *csmooth* CIAO tool with a Gaussian convolution kernel in order to create adaptively smoothed images. We applied a minimum signal-to-noise ratio of

3 and a maximum of 5. We also used the scales of the broad band in order to smooth the images in the soft, medium, and hard bands. Figs. 3.1 and 3.2 show ‘true colour images” for NGC 3310 and NGC 2276 respectively, where the soft, medium, and hard band adaptively smoothed images are show in red, green, and blue respectively. In these figures we see a population of hard discrete sources revealed by their blue colours, and soft, diffuse, emission shown in red.

3.2.1 Source Detection and Photometry

The source detection was performed, using the *wavdetect* tool (Freeman *et al.*, 2002), on the co-added exposure as well as the individual observations. We searched in the broad (0.5-7.0 keV), soft (0.5-1.2 keV), medium (1.2-2.0 keV), and hard-band (2.0-7.0 keV) images for sources on scales of 2, 4, 8, 16, and 32 pixels for the images with *binsize=0.2* (pixel scale 0.0984 arcsec/pixel) and on scales of 2, 4, 8, and 16 pixels for the images with *binsize=1.0* (with the native pixel scale of 0.492 arcsec). In the sub-pixel image of NGC 3310 we found two additional sources, more specifically sources 10, 11 and 19, 20 appeared as a single source in the *binsize=1.0* image. No additional sources were found in the sub-pixel image of NGC 2276. The final source list was created from the combination of the source lists in each band in the individual and the co-added observation. We found in total 37 sources encompassed by NCG 3310 and 23 sources in NGC 2276. The extent of NGC 2276 was defined as the D25 region reported in the 3rd Reference Catalogue (RC3; Corwin *et al.*, 1994; de Vaucouleurs *et al.*, 1991). However, since the D25 region of NGC 3310 reported in the RC3 was smaller than the optical extent of the galaxy, we defined the outline of the galaxy on the based on optical DSS images. This is parametrized as an ellipse of semimajor axis $1.545'$, semiminor axis $1.199'$, and position angle PA=180 deg centred on the nucleus of the galaxy (RA= 10:38:45.8, Dec=+53:30:12).

For each source we performed aperture photometry using an elliptical aperture encompassing at least 90% of the energy of a point source at 1.49 keV (based on a PSF map calculated with *mkpsfmap*), while taking care to avoid emission from any nearby sources. The background was measured from an annulus with inner radius ~ 1 pixel larger than the source aperture and an outer radius ($\sim$ 4-20 arcsec), excluding any encompassed sources. This way we avoid contamination by the wings of the source PSF, and obtain good count statistics for reliable photometry.

We used the *dmextract* tool to perform the photometry on all the sources within the outline of each galaxy in the individual, co-added exposures and each of the broad, hard, medium, and soft bands. In more detail, following Zezas *et al.* (2006), we measured

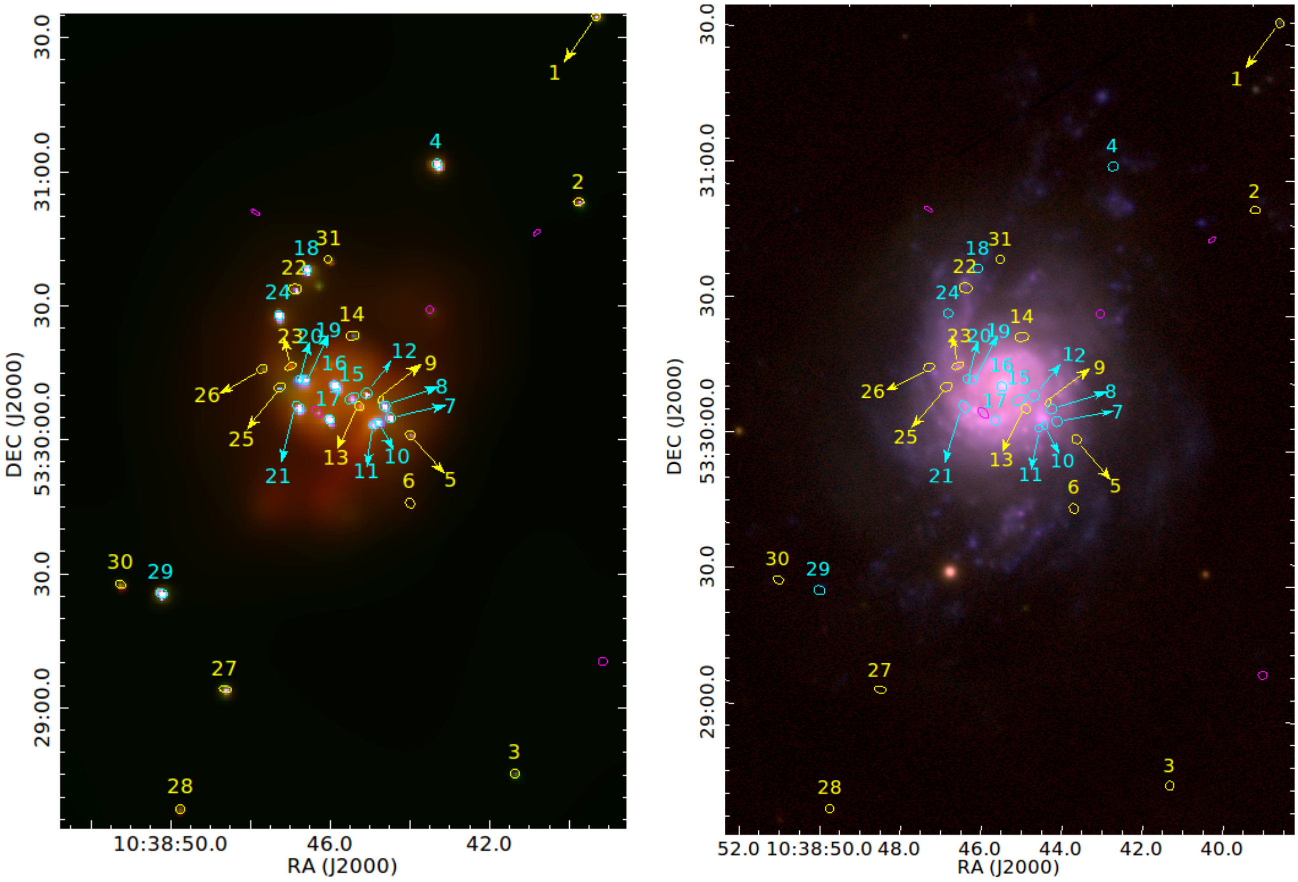

Figure 3.1: Left: An adaptively smoothed true colour X-ray image of NGC 3310 , with the soft (0.5-1.2 keV), medium (1.2-2.0 keV), and hard band (2.0-7.0 keV) shown in red, green, and blue respectively. Right: A PanSTARRS colour image with the y, i, and g bands shown in red, green, and blue respectively. The 31 sources with SNR > 3.0 are also overlaid on the two images, with the numbers corresponding to the source-IDs in Table 3.1. Cyan and yellow circles indicate sources with luminosities above and below 10^{39} erg s^{-1}respectively (i.e. the ULX limit). The two images have the same scale.

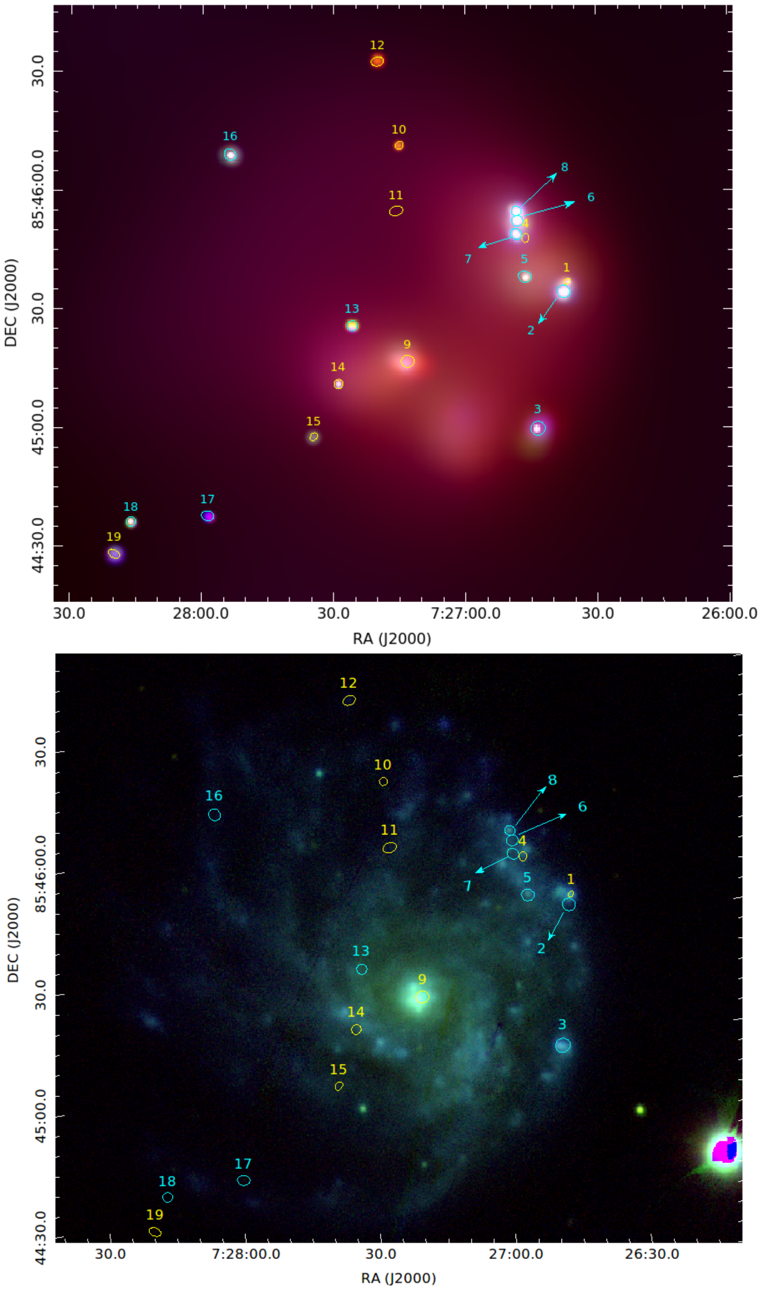

Figure 3.2: Top: An adaptively smoothed true colour X-ray image of NGC 2276 , with the soft (0.5-1.2 keV), medium (1.2-2.0 keV), and hard band (2.0-7.0 keV) shown in red, green, and blue respectively. Bottom: A PanSTARRS colour image with the y, i, and g bands shown in red, green, and blue respectively. The 19 sources with SNR > 3.0 are also overlaid on the two images, with the numbers corresponding to the source-IDs in Table 3.2. Cyan and yellow circles indicate sources with luminosities above and below 10^{39} erg s^{-1}respectively (i.e. the ULX limit). The two images have the same scale.

Table 3.1: Broad-band (0.5 – 7.0 keV) photometry of the discrete sources in NGC 3310.

Src	RA	Dec	r_1	r_2	Net counts±error	Bkg	S/N	Net counts±error	Bkg	S/N	Net counts±error	Bkg	S/N
ID	h m s	° ′ ″	″	″	OBSID 2939			OBSID 19891			co-added OBSIDs		
(1)	(2)	(3)	(4)	(5)	(6)	(7)	(8)	(9)	(10)	(11)	(12)	(13)	(14)
1	10:38:39.3	+53:31:35	0.95	0.94	74.6 ± 9.9	0.3	8.6	16.8 ± 5.2	0.2	3.2	90.5 ± 10.6	0.5	8.6
2	10:38:39.7	+53:30:53	1.13	0.78	62.7 ± 9.2	0.2	7.8	14.8 ± 5.0	0.2	3.0	74.5 ± 9.7	0.5	7.7
3	10:38:41.3	+53:28:45	0.98	1.00	21.6 ± 6.1	0.3	4.5	9.8 ± 4.3	0.2	2.3	29.4 ± 6.5	0.6	4.5
4	10:38:43.3	+53:31:02	1.13	0.96	945.6 ± 31.8	1.3	30.7	487.2 ± 23.1	0.8	21.1	1326.8 ± 37.5	2.2	35.4
5	10:38:43.9	+53:30:01	1.1	0.94	29.7 ± 8.2	8.2	4.3	18.5 ± 5.8	3.5	3.2	43.4 ± 8.5	11.6	5.1
6	10:38:43.9	+53:29:46	1.10	0.90	12.3 ± 5.5	1.6	3.1	−0.6 ± 1.9	0.6	-0.3	12.1 ± 4.8	1.9	2.5
7	10:38:44.5	+53:30:05	1.13	1.14	306.5 ± 20.2	26.4	16.1	86.7 ± 11.4	15.3	7.6	377.8 ± 22.1	48.2	17.1
8	10:38:44.6	+53:30:07	1.04	1.17	280.5 ± 19.7	29.4	15.2	87.5 ± 11.3	13.5	7.8	373.6 ± 21.6	41.4	17.3
9	10:38:44.7	+53:30:09	0.85	0.56	24.3 ± 7.9	8.6	3.7	17.7 ± 5.7	2.3	3.1	32.6 ± 8.0	12.4	4.1
10	10:38:44.8	+53:30:04	0.72	0.89	475.3 ± 24.2	26.6	20.6	125.8 ± 12.9	11.2	9.8	530.0 ± 25.0	36.0	21.2
11	10:38:44.9	+53:30:03	0.83	0.83	191.3 ± 16.9	25.6	12.2	82.0 ± 10.7	9.0	7.6	270.5 ± 18.9	37.5	14.3
12	10:38:45.0	+53:30:10	1.28	1.17	154.3 ± 15.6	24.6	10.8	43.0 ± 9.0	14.0	4.8	190.0 ± 16.5	36.0	11.5
13	10:38:45.2	+53:30:07	1.06	0.94	38.6 ± 11.5	31.3	3.8	20.7 ± 7.2	12.3	2.9	46.5 ± 11.7	47.5	4.0
14	10:38:45.4	+53:30:23	1.51	1.00	19.5 ± 7.8	10.4	3.0	8.3 ± 4.4	2.7	1.9	26.5 ± 7.4	13.5	3.6
15	10:38:45.4	+53:30:09	1.68	1.05	93.4 ± 15.3	50.5	6.7	53.7 ± 10.8	22.3	5.0	134.8 ± 16.9	75.2	8.0
16[a]	10:38:45.8	+53:30:12	1.10	0.95	1384.2 ± 39.8	53.7	35.8	312.0 ± 19.5	20.0	16.0	1587.6 ± 42.3	85.4	37.5
17	10:38:46.0	+53:30:04	1.04	1.02	1160.5 ± 36.2	34.4	33.0	351.4 ± 20.2	12.6	17.4	1438.4 ± 40.0	59.6	36.0
18	10:38:46.5	+53:30:38	0.96	0.94	307.6 ± 18.9	4.3	17.2	436.5 ± 22.1	6.5	19.8	681.2 ± 27.3	8.8	25.0
19	10:38:46.6	+53:30:13	0.96	0.89	205.7 ± 17.9	34.2	12.4	94.7 ± 11.8	13.3	8.0	288.6 ± 20.2	51.4	14.3
20	10:38:46.7	+53:30:13	0.81	0.86	381.4 ± 21.4	14.5	18.8	122.2 ± 12.6	7.8	9.7	482.9 ± 23.8	25.1	20.3
21	10:38:46.8	+53:30:07	1.40	1.05	143.8 ± 15.9	34.1	9.8	680.9 ± 27.8	22.1	24.5	780.7 ± 30.3	53.3	25.7
22	10:38:46.9	+53:30:33	1.43	1.08	80.5 ± 11.0	6.5	8.3	41.5 ± 7.9	4.5	5.3	118.3 ± 12.6	13.7	9.4
23	10:38:47.0	+53:30:16	1.37	0.72	27.9 ± 8.5	11.0	3.9	4.3 ± 4.8	7.7	0.9	29.2 ± 8.2	17.8	3.6
24	10:38:47.2	+53:30:28	0.97	0.94	825.1 ± 30.0	6.9	28.4	365.7 ± 20.2	3.3	18.1	1137.3 ± 34.9	12.7	32.5
25	10:38:47.2	+53:30:11	1.34	0.96	51.8 ± 10.4	15.1	5.7	20.5 ± 7.0	11.5	3.0	69.0 ± 10.7	19.0	6.5
26	10:38:47.7	+53:30:16	1.21	0.91	19.1 ± 7.4	7.8	3.2	9.3 ± 4.5	1.7	2.0	23.1 ± 7.0	9.9	3.3
27	10:38:48.6	+53:29:04	1.34	0.77	89.6 ± 10.7	0.4	9.4	45.8 ± 7.8	0.2	5.8	123.4 ± 12.2	0.6	10.1
28	10:38:49.7	+53:28:37	1.00	1.00	14.7 ± 5.4	0.3	3.7	14.8 ± 5.0	0.2	3.0	28.5 ± 6.5	0.5	4.4
29	10:38:50.2	+53:29:25	1.25	1.01	675.0 ± 27.1	0.9	25.9	460.4 ± 22.5	0.6	20.5	1109.3 ± 34.3	1.7	32.3
30	10:38:51.2	+53:29:27	1.14	0.86	31.5 ± 7.0	0.5	5.5	15.7 ± 5.1	0.3	3.1	43.1 ± 7.7	0.9	5.6
31	10:38:46.0	+53:30:40	0.94	0.94	11.0 ± 5.6	2.9	1.9	16.5 ± 5.2	0.5	3.2	24.1 ± 6.3	2.9	3.8

Column 1: the source identification number; columns 2 and 3: Right Ascension and Declination (J2000); columns 4 and 5: the major and minor radius of the elliptical source apertures; column 6: net source counts (and corresponding errors) for the longer (OBSID 2939) exposure; column 7: the estimated background counts within the extraction aperture of each source for the longer (OBSID 2939) exposure; column 8: the signal to noise ratio for the longer (OBSID 2939) exposure; columns 9, 10, 11: same as columns 6, 7, and 8 respectively but for the shorter exposure (OBSID 19891), column 12, 13, 14: same as columns 6, 7, and 8 respectively but for the co-added exposure.

---

[a] Nucleus of the galaxy; variable

Table 3.2: Broad-band (0.5 − 7.0 keV) photometry of the discrete sources in NGC 2276.

Src	RA	Dec	r_1	r_2	Net counts±error	Bkg	S/N	Net counts±error	Bkg	S/N	Net counts±error	Bkg	S/N
ID	h m s	° ′ ″	″	″	OBSID 4968			OBSID 15648			co-added OBSIDs		
(1)	(2)	(3)	(4)	(5)	(6)	(7)	(8)	(9)	(10)	(11)	(12)	(13)	(14)
1	7:26:36.6	+85:45:36.9	0.8	0.6	19.6 ± 5.7	1.4	4.0	8.4 ± 4.1	0.6	2.5	27.9 ± 6.5	2.1	4.8
2	7:26:37.4	+85:45:34.4	1.6	1.5	415.5 ± 21.5	4.5	20.1	90.9 ± 10.7	2.1	9.2	504.5 ± 23.6	6.5	22.1
3	7:26:43.3	+85:44:59.8	1.8	1.7	38.2 ± 7.6	4.8	5.4	5.8 ± 4.0	2.2	1.6	43.7 ± 8.2	7.3	5.6
4	7:26:46.1	+85:45:47.9	1.1	0.9	3.2 ± 3.6	2.8	1.0	21.7 ± 5.9	1.3	4.2	24.6 ± 6.5	4.4	4.1
5	7:26:46.3	+85:45:38.2	1.6	1.4	34.9 ± 7.3	4.1	5.2	9.3 ± 4.4	1.7	2.4	45.3 ± 8.2	5.7	5.9
6[a]	7:26:47.9	+85:45:52.2	1.4	1.3	183.2 ± 14.9	9.8	12.8	80.3 ± 10.2	3.7	8.5	261.2 ± 17.6	14.8	15.3
7	7:26:48.2	+85:45:48.9	1.5	1.2	107.2 ± 11.7	6.8	9.7	161.4 ± 13.8	1.6	12.5	270.5 ± 17.7	7.5	15.9
8	7:26:48.2	+85:45:54.7	1.2	1.1	323.4 ± 19.2	7.6	17.5	143.1 ± 13.1	1.9	11.7	469.4 ± 22.9	10.6	21.1
9[b]	7:27:13.0	+85:45:16.8	1.5	1.6	19.5 ± 6.6	11.5	2.9	10.7 ± 5.1	5.3	2.2	32.6 ± 8.1	17.4	3.9
10	7:27:14.8	+85:46:11.4	1.0	0.9	10.6 ± 4.4	0.4	2.9	3.7 ± 3.2	0.3	1.5	14.3 ± 5.0	0.7	3.4
11	7:27:15.5	+85:45:54.7	1.7	1.2	7.0 ± 4.0	1.0	2.1	12.4 ± 4.7	0.6	3.2	21.4 ± 5.9	1.6	4.2
12	7:27:19.8	+85:46:32.6	1.5	1.1	14.6 ± 5.0	0.4	3.5	75.6 ± 9.8	0.4	8.6	89.2 ± 10.5	0.8	9.3
13	7:27:25.6	+85:45:25.8	1.2	1.2	58.9 ± 8.8	1.1	7.4	37.8 ± 7.2	0.2	6.0	96.6 ± 10.9	1.4	9.6
14	7:27:28.7	+85:45:11.0	1.2	1.1	15.3 ± 5.2	1.7	3.4	5.8 ± 3.8	1.2	1.8	21.1 ± 6.0	2.9	3.9
15	7:27:34.4	+85:44:57.7	1.1	0.8	9.7 ± 4.3	0.3	2.8	1.7 ± 2.7	0.3	0.8	10.5 ± 4.4	0.5	2.9
16	7:27:53.5	+85:46:09.0	1.3	1.5	51.5 ± 8.3	0.5	7.0	20.7 ± 5.7	0.3	4.3	72.2 ± 9.6	0.8	8.3
17	7:27:58.5	+85:44:37.7	1.5	1.2	22.5 ± 5.9	0.5	4.5	0.8 ± 2.3	0.2	0.5	23.3 ± 6.0	0.7	4.5
18	7:28:15.9	+85:44:36.1	1.1	1.2	29.7 ± 6.5	0.3	5.2	38.6 ± 7.3	0.4	6.0	66.5 ± 9.2	0.5	8.0
19	7:28:19.7	+85:44:28.0	1.5	0.9	13.2 ± 4.8	0.8	3.2	5.5 ± 3.6	0.5	1.9	18.9 ± 5.6	1.1	3.9

Column 1: the source identification number; columns 2 and 3: Right Ascension and Declination (J2000); columns 4 and 5: the major and minor radius of the elliptical source apertures; column 6: net source counts (and corresponding errors) for the longer (OBSID 4968) exposure; column 7: the estimated background counts within the extraction aperture of each source for the longer (OBSID 4968) exposure; column 8: the signal to noise ratio for the longer (OBSID 4968) exposure; columns 9, 10, 11: same as columns 6, 7, and 8 respectively but for the shorter exposure (OBSID 15648), column 12, 13, 14: same as columns 6, 7, and 8 respectively but for the co-added exposure.

---

[a] IMBH candidate; Mezcua *et al.* (2015)

[b] Nucleus of the galaxy

the number of counts for each source in each image, the corresponding background counts from a "swiss-cheese" image from which all sources were removed, and the relative effective area at the location of each source with respect to the galaxy centre from the normalised exposure map. The SNR for each source is calculated by propagating the errors on the number of counts in the source and background areas (see also Anastasopoulou *et al.*, 2016). Throughout this paper we adopt the (Gehrels, 1986) approximation for the errors on the number of counts. In Tables 3.1 and 3.2 we present the results of the photometric analysis in the broad (0.5-7.0 keV) band for the 31 sources in NGC 3310 and the 19 sources in NGC 2276 with SNR $\geq$ 3.0. respectively.

3.2.2 Spectral Analysis

The *specextract* tool was used to extract source and background spectra of the discrete sources. The spectra for sources with more than 50 net counts were grouped to have at least 20 total counts per spectral bin in order to allow for χ^2 fitting. The spectral fits were performed with the XSPEC v12.9.0 package (Arnaud, 1996). In our analysis we considered only events in the 0.4 –8.0 keV range since events at lower or higher energies are dominated by the background. For sources with less than 50 net counts we grouped the spectra to have at least 2-5 total counts per spectral bin and the spectral fitting was performed using *sherpa* (Freeman *et al.*, 2001) with the *wstat* statistic. This is equivalent to the XSPEC implementation of the Cash statistic where the observed background data is added to the model and do not have to be modelled

We fitted simultaneously the spectra from the two separate observations (OBSID 2939 and OBSID 19891 for NGC 3310; OBSID 4968 and OBSID 15648 for NGC 2276) with all the model parameters apart from the normalization tied together. The normalization for the spectrum from each observation was left free to vary independently in order investigate for source variability.

For NGC 3310 we used only the longer exposure (OBSID 2939) for sources 6, and 23. These two sources are diffuse emission clumps and their significance in the shorter observation was very low (Table 3.3). Additionally fitting sources 1, 2, 21, and 26 simultaneously did not result in a good fit statistic and left significant residuals indicating spectral variability. Therefore we fitted the spectra for each OBSID separately.

For NGC 2276, in nine cases (Sources 1, 3, 5, 9, 10, 14, 15, 17, and 19) we used only the longer exposure since the very few counts of the shorter observation would not allow for spectral fitting (Table 3.4). All sources in NGC 2276, and all but 4 sources in NGC 3310 were fitted well with a single power-law model with photoelectric absorption (model in XSPEC: `phabs`×`po`). This model is generally used to fit the spectra of X-ray binaries (XRBs). For the majority of the sources, the best-fit photon indices are $\sim 1.7 - 2.0$, consistent with those of XRBs, while the hydrogen column density is typically greater than the Galactic (NGC 3310: $N_H^{Gal} \sim 5.52 \times 10^{20}\text{cm}^{-2}$; NGC 2276: $N_H^{Gal} \sim 1.11 \times 10^{20}\text{cm}^{-2}$; using the *Colden* tool[1]). For NGC 2276 sources 4 and 11 would not allow for spectral fitting since they had very few counts. The fit parameters for the 17 out of 19 sources of NGC 2276 for which we could perform spectral analysis are reported in Table 3.4.

For NGC 3310 source 16, which is the nucleus of the galaxy, an absorbed power-law model gave a good fit ($\chi^2/\text{dof} = 123.2/74$) and there was no sign for a FeKα emission line at 6.4 keV, in contrast to Tzanavaris & Georgantopoulos (2007) who report a line at 6.4 ± 0.1 keV with equivalent width (EW) of 0.3 keV. In order to test if our results are consistent with their work, we added a Gaussian line to the model with energy and width fixed at 6.4 keV and 0.1 keV respectively and normalisation free to vary. We found an EW of $0.23^{+0.43}_{-0.23}$ keV which is consistent with the EW of 0.3 keV reported in Tzanavaris & Georgantopoulos (2007). Sources 5, 6, 9, and 23 gave a good fit only with an absorbed thermal plasma model. Therefore we consider these sources as diffuse emission clumps within the galaxy. The fit results for the 31 sources in NGC 3310 are reported in Table 3.3.

---

[1] `http://cxc.harvard.edu/toolkit/colden.jsp`

3.2.3 X-ray colours

In order to characterize the spectra of the sources with too few counts for spectral analysis we calculated their X-ray colours. For a consistency check with the results from the spectral analysis we also calculated the X-ray colours for the sources for which we performed spectral fits. The X-ray colours are defined as $C_1 \equiv \log_{10}(S/M)$, $C_2 \equiv \log_{10}(M/H)$, $C_3 \equiv \log_{10}(S/H)$ where S, M, and H are the net counts in the soft (0.5-1.2 keV), medium (1.2-2.0 keV), and hard (2.0-7.0 keV) bands.

We calculated the X-ray colours and their uncertainties for the 31 sources in NGC 3310 and the 19 sources in NGC2276, using the Bayesian Estimation of Hardness Ratios[1] tool Park *et al.* (2006, ; BEHR). This tool evaluates the posterior probability distribution of the X-ray colours given the measured number of counts in the source and background apertures. As a result it provides reliable estimates and confidence limits even when either or both soft and hard counts are very low. In addition it can account for effective area differences between the sources or between observations. For this correction we used the average exposure within the aperture of each source (based on the broad-band exposure maps) normalized to the value at the center of each galaxy. The resulting X-ray colours and their corresponding 90% confidence intervals, are presented in Tables 3.5 and 3.6 for NGC 3310 and NGC 2276 respectively.

In order to estimate the spectral parameters of the X-ray sources from their X-ray colours we created grids on colour-colour plots and placed our sources on them. The grids were calculated by simulating absorbed power-law spectra for different values of the photon index (Γ) and the hydrogen column density (N_H) for a fiducial source at the centre of each galaxy, the reference position we normalized the source counts to. Fig. 3.3 and 3.4 show the location of the sources on the $C_2 - C_1$ grid for NGC 3310 and NGC 2276 respectively.

We see that the majority of the sources for OBSID 2939 of NGC 3310 fall on the region corresponding to $\Gamma \sim 1.5 - 2.5$ and $N_H < 0.85 \times 10^{22}$cm^{-2}, and for NGC 2276 on the region of $\Gamma \sim 1.5 - 4.0$ and $N_H < 0.85 \times 10^{22}$cm^{-2}. However there are 4 sources for OBSID 2939 of NGC 3310 (6,9,23,25), 11 sources for OBSID 19891 of NCG 3310 (1, 5, 6, 11, 13, 15, 25, 26, 28, and 31), 7 sources for OBSID 4968 of NGC 2276 (3, 9, 11, 13, 15, 17, and 19), and 9 sources for OBSID 15648 of NGC 2276 (1, 3, 5, 11, 12, 13, 15, 17, and 18) that fall outside the grid.

In the case of NGC 3310 sources 5, 6, 9, and 23 are diffuse emission sources and therefore are not expected to be consistent with a grid based on a power-law model

---

[1] http://hea-www.harvard.edu/astrostat/behr/

Table 3.3: NGC 3310 spectral parameters based on spectral fits.

Src ID (1)	Γ (2)	kT keV (3)	N_H 10^{22}cm^{-2} (4)	χ^2 (dof) (5)	Binning OBSID 2939 (6)	Binning OBSID 19891 (7)
1	$1.76^{+0.84}_{-0.37}$	-	$0.06^{+0.25}_{-0.05}$	0.4 (1)	20	-
1	$3.26^{+2.88}_{-1.73}$	-	$0.69 \leq 1.2$	6.2 (6)	-	2
2	$2.78^{+2.66}_{-1.09}$		$0.26^{+0.58}_{-0.26}$	1.1 (1)	20	-
2	$3.51^{+2.85}_{-1.88}$	-	$0.96 \leq 2.12$	13.6 (6)	-	2
3	$2.21^{+1.45}_{-1.1}$	-	$0.45 \leq 0.68$	4.4 (7)	5	5
4	$2.35^{+0.2}_{-0.18}$	-	$0.1^{+0.05}_{-0.05}$	60.0 (57)	20	2
5	-	$2.06^{+2.36}_{-1.71}$	$0.12 \leq 1.52$	18.2 (16)	5	2
6	-	$0.99^{+0.37}_{-0.90}$	$0.11 \leq 1.25$	1.5 (4)	2	-
7	$2.1^{+0.35}_{-0.31}$	-	$0.35^{+0.15}_{-0.13}$	12.5 (16)	20	20
8	$2.49^{+0.44}_{-0.38}$	-	$0.9^{+0.32}_{-0.24}$	13.5 (15)	20	20
9	-	$1.45^{+5.8}_{-0.46}$	$1.19^{+0.71}_{-1.08}$	31.8 (13)	5	2
10	$1.44^{+0.29}_{-0.26}$	-	$0.74^{+0.27}_{-0.21}$	17.6 (26)	20	20
11	$1.6^{+0.4}_{-0.36}$	-	$0.2^{+0.17}_{-0.14}$	6.7 (10)	20	20
12	$2.45^{+0.53}_{-0.48}$	-	$0.28^{+0.19}_{-0.15}$	60.5 (31)	20	5
13	$4.26^{+3.17}_{-1.78}$	-	$0.45 \leq 0.72$	15.0 (14)	20	5
14	$2.94^{+3.62}_{-1.22}$	-	$2.5^{+5.96}_{-1.9}$	25.3 (18)	2	2
15	$3.11^{+1.57}_{-1.01}$	-	$1.84^{+1.76}_{-1.2}$	51.3 (39)	20	2
16	$1.4^{+0.16}_{-0.15}$	-	$0.54^{+0.11}_{-0.09}$	123.2 (74)	20	20
17	$1.94^{+0.17}_{-0.16}$	-	$0.61^{+0.11}_{-0.09}$	69.2 (65)	20	20
18	$1.86^{+0.23}_{-0.21}$	-	$0.29^{+0.12}_{-0.1}$	51.1 (31)	20	20
19	$1.85^{+0.5}_{-0.43}$	-	$0.6^{+0.32}_{-0.23}$	9.5 (11)	20	20
20	$1.8^{+0.44}_{-0.39}$	-	$1.8^{+0.55}_{-0.44}$	15.9 (20)	20	20
21	$2.42^{+1.02}_{-0.52}$		$0.11^{+0.19}_{-0.08}$	2.4 (6)	20	-
21	$1.77^{+0.25}_{-0.23}$		$0.36^{+0.16}_{-0.14}$	20.5 (32)	-	20
22	$1.96^{+0.61}_{-0.52}$	-	$0.22^{+0.28}_{-0.21}$	8.3 (5)	20	15
23	-	$1.85^{+1.45}_{-1.81}$	$0.11 \leq 1.89$	12.2 (5)	5	-
24	$2.0^{+0.18}_{-0.17}$	-	$0.29^{+0.08}_{-0.08}$	61.9 (51)	20	20
25	$3.89^{+1.57}_{-1.2}$	-	$3.12^{+1.7}_{-1.25}$	46.4 (27)	5	2
26	$2.83^{+3.00}_{-1.62}$	-	$0.50 \leq 1.35$	0.7 (3)	5	-
26	$2.24^{+1.50}_{-1.13}$	-	$0.11 \leq 0.45$	7.1 (3)	-	2
27	$2.29^{+0.67}_{-0.54}$	-	$0.16^{+0.26}_{-0.16}$	8.5 (5)	20	15
28	$2.49^{+1.6}_{-0.81}$	-	$0.18 \leq 0.48$	7.0 (8)	5	2
29	$1.79^{+0.18}_{-0.17}$	-	$0.13^{+0.07}_{-0.06}$	40.4 (47)	20	20
30	$3.39^{+1.37}_{-1.1}$	-	$0.47^{+0.39}_{-0.32}$	23.5 (12)	5	2
31	$2.5^{+0.93}_{-0.57}$	-	$0.11 \leq 0.17$	16.1 (13)	2	2

Column 1: source ID; column 2: photon index Γ from spectral fitting; column 3: thermal plasma model temperatures (kT); column 4: line-of-sight hydrogen column density (N_H); column 5: χ^2 of the spectral fit and corresponding degrees of freedom (d.o.f); and columns 6 and 7: spectral binning for OBSIDs 2939 and 19891 respectively.

Table 3.4: NGC 2276 spectral parameters based on spectral fits.

(1)	Γ (2)	N_H 10^{22}cm^{-2} (3)	χ^2 (dof) (4)	Binning OBSID 4968 (5)	Binning OBSID 15648 (6)
1	$6.43^{+9.09}_{-3.96}$	$0.78 \leq 0.96$	0.009 (2)	5	-
2	$2.18^{+0.28}_{-0.31}$	$0.60^{+0.14}_{-0.12}$	21.7 (21)	20	20
3	$1.16^{+0.60}_{-0.50}$	$0.05 \leq 0.17$	4.5 (6)	5	2
4	-	-	-	-	-
5	$3.00^{+2.27}_{-1.33}$	$0.45^{+0.62}_{-0.39}$	2.3 (5)	5	2
6	$1.81^{+0.40}_{-0.35}$	$0.21^{+0.16}_{-0.13}$	9.7 (11)	20	20
7	$1.73^{+0.52}_{-0.45}$	$1.17^{+0.55}_{-0.43}$	15.4 (11)	20	20
8	$2.22^{+0.25}_{-0.28}$	$0.56^{+0.16}_{-0.13}$	39.6 (21)	20	20
9	$4.39^{+7.20}_{-2.68}$	$0.62 \leq 1.38$	7.6 (4)	5	-
10	$8.50^{+27.66}_{-5.70}$	$1.09 \leq 0.64$	3.3 (3)	2	-
11	-	-	-	-	-
12	$2.52^{+0.60}_{-0.57}$	$0.11 \leq 0.16$	91 (14)	5	2
13	$4.68^{+1.40}_{-1.16}$	$0.50^{+0.29}_{-0.24}$	9.3 (16)	5	2
14	$2.27^{+2.28}_{-1.30}$	$0.29 \leq 0.94$	0.9 (1)	5	-
15	$5.04^{+6.36}_{-3.16}$	$0.74 \leq 1.42$	3.3 (3)	2	-
16	$2.59^{+0.86}_{-0.75}$	$0.43^{+0.31}_{-0.26}$	22.2 (12)	5	2
17	$0.35^{+1.32}_{-1.41}$	$1.01 \leq 4.09$	0.7 (2)	5	-
18	$1.69^{+0.71}_{-0.36}$	$0.06 \leq 0.26$	16.8 (10)	5	2
19	$1.62^{+1.82}_{-1.41}$	$0.26 \leq 0.81$	1.4(4)	2	-

Column 1: source ID; column 2: photon index Γ from spectral fitting; column 3: thermal plasma model temperatures (kT); column 4: line-of-sight hydrogen column density (N_H); column 5: χ^2 of the spectral fit and corresponding degrees of freedom (d.o.f); and columns 6 and 7: spectral binning for OBSIDs 4968 and 15648 respectively.

with $\Gamma \sim 0-4$. For OBSID 2939, source 25 appears also to be very soft and with a high hydrogen column density and its spectrum, although of low quality, agrees with that values. For OBSID 2939 the remaining sources that are out of the grid agree within the errors with the expected values from the spectral parameters (see Table 3.10).

For NGC 2276 sources 11, 13, and 15 for both OBSIDS, and sources 1, 5 for OBSID 15648 are positioned above the grid indicating relatively soft spectra ($\Gamma \geq 3$), after accounting for the uncertainties on the colours. Source 17 for both OBSIDs and source 19 for OBSID 4968 appear to have hard spectra and moderate absorption, therefore, their position at the lower right (“softer colour") corner of the diagram could be attributed to an additional soft component (e.g. local diffuse emission) which cannot be recovered spectrally due to the poor quality of their spectra. Sources 3 and 9 for OBSID 4968 seem to have photon indices of about 0.7 and 2.5 respectively but very low absorption. Very low absorption also show sources 3, 12, and 18 with photon indices of 1.5, 1.7, and 0.8 respectively. For the rest of the sources we estimate their spectral parameters based on their location on the grid and we present these estimates in Tables 3.3 and 3.4.

We compared the X-ray colour based spectral parameters, to those calculated from the spectral fits (Fig. 3.5 and Fig.3.6), and we found that they agree well within the errors. We did not include sources not fitted with a single absorbed power-law model as well as for the sources not falling on the grids.

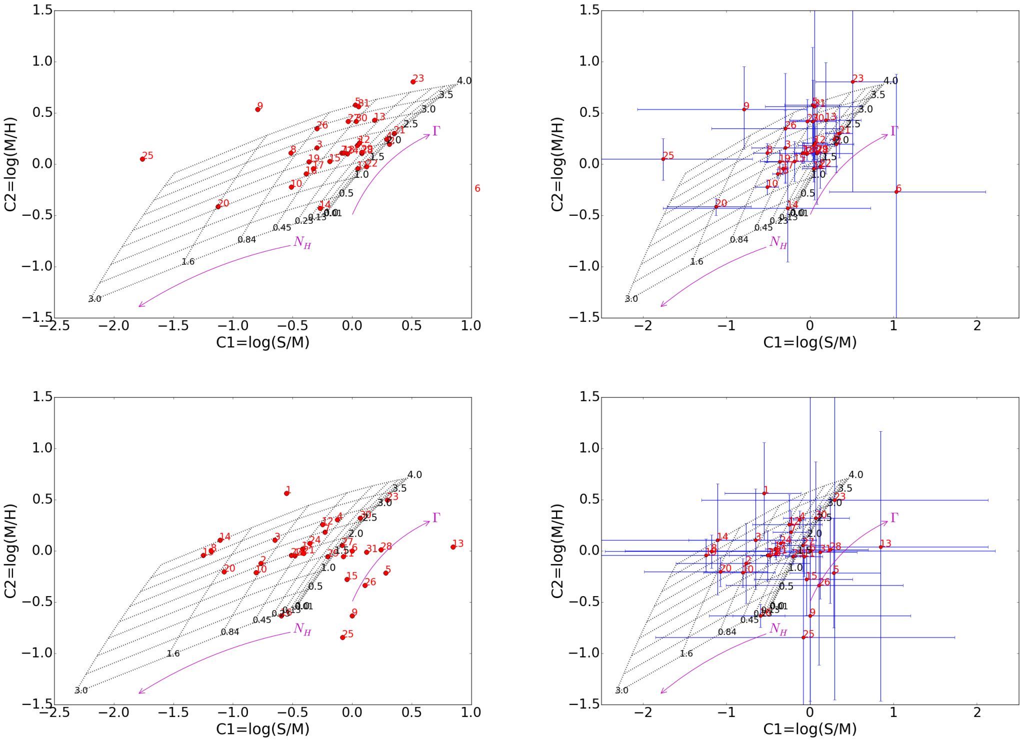

Figure 3.3: Colour-colour diagram for the X-ray sources detected in NGC 3310 showing the colours (left) and corresponding errors (right) for OBSID 2939 (top) and OBSID 19891 (bottom). The source numbers refer to the source ID in Table 3.1. A grid showing the expected colours for absorbed power-law spectra is also overlaid. The value of the photon index and the hydrogen column density (in units of 10^{22} cm^{-2}) are shown at the edge of the grid.

3.2.4 Fluxes and luminosities of the discrete sources.

Following our spectral analysis (Section 4.3.2) the flux and corresponding luminosity for each source was calculated by integrating the best-fit models (Tables 3.3 and 3.4). The errors on the fluxes are estimated by drawing model parameter values from their best-fit joint distribution and calculating the flux corresponding to the model for each set of draws. Then, the resulting fluxes are ordered and the central 90% is selected to give the error range. The errors on the luminosities were calculated by propagating the errors on the fluxes.

For sources 1, 3, 5, 9, 10, 14, 15, 17, and 19 of the shorter observation of NGC 2276 (OBSID 15648), since they had very few counts, we calculated the fluxes and luminosities (bottom section of 3.9) as follows. For each source we calculated the count-

Table 3.5: NGC 3310 X-ray colours of the discrete sources.

	OBSID 2939					OBSID 19891				
Src ID	C_1	C_2	C_3	Γ	N_H $10^{22}cm^{-2}$	C_1	C_2	C_3	Γ	N_H $10^{22}cm^{-2}$
(1)	(2)	(3)	(4)	(5)	(6)	(7)	(8)	(9)	(10)	(11)
1	0.04 ± 0.19	0.18 ± 0.22	$0.23^{+0.22}_{-0.21}$	2.2	0.20	$-0.55^{+0.44}_{-0.47}$	$0.56^{+0.5}_{-0.46}$	$0.01^{+0.6}_{-0.59}$	4.5	1.0
2	0.31 ± 0.21	0.19 ± 0.28	$0.51^{+0.25}_{-0.24}$	2.0	0.011	$-0.76^{+0.76}_{-0.84}$	-0.12 ± 0.39	$-0.88^{+0.73}_{-0.84}$	2.0	0.9
3	$-0.3^{+0.38}_{-0.4}$	$0.16^{+0.36}_{-0.35}$	$-0.13^{+0.42}_{-0.43}$	2.5	0.60	$-0.65^{+0.73}_{-0.8}$	$0.11^{+0.5}_{-0.48}$	$-0.54^{+0.76}_{-0.84}$	2.7	0.9
4	0.29 ± 0.05	0.24 ± 0.07	0.53 ± 0.07	2.2	0.1	-0.12 ± 0.07	$0.3^{+0.09}_{-0.08}$	0.18 ± 0.09	2.7	0.30
5	0.03 ± 0.33	$0.58^{+0.56}_{-0.5}$	$0.62^{+0.56}_{-0.54}$	4.0	0.60	$0.28^{+0.56}_{-0.52}$	$-0.21^{+0.54}_{-0.54}$	0.08 ± 0.43	~ 0.7	-
6	$1.03^{+1.07}_{-0.8}$	$-0.27^{+1.15}_{-1.38}$	$0.74^{+0.75}_{-0.64}$	-	-	0.0 ± 2.22	0.0 ± 2.22	0.0 ± 2.22	~ 1.5	-
7	-0.09 ± 0.11	0.11 ± 0.1	0.02 ± 0.11	2.0	0.30	$-0.23^{+0.21}_{-0.22}$	0.18 ± 0.21	-0.04 ± 0.24	2.5	0.3
8	-0.52 ± 0.16	$0.11^{+0.1}_{-0.09}$	-0.4 ± 0.16	2.5	0.90	$-1.18^{+0.72}_{-1.28}$	-0.01 ± 0.16	$-1.18^{+0.71}_{-1.29}$	3.5	2.0
9	$-0.79^{+0.75}_{-1.28}$	$0.54^{+0.42}_{-0.39}$	$-0.27^{+0.89}_{-1.36}$	-	-	0.0 ± 1.21	$-0.63^{+0.62}_{-0.83}$	$-0.63^{+0.62}_{-0.83}$	-	-
10	$-0.51^{+0.13}_{-0.14}$	-0.22 ± 0.07	-0.73 ± 0.13	1.2	0.60	$-0.81^{+0.39}_{-0.47}$	-0.21 ± 0.14	$-1.01^{+0.39}_{-0.47}$	1.7	0.9
11	0.05 ± 0.14	$-0.04^{+0.14}_{-0.13}$	0.0 ± 0.14	1.2	0.011	-0.07 ± 0.22	$-0.06^{+0.2}_{-0.19}$	-0.13 ± 0.21	~ 1.5	-
12	0.06 ± 0.15	0.21 ± 0.16	0.27 ± 0.17	2.2	0.25	$-0.25^{+0.39}_{-0.44}$	$0.26^{+0.29}_{-0.29}$	$0.01^{+0.41}_{-0.46}$	2.7	0.4
13	$0.19^{+0.42}_{-0.43}$	$0.43^{+0.56}_{-0.52}$	$0.62^{+0.6}_{-0.56}$	3.0	0.30	$0.85^{+1.29}_{-0.79}$	$0.04^{+1.13}_{-1.5}$	$0.9^{+0.7}_{-0.63}$	~ 1.5	-
14	$-0.27^{+0.99}_{-1.49}$	$-0.43^{+0.47}_{-0.52}$	$-0.71^{+0.81}_{-1.3}$	0.25	0.1	$-1.11^{+1.15}_{-1.64}$	$0.11^{+0.55}_{-0.54}$	$-0.99^{+1.15}_{-1.64}$	4.0	2.0
15	$-0.19^{+0.34}_{-0.41}$	0.03 ± 0.19	$-0.16^{+0.35}_{-0.41}$	1.7	0.35	$-0.04^{+0.56}_{-0.63}$	$-0.28^{+0.32}_{-0.35}$	$-0.32^{+0.41}_{-0.52}$	~ 0.7	-
16	-0.39 ± 0.06	-0.09 ± 0.04	-0.48 ± 0.06	1.5	0.5	$-0.6^{+0.3}_{-0.33}$	$-0.63^{+0.11}_{-0.12}$	$-1.23^{+0.27}_{-0.32}$	0.0	0.13
17	-0.32 ± 0.06	-0.04 ± 0.05	-0.37 ± 0.06	1.7	0.45	$-0.42^{+0.11}_{-0.12}$	$0.02^{+0.09}_{-0.08}$	-0.4 ± 0.12	2.0	0.45
18	-0.07 ± 0.1	0.11 ± 0.1	$0.04^{+0.1}_{-0.11}$	2.0	0.30	-0.48 ± 0.11	$-0.05^{+0.08}_{-0.07}$	-0.53 ± 0.11	1.7	0.45
19	-0.36 ± 0.18	0.02 ± 0.12	-0.34 ± 0.18	2.0	0.60	$-1.25^{+0.72}_{-1.29}$	-0.04 ± 0.16	$-1.29^{+0.72}_{-1.29}$	3.5	2.0
20	$-1.13^{+0.42}_{-0.58}$	$-0.42^{+0.08}_{-0.09}$	$-1.54^{+0.41}_{-0.59}$	1.0	1.6	$-1.07^{+0.56}_{-0.91}$	-0.2 ± 0.14	$-1.28^{+0.56}_{-0.91}$	2.2	1.5
21	0.35 ± 0.16	$0.3^{+0.25}_{-0.24}$	$0.65^{+0.24}_{-0.22}$	2.4	0.011	$-0.41^{+0.08}_{-0.09}$	-0.03 ± 0.06	-0.43 ± 0.08	1.7	0.35
22	$0.12^{+0.21}_{-0.2}$	-0.02 ± 0.21	0.1 ± 0.2	1.2	0.011	$-0.51^{+0.42}_{-0.46}$	$-0.04^{+0.24}_{-0.26}$	$-0.55^{+0.4}_{-0.46}$	1.7	0.45
23	$0.51^{+0.5}_{-0.44}$	$0.8^{+1.64}_{-1.07}$	$1.34^{+1.45}_{-0.92}$	4.5	0.23	$0.3^{+1.84}_{-1.6}$	$0.5^{+2.07}_{-1.95}$	$0.8^{+2.03}_{-1.68}$	3.2	0.01
24	-0.04 ± 0.06	0.1 ± 0.06	0.06 ± 0.06	1.8	0.23	$-0.36^{+0.1}_{-0.11}$	0.07 ± 0.08	-0.28 ± 0.11	2.2	0.35
25	$-1.76^{+1.07}_{-1.57}$	$0.05^{+0.2}_{-0.21}$	$-1.72^{+1.11}_{-1.57}$	-	-	$-0.08^{+1.81}_{-1.77}$	$-0.85^{+0.79}_{-1.32}$	$-0.93^{+0.78}_{-1.26}$	-	-
26	$-0.3^{+0.66}_{-0.89}$	$0.35^{+0.54}_{-0.52}$	$0.05^{+0.83}_{-1.02}$	3.5	0.84	$0.11^{+1.01}_{-1.11}$	$-0.34^{+0.74}_{-0.78}$	$-0.23^{+0.83}_{-1.02}$	~ 0.5	-
27	$-0.03^{+0.16}_{-0.17}$	0.42 ± 0.22	0.38 ± 0.22	3.2	0.55	-0.08 ± 0.26	$0.06^{+0.25}_{-0.26}$	$-0.03^{+0.26}_{-0.27}$	1.7	0.01
28	$0.08^{+0.43}_{-0.44}$	$0.11^{+0.48}_{-0.5}$	$0.17^{+0.48}_{-0.47}$	1.7	0.13	$0.24^{+0.46}_{-0.44}$	$0.01^{+0.51}_{-0.52}$	0.26 ± 0.46	~ 1.5	-
29	0.08 ± 0.06	0.12 ± 0.07	0.2 ± 0.07	1.7	0.13	-0.21 ± 0.09	-0.06 ± 0.08	-0.26 ± 0.09	1.5	0.13
30	$0.03^{+0.27}_{-0.28}$	$0.42^{+0.4}_{-0.38}$	$0.46^{+0.39}_{-0.38}$	3.2	0.45	$0.07^{+0.4}_{-0.39}$	$0.32^{+0.55}_{-0.54}$	$0.39^{+0.54}_{-0.52}$	2.7	0.13
31	$0.05^{+0.58}_{-0.59}$	$0.56^{+1.26}_{-0.91}$	$0.62^{+1.33}_{-0.97}$	3.7	0.50	$0.12^{+0.44}_{-0.43}$	-0.01 ± 0.46	0.12 ± 0.43	~ 1.5	-

Column 1: Source ID; columns 2, 3, 4, 7, 8, and 9: X-ray colours, and their corresponding uncertainties for OBSIDs 2939 and 19891, defined as $C_1 = \log_{10}(S/M)$, $C_2 = \log_{10}(M/H)$, $C_3 = \log_{10}(S/H)$ where S, M, and H are the net counts in the soft (0.5-1.2 keV), medium (1.2-2.0 keV), and hard (2.0-7.0 keV) bands respectively (see text for details). Columns 5, 6, 10, and 11: photon index Γ and hydrogen column density N_H based on the X-ray colours for OBSIDs 2939 and 19891.

Table 3.6: NGC 2276 X-ray colours of the discrete sources.

	OBSID 4968					OBSID 15648				
Src ID (1)	C_1 (2)	C_2 (3)	C_3 (4)	Γ (5)	N_H $10^{22}\mathrm{cm}^{-2}$ (6)	C_1 (7)	C_2 (8)	C_3 (9)	Γ (10)	N_H $10^{22}\mathrm{cm}^{-2}$ (11)
1	$0.31^{+0.40}_{-0.39}$	$0.31^{+0.63}_{-0.60}$	$0.62^{+0.58}_{-0.52}$	2.3	0.1	$-0.55^{+0.72}_{-0.86}$	$0.84^{+1.11}_{-0.88}$	$0.27^{+1.45}_{-1.3}$	-	1.0
2	$-0.33^{+0.09}_{-0.1}$	0.11 ± 0.08	-0.22 ± 0.1	2.2	0.5	$-0.31^{+0.22}_{-0.21}$	-0.02 ± 0.17	$-0.32^{+0.21}_{-0.22}$	1.7	0.3
3	$0.2^{+0.34}_{-0.35}$	$-0.24^{+0.31}_{-0.34}$	$-0.04^{+0.28}_{-0.29}$	0.7	-	$0.11^{+1.26}_{-1.41}$	$0.05^{+1.34}_{-1.26}$	$0.15^{+1.42}_{-1.46}$	1.5	-
4	$-0.34^{+1.22}_{-1.68}$	$0.42^{+1.56}_{-1.18}$	$0.07^{+1.87}_{-1.98}$	4.0	0.85	$-0.62^{+0.6}_{-0.77}$	0.15 ± 0.34	$-0.46^{+0.63}_{-0.79}$	3.0	0.9
5	$-0.21^{+0.3}_{-0.31}$	$0.47^{+0.39}_{-0.36}$	0.26 ± 0.42	4.0	0.8	$-0.36^{+0.72}_{-0.91}$	$0.8^{+1.15}_{-0.88}$	$0.42^{+1.53}_{-1.34}$	-	0.9
6	0.0 ± 0.13	$0.03^{+0.14}_{-0.13}$	0.04 ± 0.14	1.5	0.13	$-0.23^{+0.21}_{-0.22}$	0.04 ± 0.19	-0.19 ± 0.22	1.8	0.3
7	$-0.98^{+0.58}_{-0.95}$	-0.25 ± 0.15	$-1.23^{+0.58}_{-0.94}$	2.0	1.2	$-0.97^{+0.31}_{-0.32}$	-0.27 ± 0.12	$-1.23^{+0.3}_{-0.32}$	1.7	1.0
8	-0.27 ± 0.11	0.02 ± 0.09	-0.26 ± 0.11	1.9	0.45	-0.37 ± 0.17	0.03 ± 0.13	-0.34 ± 0.17	2.0	0.45
9	$0.58^{+0.6}_{-0.56}$	$0.31^{+0.99}_{-0.96}$	$0.88^{+0.88}_{-0.76}$	2.2	-	$0.16^{+0.81}_{-0.79}$	$0.54^{+1.56}_{-1.1}$	$0.7^{+1.56}_{-1.07}$	3.5	0.1
10	$0.0^{+0.62}_{-0.6}$	$0.5^{+1.15}_{-0.92}$	$0.5^{+1.15}_{-0.92}$	3.5	0.5	$-0.31^{+0.99}_{-1.15}$	$0.34^{+1.26}_{-1.03}$	$0.04^{+1.49}_{-1.42}$	3.5	0.6
11	$-0.27^{+0.73}_{-0.84}$	$0.68^{+1.30}_{-0.91}$	$-0.42^{+1.57}_{-1.26}$	~4.5	0.85	$-0.96^{+0.84}_{-1.15}$	$0.34^{+0.5}_{-0.47}$	$-0.61^{+0.96}_{-1.22}$	-	2.0
12	-0.16 ± 0.23	0.26 ± 0.25	$0.09^{+0.28}_{-0.27}$	2.6	0.45	0.27 ± 0.19	0.12 ± 0.24	0.39 ± 0.21	1.7	-
13	0.19 ± 0.19	$0.9^{+0.55}_{-0.47}$	$1.1^{+0.54}_{-0.47}$	~5.0	0.5	0.09 ± 0.24	$0.9^{+0.59}_{-0.52}$	$0.99^{+0.58}_{-0.52}$	-	0.6
14	$-0.11^{+0.51}_{-0.54}$	0.09 ± 0.46	-0.03 ± 0.55	2.0	0.3	$-0.36^{+0.95}_{-1.25}$	$0.28^{+1.01}_{-0.89}$	$-0.09^{+1.37}_{-1.53}$	3.0	0.6
15	$-0.09^{+0.48}_{-0.5}$	$0.73^{+1.03}_{-0.84}$	$0.61^{+1.07}_{-0.84}$	~4.5	0.8	$-0.04^{+1.26}_{-1.3}$	$0.65^{+1.91}_{-1.53}$	$0.61^{+1.99}_{-1.61}$	-	0.6
16	$-0.15^{+0.56}_{-0.58}$	$0.57^{+0.92}_{-0.76}$	$0.42^{+0.96}_{-0.84}$	~4.0	0.8	$-0.17^{+0.38}_{-0.38}$	0.2 ± 0.39	$0.03^{+0.42}_{-0.43}$	2.0	0.3
17	$0.57^{+0.96}_{-0.88}$	$-1.22^{+0.69}_{-0.92}$	$-0.67^{+0.4}_{-0.44}$	2.0	-	0.0 ± 2.22	$-0.61^{+1.61}_{-1.99}$	$-0.61^{+1.61}_{-1.99}$	-	-
18	$-0.11^{+0.3}_{-0.31}$	0.27 ± 0.34	$0.15^{+0.36}_{-0.34}$	2.6	0.45	-0.04 ± 0.32	$-0.22^{+0.27}_{-0.28}$	-0.26 ± 0.28	0.8	-
19	$1.03^{+1.57}_{-1.11}$	$-0.8^{+1.11}_{-1.64}$	0.21 ± 0.62	-	-	$0.0^{+0.81}_{-0.81}$	$0.19^{+1.28}_{-1.05}$	$0.19^{+1.28}_{-1.05}$	2.2	0.1

Column 1: Source ID; columns 2, 3, 4, 7, 8, and 9: X-ray colours, and their corresponding uncertainties for OBSIDs 4968 and 15648, defined as $C_1 = \log_{10}(S/M)$, $C_2 = \log_{10}(M/H)$, $C_3 = \log_{10}(S/H)$ where S, M, and H are the net counts in the soft (0.5-1.2 keV), medium (1.2-2.0 keV), and hard (2.0-7.0 keV) bands respectively (see text for details). Columns 5, 6, 10, and 11: photon index Γ and hydrogen column density N_H based on the X-ray colours for OBSIDs 4968 and 15648.

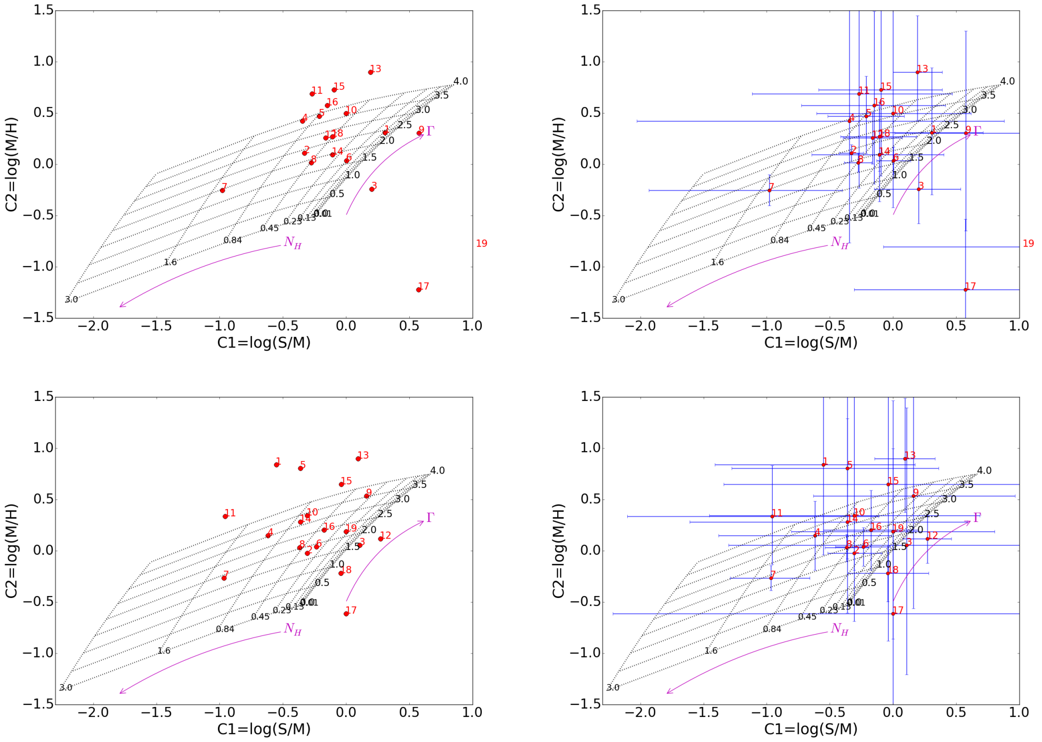

Figure 3.4: Colour-colour diagram for the X-ray sources detected in NGC 2276 showing the colours (left) and corresponding errors (right) for OBSID 4968 (top) and OBSID 15648 (bottom). The source numbers refer to the source ID in Table 3.2. A grid showing the expected colours for absorbed power-law spectra is also overlaid. The value of the photon index and the hydrogen column density (in units of $10^{22}\,\mathrm{cm}^{-2}$) are shown at the edge of the grid.

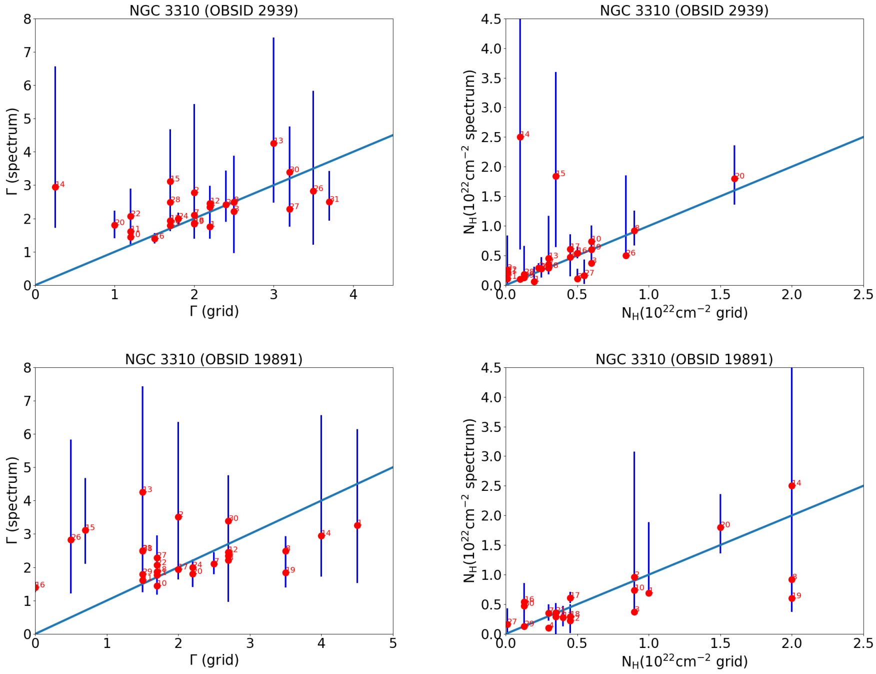

Figure 3.5: Comparison of the photon index (left) and HI column density (N_H; right) determined from the X-ray colours and spectral fits with an absorbed power-law model. Top and bottom rows correspond to the long (OBSID 2939) and short (OBSID 19891) observations of NGC 3310. The blue solid line shows the 1:1 line. The numbers indicate the source IDs.

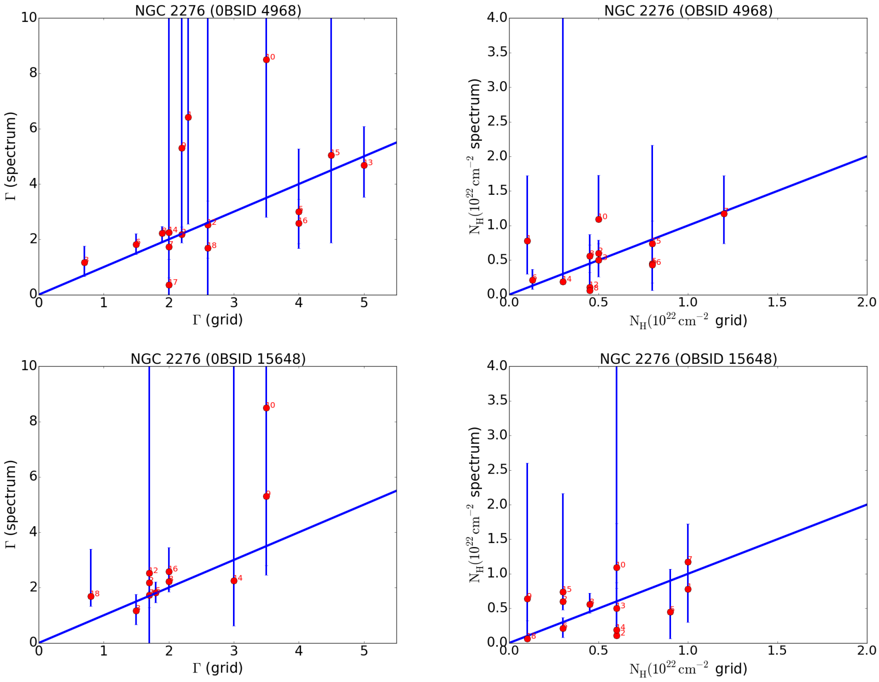

Figure 3.6: Comparison of the photon index (left) and HI column density (N_H; right) determined from the X-ray colours and spectral fits with an absorbed power-law model. Top and bottom rows correspond to the long (OBSID 4968) and short (OBSID 15648) observations of NGC 2276. The blue solid line shows the 1:1 line. The numbers indicate the source IDs.

rate-to-flux conversion factor for each of the three bands based on the best-fit spectral model from the longer observation and the ancillary response file (ARF) from the second, shorter, observation. The errors on the corresponding flux and luminosity were calculated by simply propagating the errors on the number of observed counts in the second observation.

Also for the calculation of the luminosities of NGC 2276 sources 4 and 11 for both OBSIDs, for which we could not perform spectral analysis, we used the best-fit model of source 6 which is a typical model for XRBs. We used the ARFs of each observation to calculate the count-rate-to-flux conversion. The flux and luminosity errors were calculated by propagating the count-rate errors.

The observed and absorption corrected luminosities in the broad ($0.3 - 10.0$ keV), soft ($0.3 - 2.0$ keV), and hard ($2.0 - 10.0$ keV) bands are presented in Tables 3.7 and 3.8 for NGC 3310 and Table 3.9 for NGC 2276. The limiting luminosity is 1.0×10^{38} erg s^{-1} and for both galaxies. Here we only present data for the individual exposures because of the long time span between the observations of each galaxy which results in difference instrumental sensitivity. We note that there are no sources detected at above the 3σ level in the co-added exposure, therefore, Tables 3.7 to 3.9 include all significant sources. We find 14 ULXs for NGC 3310 and 11 ULXs for NGC 2276 reaching luminosities in the broad band ($0.3 - 10$ keV) of 1.5×10^{40} erg s^{-1} and 2.1×10^{40} erg s^{-1} respectively. Adopting the distance of 32.9 Mpc reported in Wolter *et al.* (2015), for NGC 2276, results in a luminosity change of $\sim$ 40% and a total number of 8 ULXs. We estimated the contamination from background sources using the logN-logS distribution of Kim *et al.* (2007). We find that within the outline of each galaxy, at the detection limit of f($0.5 - 8.0$ keV) $= 2.5 \times 10^{-15}$erg cm^{-2} s^{-1}, $\sim$ 1.6 sources are expected to be background sources.

We note here that the number of counts, flux, and luminosity of the nuclear region (Src 9) in NGC 2276 reported in Tables 3.2 and 3.9, correspond to a region consistent with a point-like source. We used this small region in order to extract a conservative estimate of a nuclear X-ray source (e.g. an XRB or an AGN). We have also measured the flux from the full extent of the nuclear region using an elliptical aperture with major and minor radius of 7.5 and 6.3 arcsecs (consistent with the nuclear region in infrared images; Spitzer 8 microns) respectively, which correspond to a physical scale of about 1.5 kpc for the major axis. We calculated the net counts for both OBSIDs as well as for the co-added observation. We found that the extended nuclear region has 113.0 ± 13.8, 67.2 ± 10.2, and 183.2 ± 16.8 broad-band (0.5-7.0 keV) net counts for OBSID 4968, OBSID 15648 and the co-added observation respectively. We then extracted the spectrum of the longer observation. The best-fit model ($\chi^2/dof = 1.92/3$; model in XSPEC: `phabs(po+apec)`) was an absorbed power-law component plus a thermal plasma component with best-fit parameters $\mathrm{N_H} = (0.24 \pm 0.36) \times 10^{22}$ cm^{-2}, $\Gamma = 3.62 \pm 2.50$, and $\mathrm{kT} = 1.10 \pm 0.34$ keV. We followed the same procedure as mentioned in the beginning of this section, to calculate the absorbed fluxes and luminosities of both OBSIDs from their corresponding counts. The 0.3-10.0 keV band absorbed fluxes and luminosities are $(1.09 \pm 1.00) \times 10^{-14}$ erg s^{-1} cm^{-2} and $(2.5 \pm 2.3) \times 10^{39}$ erg s^{-1} for OBSID 4968 and ($1.66 \pm 1.55 \times 10^{-14}$ erg s^{-1} cm^{-2}) and $(3.8 \pm 3.4) \times 10^{39}$ erg s^{-1} for the OBSID 15648.

Table 3.7: NGC 3310 observed and absorption-corrected fluxes and luminosities (OBSID 2939).

Src	$\mathrm{fx}^{\mathrm{obs}}(\mathrm{f}_{\mathrm{x}}^{\mathrm{corr}})$	$\mathrm{fx}^{\mathrm{obs}}(\mathrm{f}_{\mathrm{x}}^{\mathrm{corr}})$	$\mathrm{fx}^{\mathrm{obs}}(\mathrm{f}_{\mathrm{x}}^{\mathrm{corr}})$	$\mathrm{L}_{\mathrm{x}}^{\mathrm{obs}}(\mathrm{L}_{\mathrm{x}}^{\mathrm{corr}})$	$\mathrm{L}_{\mathrm{x}}^{\mathrm{obs}}(\mathrm{L}_{\mathrm{x}}^{\mathrm{corr}})$	$\mathrm{L}_{\mathrm{x}}^{\mathrm{obs}}(\mathrm{L}_{\mathrm{x}}^{\mathrm{corr}})$
ID	(0.3 – 10.0 keV)	(0.3 – 2.0 keV)	(2.0 – 10.0 keV)	(0.3 – 10.0 keV)	(0.3 – 2.0 keV)	(2.0 – 10.0 keV)
	10^{-14} erg s^{-1} cm^{-2}	10^{-14} erg s^{-1} cm^{-2}	10^{-14} erg s^{-1} cm^{-2}	10^{39} erg s^{-1}	10^{39} erg s^{-1}	10^{39} erg s^{-1}
(1)	(2)	(3)	(4)	(5)	(6)	(7)
1	$1.3^{+0.4}_{-0.6}$ (1.5)	$0.5^{+0.1}_{-0.3}$ (0.6)	$0.8^{+0.4}_{-0.5}$ (0.8)	$0.8^{+0.2}_{-0.4}$ (0.9)	$0.3^{+0.1}_{-0.2}$ (0.4)	0.5 ± 0.3 (0.5)
2	$0.7^{+0.3}_{-0.8}$ (2.0)	$0.4^{+0.1}_{-0.4}$ (1.7)	0.3 ± 0.3 (0.4)	$0.5^{+0.2}_{-0.5}$ (1.2)	$0.3^{+0.1}_{-0.3}$ (1.0)	0.2 ± 0.2 (0.2)
3	$0.5^{+3.8}_{-0.4}$ (0.7)	$0.1^{+0.3}_{-0.1}$ (0.4)	$0.3^{+4.4}_{-0.3}$ (0.3)	$0.3^{+2.1}_{-0.2}$ (0.4)	$0.1^{+0.2}_{-0.1}$ (0.2)	$0.2^{+2.4}_{-0.2}$ (0.2)
4∗	$12.0^{+1.2}_{-1.1}$ (17.3)	$6.7^{+0.6}_{-0.5}$ (11.8)	5.4 ± 0.8 (5.4)	$6.7^{+0.7}_{-0.6}$ (9.7)	3.7 ± 0.3 (6.6)	3.0 ± 0.5 (3.1)
5†	$0.1^{+0.2}_{-0.1}$ (0.4)	$0.1^{+0.2}_{-0.1}$ (0.3)	0.0	0.1 ± 0.1 (0.2)	0.1 ± 0.1 (0.2)	0.0
6†	$0.04^{+0.06}_{-0.03}$ (0.09)	$0.03^{+0.06}_{-0.03}$ (0.09)	0.0	$0.02^{+0.04}_{-0.02}$ (0.05)	$0.02^{+0.03}_{-0.01}$ (0.05)	0.0
7∗	5.2 ± 0.9 (9.0)	1.6 ± 0.2 (5.3)	$3.6^{+0.9}_{-0.8}$ (3.8)	2.9 ± 0.5 (5.0)	0.9 ± 0.1 (2.9)	2.0 ± 0.5 (2.1)
8∗	$5.5^{+0.8}_{-1.1}$ (17.4)	$1.4^{+0.1}_{-0.3}$ (12.8)	$4.1^{+0.7}_{-1.0}$ (4.6)	$3.1^{+0.5}_{-0.6}$ (9.7)	0.8 ± 0.1 (7.2)	$2.3^{+0.4}_{-0.5}$ (2.6)
9†	$0.4^{+0.3}_{-0.2}$ (1.5)	$0.2^{+0.2}_{-0.1}$ (1.3)	0.2 ± 0.2 (0.3)	$0.2^{+0.2}_{-0.1}$ (0.9)	0.1 ± 0.1 (0.7)	0.1 ± 0.1 (0.2)
10∗	$15.9^{+1.9}_{-2.5}$ (21.7)	1.7 ± 0.2 (6.7)	$14.2^{+1.8}_{-2.3}$ (15.0)	$8.9^{+1.0}_{-1.4}$ (12.1)	0.9 ± 0.1 (3.7)	$7.9^{+1.0}_{-1.3}$ (8.4)
11∗	4.2 ± 0.1 (5.2)	1.0 ± 0.2 (1.9)	3.2 ± 0.9 (3.3)	2.4 ± 0.5 (2.9)	0.6 ± 0.1 (1.1)	1.8 ± 0.5 (1.8)
12∗	$2.1^{+2.1}_{-1.2}$ (4.3)	$0.9^{+0.7}_{-0.5}$ (3.1)	$1.1^{+1.7}_{-0.7}$ (1.2)	$1.2^{+1.2}_{-0.7}$ (2.4)	$0.5^{+0.4}_{-0.3}$ (1.8)	$0.6^{+0.9}_{-0.4}$ (0.7)
13	$0.8^{+23.1}_{-0.8}$ (1.0)	$0.2^{+0.5}_{-0.2}$ (0.9)	$0.2^{+3.2}_{-0.2}$ (0.2)	$0.5^{+13.0}_{-0.4}$ (0.6)	$0.1^{+0.3}_{-0.1}$ (0.5)	$0.1^{+1.8}_{-0.1}$ (0.1)
14	$0.4^{+85.4}_{-0.4}$ (4.0)	$0.2^{+0.3}_{-0.1}$ (3.5)	$0.2^{+32.8}_{-0.3}$ (0.5)	$0.2^{+47.8}_{-0.2}$ (2.2)	$0.1^{+0.2}_{-0.1}$ (1.9)	$0.1^{+18.3}_{-0.1}$ (0.3)
15∗	$2.2^{+18.0}_{-2.0}$ (16.0)	$0.4^{+2.1}_{-0.4}$ (14.3)	$1.5^{+15.0}_{-1.4}$ (1.6)	$1.2^{+10.1}_{-1.1}$ (8.9)	$0.2^{+1.2}_{-0.2}$ (8.0)	$0.8^{+8.4}_{-0.8}$ (0.9)
16[a]	$42.9^{+3.3}_{-3.7}$ (55.6)	$5.3^{+0.3}_{-0.4}$ (16.4)	$37.6^{+3.5}_{-3.6}$ (39.2)	$24.0^{+1.9}_{-2.1}$ (31.1)	2.9 ± 0.2 (9.2)	$21.1^{+2.0}_{-2.0}$ (21.9)
17∗	$25.9^{+2.0}_{-2.2}$ (45.3)	5.2 ± 0.3 (23.3)	$20.8^{+1.8}_{-2.2}$ (22.0)	$14.5^{+1.1}_{-1.3}$ (25.4)	2.9 ± 0.2 (13.1)	$11.6^{+1.0}_{-1.2}$ (12.3)
18∗	5.9 ± 0.8 (8.6)	1.6 ± 0.2 (4.1)	4.3 ± 0.7 (4.5)	$3.3^{+0.5}_{-0.4}$ (4.8)	0.9 ± 0.1 (2.3)	2.4 ± 0.4 (2.5)
19∗	$5.0^{+0.9}_{-1.3}$ (8.2)	$0.9^{+0.1}_{-0.2}$ (3.9)	$4.1^{+0.9}_{-1.2}$ (4.3)	$2.8^{+0.5}_{-0.8}$ (4.6)	0.5 ± 0.1 (2.2)	$2.3^{+0.5}_{-0.7}$ (2.4)
20∗	$14.3^{+1.6}_{-3.7}$ (28.2)	$1.0^{+0.1}_{-0.3}$ (12.8)	$13.3^{+1.9}_{-3.6}$ (15.5)	$8.0^{+0.9}_{-2.1}$ (15.8)	0.6 ± 0.1 (7.2)	$7.4^{+1.1}_{-2.0}$ (8.7)
21∗	$1.8^{+0.5}_{-0.6}$ (2.6)	$1.1^{+0.2}_{-0.5}$ (1.9)	$0.7^{+0.5}_{-0.4}$ (0.7)	$1.1^{+0.3}_{-0.4}$ (1.6)	$0.7^{+0.1}_{-0.3}$ (1.1)	$0.4^{+0.3}_{-0.2}$ (0.4)
22	$1.4^{+0.4}_{-0.5}$ (2.0)	$0.5^{+0.1}_{-0.2}$ (1.1)	0.9 ± 0.4 (1.0)	$0.8^{+0.2}_{-0.3}$ (1.1)	0.3 ± 0.1 (0.6)	0.5 ± 0.2 (0.5)
23†	$0.3^{+0.4}_{-0.3}$ (0.3)	$0.2^{+0.4}_{-0.2}$ (0.2)	$0.1^{+0.2}_{-0.1}$ (0.1)	0.2 ± 0.2 (0.2)	$0.1^{+0.2}_{-0.1}$ (0.1)	$0.05^{+0.14}_{-0.05}$ (0.05)
24∗	14.0 ± 1.3 (21.9)	4.3 ± 0.3 (11.9)	9.7 ± 1.3 (10.0)	7.9 ± 0.7 (12.3)	2.4 ± 0.2 (6.7)	5.5 ± 0.7 (5.6)
25	$1.7^{+11.7}_{-1.5}$ (63.6)	$0.3^{+1.5}_{-0.3}$ (62.0)	$1.2^{+11.4}_{-1.1}$ (1.7)	$0.9^{+6.5}_{-0.9}$ (35.6)	$0.2^{+0.8}_{-0.1}$ (34.7)	$0.7^{+6.4}_{-0.6}$ (0.9)
26	$0.3^{+3.5}_{-0.3}$ (1.1)	$0.1^{+0.7}_{-0.1}$ (0.9)	$0.2^{+5.0}_{-0.2}$ (0.2)	$0.2^{+2.1}_{-0.2}$ (0.6)	$0.1^{+0.4}_{-0.1}$ (0.5)	$0.1^{+3.0}_{-0.1}$ (0.1)
27	1.2 ± 0.4 (1.9)	$0.6^{+0.1}_{-0.2}$ (1.2)	0.6 ± 0.3 (0.6)	0.7 ± 0.2 (1.0)	0.3 ± 0.1 (0.7)	$0.3^{+0.2}_{-0.1}$ (0.4)
28	$0.3^{+13.1}_{-0.3}$ (1.5)	$0.1^{+0.7}_{-0.1}$ (1.5)	$0.1^{+6.8}_{-0.1}$ (0.1)	$0.2^{+7.3}_{-0.2}$ (0.9)	$0.1^{+0.4}_{-0.1}$ (0.8)	$0.1^{+3.8}_{-0.1}$ (0.0)
29∗	12.2 ± 1.3 (15.1)	$3.9^{+0.4}_{-0.3}$ (6.8)	8.2 ± 1.1 (8.3)	6.8 ± 0.7 (8.5)	2.2 ± 0.2 (3.8)	4.6 ± 0.6 (4.7)
30	$0.4^{+1.5}_{-0.4}$ (2.3)	$0.2^{+0.6}_{-0.2}$ (2.1)	$0.2^{+1.5}_{-0.1}$ (0.1)	$0.2^{+0.9}_{-0.2}$ (1.3)	$0.1^{+0.3}_{-0.1}$ (1.2)	$0.1^{+0.9}_{-0.1}$ (0.1)
31	$0.2^{+8.2}_{-0.2}$ (0.3)	0.1 ± 0.1 (0.3)	$0.1^{+0.2}_{-0.1}$ (0.1)	$0.1^{+4.6}_{-0.1}$ (0.2)	$0.05^{+0.05}_{-0.05}$ (0.1)	$0.05^{+0.1}_{-0.05}$ (0.05)

Column 1: The source ID, ULXs are indicated with ∗and diffuse emission clumps with †; columns 2, 3, and 4: fluxes in the broad, soft, and hard bands respectively; columns 5, 6, and 7: luminosities in the broad, soft, and hard bands respectively. The unabsorbed fluxes and luminosities are given in parenthesis.

---

[a] Nucleus of the galaxy.

Table 3.8: NGC 3310 observed and absorption-corrected fluxes and luminosities (OBSID 19891).

Src ID (1)	$fx^{obs}(f_x^{corr})$ (0.3 – 10.0 keV) 10^{-14} erg s^{-1} cm^{-2} (2)	$fx^{obs}(f_x^{corr})$ (0.3 – 2.0 keV) 10^{-14} erg s^{-1} cm^{-2} (3)	$fx^{obs}(f_x^{corr})$ (2.0 – 10.0 keV) 10^{-14} erg s^{-1} cm^{-2} (4)	$L_x^{obs}(L_x^{corr})$ (0.3 – 10.0 keV) 10^{39} erg s^{-1} (5)	$L_x^{obs}(L_x^{corr})$ (0.3 – 2.0 keV) 10^{39} erg s^{-1} (6)	$L_x^{obs}(L_x^{corr})$ (2.0 – 10.0 keV) 10^{39} erg s^{-1} (7)
1	$0.7^{+9.7}_{-0.6}$ (2.6)	$0.2^{+1.0}_{-0.2}$ (2.4)	$0.3^{+9.7}_{-0.3}$ (0.2)	$0.4^{+5.4}_{-0.3}$ (1.5)	$0.1^{+0.6}_{-0.1}$ (1.3)	$0.1^{+5.4}_{-0.1}$ (0.1)
2	$0.4^{+6.3}_{-0.4}$ (4.2)	$0.2^{+1.2}_{-0.2}$ (3.9)	$0.2^{+5.6}_{-0.2}$ (0.2)	$0.2^{+3.5}_{-0.2}$ (2.3)	$0.1^{+0.7}_{-0.1}$ (2.2)	$0.1^{+3.1}_{-0.1}$ (0.1)
3	0.4 ± 0.3 (0.5)	$0.1^{+0.1}_{-0.1}$ (0.3)	0.2 ± 0.1 (0.2)	0.2 ± 0.2 (0.3)	$0.05^{+0.05}_{-0.05}$ (0.1)	0.1 ± 0.1 (0.1)
4*	$13.4^{+1.7}_{-1.6}$ (19.3)	$7.4^{+1.0}_{-0.7}$ (13.2)	6.0 ± 0.1 (6.1)	7.5 ± 0.9 (10.8)	$4.2^{+0.5}_{-0.4}$ (7.4)	$3.4^{+0.6}_{-0.5}$ (3.4)
5†	0.4 ± 0.3 (0.5)	$0.2^{+0.2}_{-0.1}$ (0.4)	0.2 ± 0.1 (0.2)	$0.2^{+0.2}_{-0.1}$ (0.3)	0.1 ± 0.1 (0.2)	0.1 ± 0.1 (0.1)
6†	-	-	-	-	-	-
7*	$2.5^{+0.7}_{-0.6}$ (4.2)	0.8 ± 0.2 (2.5)	1.7 ± 0.5 (1.8)	$1.4^{+0.4}_{-0.3}$ (2.4)	0.4 ± 0.1 (1.4)	0.9 ± 0.3 (1.0)
8*	$2.6^{+0.6}_{-0.7}$ (8.1)	$0.6^{+0.1}_{-0.2}$ (6.0)	1.9 ± 0.5 (2.1)	$1.4^{+0.3}_{-0.4}$ (4.6)	0.4 ± 0.1 (3.4)	1.1 ± 0.3 (1.2)
9†	$0.3^{+0.4}_{-0.3}$ (1.3)	$0.1^{+0.3}_{-0.1}$ (1.1)	$0.2^{+0.2}_{-0.1}$ (0.3)	$0.2^{+0.2}_{-0.1}$ (0.7)	$0.1^{+0.2}_{-0.1}$ (0.6)	0.1 ± 0.1 (0.1)
10*	$6.7^{+1.4}_{-1.4}$ (9.2)	0.7 ± 0.1 (2.8)	6.0 ± 1.3 (6.4)	3.8 ± 0.8 (5.2)	0.4 ± 0.1 (1.6)	3.4 ± 0.7 (3.6)
11*	$3.2^{+1.3}_{-1.0}$ (3.9)	0.8 ± 0.2 (1.4)	$2.4^{+1.1}_{-0.9}$ (2.5)	$1.8^{+0.7}_{-0.6}$ (2.2)	0.4 ± 0.1 (0.8)	$1.4^{+0.6}_{-0.5}$ (1.4)
12	$1.0^{+0.6}_{-0.5}$ (2.3)	$0.4^{+0.5}_{-0.2}$ (1.7)	0.6 ± 0.3 (0.6)	$0.6^{+0.4}_{-0.3}$ (1.3)	$0.2^{+0.3}_{-0.1}$ (0.9)	0.3 ± 0.2 (0.4)
13	$0.9^{+0.3}_{-0.2}$ (0.7)	$0.2^{+0.2}_{-0.1}$ (0.6)	0.1 ± 0.1 (0.1)	$0.5^{+0.2}_{-0.1}$ (0.4)	0.1 ± 0.1 (0.3)	$0.1^{+0.0}_{-0.0}$ (0.1)
14	$0.3^{+0.4}_{-0.2}$ (2.5)	$0.1^{+0.2}_{-0.1}$ (2.2)	$0.2^{+0.3}_{-0.2}$ (0.3)	$0.2^{+0.2}_{-0.1}$ (1.4)	0.1 ± 0.1 (1.2)	0.1 ± 0.1 (0.2)
15	$1.2^{+1.1}_{-0.8}$ (12.3)	$0.2^{+0.8}_{-0.2}$ (11.0)	$0.9^{+0.6}_{-0.5}$ (1.3)	$0.7^{+0.6}_{-0.4}$ (6.9)	$0.1^{+0.4}_{-0.1}$ (6.2)	0.5 ± 0.3 (0.7)
16[a]	$11.5^{+1.8}_{-1.6}$ (14.9)	1.4 ± 0.2 (4.4)	$10.1^{+1.6}_{-1.5}$ (10.5)	$6.4^{+1.0}_{-0.9}$ (8.3)	0.8 ± 0.1 (2.5)	$5.6^{+0.9}_{-0.8}$ (5.9)
17*	$11.7^{+1.2}_{-1.4}$ (20.5)	2.3 ± 0.2 (10.5)	$9.4^{+1.1}_{-1.2}$ (9.9)	$6.6^{+0.7}_{-0.8}$ (11.5)	1.3 ± 0.1 (5.9)	$5.2^{+0.6}_{-0.7}$ (5.6)
18*	13.9 ± 1.8 (20.1)	$3.7^{+0.5}_{-0.4}$ (9.6)	$10.2^{+1.5}_{-1.6}$ (10.5)	7.8 ± 0.1 (11.2)	$2.1^{+0.3}_{-0.2}$ (5.4)	5.7 ± 0.9 (5.9)
19*	$3.4^{+1.2}_{-1.1}$ (5.7)	0.6 ± 0.2 (2.7)	$2.8^{+1.1}_{-1.0}$ (3.0)	$1.9^{+0.7}_{-0.6}$ (3.2)	0.4 ± 0.1 (1.5)	$1.6^{+0.6}_{-0.5}$ (1.7)
20*	$7.1^{+1.5}_{-2.1}$ (14.0)	0.5 ± 0.1 (6.4)	$6.6^{+1.6}_{-2.0}$ (7.7)	$4.0^{+0.8}_{-1.2}$ (7.9)	0.3 ± 0.1 (3.6)	$3.7^{+0.9}_{-1.1}$ (4.3)
21*	$23.8^{+2.6}_{-2.9}$ (34.3)	5.3 ± 0.6 (15.2)	$18.5^{+2.5}_{-2.8}$ (19.1)	$13.3^{+1.5}_{-1.6}$ (19.2)	3.0 ± 0.3 (8.5)	$10.4^{+1.4}_{-1.6}$ (10.7)
22	1.3 ± 0.5 (1.9)	$0.4^{+0.1}_{-0.2}$ (1.0)	0.9 ± 0.4 (0.9)	0.7 ± 0.3 (1.1)	0.2 ± 0.1 (0.6)	0.5 ± 0.2 (0.5)
23†	-	-	-	-	-	-
24*	$11.0^{+1.4}_{-1.3}$ (17.2)	$3.4^{+0.3}_{-0.4}$ (9.3)	$7.6^{+1.2}_{-1.0}$ (7.9)	$6.2^{+0.8}_{-0.7}$ (9.6)	1.9 ± 0.2 (5.2)	$4.3^{+0.7}_{-0.6}$ (4.4)
25	$0.6^{+0.6}_{-0.4}$ (31.4)	$0.1^{+0.2}_{-0.1}$ (30.6)	$0.5^{+0.4}_{-0.3}$ (0.8)	$0.3^{+0.3}_{-0.2}$ (17.6)	$0.1^{+0.1}_{-0.0}$ (17.1)	0.3 ± 0.2 (0.5)
26	$0.2^{+1.3}_{-0.2}$ (0.4)	0.1 ± 0.1 (0.2)	$0.1^{+1.0}_{-0.1}$ (0.1)	$0.1^{+0.7}_{-0.1}$ (0.2)	$0.05^{+0.1}_{-0.05}$ (0.1)	$0.05^{+0.5}_{-0.05}$ (0.1)
27	1.4 ± 0.5 (2.3)	0.7 ± 0.2 (1.5)	$0.8^{+0.4}_{-0.3}$ (0.8)	0.8 ± 0.3 (1.3)	0.4 ± 0.1 (0.8)	0.4 ± 0.2 (0.4)
28	$0.2^{+0.2}_{-0.1}$ (1.9)	$0.1^{+0.4}_{-0.2}$ (1.8)	0.1 ± 0.1 (0.1)	0.1 ± 0.1 (1.1)	$0.05^{+0.2}_{-0.1}$ (1.0)	$0.05^{+0.05}_{-0.05}$ (0.05)
29*	$15.2^{+1.9}_{-1.7}$ (18.9)	$4.9^{+0.6}_{-0.5}$ (8.5)	$10.3^{+1.6}_{-1.5}$ (10.4)	$8.5^{+1.1}_{-0.9}$ (10.6)	2.8 ± 0.3 (4.7)	$5.8^{+0.9}_{-0.8}$ (5.8)
30	$0.3^{+0.4}_{-0.2}$ (2.2)	$0.2^{+0.3}_{-0.1}$ (2.1)	0.1 ± 0.1 (0.1)	$0.2^{+0.2}_{-0.1}$ (1.3)	$0.1^{+0.2}_{-0.1}$ (1.2)	$0.1^{+0.05}_{-0.05}$ (0.1)
31	$0.2^{+0.2}_{-0.1}$ (1.0)	$0.2^{+0.2}_{-0.1}$ (0.9)	0.1 ± 0.1 (0.1)	0.1 ± 0.1 (0.6)	0.1 ± 0.1 (0.5)	$0.1^{+0.05}_{-0.05}$ (0.1)

Column 1: The source ID, ULXs are indicated with ∗and diffuse emission clumps with †; columns 2, 3, and 4: fluxes in the broad, soft, and hard bands respectively; columns 5, 6, and 7: luminosities in the broad, soft, and hard bands respectively. The unabsorbed fluxes and luminosities are given in parenthesis.

---

[a] Nucleus of the galaxy.

Table 3.9: NGC 2276 observed and absorption-corrected fluxes and luminosities for OBSID 4968 (top) and for OBSID 15648 (bottom).

Src ID (1)	$fx^{obs}(f_x^{corr})$ (0.3 – 10.0 keV) 10^{-14} erg s^{-1} cm^{-2} (2)	$fx^{obs}(f_x^{corr})$ (0.3 – 2.0 keV) 10^{-14} erg s^{-1} cm^{-2} (3)	$fx^{obs}(f_x^{corr})$ (2.0 – 10.0 keV) 10^{-14} erg s^{-1} cm^{-2} (4)	$L_x^{obs}(L_x^{corr})$ (0.3 – 10.0 keV) 10^{39} erg s^{-1} (5)	$L_x^{obs}(L_x^{corr})$ (0.3 – 2.0 keV) 10^{39} erg s^{-1} (6)	$L_x^{obs}(L_x^{corr})$ (2.0 – 10.0 keV) 10^{39} erg s^{-1} (7)
			OBSID 4968			
1*	$0.5^{+135.7}_{-0.5}$ (58.4)	$0.3^{+7.3}_{-0.3}$ (38.4)	$0.2^{+27.9}_{-0.2}$ (20.0)	$1.0^{+270.3}_{-1.0}$ (116.3)	$0.6^{+14.5}_{-0.6}$ (76.5)	$0.4^{+55.6}_{-0.4}$ (39.8)
2*	$8.5^{+1.0}_{-1.2}$ (17.8)	2.1 ± 0.2 (10.7)	6.4 ± 1.2 (6.8)	$16.9^{+2.0}_{-2.4}$ (35.5)	4.2 ± 0.4 (21.3)	12.7 ± 2.4 (13.5)
3*	$1.1^{+1.4}_{-0.6}$ (1.1)	0.2 ± 0.1 (0.2)	$0.9^{+1.4}_{-0.6}$ (0.9)	$2.2^{+2.8}_{-1.2}$ (2.2)	0.4 ± 0.2 (0.4)	$1.8^{+2.8}_{-1.2}$ (1.8)
4	0.06 ± 0.07 (0.08)	0.019 ± 0.02 (0.04)	0.04 ± 0.04 (0.04)	0.15 ± 0.16 (0.19)	0.05 ± 0.05 (0.07)	0.1 ± 0.1 (0.1)
5*	$0.6^{+2.9}_{-0.5}$ (1.9)	$0.2^{+0.8}_{-0.2}$ (1.7)	$0.2^{+2.3}_{-0.2}$ (0.2)	$1.2^{+5.8}_{-1.0}$ (3.8)	$0.6^{+1.6}_{-0.4}$ (3.4)	$0.6^{+4.6}_{-0.4}$ (0.4)
6*	3.6 ± 0.7 (4.8)	1.1 ± 0.2 (2.1)	2.5 ± 0.7 (2.6)	7.2 ± 1.4 (9.6)	2.2 ± 0.4 (4.2)	5.0 ± 1.4 (5.2)
7*	$3.6^{+0.7}_{-1.3}$ (6.2)	$0.4^{+0.6}_{-0.1}$ (2.6)	$3.2^{+0.7}_{-1.1}$ (3.6)	$7.2^{+1.4}_{-2.6}$ (12.3)	$0.8^{+0.5}_{-0.1}$ (5.2)	$6.4^{+1.4}_{-1.8}$ (7.2)
8*	$5.8^{+0.5}_{-0.6}$ (12.9)	1.7 ± 0.1 (8.2)	4.1 ± 0.5 (4.7)	$11.6^{+1.0}_{-1.2}$ (25.7)	3.4 ± 0.2 (16.3)	8.2 ± 1.0 (9.4)
9^a	$0.2^{+1.9}_{-0.2}$ (11.7)	$0.15^{+0.8}_{-0.1}$ (11.6)	$0.05^{+0.7}_{-0.05}$ (0.05)	$0.4^{+3.8}_{-0.4}$ (23.3)	$0.3^{+1.6}_{-0.2}$ (23.1)	$0.1^{+1.4}_{-0.1}$ (0.1)
10	$0.2^{+0.2}_{-0.1}$ (0.2)	$0.2^{+0.2}_{-0.1}$ (0.2)	$0.04^{+0.17}_{-0.03}$ (0.04)	$0.5^{+0.4}_{-0.2}$ (0.4)	$0.4^{+0.4}_{-0.2}$ (0.4)	$0.1^{+0.3}_{-0.1}$ (0.1)
11	0.13 ± 0.06 (0.17)	0.04 ± 0.02 (0.08)	0.09 ± 0.05 (0.01)	0.31 ± 0.16 (0.5)	0.09 ± 0.04 (0.2)	0.22 ± 0.10 (0.22)
12	0.3 ± 0.2 (0.3)	0.1 ± 0.1 (0.2)	0.1 ± 0.1 (0.1)	$0.6^{+0.4}_{-0.3}$ (0.6)	0.3 ± 0.1 (0.4)	0.3 ± 0.2 (0.2)
13*	$0.8^{+4.4}_{-0.7}$ (15.5)	$0.5^{+3.4}_{-0.5}$ (15.4)	$0.1^{+1.3}_{-0.1}$ (0.1)	$1.6^{+8.8}_{-1.4}$ (30.9)	$1.2^{+6.8}_{-1.0}$ (30.7)	$0.4^{+2.6}_{-0.2}$ (0.2)
14	$0.2^{+0.4}_{-0.1}$ (0.5)	$0.1^{+0.2}_{-0.1}$ (0.3)	$0.2^{+4.7}_{-0.2}$ (0.2)	$0.4^{+0.8}_{-0.2}$ (1.0)	$0.1^{+0.4}_{-0.2}$ (0.6)	$0.3^{+9.4}_{-0.4}$ (0.4)
15	$0.2^{+42.1}_{-0.2}$ (6.3)	$0.14^{+2.74}_{-0.14}$ (6.31)	$0.03^{+11.7}_{-0.001}$ (0.03)	$0.4^{+83.9}_{-0.4}$ (12.5)	$0.3^{+5.5}_{-0.3}$ (12.6)	$0.1^{+23.3}_{-0.1}$ (0.1)
16*	$0.8^{+2.1}_{-0.6}$ (2.2)	$0.3^{+0.6}_{-0.3}$ (1.7)	$0.5^{+2.0}_{-0.4}$ (0.5)	$1.6^{+4.2}_{-1.2}$ (4.4)	$0.6^{+1.2}_{-0.6}$ (3.4)	$1.0^{+4.0}_{-0.8}$ (1.0)
17*	$2.3^{+6.7}_{-1.9}$ (2.2)	$0.05^{+0.04}_{-0.03}$ (0.05)	$2.3^{+8.4}_{-1.9}$ (2.3)	$4.6^{+13.3}_{-3.8}$ (4.6)	0.1 ± 0.1 (0.1)	$4.5^{+16.7}_{-3.8}$ (4.6)
18*	0.5 ± 0.2 (0.7)	0.2 ± 0.1 (0.3)	0.4 ± 0.2 (0.4)	1.0 ± 0.4 (1.4)	0.4 ± 0.2 (0.6)	0.6 ± 0.4 (0.8)
19	$0.3^{+5.5}_{-0.3}$ (0.4)	$0.1^{+0.2}_{-0.1}$ (0.2)	$0.3^{+5.1}_{-0.3}$ (0.3)	$0.6^{+11.0}_{-0.6}$ (0.8)	$0.2^{+0.4}_{-0.2}$ (0.4)	$0.4^{+10.2}_{-0.6}$ (0.6)
			OBSID 15648			
1	0.19 ± 0.10 (62.7)	0.18 ± 0.09 (62.69)	0.01 ± 0.01 (0.01)	0.47 ± 0.23 (150.31)	0.44 ± 0.22 (150.28)	0.03 ± 0.01 (0.03)
2*	4.4 ± 1.0 (9.1)	1.1 ± 0.2 (5.3)	3.2 ± 0.8 (3.5)	8.2 ± 2.0 (18.1)	2.2 ± 0.4 (10.6)	7.0 ± 1.6 (7.0)
3	0.4 ± 0.3 (0.4)	0.1 ± 0.1 (0.1)	0.3 ± 0.2 (0.3)	0.8 ± 0.6 (0.8)	0.2 ± 0.2 (0.2)	0.6 ± 0.4 (0.6)
4	1.0 ± 0.3 (1.4)	0.3 ± 0.1 (0.6)	0.7 ± 0.2 (0.8)	2.2 ± 0.6 (2.8)	0.6 ± 0.2 (1.2)	1.6 ± 0.4 (1.6)
5	0.3 ± 0.1 (1.2)	0.2 ± 0.1 (1.1)	0.1 ± 0.1 (0.2)	0.8 ± 0.2 (2.4)	0.4 ± 0.4 (2.2)	0.4 ± 0.2 (0.4)
6*	4.0 ± 0.5 (10.6)	1.2 ± 0.2 (2.3)	2.8 ± 0.9 (2.8)	8.0 ± 1.0 (10.2)	2.4 ± 0.6 (4.6)	5.6 ± 1.8 (5.6)
7*	11.1 ± 0.4 (13.8)	1.2 ± 0.3 (8.7)	10.7 ± 0.3 (11.8)	23.9 ± 0.8 (57.5)	2.4 ± 0.4 (32.3)	21.5 ± 0.6 (23.5)
8*	6.3 ± 0.6 (14.9)	1.9 ± 0.2 (8.7)	4.4 ± 0.4 (5.0)	12.5 ± 1.2 (29.7)	3.8 ± 0.2 (17.3)	8.8 ± 0.8 (10.0)
9	0.26 ± 0.13 (6.68)	0.2 ± 0.1 (6.61)	0.06 ± 0.03 (0.07)	0.63 ± 0.3 (16.01)	0.48 ± 0.23 (15.84)	0.15 ± 0.07 (0.17)
10	0.084 ± 0.073 (562.8)	0.082 ± 0.071 (562.8)	0.002 ± 0.001 (0.002)	0.201 ± 0.174 (1349.1)	0.197 ± 0.171 (1349.1)	0.004 ± 0.004 (0.006)
11	0.6 ± 0.2 (0.8)	0.2 ± 0.1 (0.3)	0.4 ± 0.2 (0.4)	1.2 ± 0.4 (1.6)	0.4 ± 0.2 (0.6)	0.8 ± 0.4 (1.0)
12*	$2.6^{+4.2}_{-1.9}$ (3.8)	$1.2^{+1.0}_{-0.6}$ (2.4)	$1.4^{+2.4}_{-0.9}$ (1.5)	$5.2^{+8.4}_{-3.8}$ (7.6)	$2.4^{+1.6}_{-1.2}$ (4.8)	$2.8^{+4.8}_{-1.8}$ (3.0)
13*	$0.9^{+1.0}_{-0.5}$ (24.1)	$0.7^{+0.8}_{-0.4}$ (23.9)	0.1 ± 0.1 (0.1)	$1.6^{+2.0}_{-1.0}$ (48.0)	$1.4^{+1.6}_{-0.8}$ (47.6)	0.2 ± 0.2 (0.2)
14	0.2 ± 0.2 (0.4)	0.1 ± 0.1 (0.3)	0.1 ± 0.1 (0.1)	0.4 ± 0.4 (0.8)	0.2 ± 0.2 (0.6)	0.2 ± 0.2 (0.2)
15	0.04 ± 0.06 (2.64)	0.03 ± 0.05 (2.63)	0.01 ± 0.01 (0.01)	0.1 ± 0.15 (6.32)	0.08 ± 0.12 (6.3)	0.02 ± 0.03 (0.02)
16*	$0.8^{+0.6}_{-0.5}$ (2.2)	$0.3^{+0.5}_{-0.2}$ (1.7)	0.5 ± 0.2 (0.5)	$1.6^{+1.2}_{-1.0}$ (4.4)	$0.6^{+1.0}_{-0.4}$ (3.4)	$1.0^{+0.5}_{-0.4}$ (1.0)
17	0.04 ± 0.11 (0.05)	0.01 ± 0.03 (0.02)	0.03 ± 0.08 (0.03)	0.1 ± 0.28 (0.12)	0.03 ± 0.08 (0.05)	0.07 ± 0.19 (0.07)
18*	$2.3^{+2.5}_{-1.2}$ (2.9)	$0.7^{+0.4}_{-0.3}$ (1.2)	$1.6^{+2.3}_{-0.9}$ (1.7)	$4.6^{+5.0}_{-2.4}$ (5.8)	1.4 ± 0.8 (2.4)	$3.2^{+4.6}_{-1.8}$ (3.4)
19	0.4 ± 0.3 (0.5)	0.1 ± 0.1 (0.2)	0.3 ± 0.2 (0.3)	0.8 ± 0.6 (1.0)	0.2 ± 0.2 (0.4)	0.6 ± 0.6 (0.6)

Column 1: The source ID, ULXs are indicated with ∗and diffuse emission clumps with †; columns 2, 3, and 4: fluxes in the broad, soft, and hard bands respectively; columns 5, 6, and 7: luminosities in the broad, soft, and hard bands respectively. The unabsorbed fluxes and luminosities are given in parenthesis.

3.2.5 Variability

We searched for inter-observation variability of the sources detected in NGC 3310 and NGC 2276 using the CIAO *glvary* tool. This tool is based on the Gregory-Loredo variability detection method (Gregory & Loredo, 1992) which compares the photon-arrival times with a uniform distribution. Since the dither pattern of *Chandra* may result in a false variability signal because of pixel-to-pixel effective area variations we first ran the *dither_region* tool which generates the time-dependent source area accounting for bad pixels, chip gaps, node boundaries etc. The variability of a source is encoded in the variability index (varindex) which takes into account the variability probability and the odds ratio for the photon arrival times to be non-uniformly distributed. Sources with a variability index (varindex) larger than 6 are considered variable, with larger values of the varindex indicate higher degree of variability.

For NGC 3310 and OBSID 2939, the nucleus (Src 16) showed evidence of variability with *varindex=9* indicating that it is definitely a variable source. Inspecting its lightcurve (Fig. 3.7) one can see a gradual increase in the observed counts for about 2/3 of the exposure time and a decrease at the last 1/3. This translates to a luminosity change of a factor of 1.7 starting with $(1.65 \pm 0.08) \times 10^{40}$ erg s^{-1} at the lowest to $(2.84 \pm 0.08) \times 10^{40}$ erg s^{-1} at the highest count rate, assuming the best-fit spectrum from the total exposure. However analysing data from the shorter observation (OBSID 19891), we found that Src 16 is not variable at this observation with varindex=0 but corresponds to a luminosity of $6.4 \pm 0.1 \times 10^{39}$ erg s^{-1}, which is about 2.5 times lower than the average luminosity of OBSID 2939.

Comparing also the luminosities of the two OBSIDs (Tables 3.7 and 3.8) we find that 8 out of 31 sources show long-term variability based on the broad-band luminosities of the two observations. Two sources are brighter (Sources 18 and 21) in the shorter exposure and 6 sources are brighter in the longer observation (Sources 7, 8, 10, 16, 17, and 20). All of these variable sources have luminosities above the ULX limit in both observations. Sources 16 (nucleus) and 21 show the most extreme variability of all by changing the broad-band luminosity 4 and 13 times respectively.

For NGC 2276, none of the sources observed during the OBSID 4968 showed any evidence of short-term variability. In OBSID 15648 sources 1 and 2 have non-zero variability indices and are probably not variable (*varindex=2*) and considered not variable (*varindex=1*) respectively. However Src 3 is likely to be variable (*varindex=4*) and its lightcurve (Fig. 3.8) shows characteristics of a fast rise and exponential decay (FRED) flare with an amplitude of 0.0013 counts/s. This corresponds to a luminosity change of

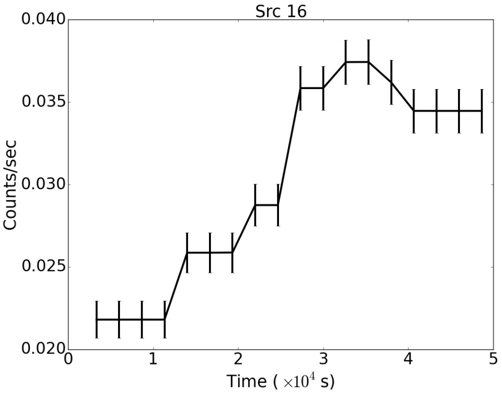

Figure 3.7: Lightcurve of Src 16 NGC 3310 -Lightcurve of the nucleus of NGC 3310 (Src 16), extracted from OBSID 2939 divided in bins of ∼ 2.67 ks. We see a clear rise of the source intensity during the observation.

($4.5 \pm 1.0 \times 10^{39}$ erg s^{-1}).

We also searched for long-term variability in NGC 2276 by comparing the luminosities between the two OBSIDs (Table 3.9). We find that 7 out of 19 sources show long-term variability based on the broad-band luminosities of the two observations. Five sources are brighter (Sources 4, 7, 11, 12, and 18) in the shorter exposure and 2 sources are brighter in the longer observation (Sources 2 and 17). Out of the 7 variable sources, four (Sources 2, 7, 17, and 18) have luminosities above the ULX limit in the longer exposure whereas one (Src 12) has a luminosity in excess of 10^{39}ergs^{-1} in the shorter exposure.

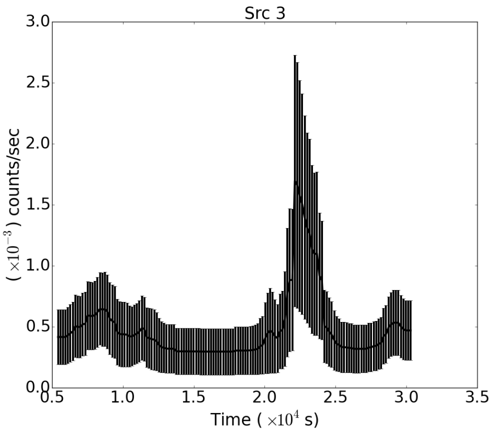

Figure 3.8: Lightcurve of Src 3 in NGC 2276 -Lightcurve of source 3 in NGC 2276, extracted from OBSID 15648 in bins of ~ 174 s. We clearly see a flare with a duration of ~ 500 sec.

3.2.6 Integrated and extended X-ray emission of NGC 3310

In the following section we present the analysis on the integrated and extended emission of NGC 3310. We do not perform the same analysis for NGC 2276 since its was analysed previously in detail (Rasmussen *et al.*, 2006; Wolter *et al.*, 2011, 2015). Therefore we extracted the integrated spectrum of NGC 3310 included in the outline of the galaxy from each observation. We determined the background spectrum from a source-free area outside the galaxy using the *specextract* tool. We fitted simultaneously the spectra from the two separate observations (OBSID 2939 and OBSID 19891) with all the model parameters apart from the normalizations tied together. We obtained the best-fit ($\chi^2_\nu/\mathrm{dof} = 626.04608$) with a model consisting of two thermal plasma components and a power-law component (`phabs(powerlaw+apec+apec)`) seen through a common absorber. The best-fit parameters are $\Gamma = 1.57 \pm 0.06$, $\mathrm{N_H} = (0.17 \pm 0.03) \times 10^{22}$ cm^{-2}, $\mathrm{kT_1} = 0.22 \pm 0.02$ keV and $\mathrm{kT_2} = 0.77^{+0.05}_{-0.04}$ keV (Table 3.10). The total absorbed and unabsorbed luminosities based on this joint fit in the broad ($0.3 - 10.0$ keV), soft ($0.3 - 2.0$ keV), and hard ($2.0 - 10.0$ keV) bands are shown in Table 3.11.

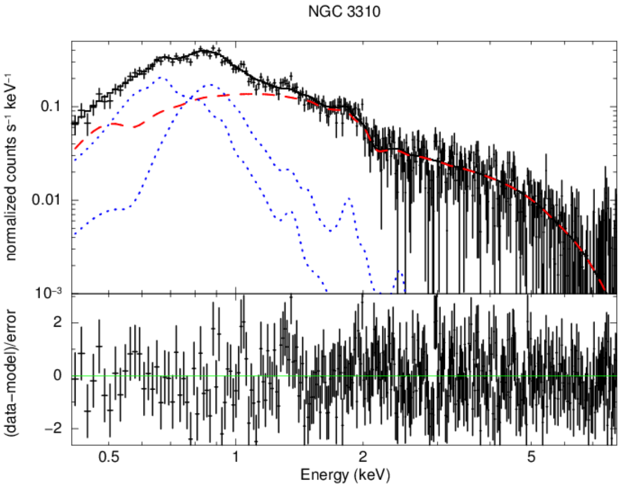

Figure 3.9: The integrated spectrum of NGC 3310. -(Top panel) The integrated X-ray spectrum of NGC 3310 (OBSID 2939), along with the best-fit folded model (Table 3.10) consisting of: an absorbed power-law (dashed red line), and two APEC components (dotted blue lines). (Bottom panel) The fit residuals in terms of sigma with error bars of size 1σ.

3.2.6.1 Luminosity of X-ray binaries and ULXs

In order to determine the luminosity of the XRB populations, we measured the integrated emission of both resolved and unresolved XRBs in NGC 3310 by extracting the integrated spectrum of the galaxy and measuring the flux of only the power-law component (best-fit results in Table 3.10). Since NGC 3310 may host an AGN, we also measured the luminosity of the extra-nuclear XRB population by extracting the spectrum of the galaxy, but this time excising the nucleus. We fitted these spectra from each observation using the same model as for the total galaxy spectrum (`phabs(powerlaw+apec+apec)`) resulting in a good fit ($\chi^2/\mathrm{dof} = 620.01/582$). The best-fit parameters are listed in Table 3.10, and the total and XRB (power-law component) luminosity in Table 3.11.

We calculated the total flux of the ULXs by extracting a spectrum from a region consisting of all their apertures and using a background spectrum from a source-free area outside the outline of the galaxy. However due to variability (namely 14 ULXs for OBSID 2939 and 12 ULXs for OBSID 19891), we used different apertures for each observation and fitted the spectra for each observation separately A model consisting of an absorbed power-law and a thermal-plasma model gave good fit for both observations ($\chi^2 = 214.67/185$ and $\chi^2 = 124.67/132$). The best-fit parameters for this fit are presented in Table 3.10 and the corresponding absorbed and unabsorbed luminosities for the overall spectrum in Table 3.11.

We also tried a model consisting of an absorbed thermal-plasma and a disk blackbody model which has been successfully used to model the spectra of ULXs (Gladstone *et al.*, 2009; Rana *et al.*, 2015). This resulted in unrealistic values for the component parameters of the shorter observation (OBSID 19891) but gave a good fit for the longer observation (OBSID 2939; $\chi^2 = 216.54/185$) with best-fit parameters $\mathrm{N_H} = (0.08 \pm 0.03) \times 10^{22}$ cm^{-2}, $\mathrm{kT} = 0.42^{+1.58}_{-0.19}$ keV and $\mathrm{T_{in}} = 1.58^{+0.07}_{-0.08}$ keV which resulted in a total observed luminosity of $\mathrm{L}(0.3 - 10\ \mathrm{keV}) = 6.2 \pm 0.5 \times 10^{40}$erg s^{-1}.

3.2.6.2 Luminosity of the diffuse emission

We measure the total diffuse emission of NGC 3310 and the diffuse emission of three morphologically distinct areas (ring, north and south spiral arm; Fig.3.10), defined using the 8μm IRAC *Spitzer* infrared image, in the broad ($0.3 - 10.0$ keV) , soft ($0.3 - 2.0$ keV), and hard ($2.0 - 10.0$ keV) bands. In order to measure the luminosity of the diffuse X-ray emission of NGC 3310, we created “swiss cheese” images for each observation and in each of the three bands by removing the regions corresponding to the 27 detected X-ray sources. To obtain a picture of its spectral parameters we extracted a spectrum from the entire region of the galaxy (also excluding the discrete X-ray sources) and a background spectrum from a source-free area outside the outline of the galaxy using the *specextract* tool. We did the same for the north spiral arm, the ring, and the south spiral arm areas (Fig. 3.10). The spectra from the two observations were fitted simultaneously with an absorbed power-law model (to account for unresolved X-ray binaries) plus two thermal plasma model components for the total and the ring diffuse emission. For the spiral arms the spectra were fitted with an absorbed power-law model plus a thermal plasma model component. The spectral parameters for the two observations were tied together (including the model normalisation) and a constant that was free to float was introduced in order to account for variations of the overall intensity between the two observations (e.g due to calibration deferences). Since the normalisation of the power-law component of the spectral fits to the integrated ULX spectra, do not show any significant variation (Table 3.10) we opted to tie together the two normalisations for the fits of the two observations. The best-fit parameters for these models and their corresponding errors are shown in Table 3.10.

Since the spectrum of the diffuse emission of the galaxy does not account for the diffuse emission that lies within the excised source regions we cannot directly compute

Table 3.10: Spectral fitting parameters of integrated spectrum of galaxy, binaries, ULXs, and diffuse emission of NGC 3310

	Power-law				Thermal plasma			
Region	N_H 10^{22} cm^{-2}	Γ	Norm (OBSID 2939)	Norm (OBSID 19891)	kT keV	Norm (OBSID 2939)	Norm (OBSID 19891)	χ^2/dof
(1)	(2)	(3)	(4)	(5)	(6)	(7)	(8)	(9)
Total galaxy	0.17 ± 0.03	1.57 ± 0.06	$38.11^{+2.88}_{-2.36}$	$34.10^{+2.86}_{-2.37}$	0.22 ± 0.02	$40.5^{+30.7}_{-11.0}$	$40.3^{+32.8}_{-12.4}$	626.04/608
					$0.77^{+0.05}_{-0.04}$	12.0 ± 2.5	10.5 ± 2.5	
Total galaxy- (no nucleus)	0.17 ± 0.04	1.65 ± 0.07	$33.89^{+2.45}_{-2.26}$	$34.42^{+2.79}_{-2.56}$	0.22 ± 0.02	$40.8^{+29.7}_{-11.0}$	$39.5^{+31.6}_{-12.3}$	620.01/582
					0.78 ± 0.05	12.2 ± 3.0	10.0 ± 3.0	
ULXs (OBSID 2939)	$0.27^{+0.05}_{-0.04}$	1.72 ± 0.07	$25.5^{+2.38}_{-2.04}$	-	0.18 ± 0.03	$9.90^{+10.4}_{-5.85}$	-	214.67/185
ULXs (OBSID 19891)	$0.49^{+0.22}_{-0.15}$	2.08 ± 0.15	$34.7^{+9.12}_{-6.20}$	-	0.28 ± 0.04	$14.72^{+93.76}_{-14.18}$	-	124.73/132
Diffuse (total)	0.15 ± 0.04	$1.82^{+0.24}_{-0.22}$	$10.1^{+1.8}_{-1.5}$	$10.1^{+1.8}_{-1.5}$	0.78 ± 0.04	$11.0^{+3.4}_{-2.1}$	$11.0^{+3.4}_{-2.1}$	495.13/460
					0.22 ± 0.02	$31.8^{+21.1}_{-10.4}$	$31.8^{+21.1}_{-10.4}$	
Diffuse (north)	$0.71^{+0.07}_{-0.08}$	$1.92^{+0.31}_{-0.30}$	$1.5^{+0.4}_{-0.3}$	$1.5^{+0.4}_{-0.3}$	$0.19^{+0.02}_{-0.01}$	$116.7^{+97.5}_{-60.2}$	$116.7^{+97.5}_{-60.2}$	64.76/44
Diffuse (south)	$0.50^{+0.09}_{-0.21}$	$2.66^{+0.67}_{-0.58}$	$1.2^{+0.7}_{-0.5}$	$1.2^{+0.7}_{-0.5}$	0.19 ± 0.03	$46.33^{+50.86}_{-39.20}$	$46.33^{+50.86}_{-39.20}$	33.51/34
Diffuse (ring)	0.16 ± 0.04	$2.09^{+0.16}_{-0.15}$	$5.3^{+0.9}_{-0.7}$	$5.3^{+0.9}_{-0.7}$	0.23 ± 0.02	$13.1^{+7.05}_{-4.30}$	$13.1^{+7.05}_{-4.30}$	201.94/154
					$0.77^{+0.05}_{-0.04}$	$6.30^{+1.55}_{-1.13}$	$6.30^{+1.55}_{-1.13}$	

Column 1: the regions used to extract the spectra. For the ULX population, we present spectral fit results for each OBSID separately as described in Section 3.2.6.1. The regions of diffuse emission total, north, south, and ring correspond to the diffuse emission of the entire galaxy, the north, south spiral arm and ring respectively (after removing all resolved sources); column 2: HI column density along the line of sight; columns 3, 4, and 5: the power-law photon index and the normalisation for each observation (in units of 10^{-5} photons keV^{-1} cm^{-2} s^{-1} at 1 keV); columns 6, 7, and 8 : the temperature of the thermal plasma component (APEC) and the normalisation of each observation (expressed as $\frac{10^{-19}}{4\pi D^2} \int n_e n_H dV$ where n_e and n_H are the electron and hydrogen densities integrated over the volume V of the emitted region and D is the distance to the source in cm); column 9: the χ^2 and the degrees of freedom for each spectral fit.

Table 3.11: NGC 3310 luminosities of the integrated spectrum of the galaxy, X-ray binaries, ULXs, and the diffuse emission

Region	OBSID	$\mathrm{L_x^{obs}(L_x^{corr})}$ $(0.3 - 10.0$ keV) 10^{40} erg $\mathrm{s^{-1}}$	$\mathrm{L_x^{obs}(L_x^{corr})}$ $(0.3 - 2.0$ keV) 10^{40} erg $\mathrm{s^{-1}}$	$\mathrm{L_x^{obs}(L_x^{corr})}$ $(2.0 - 10.0$ keV) 10^{40} erg $\mathrm{s^{-1}}$
(1)	(2)	(3)	(4)	(5)
	19891	15.6 ± 0.7 (22.7)	5.6 ± 0.3 (12.5)	10.0 ± 0.6 (10.2)
	19891	11.8 ± 0.7 (14.6)	3.1 ± 0.3 (5.8)	8.7 ± 0.6 (8.9)
	19891	6.2 ± 0.5 (13.0)	1.8 ± 0.2 (8.3)	4.4 ± 0.3 (4.7)
	19891	5.1 ± 0.6 (6.3)	2.9 ± 0.2 (4.2)	0.8 ± 0.6 (0.8)

Column 1: The region IDs (see Table 3.10); column 2: the OBSID; columns 3, 4, and 5: the broad, soft and hard-band luminosity respectively. The unabsorbed luminosities are given in the parenthesis. The component indicated as “total galaxy" includes emission from the entire galaxy whereas the “Binaries" component include the emission from the power-law component of the galaxy without its nuclear region (see row 2; Table 3.10). “ULXs" corresponds to the power-law component of the integrated spectrum of the ULXs described in Section 3.2.6.1. The diffuse emission (total) corresponds to the diffuse emission of the entire galaxy (after excising all resolved sources, and correcting for the corresponding area).

the flux and consequently the luminosity of the diffuse emission of NGC 3310. For this reason, following the same approach as in Anastasopoulou *et al.* (2016), we created an image of the diffuse emission by interpolating the pixel values in the source regions based on the intensity in annular regions surrounding them, using the *dmfilth* tool. These annular regions were the same as those used to measure the background in the spectral analysis. Using the best-fit spectral model of the diffuse emission of the galaxy from each of the two observations, and making the implicit assumption that the spectrum in the source regions is on average the same as in the rest of the galaxy, we calculated the flux and the corresponding luminosity of the diffuse emission in the soft and hard bands by rescaling the model-predicted fluxes by the ratio of the counts in the interpolated image and the swiss-cheese image in each band. The absorbed, as well as the corrected luminosities for OBSIDs 2939 and 19891 are reported in Table 3.11.

For NGC 2276 we do not perform any further analysis on the diffuse emission of the galaxy since it was studied in great detail by Rasmussen *et al.* (2006). In summary, they find that the interstellar medium is compressed at the western edge as the galaxy moves supersonically through the IGM ($\sim 850\,\mathrm{km\,s^{-1}}$). The detailed temperatures and luminosities of the diffuse emission can be seen in Table 2 of Rasmussen *et al.* (2006).

3.2.7 Sub-galactic scaling relations

In this section we study the link between the X-ray emission of the X-ray binary populations of NGC 3310 and NGC 2276 with their star formation rates (SFR) and stellar masses at sub-galactic scales. Furthermore we examine the applicability of the galaxy-wide scaling relations in these smaller scales.

3.2.7.1 NGC 3310

In order to examine whether sub-galactic regions of the galaxy follow the galaxy-wide scaling relations or not, we used as reference the linear relation $\mathrm{L}^{\mathrm{XRBS}}_{0.5-8.0\mathrm{keV}}(\mathrm{erg s^{-1}}) = 2.61 \times 10^{39} SFR(M_{\odot} yr^{-1})$ of Mineo *et al.* (2012a) between the integrated luminosity of HMXBs and SFR. We defined morphologically three sub-galactic regions (ring, north and south spiral arms; Section 3.2.6.2; Fig. 3.10). For these three regions as well as for the entire galaxy we calculated the XRB X-ray luminosity by simultaneously fitting the X-ray spectra of both observations, accounting only for the power-law component of each spectrum which is representative of the X-ray binaries. The total luminosity of the X-ray binaries is reported in Table 3.11 for each observation. We then calculated the SFR for each of these regions from the *Spitzer* MIPS 24μm image using the calibration from Rieke *et al.* (2009). In Fig. 3.11 we report the average luminosities of these two observations, calculated in the $0.5-8.0$ keV band reported in Mineo *et al.* (2012a) for the X-ray luminosity versus SFR correlation. This correlation is shown in Fig. 3.11 as the reference solid line. We interestingly notice (Fig. 3.11; top panel) that the total galaxy and its south spiral arm follow the scaling relation but the regions containing the ULXs (north spiral arm and ring) show an excess of the HMXB X-ray luminosity (Fig.3.11).

In order to examine the scaling relations in sub-galactic scales regardless of particular morphological features, we calculated the SFR of 11 semi-annuli on the north and 11 on the south around the nucleus of the galaxy with a thickness of about 10 arcsec. The annuli are shown also in Fig.3.10. Moreover, since the regions we study may contain a non-negligible contribution of LMXBs, we then compared with the scaling relation of Lehmer *et al.* (2010) which correlates the hard X-ray luminosity (2.0-10 keV) of XRBs per SFR to the sSFR. In this comparison we used the 2.0-10.0 keV luminosity of the power-law component from the spectral fits in each of the four regions (total galaxy, ring, north and south spiral arms). Due to the small number of counts in each annular region, it was not possible to fit the individual spectra. Instead, we calculated the X-ray luminosity in each annulus based on the counts of the co-added image in the 2-10 keV band (the effective area and the background between the two observations do not change significantly), using as background region an annulus around the galaxy. To convert the count rate to flux we used the exposure weighted sum of the conversion factors from the two observations, resulting from the power-law component in the nucleus-free integrated spectrum of the galaxy. Alternatively weighting by the number of counts gives essentially identical results (less than 1%). The SFR of the annular regions was computed again from the *Spitzer* MIPS 24μm image using the calibration from Rieke *et al.* (2009). The stellar mass of the sub-galactic regions was computed using IRAC images at 3.6μm and the calibration relation from Zhu *et al.* (2010). In Fig. 3.12 we plot the X-ray luminosity per SFR of each of those regions against the sSFR. The annuli are enumerated from 1-11 starting from the inner annulus to the outer annulus and we show them (Fig. 3.10) with black stars for the north part and red circles for the south part. Some annuli are not shown because they have too few counts to be considered significant (north annuli: 8, 9, 10, and 11).

We find (Fig. 3.12; top panel) that there is an excess in the Lx/SFR-sSFR scaling relation for the north spiral arm and the ring of the galaxy which host the ULXs, whereas the entire galaxy and the south spiral arm follow the Lehmer *et al.* (2010) relation. Furthermore, we observe that there is indeed an excess of hard luminosity per SFR for the inner annuli which contain the ULXs. The outer annuli of the galaxy unless containing a ULX fall bellow the scaling relation line but within the errors are consistent with the correlation. Overall in spite of the fact that the entire galaxy follows the scaling relations, we observe an excess in the hard X-ray luminosity of the XRBs for the regions containing ULXs.

3.2.7.2 NGC 2276

For NGC 2276 we followed the same analysis procedure for measuring the X-ray luminosity, SFR, and stellar mass as for NGC 3310 (see Section 3.2.7.1). We divided the galaxy in two regions (west and east), in order to investigate whether the ram pressure on the west side of the galaxy enhanced its SFR in comparison to the east side. We also divide the galaxy in 8 semi-annuli with thickness of about 20 arcsec in order to include enough counts to allow measurement of the X-ray luminosity. The different regions of the galaxy and the 8 semi-annuli are shown in Fig.3.10. We calculated the SFR and we found that there is marginal difference between the two sides of the galaxy (Table 3.12).

Plotting the integrated luminosity of the galaxy and the luminosity of the two sides on the galaxy-wide scaling relation of Mineo *et al.* (2012a) we see that there is an excess of the HMXBs X-ray luminosity at the west side of the galaxy which contains the brightest ULXs, (bottom plot; Fig. 3.11) as well as for the entire galaxy. In Fig. 3.12 we plot the X-ray luminosity per SFR of the entire galaxy, the two sides as well as the annular regions against the sSFR. The annuli are enumerated from 1 to 4 starting from the inner annulus to the outer annulus. The black stars correspond to the west part and red circles to the east part of the galaxy. Some annuli are not shown because the number of their counts is too low to be considered significant (west: 1; east: 4). We observe again, as in NGC 3310, an excess in the hard X-ray luminosity of the XRBs for the regions containing ULXs (especially the bright ones) but this time also an excess in the hard X-ray luminosity of the entire galaxy although of smaller scale. However the east side of the galaxy follows the standard scaling relation of Mineo *et al.* (2012a).

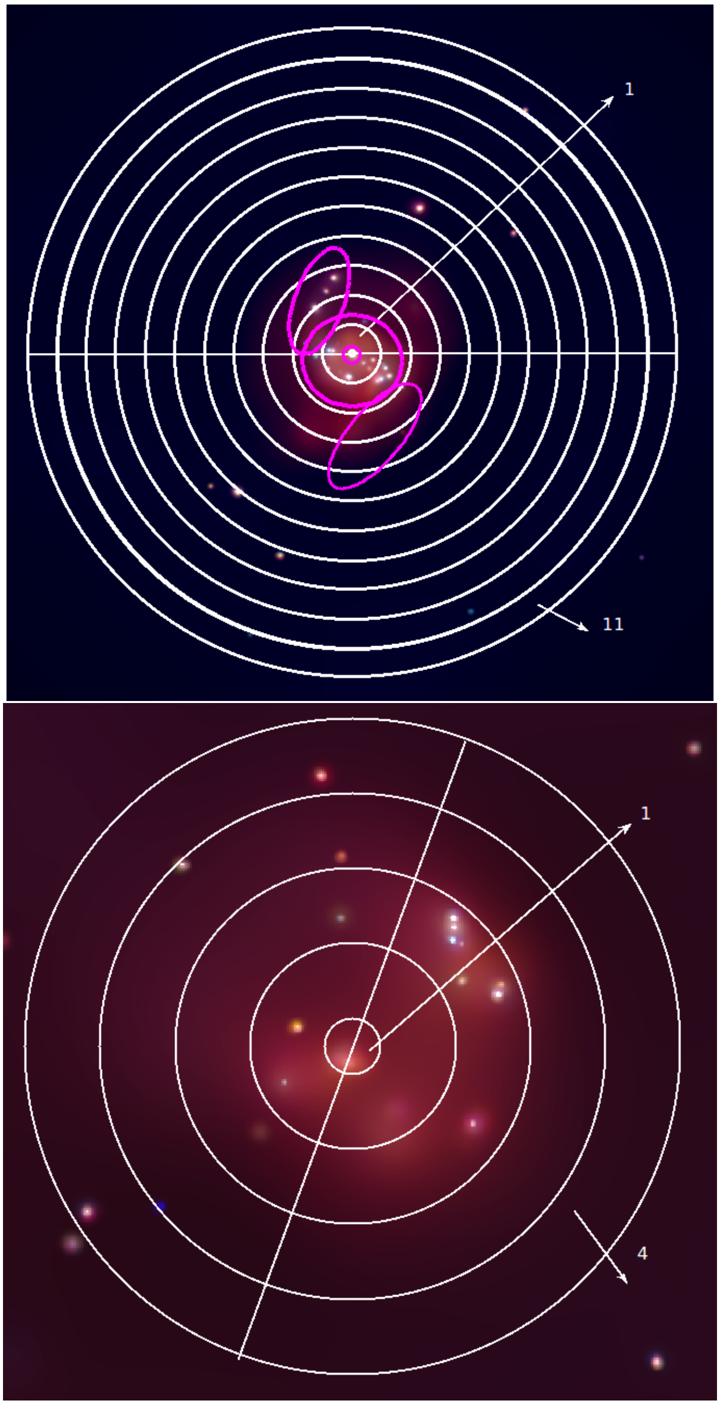

Figure 3.10: Top: X-ray colour image of NGC 3310. Overlaid are the three regions used to measure the X-ray luminosity of the X-ray binary populations in the ring, north, and south spiral arm (magenta colours). We also show the 11 semi-annuli used to measure the X-ray binary X-ray emission in different regions of NGC 3310 . Bottom: X-ray colour image of NGC 2276. The diagonal line shows the separation between the west and east side of the galaxy. The annuli show the regions used to measure the X-ray emission of X-ray binaries in NGC 2276 in sub-galactic scales. The orientation of the images is top-north and left-east.

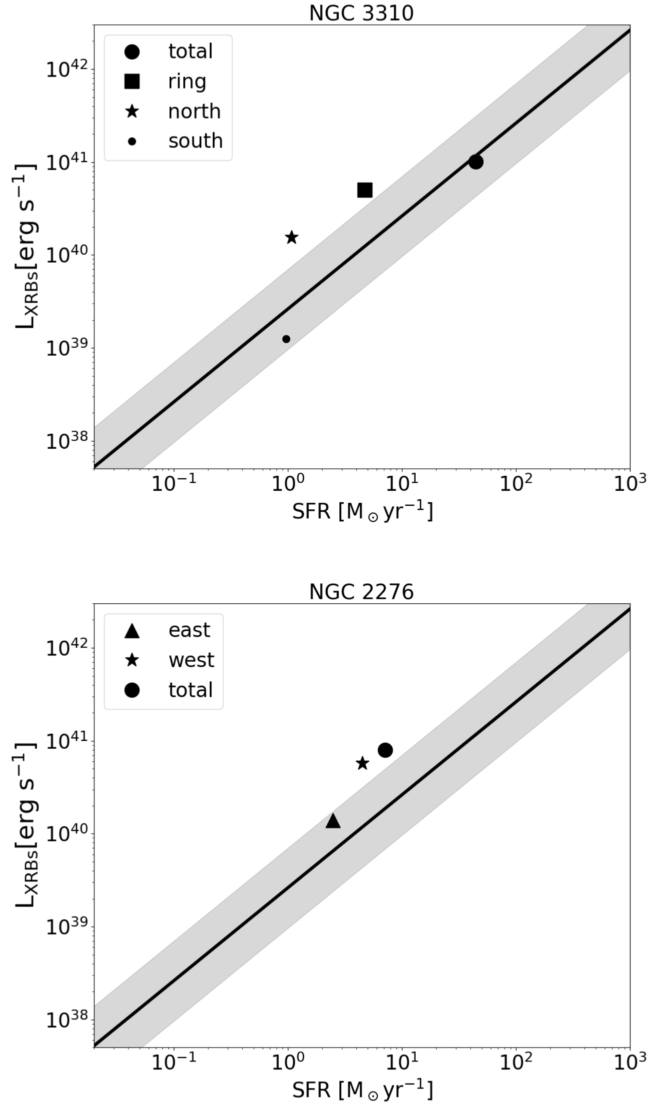

Figure 3.11: Luminosity of HMXBs (0.5-8.0 keV) versus SFR in different regions of NGC 3310 (top) and NGC 2276 (bottom). For NGC 3310 the emission from the ring, the north spiral arm and the south spiral arm are shown with the square, the star, and the dot respectively. For NGC 2276 the emission from the west and east side are depicted with the star and the triangle respectively. The black circle in both cases corresponds to the total emission of the galaxy. The black line and shaded area indicate the best-fit correlation of Mineo *et al.* (2012a) and its 1σ scatter.

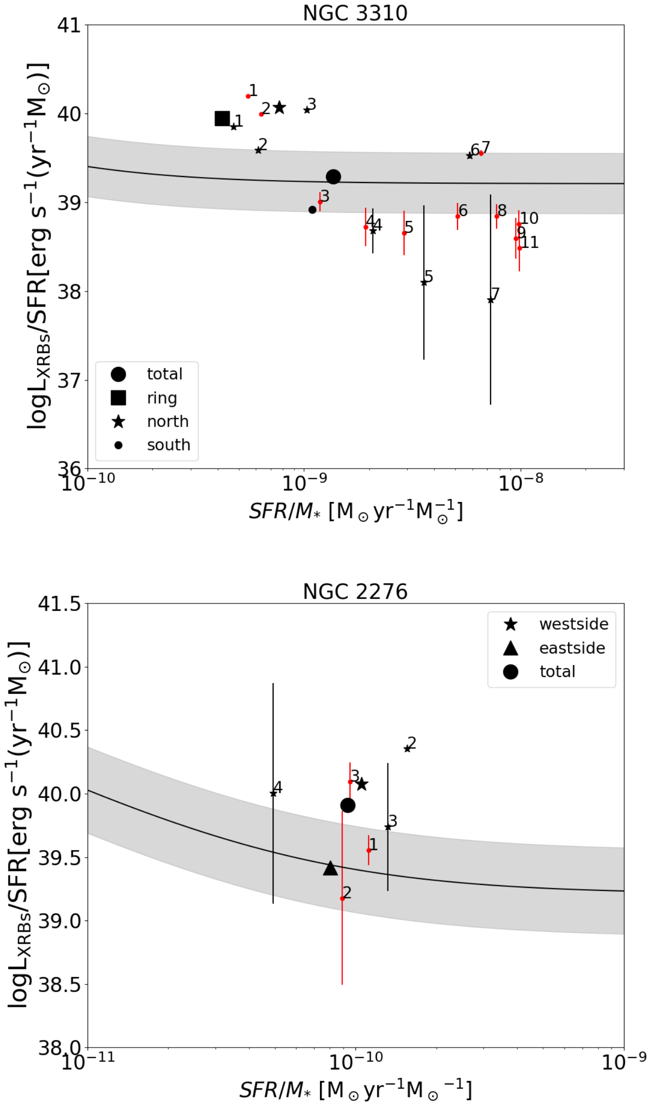

Figure 3.12: Luminosity of XRBs (2-10 keV) per SFR versus sSFR for different regions in NGC 3310 (top) and NGC 2276 (bottom). For NGC 3310 the emission from the ring, the north spiral arm and the south spiral arm are shown with the square, the star and the dot respectively. The enumerated small black stars indicate the north semi-annuli while the enumerated red dots indicate the south semi-annuli. For NGC 2276 the emission form the west and east side are depicted with the star and the triangle respectively. The enumerated small black stars indicate the west semi-annuli while the enumerated red dots indicated the east semi-annuli. The black circle in both cases corresponds to the total emission of the galaxy. The black line and shaded area indicate the best-fit correlation of Lehmer *et al.* (2010) and its 1σ scatter.

Table 3.12: Star formation rates of NGC 2276 and NGC 3310

Region	SFR (24μm) $M_{\odot}yr^{-1}$
NGC 3310	44.7
ring	4.7
north	1.1
south	1.0
NGC 2276 west	3.6
NGC 2276 east	2.5

3.3 DISCUSSION

In the previous sections we presented the results from the analysis of the discrete sources (photometry, spectral, timing analysis), the spectral properties of the integrated galactic emission as well as the applicability of galaxy-wide scaling relations at sub-galactic scales. In this section we examine the contribution of the XRBs, ULXs, and the diffuse emission to the integrated luminosity of the NGC 3310. We also examine whether the variations of the sub-galactic regions on the galaxy-wide scaling relations are a result of stochastic effects or underlying factors such as age or metallicity the stellar populations.

3.3.1 Diffuse emission of NGC 3310

Based on the results reported in Table 3.11 we see that the contribution of the diffuse emission observed (i.e. absorbed) to the absorbed total luminosity of the galaxy is: 30% in the broad band (0.3-10.0 keV), 57% in the soft band (0.3-2.0 keV), and 7% in the hard band (2.0-10.0 keV).

The soft X-ray luminosity of the galaxy is dominated by the diffuse emission, indicating thermal gas which is mostly concentrated on the ring of the galaxy and is characterized by a low (kT $\sim$ 0.20 keV) and a high (kT $\sim$ 0.70 keV) temperature component. These temperatures (Table 3.10) are consistent within the errors with results found in other star-forming galaxies (e.g. Antennae, M101,Arp299 Anastasopoulou *et al.*, 2016; Baldi *et al.*, 2006a; Fabbiano *et al.*, 2003; Kuntz & Snowden, 2010; Mineo *et al.*, 2012b).

We also notice that the hard diffuse emission of the ring and the north spiral arm contribute all (~80% and ~20%) of the diffuse hard emission of the galaxy. Since the vast majority of the sources lay on these areas, it is expected that they would also dominate the diffuse hard X-ray emission of the galaxy. Moreover, the ring seems to be the main source of soft diffuse emission since it is responsible for half the diffuse emission of the galaxy.

3.3.2 Nature of the X-ray sources

From the spectral analysis results for NGC 3310 (Table 3.11) we find that the resolved and unresolved XRBs (power-law component) account for 70% broad-band ($0.3 - 10$ keV), 50% soft-band ($0.3 - 2.0$ keV), and 77% hard-band ($2.0 - 10$ keV,) absorbed luminosity of the galaxy. Their corresponding contribution to the absorption-corrected luminosity is 61% in the broad band, 45% in the soft band and 78% in the hard band. As expected from other star-forming galaxies (e.g. Fabbiano, 2003; Lira *et al.*, 2002) the XRBs dominate in the hard X-ray emission of the galaxy.

In NGC 2276 we observe that the ratio between ULX and lower luminosity sources is larger in the west (shocked) region of the galaxy. Interestingly, the total number of XRBs is marginally larger on the east side of the galaxy. More specifically, on the west side we find 8 sources out of which 7 are ULXs, whereas on the east side we find 10 sources out of which 4 are ULXs. In Fig. 3.13 we plot the cumulative distribution of the luminosity of the XRBs in the two sides of the galaxy. We notice that the X-ray sources on the west side are about five times more luminous than those on the east side of the galaxy and appear to have a flatter distribution of luminosities. This behaviour does not change when we adopt the distance of 32.9 Mpc. We discuss in following sections what could be the cause of this difference in the total luminosity between the two sides of the galaxy.

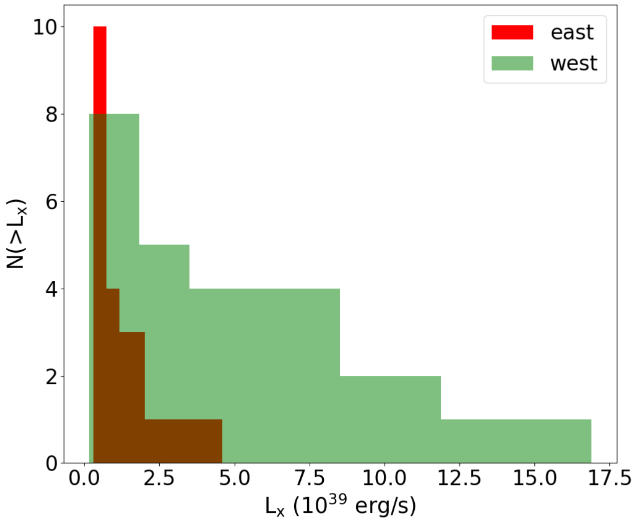

Figure 3.13: Luminosity distributions of the X-ray sources in the two sides of NGC 2276 -Cumulative distribution of the luminosity of the X-ray sources in the two sides of NGC 2276, showing an excess of luminous sources in the west side.

3.3.3 What is the cause for the excess?

As described previously (Section 3.2.7), sub-galactic regions of NGC 3310 and NGC 2276 containing ULXs, and especially the brightest ones in the case of NGC 2276, are located above the galaxy-wide scaling relations of the hard X-ray luminosity versus the SFR and the stellar mass. The important question is whether this is a statistical sampling effect or if it has a physical origin.

In order to evaluate the significance of this excess we simulated the luminosity we would expect in the different regions of the two galaxies based on the galaxy-wide scaling relations, and we calculated the probability to get the observed luminosity by chance.

In more detail, we first calculated the expected number of LMXBs and HMXBs in each region, based on the normalisation of the XLFs with stellar mass (Gilfanov, 2004) and SFR (Mineo *et al.*, 2012a) respectively. We assumed two limiting luminosities ($L_{\rm min} = 10^{36}$erg s^{-1} and $L_{\rm min} = 10^{37}$erg s^{-1}) for integrating the number of XRBs, in the XLF of Mineo *et al.* (2012a) and limiting luminosity of $L_{\rm min} = 2 \times 10^{37}$erg s^{-1} for the XLF of Gilfanov (2004). This is supported by the finding of (Mineo *et al.*, 2014) that in NGC 2206/IC 2163 the global scaling relations between the X-ray luminosity of

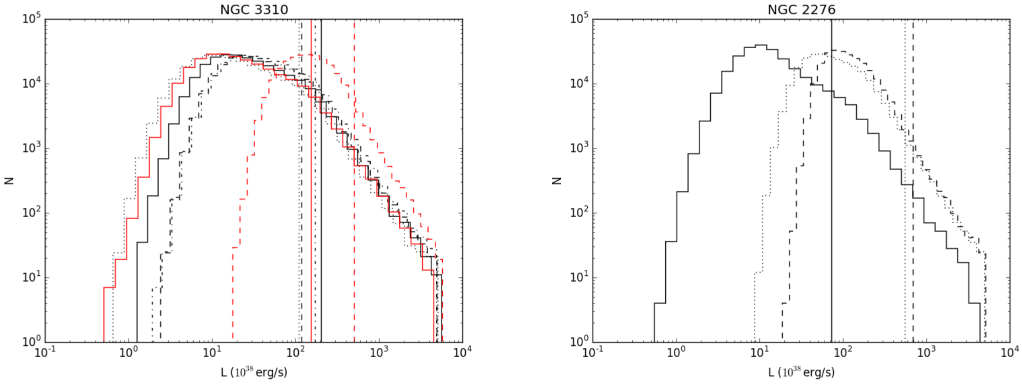

Figure 3.14: Distributions of the expected luminosity in different regions of NGC 3310 (left) and NGC 2276 (right) drawn from the scaling relations of X-ray binaries with SFR and stellar mass (see Section 3.3.3. Each histogram corresponds to a different region which show an excess in the luminosity of the X-ray binaries they host. The vertical lines correspond to the observed luminosities of each region. For NGC 3310: dashed: 1st north semi-annulus, dotted: 3rd north semi-annulus, solid: 1st south semi-annulus, dash-dot: 2nd south semi-annulus, red dashed: ring, red solid: north spiral arm. For NGC 2276: dashed: west side, dotted: 2nd west semi-annulus, solid: 3rd east semi-annulus.

ULXs and SFR also hold in local scales.

Then, we obtained 500 samples of LMXBs and HMXBs from a Poisson distribution, with mean equal to the expected number of HMXBs and LMXBs, in each sub-galactic region based on the aforementioned scaling relations and their local SFR and stellar mass (derivation described in Section 3.2.7). For each of these number of HMXBs and LMXBs in each region we obtained 500 samples of luminosities drawn from their corresponding XLF, for each population. The total luminosity for each region was calculated by summing the luminosities of the individual sources in the region. This resulted in two distributions of 250,000 total luminosities for each region, one for LMXBs and one for HMXBs. We then added the two distributions for each region to get the distribution of total XRB luminosities in each region. This way we accounted for fluctuations on the number of sources in each region as well as stochastic effects on their luminosity.

Fig. 3.14 shows the histograms of simulated total luminosities. Each histogram corresponds to a different region which shows an excess in the XRB luminosity for NGC 3310 and NGC 2276. The probability to get the observed excess by chance is given by the tail of the luminosity histograms for each region. We find that for every region showing an excess in the scaling relations the probability of measuring such a high value only due to statistical fluctuation is between 1% and 7% for the various regions of NGC 2276 and between 3% and 13% for the various regions of NGC 3310. This test indicates that the excess of X-ray luminosity for the XRBs we observe in the scaling relations could have a physical origin.

3.3.3.1 What is the physical origin of this excess?

An obvious answer could be that differences in the SFR are responsible for the excess in the luminosity of the XRB population. However we argue that this is not the case, since all relations presented in this paper are normalised by the SFR. In NGC 2276 in particular we measure more or less the same SFR between the two sides of the galaxy.

A metallicity effect?

Metallicity could be a factor causing the observed excess in the hard X-ray luminosity. Theoretical models suggest that lower metallicities are associated with higher X-ray luminosities for a given stellar population (Fragos *et al.*, 2013). Recent studies have shown that low-metalicity regions could result in higher numbers of HMXBs and in particular ULXs (Brorby *et al.*, 2014; Douna *et al.*, 2015; Linden *et al.*, 2010; Prestwich *et al.*, 2013), although with significant scatter.

NGC 3310 is a low metallicity galaxy (young star clusters peak at $Z=0.4Z_{\odot}$; de Grijs *et al.*, 2003a,b) which could explain the large number of ULXs observed. However, the areas containing the ULXs do not seem to be of much lower metallicity. According to de Grijs *et al.* (2003a), who studied the star clusters in NGC 3310, the distribution of metallicities in the ring of the galaxy (where the majority of ULXs reside) and outside the ring do not show any differences. Additionally, Miralles-Caballero *et al.* (2014a) found a rather flat gaseous abundance gradient for about a hundred HII regions located on the disk and the spiral arms.

Measurements of the diffuse X-ray gas on the main body of NGC 2276 show that it is of low metallicity ($\sim 0.06 - 0.11 Z/Z_{\odot}$, Rasmussen *et al.*, 2006), with no metallicity differences between the two sides of the galaxy, though we could not find any reliable metallicity measurements of the stellar populations. However, since it has been found that the metallicity gradient of galaxies (e.g. Maragkoudakis *et al.*, 2018) has a radial dependence and we are studying two symmetric sides of the galaxy with respect to its center we would not expect significant differences of the metallicity between the two sides of the galaxy.

An age effect?

Another factor explaining the observed excess in the hard X-ray luminosity of the different regions of the galaxy could be the age variations of the stellar populations. Theoretical work (Fragos *et al.*, 2013; Linden *et al.*, 2010) supports that the luminosity of the HMXBs peaks at younger HMXB populations and that the younger X-ray binaries populations result in more luminous sources. There is also increasing observational evidence for measurable dependence of the number and/or the X-ray luminosity of XRBs as function of their age (e.g. Antoniou & Zezas, 2016; Antoniou *et al.*, 2018; Lehmer *et al.*, 2017). Similarly, (Mineo *et al.*, 2014) tentatively attributed a dependence of the number of ULXs in NGC 2206/IC 2163 on the FIR to UV luminosity ratio on variations of the local star-formation timescales (although FIR to UV luminosity variations could also result from dust extinction).

In the case of NGC 3310 hundreds of star clusters (HST; de Grijs *et al.*, 2003b; Elmegreen *et al.*, 2002) have been found. According to de Grijs *et al.* (2003a), young clusters (ages peaking at $\sim$ 30 Myr) reside predominately at the ring and northern spiral arm where the majority of ULXs are located.

The difference in the total luminosity of the XRBs between two sides of NGC 2276 (the west side is $\sim$ 5 times more luminous) could be explained by a younger XRB population on the west side of the galaxy. Younger stellar population in this side of the galaxy are expected from the compression-induced star-forming activity. In fact, Hα and FUV images (see Fig. 3.15) show that the west side of the galaxy is brighter than the east side. The FUV emission is produced by stars up to $\sim$ 100 Myr old while the Ha emission is powered by stars up to 10 Myr old (Kennicutt & Evans, 2012). The stark contrast of the Ha intensity between the west and the east side of the galaxy strongly indicates that the west side is dominated by young (up to $\sim$ 10Myr) stellar populations.

Implication for scaling relations

Based on the above arguments we favor the age-dependence of the ULX populations as the driving factor for the excess we see in the sub-galactic X-ray luminosity scaling relations with respect to the galaxy-wide scaling relations. Although metallicity may have an effect which needs to be explored more systematically, the relatively shallow metallicity gradients typically seen within star-forming galaxies (Maragkoudakis *et al.*, 2018; Moustakas *et al.*, 2010) support the notion that the dominant factor of scatter in sub-galactic X-ray luminosity scaling relations is stellar population age variations. For the younger populations ($<$ 100 Myr) such age variations may have a dramatic effect since their X-ray output may change by more than one order of magnitude per unit stellar mass for age differences as small as $\sim 10 - 20$ Myr Fragos *et al.* (2013). Interestingly, the regions we are probing have SFR and sSFR similar to those observed in local dwarf galaxies. This has the important implication that star-formation history variations (in addition to stochastic sampling of the X-ray luminosity function) could

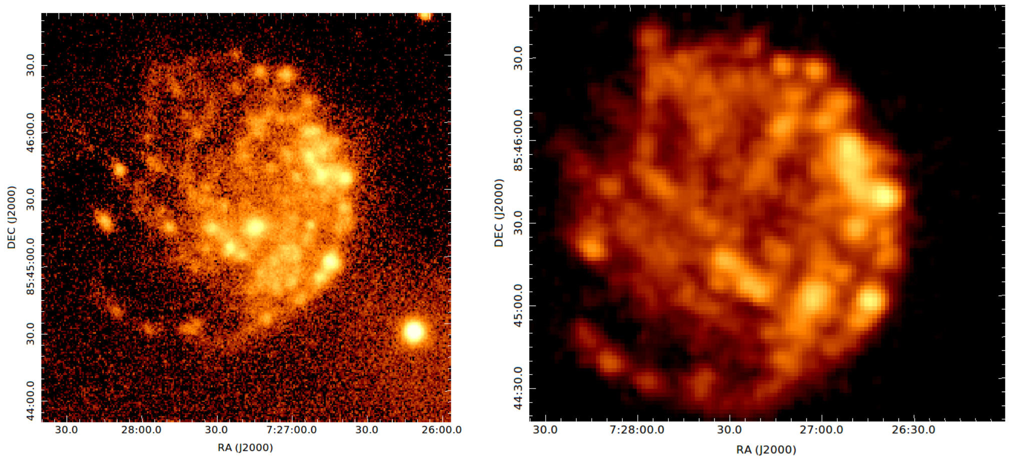

Figure 3.15: Hα (left) and GALEX FUV (right) images of NGC 2276 showing intense star-formation on the compression front in the west side of the galaxy. The presence of strong Hα and FUV emission suggests the presence of young ($\sim$ 10 Myr) stellar populations. (The Hα observations are taken at the Observatoire de Haute Provence(OHP), France.)

play a possibly important role in producing the scatter we observe in the galaxy-wide X-ray luminosity - SFR scaling relations in the low SFR regime.

3.4 SUMMARY

In this work we have analysed ACIS-S *Chandra* observations for the galaxies NGC 3310 and NGC 2276. For NGC 3310 we find 27 X-ray discrete sources (SNR>3.0) down to 1.0×10^{38} erg s^{-1}. Fourteen of those sources are ULXs located on the ring and north spiral arm reaching 1.5×10^{40} erg s^{-1}. The majority of sources are fitted well with an absorbed power-law model (N_H greater than Galactic; Γ ~1.7-2.0; typical for XRBs). We also find that the nucleus of the galaxy is variable but there is no sign of an AGN. The contribution of XRBs is more than 80% to the hard (2.0-10.0 keV) galaxy luminosity. The diffuse emission component (kT=0.2 keV and 0.8 keV) is 60% of the soft (0.3-10.0 keV) emission of the whole galaxy.

For NGC 2276 we find 19 X-ray discrete sources (SNR>3.0) down to $L(0.3-10.0\mathrm{keV}) = 1.0\times10^{38}$ erg s^{-1}. Eleven of those sources are ULXs. Five of them are located on the east and six on the west side of the galaxy. We also find that the total luminosity of the XRBs on the west side of the galaxy is five times larger than the luminosity of XRBs in the east side and almost every ULX on the west side is brighter than those in the east side.

Moreover we find that the ULX-hosting areas of both galaxies are located above the L_X-SFR and L_X/SFR-sSFR scaling relations. This indicates that sub-galactic regions follow the galaxy-wide scaling relations but with much larger scatter resulting from the age (and possibly metallicity) of the local stellar populations in agreement with recent theoretical and observational results. This indicates age differences could be the origin of the scatter we observe in the low SFR regime in the L_X-SFR scaling relations.

4

XMM-Newton survey of star-forming galaxies in the local Universe: X-ray binary scaling relations

4.1 Introduction

The integrated X-ray emission of normal galaxies (galaxies not hosting an AGN), is dominated by the emission of their X-ray binary (XRB) population in the hard X-rays ($\gtrsim$2 keV) and the diffuse gas emission in the soft X-rays ($\lesssim$2 keV) (for a review see: Fabbiano, 2003). The XRBs are classified as High-Mass X-ray binaries (HMXBs) if their donor stars are massive (O,B spectral types; $\gtrsim$8 $M_\odot$) or Low-Mass X-ray binaries (LMXBS) if they are lower mass stars ($\lesssim$1 $M_\odot$). In the first case, the XRBs are expected to be associated with on-going or recent star-forming activity, while in the latter case to be associated with older stellar populations. Systematic studies showed that the integrated hard X-ray luminosity or the numbers of XRBs they host, scale linearly with the star-formation rate (SFR) in the case of the young HMXBs (e.g. Lehmer *et al.*, 2010, 2016, 2019; Mineo *et al.*, 2012a), or stellar mass (M_*) in the case of LMXBs (e.g. Boroson *et al.*, 2011; Gilfanov, 2004; Lehmer *et al.*, 2010).

Such scaling relations are important because they provide insights for the connection between the X-ray output of galaxies and their stellar populations. They are a direct measure of the production rate of XRBs per unit SFR and stellar mass. As such they provide important constrains on populations synthesis models for XRBs, and point to studies of the evolution of XRB populations in higher redshifts. The first studies of the X-ray luminosity-SFR scaling relations focused on linear fits of the form $Lx = \alpha \cdot SFR$. The reference work of Mineo *et al.* (2012a) find a scaling of $\alpha = 2.6 \times 10^{39} ergs^{-1}(M_{\odot}yr^{-1})^{-1}$ and large scatter of ~0.4 dex. Lehmer *et al.* (2010) in a study of 17 luminous infrared galaxies, introduced a scaling relation of the form $Lx = \alpha M + \beta SFR$, which accounts for the young HMXBs, but also the contamination by the underlying LMXBs traced by the stellar mass of the galaxy. They find values of $\alpha = (9.05 \pm 0.37) \times 10^{28} ergs^{-1}M_{\odot}^{-1}$ and $\beta = (1.62 \pm 0.22) \times 10^{39} ergs^{-1}(M_{\odot}yr^{-1})^{-1}$. They found that this correlation has a ≈0.1-0.2 dex less scatter, than the L_X-SFR correlation and showed that HMXBs dominate the galaxy-wide X-ray emission for galaxies with sSFR(≡SFR/M_*)$\gtrsim$ $5.9 \times 10^{-11} yr^{-1}$. Studies of local galaxies at sub-galactic scales have revealed that the galaxy-wide scaling relations are still valid for that small scales but with much larger scatter that possibly results from differences in the ages of the stellar populations (Anastasopoulou *et al.*, 2019; Kouroumpatzakis et al., 2019).

Moreover the scaling relations have been found to be dependent on other physical parameters of the galaxy like the age and the metallicity. For a number of powerful star-forming galaxies the Lx-SFR scaling relations are elevated for lower metallicities, a result that is possibly driven by higher numbers of HMXBs (e.g. Basu-Zych *et al.*, 2013a; Brorby *et al.*, 2014). Even in the case of LMXB, studies of nearby early type galaxies (e.g Boroson *et al.*, 2011; Lehmer *et al.*, 2014) showed that there is a dependence with the stellar age for the Lx(LMXBs)-M_*, where young early type galaxies show an excess of luminous LMXBs in comparison to old early type galaxies, behaviour explained by the evolution of the LMXB population with time. Evolution of the scaling relation with the redshift of the galaxy have also been reported (e.g. Aird *et al.*, 2017; Basu-Zych *et al.*, 2013b; Fornasini *et al.*, 2018; Lehmer *et al.*, 2016; Mineo *et al.*, 2014) which is probably the result of the decrease in mean stellar age and metallicity with look-back time. This explanation has been confirmed by Fornasini *et al.* (2019), who found evidence connecting directly the redshift evolution of Lx/SFR and the metallicity dependence of HMXB dominated galaxies.

Those dependences of the scaling relations with metallicity, age, and redshift are also in agreement with the theoretical expectations from XRB population synthesis models (e.g. Fragos *et al.*, 2013; Linden *et al.*, 2010; Wiktorowicz *et al.*, 2015). These studies showed that the total X-ray luminosity of population of XRBs may vary by ∼1 index as result of their age or metallicity. This has been confirmed by the age and metallicity evolution of the scaling relations. These variations could contribute to the large scatter observed in the integrated X-ray luminosities scaling relations of local galaxy samples. However, all observational studies so far have been based on small samples of local galaxies (a couple dozen) that do not reflect all the conditions of star formation in the local Universe. As a result they may not give a representative picture of the Lx scaling relations as function of stellar mass and SFR, or its scatter.

In this work we aim to study the scaling relations between the luminosity of the X-ray binary populations the SFR and M_* of the host galaxy on a much larger scale, i.e. all known galaxies in the local Universe, and therefore the most representative sample of local galaxies used so far. This would provide important insights on whether the correlations used so far, based on smaller samples, represent the majority of galaxies, and whether the correlations themselves can be treated as universal and used to infer the X-ray binary component in any local galaxy.

The structure of this paper is as follows: in Section 4.2 we describe the sample and in Section 4.3 the data analysis. We present the photometric and spectroscopic results of the *XMM-Newton* analysis in Sections 4.3.1 and 4.3.2. The scaling relations are presented in Section 4.4, and in Section 4.5 we discuss our results. All errors correspond to the 90% confidence interval unless otherwise stated.

4.2 Galaxy sample

Our sample of galaxies is the result of cross-matching between the `HECATE` catalogue (Kovlakas et al., 2019) which contains all known galaxies within a volume of 200 Mpc, in combination with all *XMM-Newton* archival observations up to September of 2019. In our study we include even galaxies not detected in the X-rays, yielding a less biased sample. In the following sections we describe the catalogue as well as the matching process in detail.

4.2.1 The `HECATE` catalogue

The HECATE catalogue is a master catalogue of ∼ 164000 galaxies from the HyperLEDA (Makarov *et al.*, 2014) with Virgo-Infall corrected velocity (< 14000 km/s) and accurate positions (astrometric uncertainty <10 arcsec). It provides robust distance estimates for all the galaxies; redshift independent distances by combining available

NED-D measurements and redshift dependent distances with uncertainties accounting for local Universe over-densities, peculiar velocities and systematic effects. The catalogue also provides multi-wavelength photometry, and stellar population parameters (SFR, M_*, and metallicity) for a large percentage of the galaxies. The SFR were derived based on the total infrared luminosities using *IRAS* and *WISE* measurements. The stellar masses were derived based on Ks-band luminosities using *2MASS* measurements. For further information and details see Kovlakas et al. (2019) and references therein.

To identify the AGN in our sample we have used multi-dimensional spectral-line diagnostics (40K galaxies; Stampoulis *et al.*, 2019), the *Chandra* survey of She *et al.* (2017), the *LAMOST* survey of Wang *et al.* (2018) as well as the work of Ho *et al.* (1997). We classify a galaxy as AGN, when at least one of the 4 catalogues classifies it as such. Also, in order to be conservative, we exclude galaxies without any available information to identify the presence of AGN.

4.2.2 The *XMM-Newton* sample of galaxies

For the purpose of this study we used only the galaxies with available information on the SFR, M_*, and their AGN content. Therefore, we cross-correlated the `HECATE` catalogue with all public *XMM-Newton* observations (10785) up to September of 2019. For the cross-correlation we used the Sky Ellipses option of TOPCAT which searches for overlapping elliptical regions on the sky taking into account the coordinates, and angular extent (major, minor radii, and position angle). We searched for matches for all `HECATE` galaxies up to 16 arcmin based on their sizes and the size of the FOV of *XMM-Newton* . This resulted in 4885 OBSIDs and 12843 galaxies out of which 988 non-AGN galaxies, with available physical parameters, observed in total at 1971 OBSIDs.

After performing the initial calibration of the observations (described in detail in Section 4.3), we visually inspected the images and background light-curves of all observations. We removed 109 observations that were severely affected by background flaring and therefore could not be used for further analysis. An additional 125 observations could not be used due to various reasons (galaxy within dense cluster, window-mode observations, etc.). However we have kept observations that the galaxies were at least partially covered. This resulted in **1932 OBSIDs**, with **650 galaxies** with available information on SFR, M_*, and AGN content which we will from now on referring to as the **star-forming sample**.

However, in order to have X-ray photometric and spectroscopic information of the detected galaxies regardless of the SFR, M_* and AGN activity information, we cross-

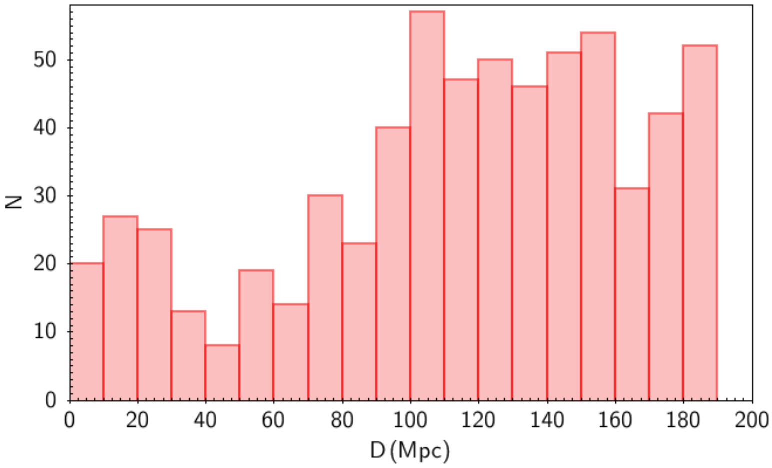

Figure 4.1: Distribution of distances for the *XMM-Newton* star-forming sample.

correlated the `HECATE` catalogue with the *XMM-Newton* DR8 detection catalogue. This resulted in **2188 OBSIDS** and **2543 galaxies**: from now on we are referring to it as the **detection sample**.

Table 4.2 presents the star-forming sample used in this work along with the basic information for the galaxies. Fig. 4.1 shows the distribution of the distances for the star-forming sample. We see that the star-forming sample has a uniform coverage up to the maximum distance in the catalogue. Fig. 4.2 shows the distribution of the star-forming galaxies (yellow points) on the SFR-M_* plane overlaid on the *XMM-Newton* sample (red points) and full `HECATE` catalogue (blue points). We see that our sample covers the full range of SFR and M_* of star-forming galaxies observed with *XMM-Newton* (sSFR$> 10^{-11}$ yr^{-1}). The lack of objects at lower sSFR is due to the lack of sensitive optical emission line data, that does not allow us to characterize the presence of AGN. However, we do see a bias in the low SFR, low M_* regime, where very few objects have been observed in the X-ray band.

In Table 4.3 we present the log of the X-ray observations used in this work, and the fraction of the angular area of the galaxy covered in each observation. In summary, the exposure times range from 1 to 120 ks, with the majority of our galaxies having exposure times between 10 and 50 ks. In Fig.4.3 we show the distribution of the galaxy coverage for all the observations in our star-forming sample. We see that the vast majority of galaxies (70%) have more than 90% of their angular extent covered by the *XMM-Newton* observations.

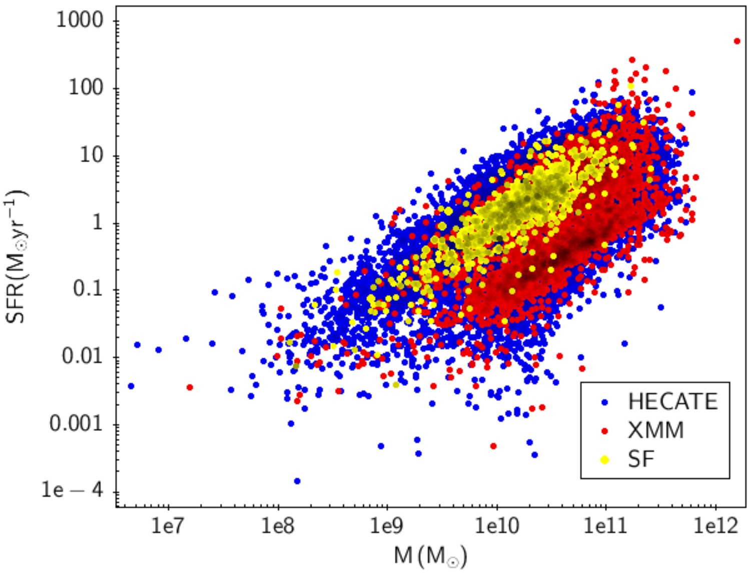

Figure 4.2: SFR versus M_* for the *XMM-Newton* star-forming sample (yellow points) overlaid on the *XMM-Newton* data (red points) of all galaxies, and the full HECATE sample (blue points).

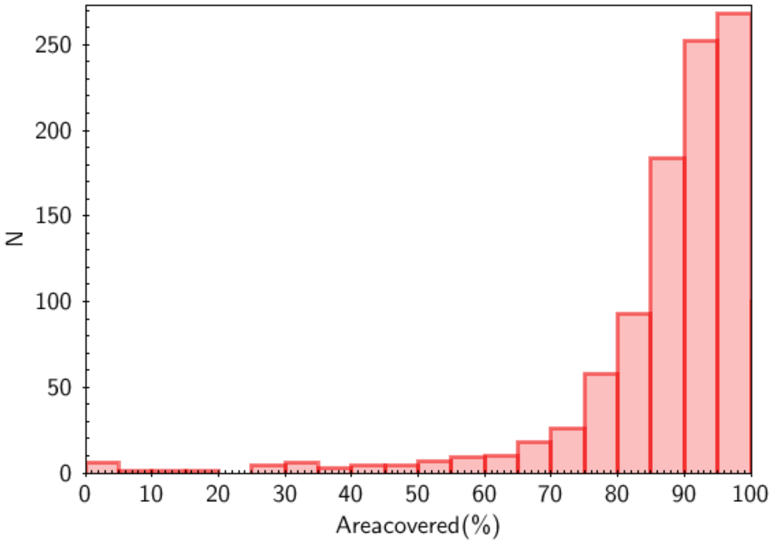

Figure 4.3: Distribution of the galaxy angular area coverage for the star-forming sample.

4.3 Data Analysis

We reduced and analysed all EPIC archival observations for the star-forming as well as the detection sample, using the *XMM-Newton* Science analysis system (SAS) v17.0.0. In more detail, we produced calibrated event files using the *emchain* SAS task for the MOS cameras and *epchain* SAS task for the pn camera. The latter was also used to create out-of-time event files for the pn camera using *withoutoftime=Y*, in order to subtract out-of-time events and properly correct for the charge transfer inefficiency (CTI). We also used the *emtaglenoise* tool to flag noisy MOS CCDs at low energies (Kuntz & Snowden, 2008).

In order to filter background flares we created good time interval (GTI) files using the SAS task *tabgtigen* with a constant cut-off of 2.5 cts/s and 8.0 cts/s for the EPIC MOS and EPIC pn exposures respectively. We then created more restrictive GTI files using the sigma-clipping method to remove residual flaring even below those thresholds. We created a background light-curve for each detector, which were visually inspected to ensure the removal of the background flares. The final outcome was filtered event lists for each detector.

We created images and exposure maps for EPIC pn and MOS in the five basic bands of *XMM-Newton* using the clean event files and the tool *eimageget*. From now on we will refer to them as Band 1: 0.2 – 0.5 keV, Band 2: 0.5 – 1.0 keV, Band 3: 1.0 – 2.0 keV, Band 4: 2.0 – 4.5 keV, Band 5: 4.5 – 12.0 keV. The images from EPIC pn were also corrected for the emission from Copper, that comes from the electronics, at 7200-9200 eV. To account for the background, we created background maps in the 5 bands for the pn and MOS using the *esplinemap* SAS task. The background maps for the EPIC pn include also the out-of-time events.

4.3.1 Photometry

We then performed aperture photometry for both the detection and the star-forming *XMM-Newton* sample of galaxies for all detectors and observations using the *dmextract* tool of CIAO. As apertures we used the sizes of the galaxies from the `HECATE` catalogue folded with the average PSF of the *XMM-Newton* detectors for a fractional encircled energy of 90%.

The background for each observation (OBSID) and detector for every source was estimated by performing aperture photometry on the corresponding exposure corrected background maps, using the same apertures as in the source photometry. In order to remove artefacts at the chip edges we applied a mask on the exposure-map corrected image. For the division, multiplication and subtraction of images we have used the ftool *farith*.

Finally, we ran *dmextract* on the images and background maps, as well as the exposure-map corrected, masked images and background maps, and extracted their count and count-rates respectively. The errors on the final photometry, were calculated by propagating the errors on the source and background photometry.

The photometry for the 97 galaxies of the star-forming sample with SNR>3.0 and coverage more than 90% is presented in Table 4.4 for the different *XMM-Newton* bands and all detectors.

For galaxies of the star-forming sample with SNR<3.0 and area coverage more than 90% (498 galaxies) we calculated the probability distributions, and confidence intervals on the source intensity using the BEHR code (Park *et al.*, 2006),with a flat prior and Gibbs sampling. This analysis was performed on the source intensities in the *XMM-Newton* Band 2, 3, and 4 (0.5-4.5 keV) and the *XMM-Newton* Band 4 (2.5-4.5 keV).

4.3.2 Spectral Analysis

4.3.2.1 Extraction of spectral files

We have performed spectral analysis for all the galaxies of the detection and star-forming samples. We extracted spectra and calibration files for the galaxies that we had at least 10 counts in the combined 2 3 and 4 bands of *XMM-Newton* .

In order to extract the source and background spectra, we used the *evselect* SAS task, and limited the patterns to singles and doubles for both EPIC pn and MOS event files. For the extraction of the source spectra we used the same galaxy regions as in the photometry (see Section 4.3.1). For the extraction of the background spectra, we used the *ebkgreg* SAS task to determine the best background regions. The task searches for the best possible background region, in the same CCD as the source. In the case of EPIC pn it avoids regions including the same RAWY column with other bright sources in the field. In order to exclude contaminating sources from the background region, we excluded all discrete sources reported in the Processing Pipeline Subsystem products (PPS) files, included in the *XMM-Newton* science archive. We converted this list to a FITS region using the *dmmakereg* tool of CIAO, which was then supplied to *evselect* to filter out any events associated with detected sources.

We then extracted the Auxiliary Response Files (ARF) for the source spectra and the Redistribution Matrix Files (RMF) using the SAS task *arfgen* and *rmfgen* respectively. We used the options *extendedsource=yes* and *detmaptype=flat* for galaxies with sizes greater that 80 arcseconds.

As a final step, we calculated the area of the galaxy and background region respectively (BACKSCAL keyword). The area of the galaxies has been calculated during the ARF creation with the option *setbackscale=yes* on the *arfgen* where for the calculation of the background we used the *backscale* SAS task.

4.3.2.2 Spectral fitting

We performed spectral fits for 1713 galaxies (5804 spectra) with more than 25% coverage and more than 120 net counts (in the combined *XMM-Newton* band 2, 3, and 4) using the *Sherpa* fitting package (Freeman *et al.*, 2001). We used chi-square statistic (*chi2xspecvar*). In order to allow for chi-square fitting, and avoid negative bin counts we grouped the spectra in bins of 15 net counts using the *set_grouping* and *set_quality* routines of *Sherpa.*

We fitted simultaneously the spectra from all the separate observations and detectors available for each galaxy. All other model parameters were tied together. In order to account for residual calibration offsets between the different detectors, we introduced one multiplicative parameter that applies on the whole spectrum. For galaxies that have been observed in multiple instances, we introduced one more multiplicative constant to account for differences in the area coverage, long-term variability, or long-term residual variations in the calibration.We fitted the galaxies using 10 different models, having always two absorptions applied to the entire model. One frozen to the Galactic absorption value (calculated using the ftool NH) and a second to account for the intrinsic absorption of each galaxy. As a consequence the full model consists of `const1d.obs*const1d.detec*(xsphabs.abs1* xsphabs.abs2*model)`, where `const1d.obs` and `const1d.detec` are the constants assigned to each observation and detector respectively, `xsphabs.abs1` refers to the Galactic absorption and `xsphabs.abs2` to the intrinsic absorption. With `model` we are referring to one of the following 10 models:

1. `powlaw1d`
2. `xsapec`
3. `powlaw1d+xsapec`
4. `powlaw1d+xsapec+xsapec`
5. `(xspcfabs*powlaw1d)+xsapec`
6. `(xspcfabs*powlaw1d)+xsapec+xsapec`
7. `powlaw1d+xsapec+xsgaussian`

8. `powlaw1d+xsapec+xsapec+xsgaussian`
9. `xspcfabs*(powlaw1d+xsgaussian+xsapec`
10. `xspcfabs*(powlaw1d+xsgaussian+xsapec+xsapec`

In order to choose the appropriate model for each galaxy, we first fitted all the spectra with an absorbed power-law model and an absorbed power-law plus a thermal plasma component model (models 1 and 2). Then, we visually inspected all the fit residuals for characteristic features. Depending on the shape of the residuals and in combination with the quality of the fit (χ^2_ν>1.2), we introduced extra component models. For example in cases:

a) where a FeKα line at around 6.4 keV was prominent we introduced a Gaussian line,

b) we had residuals in the soft part of the spectrum we introduced a second thermal plasma component,

c) where the power-law component was flat (Γ <1.3) and/or a hump was visible at hard energies we introduced a partial covering fraction absorption,

d) where a combination of the above was required, we used more complex models (models 5, 7, 8, and 9).

The final selection of the best-fit model was performed after comparing the quality of the fits and visually inspecting all available models for each galaxy. The majority of the galaxies were fitted well with models 1, 2, and 3 (Fig. 4.4; left). However, 330 galaxies required more complicated models (e.g. see Fig 4.4; right) typical for AGN, e.g showing a strong FeKα lines, flat or heavily absorbed spectra above 4 keV. It is interesting that 280 of these galaxies have not yet been identified as AGN by any of the catalogues we are using (see section 4.2.1).

We present in Table 4.5 the spectral fitting results for the 58 galaxies of the star-forming *XMM-Newton* sample that allowed for spectral fitting. The complete spectral atlas for the *XMM-Newton* galaxy survey will be presented in a separate publication.

4.3.3 Fluxes and luminosities for the X-ray binary populations

We calculated fluxes in the two commonly used bands in the scaling relations: broad (0.5-8.0 keV) and hard (2-10 keV). As starting point we used the measured count rates in the combination of the standard *XMM-Newton* bands that is closest to the broad and hard bands: sum of bands 2, 3, and 4 for the broad band, and band 4 for the hard band. We did not use band 5 of *XMM-Newton* , because it is dominated by background emission. For the calculation of the count rate to flux conversion we used the CIAO

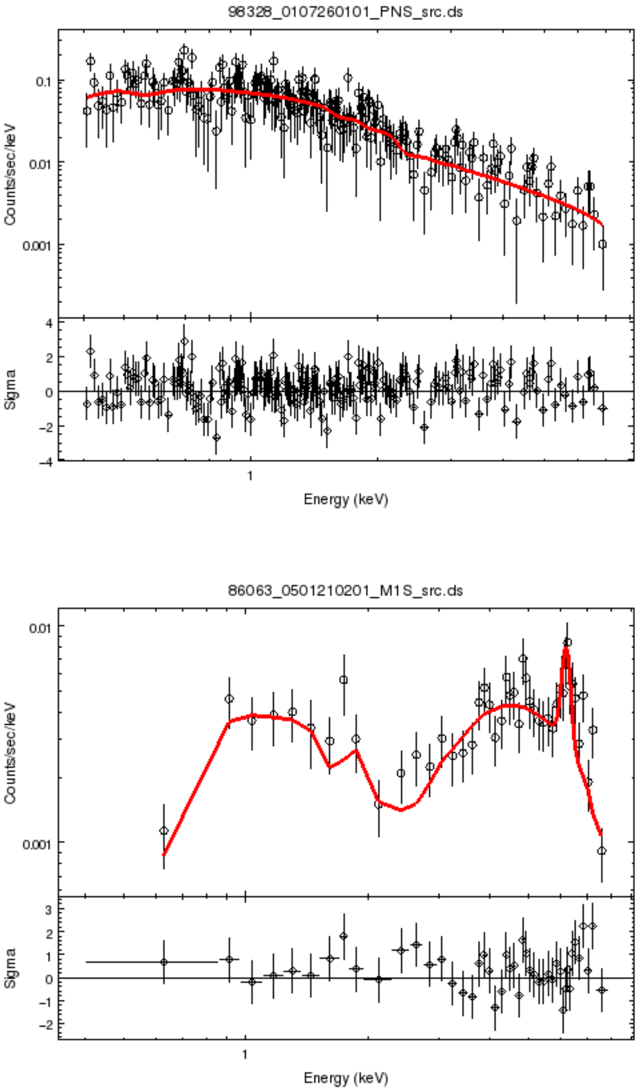

Figure 4.4: Top panel: Typical spectrum of a star-forming galaxy fitted with model 1. Bottom panel: Typical spectrum of an AGN with a prominent FeKα line at 6.4 keV fitted with model 9.

tool *modelflux*. We provided the ARF file of each observation and detector for every galaxy and assumed an absorbed power-law model with a photon index of Γ=1.7 and Galactic absorption. In Table 4.4 we show along with the photometry the count-rate conversion factors of the broad and hard bands. The final fluxes in the broad and hard band were the average of all the fluxes in each detector and observation for a particular galaxy.

In the case of the non-detected galaxies we calculated their fluxes using their upper limits on the number of counts. We then used a count-rate to flux conversion using the CIAO tool *modelflux* and assuming an absorbed power-law model with a photon index of Γ=1.7 and Galactic absorption. In the case of multiple observations for a single galaxy we adopted the observation that had the largest coverage and gave the most stringent constrain on the flux upper limit. We then calculated the luminosities using the distances of the `HECATE` catalogue. The errors are a result of error propagation from the number of counts.

Regarding the spectroscopy, and since we are interested in the normal galaxies of the sample, we calculated fluxes and luminosities only for objects that are fitted with spectral models 1, 2, 3, and 4. We calculated the best-fit model fluxes using the following method: We first used the *sample_flux* command, which samples parameter values from the covariance matrix of the fit. Then for each set of parameter draws, we calculated the observed flux using the *calc_energy_flux*. Finally from the distribution of the resulting fluxes we calculated the median value and the uncertainties at the 90% interval. To calculate the fluxes of only the power-law component (i.e the fluxes of the X-ray binary population) we repeated the same procedure but this time setting to 0 the value of the normalisation of the thermal plasma component parameter. We did not use *sample_flux* to calculate directly the fluxes and uncertainties, because it ignores zero-valued flux draws. This truncation of the draws for the faint galaxies biases the fluxes upward and affect the uncertainties[1]. Therefore with our method we are certain that everything is computed correctly.

As a final step we calculated the luminosities based on the distances in the `HECATE` catalogue. In Table 4.6, we show the photometric and spectroscopic luminosities along with their corresponding errors for the star-forming sample of galaxies in the broad and hard bands and in Table 4.7 we present the 90% confidence upper bounds on the source luminosity for the very faint sources.

---

[1] Also there is some kind of bug concerning the calculation of confidence flux intervals when fitting multiple datasets.

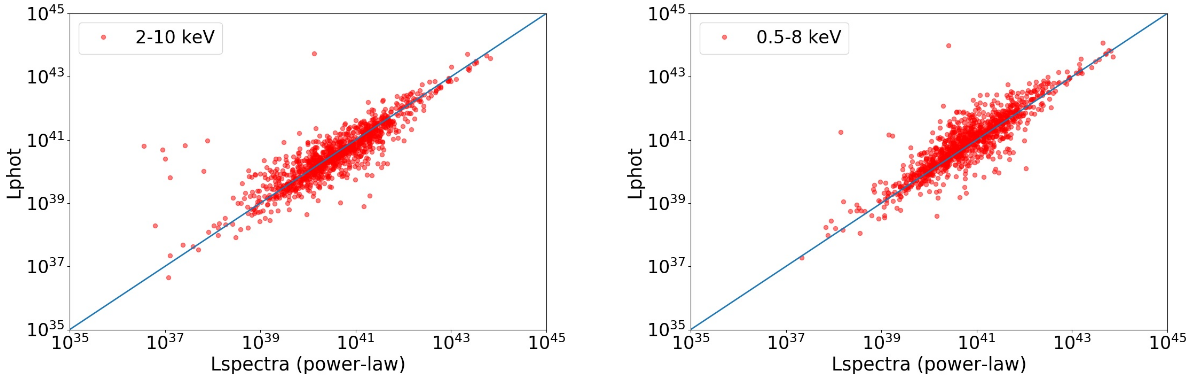

Figure 4.5: Luminosity calculated from the photometry versus the luminosity calculated from the the spectroscopy on the x axis. The blue line is the 1:1 line.

4.3.4 Calibration of the photometric fluxes

The luminosities based on the spectral analysis are certainly more reliable since they isolate the power-law component associated with the X-ray binaries, and they account for the actual spectrum of each object. A comparison between the spectroscopic luminosities and these derived from the photometric analysis can be used to quantify any bias in the latter. In addition the scatter of these comparison can give a picture of the uncertainty of the photometric luminosities due to the use of a fixed spectral model instead for the optimal model for each source. In Fig.4.5 we present the luminosity of the photometry versus the luminosity of the spectroscopy for the common galaxies of both star-forming and detection *XMM-Newton* samples with the data following the 1:1 line. However, we see that in the case of the broad band there is an excess of points above the line.

We see that overall there is generally good agreement. In fact, the median value of the ratio of the luminosities, is 1.2 indicating that the luminosity of the photometry in the broad band is overestimated compared to the spectroscopic luminosity by about 20%. To account for this bias we correct downwards the photometric luminosities of all galaxies. However, we do not observe any such bias in the hard band (median of the Lphot/Lspec= 0.96). This indicates that the excess of the photometric luminosities is the result of spectroscopic variations that influence soft part of the spectrum; such as the presence of a thermal component, differences between the actual absorption and that assumed in our analysis.

4.4 Correlations with stellar population parameters

In this section we investigate the correlation of the luminosity of the X-ray binary population in each galaxy as a function of their SFR and M_* and therefore using only the star-forming *XMM-Newton* sample.

4.4.1 Fitting method

In order to calculate the correlation between the luminosity of the X-ray binary population versus the SFR and the M_* of the host galaxy we have used a maximum likelihood fit method which accounts for the probability distributions of the flux for each galaxy in the sample.

The approach therefore accounts seamlessly for the often skewed luminosity distributions of the spectroscopic sample (resulting from the spectral uncertainties and the non-linear count-rate to flux conversion; cf. Zezas *et al.* (2007)), and the non-detections. The probability distributions of the spectroscopic data were calculated using 10^3 draws from the fit covariance matrix of the model spectral parameters as described in Section 4.3.3. The photometric luminosity distributions were calculated by sampling (10^3 times) from a Gaussian distribution with mean the photometric luminosity value (as reported in Table 4.6) and standard deviation the luminosity error. For the non-detections we used the set of draws from the posterior distribution of the source intensities calculated with BEHR (Section 4.3.1) with 10^6 number of draws for each galaxy.

In order to fit the data we considered two fitting models. The first model addresses the scaling of the Lx with SFR and it has been used to measure the X-ray output of HMXBS. However, we allow for non-linear scaling with SFR and we introduced an intrinsic scatter parameter ($logLx = \alpha \cdot logSFR + \beta + \sigma$). The second model, was introduced by Lehmer *et al.* (2010) in order to account for the contribution of the LMXB population in star-forming galaxies and is of the form $Lx = 10^{\alpha} \cdot SFR + 10^{\beta} \cdot M_* + \sigma$, where α and β are the scaling factors accounting for the relative contribution in the X-ray output of the galaxy from the young (HMXBs) and old (LMXBs) stellar populations. Again we introduce an intrinsic scatter parameter (σ) modelled as a Gaussian random variable with mean μ=0 and standard deviation σ. The ratio of ($10^{\alpha}/10^{\beta}$) gives the sSFR above which the HMXB population dominates the emission of the galaxy. We perform the fits using combinations of the two models, the broad

Table 4.1: Maximum-likelihood fits

		Lx-SFR			Lx/SFR-sSFR	
Data	α	β	σ	α	β	σ
			Broad band (0.5-8 keV)			
Detections	$0.75^{+0.08}_{-0.02}$	40.15 ± 0.03	0.52 ± 0.02	$40.01^{+0.08}_{-0.04}$	$29.29^{+0.19}_{-0.05}$	$0.63^{+0.02}_{-0.01}$
Full	$0.85^{+0.03}_{-0.15}$	39.65 ± 0.04	0.73 ± 0.02	$39.62^{+0.06}_{-0.21}$	$29.29^{+0.05}_{-0.48}$	$0.84^{+0.03}_{-0.01}$
HMXB (Detections)	$0.72^{+0.07}_{-0.06}$	$40.15^{+0.05}_{-0.03}$	0.52 ± 0.02	-	-	-
HMXB (Full)	$0.84^{+0.08}_{-0.07}$	39.63 ± 0.04	$0.75^{+0.04}_{-0.02}$	-	-	-
			Hard band (2.0-10 keV)			
Detections	$0.67^{+0.07}_{-0.03}$	$39.91^{+0.04}_{-0.03}$	0.56 ± 0.02	$39.85^{+0.11}_{-0.12}$	$29.11^{+0.20}_{-0.21}$	$0.75^{+0.07}_{-0.02}$
Full	$0.55^{+0.05}_{-0.03}$	39.62 ± 0.03	$0.62^{+0.02}_{-0.01}$	$39.59^{+0.19}_{-0.60}$	$29.53^{+0.12}_{-0.77}$	0.81 ± 0.02
HMXB (Detections)	$0.59^{+0.06}_{-0.07}$	39.92 ± 0.07	$0.60^{+0.06}_{-0.03}$	-	-	-
HMXB (Full)	$0.53^{+0.04}_{-0.03}$	$39.59^{+0.03}_{-0.04}$	0.64 ± 0.02	-	-	-

Best-fit parameters from the Lx-SFR and Lx/SFR-sSFR maximum likelihood fit along with their 1σ uncertainties for the two models considered: (a) $logLx = \alpha \cdot logSFR + \beta + \sigma$ and (b) $Lx = 10^{\alpha} \cdot SFR + 10^{\beta} \cdot M_{*} + \sigma$. The parameter $sigma$ represents the intrinsic scatter in the correlations. The fits were performed for three samples: only the detections (Detections), the complete sample (Full), and the HMXB dominated galaxies.

and hard band, and considering only the detected galaxies at first, and then including the non-detections as well. We also perform the Lx-SFR fits for only the HMXB dominated galaxies identified based on the criterion of Kouroumpatzakis et al. (2019) (sSFR$> 6.11 \times 10^{-11} yr^{-1}$). We present the results of the maximum likelihood fits in Table 4.1.

4.4.2 Correlation with the SFR

Figs 4.6 and 4.7 present the correlation of the luminosity of the XRB population and the SFR for the broad and the hard band respectively. Examining the results of our maximum likelihood fits we see that the Lx-SFR scaling relation is always sub-linear with index α ranging form 0.53 to 0.85 with the smallest values in the hard band. The values of β (i.e. Lx-SFR scaling factor) range from 39.63 to 40.15 for the broad band, and from 39.62 to 39.91 for the hard band depending on the considered sample.

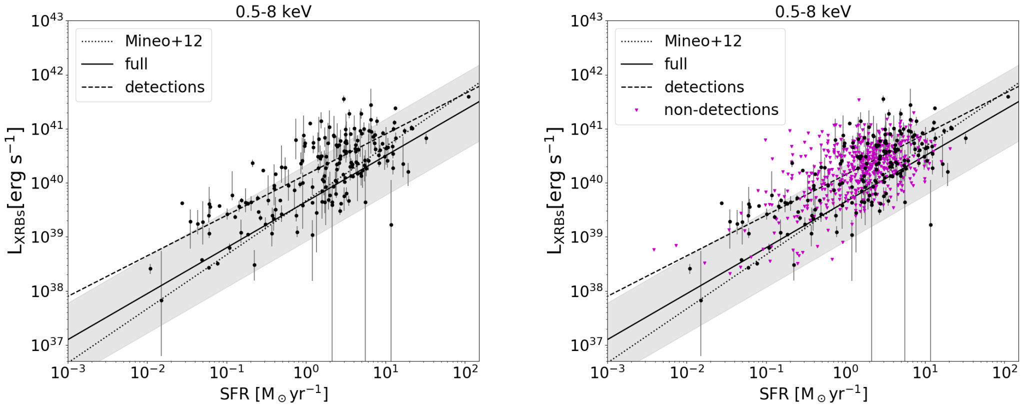

Figure 4.6: Correlation of the 0.5-8 keV luminosity of the XRB population and SFR. The left panel shows only the detections (black circles), and the right panel also includes the non-detections (magenta triangles). The solid line shows the best-fit line for the full sample, while the dashed line shows the best-fit line only for the detections. The shaded area indicates the 1σ scatter. For reference we also plot the best-fit relation of Mineo *et al.* (2012a) (dotted line).

The inclusion of non-detected galaxies results always to the smallest value of the β parameter. The scatter ranges from 0.53 to 0.75 and is increasing with the inclusion of the non-detected galaxies. We also note that the fits for the HMXB dominated galaxies are identical with the fit results for the overall sample. This indicates that either the LMXB contribution is very small and does not affect the fit results in the overall sample, or the criterion used to separate HMXB-dominated galaxies is not sufficient and there is still some contamination from LMXBs that is unaccounted for.

4.4.3 Correlation with the SFR and M$_*$

Figs 4.8 and 4.9 show the correlation for the X-ray luminosity of the XRB population with the SFR and M$_*$ of their host galaxy for the broad and hard band respectively. We see from our fit results (Table 4.1) that the parameter α, that measures the scaling of Lx with SFR, ranges from 39.59 to 40.01. The inclusion of the upper limits always makes the value of this parameter smaller. The parameter β that measures the scaling of Lx with M$_*$, ranges from 29.11 to 29.53 with the inclusion of the upper limits in this case increasing the factor for the hard band and leaving it unchanged for the broad band. The scatter of the correlation ranges from 0.63 to 0.84 with the inclusion of non-detected galaxies always increasing the scatter.

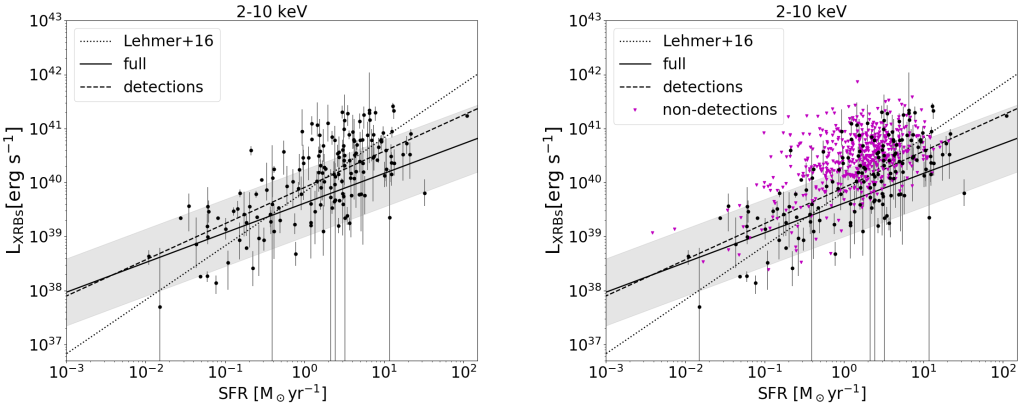

Figure 4.7: Correlation of the 2-10 keV luminosity of the XRB population and SFR. The left panel shows only the detections (black circles), and the right panel also includes the non-detections (magenta triangles). The solid line shows the best-fit line for the full sample, while the dashed line shows the best-fit line only for the detections. The shaded area indicates the 1σ scatter. For reference we also plot the best-fit relation of Lehmer *et al.* (2019) (dotted line).

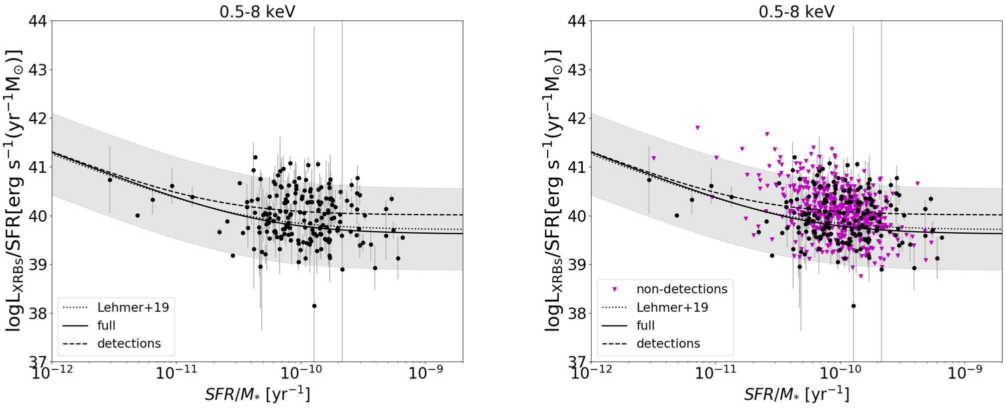

Figure 4.8: Correlation of the 0.5-8 keV luminosity of the XRB population, SFR and M_*. The left panel shows only the detections (black circles), and the right panel also includes the non-detections (magenta triangles). The solid line shows the best-fit line for the full sample, while the dashed line shows the best-fit line only for the detections. The shaded area indicates the 1σ scatter. For reference we also plot the best-fit relation of Lehmer *et al.* (2019) (dotted line).

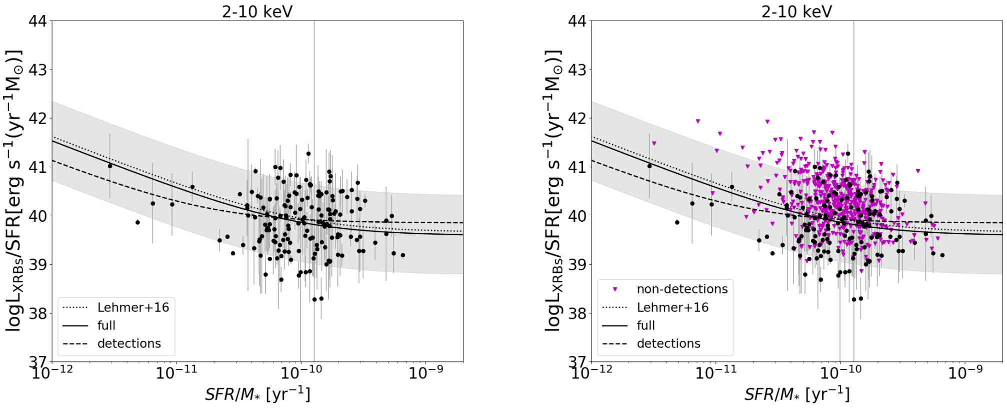

Figure 4.9: Correlation of the 2-10 keV luminosity of the XRB population, SFR and M_*. The left panel shows only the detections (black circles), and the right panel also includes the non-detections (magenta triangles). The solid line shows the best-fit line for the full sample, while the dashed line shows the best-fit line only for the detections. The shaded area indicates the 1σ scatter. For reference we also plot the best-fit relation of Lehmer *et al.* (2016) (dotted line).

4.5 DISCUSSION

4.5.1 Extent in SFR and M_*

As seen in Fig. 4.2, our sample covers 4 orders of magnitude in SFR, extending previous studies (e.g. Mineo *et al.*, 2012a) to 1 dex lower SFR. However, our sample is somewhat conservative since it lacks the highest sSFR galaxies included in other studies of the Lx-SFR scaling relations (e.g. Lehmer *et al.*, 2016; Mineo *et al.*, 2012a). This is because our sample is local (D<200 Mpc) while the majority of the most intensely star-forming galaxies are found in larger distances. In addition, our conservative approach of excluding any galaxies for which we do not have the required information to address the presence of an AGN, removes a very large fraction of the full sample. In fact the majority of the objects with such available information is from the SDSS sample, limiting our pool of objects to only a fraction of the sky. However, our sample of 650 objects is still the largest of local galaxies reflecting a very wide range of star-forming activity.

4.5.2 Lx-SFR-M$_*$ correlation

Since the HMXB luminosity traces the star-forming activity of a galaxy, one would expect that the Lx-SFR scaling relation would be linear if the X-ray luminosity was only due to the HMXB emission. Indeed this has been confirmed from scaling relations based on smaller samples of local galaxies (e.g. Mineo *et al.*, 2012a). We find however (Table 4.1), that the Lx-SFR is sub-linear for all the samples and bands considered and gets closer to linear (0.85) only for our full sample and the broad band (0.5-8 keV).

At low-SFRs (<0.1 M$_\odot$/yr; e.g. Fig. 4.6, we see that a few galaxies ($\sim$ 7) exhibit very high luminosities (above the ULX limit) and are located about 1 dex above the best-fit line. Since these galaxies are at least partly responsible for the non-linear relation, it is worth examining more closely their nature. In our sample we have included all galaxies in the local Universe that had SFR and M$_*$ measurements. This indicated that the sub-linear behaviour could be the result of LMXBs, which would dominate especially in low-SFR galaxies. Based on the revised sSFR limit of Kouroumpatzakis et al. (2019) for separating HMXBs from LMXBs dominated galaxies, we find that a few galaxies (PGC: 40562, 37692, 51210, 47368) are LMXB dominated galaxies, and in particular galaxy PGC40562 (NGC 4387) is an elliptical galaxy with the lowest sSFR ($2.9{\times}10^{-12}$ $M_\odot yr^{-1} M_\odot^{-1}$) of the galaxies in the low-SFRs. However, when we performed the fits only for the HMXB galaxies we see (Table 4.1) that the sub-linear behaviour remains and in general the fits remain unchanged. This means that either there is still contamination from the LMXB population that we are not removing with this criterion, or the LMXB population is not large enough to affect significantly our results, and/or there is an additional source of emission for the low-SFR galaxies.

One explanation could be that those galaxies, host ULXs that dominate the emission of the entire galaxy. Indeed that is the case for two of these galaxies PGC51210 (NGC 5585; Swartz *et al.*, 2011) and PGC47368 (NGC 5204 X-1; Mukherjee *et al.*, 2015). For the rest of the galaxies, which also among the brightest in the region (PGC: 28990, 1817480, and 55616), we don't have any information on their ULX content, but that the fact that they are HMXB dominated galaxies with luminosities that exceed the $10^{39} ergs^{-1}$ mark, in both full and hard bands, supports the ULX scenario. Another reason which could explain the possible existence of so many ULX-hosting galaxies in the low-SFR in our sample, could be partly observational bias. Meaning *XMM-Newton* galaxies are proposed to be observed on the basis of either presence of ULXs or expected enhanced X-ray emission.

To test this issue, while accounting for both the population of HMXBs and LMXBs, we examine the Lx/SFR-sSFR correlation. The sSFR provides a metric of the ratio between young and old stellar populations. This ratio also correlates with the relative contribution of HMXBs, and LMXBs, in the total luminosity of a galaxy. Following Section 4.4.1 we formulate the total X-ray luminosity as the sum of these two sub-components which correlate with SFR and M_* respectively; $Lx = \alpha \cdot SFR + \beta \cdot M_*$. Then the relative contribution of each sub-component is $L(HMXB)/L(LMXB) = (\alpha/\beta) \cdot SFR/M_* = (\alpha/\beta) \cdot sSFR$. So the sSFR can be used as a proxy for the relative contribution of the HMXB and LMXB populations in the integrated X-ray emission of a galaxy, if the X-ray output efficiency (parameters α and β) is known. Therefore the sSFR has been considered more accurate to represent correlations of star-forming galaxies that will have contributions of both populations (Lehmer *et al.*, 2010). However our results show (Table 4.1) that the scatter of this correlation is larger than the Lx-SFR correlation. If the contribution of the LMXB population in the Lx-SFR correlation was the only reason to expect variations then those variations would be even smaller when we account for the LMXB population emission in the Lx/SFR-sSFR. However the fact that we have similar and larger scatter in the Lx/SFR-sSFR indicates that other factors come into play, like the age and/or metallicity of the stellar populations.

4.5.3 Comparison with other works

In our comparisons we consider the full sample since it is less biased than the detection sample. With the exception of the sub-linearity observed in the Lx-SFR, there is in general very good agreement with previous works on local galaxies. Mineo *et al.* (2012a) found a value of $\beta = 39.67 \pm 0.06$ $(ergs^{-1}(M_{\odot}yr^{-1})^{-1})$ in the broad band which is in very good agreement with our results (see Table 4.1; Fig.4.6). Lehmer *et al.* (2016) for the lowest redshift bin in their sample and the hard band find $\beta = 39.83 \pm 0.08$ $(ergs^{-1}(M_{\odot}yr^{-1})^{-1})$ which is again within the range of our results. Our detection sample has a bit larger value of the parameter β compared to the works of (see Table 4.1; Fig.4.7).

For the Lx/SFR-sSFR correlation, our results agree very well with previous results from smaller samples of local galaxies. For example, Lehmer *et al.* (2019) using the soft band find $\alpha = 39.71^{+0.14}_{-0.09}$ and $\beta = 29.25^{+0.07}_{-0.06}$, and Lehmer *et al.* (2016), for the lowest redshift bin in their sample, and the hard band (2-10 keV) find $\alpha = 39.66 \pm 0.16$ and $\beta = 29.62^{+0.33}_{-0.45}$. Both results agree well with our results in the corresponding energy bands. For the detection sample the α parameter is always larger than the comparison works, while β always agrees within the errors (see Table 4.1; Figs 4.8 and 4.9).

4.5.4 Intrinsic scatter in the correlations

An important question regarding the scaling relations of the X-ray luminosity versus the SFR and M_* is whether they are universal. For example could they be used to correct for the XRB component in studies of AGN or thermal gas for distant galaxies? Recent theoretical as well as observational work has shown that the scatter in this correlations is larger than expected from just the errors in the quantities involved and that the correlations are far from being universal. For example Fragos *et al.* (2013) find, using population synthesis models variations in the X-ray output of a stellar population depending on its age and metallicity (Fig 1.6).

Systematic studies of the formation rate and X-ray luminosity of XRBs as function of age show evolution consistent with the model prediction (Antoniou *et al.*, 2019; Lehmer *et al.*, 2019). These kind of variations have been seen also observationally for targeted samples of local galaxies with low metallicities (Basu-Zych *et al.*, 2013a; Brorby *et al.*, 2014; Douna *et al.*, 2015) or at early type galaxies covering a range of ages (Kim & Fabbiano, 2010; Lehmer *et al.*, 2014). Studies of local galaxies at sub-galactic scales (Anastasopoulou *et al.*, 2019; Kouroumpatzakis et al., 2019), have shown that variations in the scaling relations are possibly driven by differences ages of the stellar populations.

Indeed in this study we observe about 2 times larger scatter (Table 4.1) than has been seen in smaller samples of galaxies ($\sigma \sim 0.3$). Since our sample contains all star-forming galaxies, observed in the local Universe without any restriction on metallicity, or sSFR, we expect to have larger variations reflecting differences in the metallicity/and or ages of the stellar populations in comparison to the scatter observed for much smaller samples of galaxies. Part of this scatter maybe due to the fact that a single very bright source (i.e. ULX) outshines the emission of the galaxy like in the case of the low-SFR galaxies we have discussed in Section 4.5.2. We also find that the scatter increases when we include the non-detections. This holds for both energy bands and for both types of correlations (Lx-SFR and Lx/SFR-sSFR). Moreover the scatter of the Lx/SFR-sSFR correlation between the full and hard band agree while the Lx-SFR correlation is tighter for the hard band. That could be a sign of additional scatter introduced for the broad band because of the thermal-gas contribution in the soft emission of those galaxies.

4.6 SUMMARY

In this work we present the most extensive X-ray survey of nearby galaxies. We have analysed in total 2645 *XMM-Newton* observations including 3041 galaxies within a volume of 200 Mpc. We have performed photometric analysis for all of the galaxies and performed spectroscopic analysis for the 1713 galaxies that allowed for spectral fitting. Based on our spectral fits we identify in our sample 330 AGN, where 280 were not identified so far by some other method. Overall, we classify 650 galaxies as non-AGN out of those that have physical parameter information (SFR and M_*) from the `HECATE` catalogue. These star-forming galaxies cover 4 orders of magnitude in SFR and M_* in the local Universe.

We performed maximum likelihood fits for our star-forming sample (650 galaxies). In our sample we include non-detected galaxies yielding a less biased sample. We measure the correlations of the Lx-SFR and Lx/SFR-sSFR and find in the broad band:
$logLx(0.5-8\ keV) = 0.85 \cdot logSFR + 39.65 + \sigma(0.73)$
$Lx(0.5-8\ keV) = 10^{39.62} \cdot SFR + 10^{29.29} \cdot M_* + \sigma(0.84)$
and in the hard band:
$logLx(2-10\ keV) = 0.55 \cdot logSFR + 39.62 + \sigma(0.62)$
$Lx(2-10\ keV) = 10^{39.59} \cdot SFR + 10^{29.53} \cdot M_* + \sigma(0.81)$
Where $\sigma(x)$ denotes a Gaussian distribution with mean $\mu = 0$ and $\sigma = x$.

We find that the Lx-SFR scaling relations show a sub-linear behaviour, which could be explained by additional X-ray emission in the low-SFR, from ULX-galaxies, and/or LMXB populations. In general our results agree well with previous works based on smaller samples of local galaxies but with much higher intrinsic scatter. We attribute this increase of the scatter to the dramatic increase in the number of galaxies we observe, which accounts for all different conditions of star forming activity and metal content in the local Universe yielding a far more representative sample of local galaxies.

4.7 Tables

Table 4.2: Master table of star-forming galaxies

PGC (1)	RA deg (2)	DEC deg (3)	R1 arcmin (4)	R2 arcmin (5)	PA deg (6)	D Mpc (7)	SFR $M_\odot/yr$ (8)	M $10^{10}M_\odot$ (9)
1014	3.723	-39.197	14.927	1.524	100.95	2.064	0.186	0.237
1142	4.358	-0.978	0.427	0.216	143.7	73.165	2.127	3.145
2365	9.828	0.892	0.469	0.362	34.57	56.599	0.688	1.164
2388	9.895	0.86	0.853	0.659	146.01	52.633	2.665	4.983
2758	11.786	-20.76	9.839	2.773	166.8	3.656	0.081	0.251
3238	13.723	-37.684	9.704	6.531	114.35	1.963	0.049	0.19
3781	15.912	-0.491	0.51	0.14	165.93	69.87	0.326	0.409
4195	17.659	-0.278	0.589	0.177	176.16	72.589	1.64	2.43
4371	18.258	-0.115	0.242	0.214	42.73	150.154	1.242	1.109
4420	18.443	0.306	0.363	0.218	90.84	174.238	8.394	10.01
4465	18.607	0.536	0.332	0.264	158.31	163.133	5.279	6.572
4616	19.223	0.153	0.294	0.165	111.6	76.809	0.441	0.334
4734	19.769	-0.139	0.731	0.106	65.68	79.799	0.691	0.714
4806	20.032	0.077	0.34	0.142	71.7	75.262	2.193	1.885
4916	20.339	0.09	0.499	0.244	100.75	46.022	0.832	0.426
4979	20.538	0.946	1.503	0.476	59.93	21.913	0.487	0.657
5127	20.978	0.282	0.334	0.147	138.6	73.847	1.788	0.875
5189	21.159	-0.063	0.495	0.127	54.62	113.018	2.478	4.263
5193	21.145	3.794	2.046	0.803	130.0	30.454	12.35	7.296
5238	21.262	0.444	0.405	0.231	103.86	117.99	8.642	10.7
6029	24.405	0.04	0.367	0.124	34.52	66.749	0.567	0.317
6169	25.031	-9.272	0.535	0.197	21.71	102.922	3.229	4.07
6630	27.127	-0.063	0.163	0.122	175.15	72.255	0.304	0.185
6972	28.225	36.053	0.521	0.336	28.5	35.645	1.205	1.016
8837	34.749	0.33	0.344	0.177	95.19	121.212	10.98	6.701
9623	37.935	-0.946	0.253	0.117	41.77	81.137	2.952	2.62
9677	38.159	0.594	0.184	0.117	85.94	90.434	0.347	0.689
9680	38.164	0.617	0.303	0.208	69.02	84.692	3.645	3.2
11563	46.052	-1.193	0.527	0.24	136.68	52.354	0.844	1.364
11631	46.451	-0.177	0.275	0.247	164.35	80.194	3.614	3.562
11650	46.56	-0.344	0.206	0.133	169.2	116.785	2.139	3.864
12286	49.566	-66.498	5.533	4.571	26.85	4.234	0.286	0.296
12418	49.929	0.565	0.443	0.176	164.1	101.373	4.567	2.482
12486	50.074	0.524	0.199	0.095	133.4	101.395	0.853	1.093
12785	51.298	-6.181	0.477	0.319	41.31	133.045	32.29	22.17
12803	51.381	-6.129	0.274	0.182	94.61	141.112	12.7	6.242

14236	59.91	-67.637	1.828	0.734	123.48	15.472	2.919	1.492
15345	67.705	64.848	1.954	1.079	119.0	3.208	0.222	0.13
16282	73.556	-53.361	0.935	0.719	53.12	5.461	0.015	0.032
21396	114.214	65.602	9.976	5.035	126.33	3.173	0.252	0.592
21838	117.039	43.591	0.316	0.185	132.95	129.806	2.676	5.063
21978	117.766	17.963	0.371	0.281	71.86	117.166	1.985	1.0
22645	121.067	30.183	0.33	0.107	55.73	59.508	1.064	0.634
22766	121.678	39.09	0.57	0.419	158.29	142.561	6.626	12.08
22805	121.853	39.194	0.697	0.619	86.12	56.041	3.171	4.184
23146	123.839	21.558	0.592	0.116	54.14	67.858	1.326	1.379
23359	124.912	21.065	0.213	0.123	171.33	59.012	0.211	0.184
23504	125.722	3.571	0.614	0.487	64.55	39.302	0.712	1.425
23850	127.5	52.697	0.393	0.346	15.94	61.289	2.428	3.676
24169	129.031	25.113	0.323	0.137	171.93	99.099	3.718	1.902
24660	131.668	29.867	0.184	0.148	159.76	82.712	0.691	0.776
25046	133.778	58.537	0.335	0.113	176.55	159.72	3.775	3.074
25056	133.861	20.054	0.239	0.212	85.2	126.496	2.276	1.905
25180	134.474	17.091	0.349	0.193	109.65	85.273	3.554	1.398
25363	135.438	0.522	0.391	0.14	134.49	74.585	0.545	0.591
25447	135.934	55.597	0.299	0.158	51.18	154.106	7.868	4.229
25470	136.133	13.161	0.315	0.133	164.08	115.639	5.736	3.591
25506	136.305	-0.497	0.538	0.086	38.53	112.609	5.41	3.946
26471	140.314	3.151	0.597	0.157	148.02	55.719	1.18	0.552
26495	140.44	39.525	0.75	0.135	104.44	50.87	0.528	0.7
26510	140.498	3.379	0.42	0.166	149.97	114.489	2.967	1.961
26572	140.785	50.835	0.548	0.444	26.67	107.525	1.985	0.843
26628	140.964	23.076	0.284	0.19	85.75	133.222	6.0	1.106
26635	141.01	23.075	0.321	0.268	160.46	132.2	3.866	3.929
26897	142.136	50.794	0.542	0.259	166.99	105.405	2.381	5.062
27077	143.042	21.502	5.97	2.642	21.97	8.966	3.043	5.448
27505	144.705	41.689	0.284	0.09	5.58	172.623	4.947	3.471
27658	145.296	39.005	0.187	0.151	60.11	184.8	4.262	2.981
27731	145.545	38.71	0.187	0.157	152.81	163.851	2.147	1.914
27844	145.944	48.291	0.44	0.259	102.46	105.254	1.567	1.365
27988	146.438	17.799	0.191	0.154	78.01	117.987	4.908	1.853
28655	148.968	69.68	5.495	2.553	65.75	3.487	8.195	2.913
28682	149.084	27.228	0.439	0.37	56.71	19.647	0.749	0.48
28848	149.795	69.258	0.321	0.18	53.47	21.527	0.007	0.015
28990	150.31	55.718	0.294	0.211	99.76	22.184	0.06	0.093
29233	151.199	5.369	0.379	0.109	34.84	56.653	0.11	0.232
29363	151.62	12.871	0.361	0.27	158.6	126.297	3.02	1.786
29711	153.035	46.294	0.594	0.188	152.77	103.814	4.594	4.409
30087	154.571	41.424	3.698	3.589	0.0	14.276	1.587	4.62
30109	154.651	59.669	0.253	0.142	106.8	182.828	20.64	7.818
30327	155.447	12.919	0.343	0.173	35.93	118.777	2.227	3.902

30663	156.629	12.533	0.335	0.172	167.89	137.798	7.332	9.194
30948	157.506	50.847	0.34	0.242	69.83	182.686	7.152	3.83
31707	159.894	-0.253	0.258	0.156	23.08	76.872	0.597	0.39
31839	160.338	6.279	0.261	0.172	52.74	140.18	2.61	1.537
31856	160.435	40.041	0.366	0.29	69.96	177.799	13.17	17.84
31991	160.963	21.468	0.34	0.268	58.91	104.724	1.517	2.327
32215	161.769	37.561	0.306	0.264	134.22	99.611	0.843	0.679
32341	162.219	50.037	0.405	0.179	166.45	100.592	4.44	3.592
32434	162.479	32.991	1.549	0.635	97.47	21.777	2.215	1.034
32464	162.565	32.768	0.394	0.155	120.69	25.452	0.264	0.149
32543	162.836	32.766	1.009	0.424	177.38	15.832	0.144	0.225
32584	162.943	32.9	1.244	0.39	111.0	27.29	3.454	3.164
32706	163.41	34.033	0.448	0.217	72.5	28.788	0.186	0.211
32827	163.869	57.906	0.291	0.213	130.62	101.522	1.953	1.133
32907	164.212	6.906	0.475	0.248	61.01	93.043	1.512	1.036
33428	165.992	41.066	0.261	0.188	124.82	102.523	1.24	1.744
33437	165.991	38.238	0.256	0.132	135.53	127.999	7.243	3.508
33500	166.289	38.069	0.376	0.253	126.76	119.927	4.16	5.059
33571	166.519	43.331	0.553	0.181	110.3	47.69	1.0	1.307
33887	167.538	28.612	0.227	0.163	68.78	129.812	2.718	2.235
33953	167.735	61.347	0.603	0.124	9.37	27.343	0.26	0.361
34257	168.654	12.818	2.344	0.925	90.62	8.825	0.769	1.479
34462	169.318	29.336	0.16	0.127	128.53	102.795	1.635	0.773
34612	169.733	13.093	3.819	0.984	173.33	12.073	0.468	9.608
34661	169.94	57.846	0.305	0.14	51.01	183.11	10.3	6.252
34667	169.927	54.027	0.403	0.1	142.83	144.715	5.127	5.911
34692	170.052	67.242	0.624	0.253	8.6	21.912	0.37	0.389
34767	170.262	53.17	1.858	1.542	118.0	15.483	1.843	2.698
34804	170.365	24.405	0.301	0.145	167.68	98.335	3.031	1.954
34896	170.607	47.106	0.288	0.183	159.06	105.432	1.66	1.159
34949	170.774	5.578	0.271	0.13	67.89	153.764	2.895	2.91
34963	170.808	46.998	0.406	0.193	168.17	105.063	1.775	3.323
35321	172.14	58.563	1.205	0.94	40.82	47.224	110.6	16.79
35544	172.909	-3.648	0.361	0.195	149.44	184.326	4.564	8.507
35595	173.081	55.923	0.46	0.103	175.45	90.582	2.826	2.083
35609	173.137	52.939	0.221	0.143	178.57	113.458	1.082	1.476
35631	173.195	52.941	0.494	0.087	173.22	148.496	4.343	24.96
35678	173.348	55.072	0.195	0.143	167.45	36.252	0.116	0.135
35762	173.621	48.951	0.288	0.184	63.11	119.59	1.559	0.665
35838	173.902	15.975	0.189	0.115	160.44	72.735	0.413	0.344
35906	174.122	21.433	0.186	0.162	126.37	153.587	7.331	3.549
36181	174.985	16.955	0.298	0.174	13.83	46.023	0.647	0.479
36198	175.055	-0.412	0.177	0.141	84.26	93.029	1.231	0.624
36308	175.52	10.384	0.343	0.262	25.34	85.943	3.105	2.997
36349	175.602	20.119	0.469	0.281	109.45	89.596	9.12	5.639

36371	175.688	20.032	0.47	0.212	114.58	71.612	2.263	3.371
36388	175.759	19.65	0.531	0.248	110.98	100.367	1.846	4.539
36406	175.805	20.005	0.311	0.181	102.51	100.94	4.435	0.919
36477	175.996	20.077	0.395	0.339	67.25	96.554	4.053	7.2
36671	176.442	3.03	0.632	0.138	179.37	83.033	3.618	1.968
37013	177.635	55.058	0.351	0.181	45.88	78.807	1.611	2.922
37173	178.071	4.111	0.21	0.131	25.02	161.348	10.08	3.219
37180	178.098	3.974	0.22	0.199	31.16	96.125	0.897	1.195
37282	178.417	43.461	0.762	0.235	33.14	84.653	11.24	9.53
37410	178.811	52.315	0.256	0.177	172.77	146.435	0.787	1.007
37466	178.938	55.321	1.836	0.493	117.41	20.582	0.403	1.041
37692	179.642	42.734	1.067	0.853	158.89	20.032	0.043	0.466
37747	179.812	42.567	0.289	0.217	90.82	127.688	4.971	3.123
37976	180.513	29.848	0.541	0.288	9.74	46.04	1.227	0.723
38138	180.976	1.891	0.497	0.144	131.98	103.177	4.016	3.769
38163	181.04	20.185	0.578	0.086	40.2	142.561	10.85	8.827
38250	181.246	58.107	0.522	0.363	73.05	38.859	0.118	0.129
38406	181.657	65.064	0.321	0.158	124.63	185.217	9.391	5.316
38507	181.97	43.111	0.347	0.192	147.57	13.848	0.017	0.013
38508	181.986	65.114	0.258	0.231	65.47	24.385	0.053	0.567
38569	182.192	47.223	0.242	0.218	76.81	185.325	4.899	6.06
38672	182.453	47.168	0.387	0.22	131.3	137.315	6.985	11.29
38885	183.049	13.246	0.621	0.335	161.4	30.479	0.442	1.035
39152	183.769	14.029	1.109	0.202	120.22	40.788	0.911	1.624
39225	183.914	36.326	3.396	2.642	0.0	2.921	0.076	0.103
39280	184.036	-3.57	0.428	0.376	109.33	70.156	1.401	0.985
39422	184.373	37.808	8.109	3.622	44.77	4.323	0.059	0.268
39578	184.707	14.417	2.518	2.371	0.0	14.038	4.862	5.868
39655	184.842	5.91	0.367	0.203	164.32	18.061	0.112	0.074
39783	185.065	33.661	0.348	0.234	71.96	93.906	5.31	5.044
39840	185.159	46.292	0.851	0.674	137.69	20.853	0.225	0.232
39922	185.319	4.596	0.802	0.555	9.82	34.356	0.203	3.138
39950	185.387	14.606	1.268	0.698	136.55	19.618	2.679	2.782
40001	185.478	4.474	3.443	3.281	0.0	12.78	3.656	5.263
40157	185.736	2.747	0.577	0.182	102.35	26.901	0.004	0.12
40273	185.952	7.187	0.818	0.416	18.4	18.28	0.218	0.221
40307	186.009	5.313	0.308	0.135	19.0	100.071	2.913	1.377
40425	186.201	18.195	0.547	0.408	133.78	15.755	0.011	0.081
40461	186.273	5.329	0.303	0.18	127.46	29.665	0.092	0.216
40562	186.424	12.81	0.789	0.468	138.12	17.644	0.035	1.195
40644	186.532	13.113	1.758	0.502	88.94	16.154	1.191	1.853
40705	186.634	12.611	1.042	0.729	53.07	15.928	0.243	0.539
40809	186.799	9.42	1.52	0.787	95.25	15.974	0.39	1.037
40827	186.821	30.623	0.305	0.171	44.41	127.126	2.404	2.708
40962	187.028	13.912	0.491	0.293	89.08	103.676	5.153	3.087

41107	187.249	7.851	0.489	0.26	164.14	104.676	3.175	6.165
41189	187.408	7.824	0.641	0.432	1.15	15.544	0.308	0.38
41320	187.616	14.16	0.344	0.209	56.03	59.156	1.325	0.918
41566	188.093	0.012	0.262	0.149	89.43	181.412	19.15	4.839
41639	188.215	20.184	0.555	0.127	98.12	46.679	0.244	0.255
41729	188.415	9.175	1.754	0.453	34.49	15.868	0.287	0.533
41763	188.486	15.355	0.753	0.551	151.01	15.09	0.109	0.235
41823	188.613	2.188	3.54	1.273	120.71	14.916	3.077	3.858
41857	188.681	9.005	0.277	0.209	136.09	176.967	21.05	10.67
41912	188.802	26.533	0.433	0.095	155.33	91.098	0.833	0.788
41936	188.863	12.75	0.439	0.394	68.05	17.04	0.035	0.158
41950	188.911	-0.206	0.484	0.099	42.04	97.677	1.659	1.933
41967	188.926	-0.215	0.196	0.124	89.44	97.707	10.51	3.519
42362	189.89	47.623	0.498	0.216	76.56	101.134	6.471	7.278
42408	189.997	61.609	2.937	1.145	122.25	5.623	0.247	0.437
42561	190.344	61.712	0.366	0.195	41.64	160.554	6.825	7.562
42637	190.533	32.542	7.227	1.099	85.65	7.374	2.373	2.482
42699	190.656	14.357	0.885	0.373	32.66	22.594	0.679	0.463
42727	190.698	33.288	0.597	0.116	58.83	99.447	3.081	4.125
42816	190.886	11.582	1.374	1.18	138.67	17.34	1.344	3.191
42999	191.383	-0.536	0.794	0.459	3.12	16.479	0.152	0.28
43270	192.133	-3.469	0.303	0.186	95.06	102.583	1.12	0.98
43511	192.765	27.37	0.314	0.198	29.9	21.979	0.127	0.112
43843	193.467	31.107	0.364	0.179	24.7	125.044	3.671	2.439
44418	194.542	24.349	0.205	0.149	140.04	98.55	2.399	1.344
44536	194.758	34.861	1.905	0.724	17.99	9.893	0.101	0.034
44586	194.846	28.489	0.218	0.146	172.57	101.519	0.895	0.792
44646	194.918	34.814	0.31	0.126	179.59	143.063	2.687	2.476
44968	195.533	27.648	0.313	0.22	86.67	100.403	3.841	3.562
45594	197.286	53.944	0.372	0.243	148.23	38.337	0.357	0.363
45659	197.452	11.651	0.45	0.261	30.51	85.901	2.02	1.277
45700	197.584	32.483	0.661	0.138	12.59	67.225	1.714	1.452
46367	199.63	55.495	0.27	0.186	105.1	113.287	0.207	0.434
46616	200.305	33.079	0.257	0.162	14.89	153.972	2.267	1.589
46736	200.713	31.826	0.426	0.208	146.08	76.0	1.176	0.876
46851	201.066	31.345	0.69	0.158	5.12	68.699	1.861	2.349
46859	201.101	13.938	0.6	0.228	173.78	98.677	2.047	4.671
46963	201.398	31.93	0.243	0.185	167.15	155.303	4.594	2.715
47333	202.338	33.824	0.31	0.23	57.28	106.887	0.515	0.319
47337	202.351	11.797	0.43	0.115	134.2	92.96	2.131	4.389
47357	202.358	11.91	0.453	0.243	76.88	94.394	2.063	1.414
47368	202.402	58.42	2.249	1.412	5.46	4.776	0.027	0.063
47503	202.715	-1.779	0.305	0.15	11.53	148.225	11.78	9.18
47555	202.882	-2.019	0.474	0.15	125.15	146.07	4.966	3.491
47569	202.952	-1.894	0.339	0.148	56.98	90.139	4.232	2.971

48240	204.684	4.459	0.302	0.226	10.57	101.229	1.755	1.132
48276	204.823	28.035	0.282	0.119	149.0	152.284	7.713	4.364
48673	206.066	57.933	0.286	0.247	2.16	144.074	2.608	3.412
49221	207.973	64.373	0.325	0.106	179.04	29.787	0.185	0.034
49399	208.526	5.356	0.426	0.315	178.25	76.336	0.423	1.073
49468	208.744	5.334	1.416	0.333	15.9	25.68	0.598	1.621
49921	210.326	2.997	0.179	0.113	31.06	143.176	7.471	3.777
50063	210.802	54.349	11.994	11.534	0.0	8.945	5.472	8.786
50505	212.291	53.821	0.432	0.169	174.88	33.568	0.244	0.215
50572	212.516	17.552	0.275	0.174	47.84	79.045	0.437	0.31
50581	212.513	54.218	0.887	0.185	37.71	31.358	0.245	0.351
50584	212.529	17.616	0.377	0.306	33.73	80.321	1.672	0.311
50792	213.351	43.845	0.205	0.13	140.42	146.622	4.169	2.463
50810	213.417	43.867	0.378	0.294	145.05	146.76	8.501	13.94
50881	213.681	-0.282	0.305	0.163	6.52	157.075	9.714	5.655
50886	213.683	43.98	0.184	0.149	17.8	147.195	1.805	0.862
50944	213.91	36.375	0.243	0.215	50.23	68.249	0.96	1.082
50952	213.937	36.178	0.339	0.222	7.88	105.22	1.487	2.136
50957	213.933	54.043	0.303	0.257	165.45	167.724	6.052	8.17
51210	214.951	56.729	2.133	1.309	33.32	7.665	0.06	0.164
51319	215.469	39.979	0.499	0.411	40.25	74.711	1.019	3.589
51353	215.615	0.059	0.311	0.233	31.59	132.35	17.29	5.9
51460	216.099	26.69	0.367	0.269	27.81	152.062	4.052	5.763
51485	216.25	23.125	0.145	0.145	0.0	72.588	1.419	1.026
51643	216.962	25.838	0.513	0.253	95.73	64.033	0.565	2.804
51667	217.056	25.947	0.301	0.219	134.24	59.23	1.699	3.471
51791	217.442	-0.152	0.453	0.101	114.97	124.842	7.743	5.502
51793	217.461	13.8	0.43	0.121	147.2	77.268	0.633	0.951
52112	218.711	3.645	0.284	0.242	110.34	119.25	2.957	3.58
52318	219.577	64.172	0.28	0.141	59.31	151.824	21.58	8.608
52633	221.057	2.135	0.207	0.17	109.86	114.932	3.997	1.843
52939	222.372	9.079	0.373	0.221	102.21	164.418	7.187	4.403
53013	222.729	4.949	0.231	0.186	136.98	60.226	0.616	0.648
53231	223.427	3.583	0.849	0.528	123.03	25.529	0.413	0.687
53245	223.464	3.485	0.392	0.156	121.49	114.079	4.952	4.445
53559	224.898	49.327	0.358	0.167	156.89	114.596	3.502	3.175
53561	224.941	49.504	0.64	0.159	115.63	113.955	4.749	6.524
53683	225.515	1.841	0.521	0.47	139.16	20.117	0.152	0.128
53742	225.867	10.6	0.259	0.19	28.06	152.757	9.772	6.079
54032	226.997	1.232	0.324	0.271	99.95	145.222	12.49	11.72
54189	227.771	5.52	0.322	0.22	174.12	144.969	1.882	1.579
54219	227.88	5.246	0.234	0.171	165.53	159.95	6.169	3.243
54386	228.55	13.894	0.308	0.198	23.68	87.498	0.482	0.503
54470	228.973	56.329	5.649	0.877	155.58	16.596	2.738	9.608
54479	229.019	6.848	0.373	0.253	156.64	152.342	10.09	8.022

54871	230.593	8.645	0.297	0.127	53.74	149.412	0.778	3.517
54903	230.733	8.521	0.228	0.153	19.05	87.498	1.591	0.822
54942	230.835	8.723	0.235	0.18	87.2	150.159	6.499	4.299
55307	232.9	7.35	0.313	0.081	137.76	138.552	1.895	2.153
55599	234.173	54.522	0.19	0.144	168.98	161.152	1.013	1.587
55616	234.267	55.264	0.14	0.12	142.07	15.471	0.062	0.022
55696	234.761	5.841	0.292	0.188	155.07	170.159	12.27	9.211
55717	234.887	17.432	0.288	0.216	120.81	123.17	4.524	3.571
55732	234.92	17.459	0.268	0.091	94.31	122.816	0.711	0.985
55902	236.01	7.847	0.177	0.077	103.29	154.706	1.469	1.637
55929	236.217	36.479	0.229	0.179	111.81	50.515	0.079	0.119
55976	236.441	2.41	0.314	0.122	79.22	58.77	3.024	2.248
55992	236.556	2.453	0.321	0.158	52.97	56.362	0.143	0.246
56370	238.753	11.074	0.294	0.14	113.45	226.986	8.05	12.32
56387	238.868	34.178	0.316	0.214	37.43	132.787	2.648	2.76
56536	239.633	27.473	0.365	0.182	55.35	129.743	1.707	1.857
56558	239.717	26.136	0.345	0.281	15.46	137.71	3.85	2.845
56907	241.038	42.889	0.621	0.084	59.57	151.955	6.274	9.274
57924	245.453	-2.283	2.223	0.889	58.97	20.947	1.203	2.55
58090	246.359	39.508	0.173	0.153	175.46	134.687	2.707	1.637
58126	246.638	38.804	0.229	0.155	110.32	145.024	1.153	1.54
58130	246.652	35.045	0.227	0.198	77.96	143.464	4.187	2.843
58132	246.655	39.128	0.454	0.177	44.18	148.206	10.68	8.278
58152	246.734	39.037	0.344	0.219	63.78	150.197	6.515	4.092
58173	246.814	38.954	0.247	0.146	139.55	120.02	1.319	1.072
58189	246.893	39.101	0.264	0.137	61.4	144.729	2.59	1.875
58221	247.012	41.142	0.193	0.127	153.64	123.078	1.362	0.876
58299	247.222	39.56	0.215	0.173	176.0	123.499	0.488	1.814
58377	247.592	40.924	0.344	0.297	102.03	130.052	3.35	3.358
58379	247.567	40.66	0.483	0.086	175.61	120.02	1.605	3.948
58715	250.01	43.694	0.324	0.284	32.88	146.289	2.446	3.069
58813	250.599	25.087	0.815	0.265	162.59	99.524	12.45	3.942
59498	255.764	61.044	0.661	0.317	102.45	57.345	1.015	2.109
59714	257.384	34.427	0.33	0.285	151.94	103.857	3.475	4.515
59740	257.917	59.996	0.409	0.321	16.65	72.666	1.482	1.927
60162	260.671	60.011	0.368	0.217	28.04	81.359	1.077	0.669
61742	274.943	74.568	1.659	0.815	37.17	19.552	3.221	3.259
65001	308.719	60.154	5.701	5.42	0.0	6.707	3.895	5.635
67045	324.12	-54.558	4.074	0.815	128.2	8.61	0.375	0.708
71031	349.728	-42.239	1.513	0.614	33.74	26.194	3.769	5.231
71066	349.838	-42.257	2.404	0.789	55.24	22.334	2.414	3.852
73823	18.548	0.164	0.238	0.134	100.88	181.931	2.932	3.327
73836	18.681	0.09	0.175	0.121	8.06	181.583	2.526	3.127
73854	18.784	0.227	0.229	0.156	87.46	178.232	7.09	3.161
73858	18.787	0.297	0.2	0.121	33.01	184.009	0.962	2.032

73862	18.808	0.289	0.179	0.107	65.76	184.262	2.698	1.579
73875	18.861	0.205	0.161	0.117	115.47	176.741	2.551	1.976
73878	18.87	0.515	0.188	0.161	95.33	179.209	3.245	3.149
82353	139.003	44.352	0.196	0.148	100.48	135.101	1.332	0.784
82589	152.772	46.636	0.189	0.162	132.33	104.946	0.457	0.442
83462	167.625	28.699	0.26	0.158	144.54	143.804	1.803	3.243
84609	230.822	8.813	0.309	0.139	61.88	152.993	2.245	2.118
86372	183.668	36.405	0.166	0.102	161.83	176.391	3.377	1.452
86872	134.063	37.756	0.198	0.132	113.57	173.38	3.232	3.994
87110	154.502	37.207	0.169	0.144	79.51	183.389	8.275	2.856
91254	196.533	26.322	0.313	0.054	164.15	149.225	2.883	2.779
94158	169.091	29.44	0.232	0.175	61.35	121.59	2.442	2.392
97397	173.346	49.038	0.342	0.127	37.24	132.548	4.871	2.256
100271	159.826	-0.229	0.279	0.148	170.83	77.167	0.384	0.548
101487	197.769	30.483	0.188	0.106	143.29	91.376	0.454	0.61
104424	180.341	-3.367	0.232	0.115	61.85	80.737	1.338	1.143
104426	180.38	-3.617	0.22	0.105	8.02	107.749	1.179	0.488
139806	185.51	10.621	0.235	0.201	124.47	105.501	1.545	1.375
140771	259.833	57.9	0.323	0.107	5.26	122.952	4.216	4.302
140989	329.524	-7.845	0.45	0.173	53.52	72.04	1.711	2.191
142890	181.431	31.189	0.244	0.142	9.35	120.943	2.006	1.558
144745	35.08	-8.08	0.269	0.141	52.06	158.371	5.702	7.523
153343	134.677	0.191	0.272	0.147	130.22	161.236	2.785	4.07
160382	225.162	1.697	0.252	0.13	84.52	119.808	1.642	2.194
165113	185.742	10.478	0.221	0.184	41.54	107.315	0.965	2.434
165662	229.162	-0.041	0.2	0.174	117.55	153.769	13.32	3.486
166830	19.508	0.315	0.264	0.147	41.21	162.212	2.554	2.327
166849	164.774	1.604	0.166	0.103	111.38	184.865	1.723	2.795
169478	187.833	14.195	0.171	0.136	56.16	84.169	0.169	0.392
169870	174.19	21.71	0.221	0.186	42.12	105.438	1.444	1.021
170401	346.377	-8.58	0.412	0.19	127.2	135.157	9.86	8.716
173666	19.094	-0.209	0.208	0.106	129.38	169.06	4.108	3.185
184842	224.533	-1.312	0.279	0.131	150.18	29.91	0.048	0.099
200253	148.293	7.874	0.226	0.132	162.75	162.411	13.36	2.402
200317	214.977	51.895	0.351	0.266	30.41	123.504	3.369	1.971
212739	20.76	-0.324	0.248	0.168	110.03	176.025	1.412	2.799
212839	27.263	12.874	0.123	0.097	157.04	105.45	0.697	0.773
213686	155.395	23.959	0.366	0.139	75.65	105.255	1.284	1.168
213777	165.892	45.17	0.262	0.157	101.39	94.768	0.604	0.981
213880	176.538	20.448	0.263	0.128	78.75	102.028	1.274	1.317
213971	184.551	29.252	0.168	0.112	107.3	106.06	0.621	0.727
214216	212.419	17.519	0.294	0.101	174.61	63.221	0.302	0.727
214224	212.425	54.237	0.213	0.093	24.5	174.972	2.052	2.735
215038	202.86	-1.685	0.286	0.156	168.4	94.391	1.968	0.944
993850	24.183	-9.211	0.218	0.085	124.6	152.811	1.894	1.454

995501	24.496	-9.077	0.259	0.102	160.32	156.17	1.225	2.358
999709	38.602	-8.748	0.291	0.077	77.36	172.08	2.299	3.702
1002198	24.211	-8.556	0.299	0.223	37.69	160.725	3.903	5.282
1035578	51.331	-6.206	0.185	0.085	42.81	140.37	1.121	2.754
1126633	37.779	-1.105	0.258	0.216	106.22	160.797	1.903	4.188
1127439	45.922	-1.074	0.248	0.183	47.14	56.525	0.92	0.731
1127665	160.33	-1.064	0.239	0.164	166.78	118.96	0.664	0.649
1131909	41.711	-0.899	0.236	0.097	166.16	151.599	1.44	2.592
1132617	202.579	-0.871	0.144	0.087	108.75	153.958	1.609	1.319
1141653	19.525	-0.506	0.213	0.12	131.37	182.718	1.174	2.766
1143153	322.613	-0.445	0.397	0.091	129.29	84.599	1.349	0.806
1143577	20.692	-0.426	0.315	0.257	165.64	69.447	0.363	0.662
1146872	14.56	-0.297	0.198	0.176	97.42	180.983	2.312	1.998
1150845	26.116	-0.144	0.299	0.073	74.6	173.675	1.286	1.727
1151122	16.64	-0.134	0.364	0.111	16.96	73.376	0.312	0.338
1151377	136.738	-0.124	0.198	0.151	169.08	76.033	0.57	0.273
1151586	14.303	-0.115	0.18	0.117	128.09	182.107	2.17	1.868
1153648	352.847	-0.031	0.238	0.105	99.32	69.074	0.128	0.173
1154030	15.038	-0.017	0.213	0.174	21.22	166.351	1.654	1.374
1154498	221.015	0.0	0.296	0.096	62.22	141.074	6.609	2.337
1154576	14.833	0.003	0.223	0.153	144.69	173.819	1.587	1.881
1156435	333.859	0.073	0.305	0.104	21.81	183.584	15.91	6.557
1157161	14.374	0.103	0.239	0.158	141.24	179.103	1.304	1.17
1157504	333.873	0.116	0.15	0.114	71.76	184.157	1.644	1.538
1157594	229.364	0.119	0.22	0.157	22.56	142.175	2.257	1.275
1159277	18.227	0.187	0.202	0.135	57.91	175.318	3.666	2.438
1159724	220.873	0.204	0.4	0.096	21.66	119.376	0.714	1.045
1160119	229.75	0.218	0.236	0.127	28.82	154.374	6.512	2.545
1160491	17.417	0.231	0.233	0.122	86.24	182.978	3.065	4.076
1160736	16.672	0.24	0.161	0.088	104.91	180.301	1.971	3.466
1161644	17.67	0.274	0.224	0.184	77.44	182.824	2.339	3.47
1161668	17.159	0.275	0.167	0.123	6.64	178.942	2.557	2.876
1164082	17.559	0.366	0.168	0.135	170.37	182.735	4.835	2.068
1164755	49.973	0.391	0.135	0.117	61.37	99.582	0.859	0.668
1166532	17.898	0.462	0.437	0.105	178.53	68.123	0.53	0.767
1166629	25.386	0.466	0.213	0.137	144.54	169.127	6.522	3.911
1168578	19.854	0.538	0.243	0.118	4.34	183.194	0.598	1.852
1176661	135.746	0.831	0.162	0.086	13.49	110.777	0.611	0.578
1179785	20.452	0.943	0.223	0.149	101.16	78.412	0.581	0.534
1180313	10.851	0.96	0.217	0.086	123.2	142.927	1.585	1.51
1186693	135.478	1.172	0.323	0.126	51.55	78.635	0.266	0.43
1199361	149.594	1.585	0.251	0.124	30.12	113.874	1.205	1.168
1211119	225.399	1.948	0.153	0.11	61.16	120.188	0.098	1.369
1234778	239.626	2.691	0.234	0.077	179.68	135.302	1.175	2.981
1242633	226.571	2.991	0.169	0.092	48.85	178.457	2.68	2.254

1254758	218.845	3.573	0.177	0.081	173.87	126.022	1.025	1.225
1258884	218.859	3.808	0.235	0.097	43.52	125.368	1.638	1.718
1259470	125.738	3.842	0.244	0.182	34.08	119.609	0.712	3.137
1265456	125.851	4.238	0.192	0.121	122.36	116.209	0.44	1.264
1265554	125.998	4.246	0.288	0.125	176.46	121.104	0.848	1.046
1266959	229.01	4.347	0.231	0.09	110.94	149.694	2.194	3.965
1267212	125.772	4.363	0.273	0.163	116.12	107.131	2.36	2.204
1267864	228.588	4.411	0.18	0.126	23.7	156.666	1.193	1.429
1273805	233.313	4.824	0.135	0.069	45.12	150.536	1.306	1.692
1284684	228.064	5.516	0.147	0.124	46.05	177.742	5.596	2.605
1290867	172.629	5.892	0.142	0.102	77.89	143.32	9.984	2.552
1293678	229.638	6.049	0.273	0.124	153.37	184.54	7.906	8.143
1294315	153.317	6.086	0.223	0.086	58.64	130.926	1.271	1.924
1297733	160.423	6.278	0.214	0.175	81.24	118.423	0.809	1.257
1307172	229.223	6.772	0.126	0.091	9.21	126.339	0.841	1.02
1320598	232.967	7.388	0.204	0.141	91.38	137.56	0.724	2.233
1355941	165.162	8.906	0.259	0.191	158.71	141.327	2.007	1.58
1357606	222.622	8.994	0.18	0.145	145.01	162.575	5.636	2.491
1385124	214.317	10.831	0.31	0.132	65.88	101.877	1.055	0.613
1390199	241.772	11.2	0.214	0.124	23.72	179.306	3.377	3.537
1399144	202.402	11.814	0.342	0.167	45.45	108.476	2.326	2.529
1402425	243.998	12.018	0.299	0.104	4.53	139.934	2.753	3.001
1412010	156.547	12.574	0.27	0.099	172.47	127.516	3.024	1.832
1420321	151.718	12.987	0.237	0.119	50.82	152.738	3.292	2.646
1425153	149.747	13.197	0.232	0.171	34.08	170.752	2.31	1.682
1427577	130.056	13.3	0.283	0.109	30.24	132.408	4.246	2.962
1444428	201.057	13.93	0.19	0.146	40.63	105.035	0.612	0.522
1445759	201.283	13.976	0.22	0.152	28.96	101.973	0.209	0.398
1455644	16.858	14.343	0.2	0.146	126.64	165.346	2.109	2.141
1461143	20.003	14.557	0.183	0.126	30.48	157.313	1.713	1.861
1479647	119.922	15.256	0.278	0.101	95.92	184.835	4.695	5.093
1487667	18.158	15.551	0.252	0.145	53.11	175.023	2.764	2.362
1488517	18.183	15.589	0.179	0.13	41.22	175.723	0.965	2.081
1490109	121.582	15.655	0.189	0.14	27.26	181.455	4.955	3.595
1490643	18.318	15.677	0.195	0.137	13.8	155.395	1.544	2.273
1490808	18.437	15.683	0.151	0.104	123.63	181.278	3.314	2.887
1495724	240.44	15.891	0.294	0.1	169.06	155.186	0.943	3.107
1509913	139.629	16.486	0.153	0.13	97.27	140.204	2.13	1.17
1509990	139.479	16.489	0.262	0.089	63.34	122.122	0.871	1.776
1527695	172.186	17.227	0.212	0.149	62.86	88.194	1.587	0.946
1531425	234.749	17.382	0.139	0.094	131.43	175.652	1.538	2.12
1538974	148.823	17.687	0.153	0.123	172.91	182.608	9.91	5.249
1554617	117.758	18.263	0.195	0.12	20.28	182.073	2.356	1.203
1558878	116.92	18.412	0.122	0.082	175.24	169.489	0.587	1.216
1559618	117.199	18.438	0.125	0.1	73.73	184.806	1.923	1.216

1560165	116.963	18.458	0.154	0.085	126.89	170.706	3.622	1.667
1561298	208.884	18.498	0.135	0.098	152.99	114.391	1.058	0.874
1573473	120.404	18.885	0.346	0.213	106.47	157.794	9.191	11.65
1582573	219.023	19.16	0.301	0.269	32.71	184.201	5.213	7.842
1584516	222.937	19.218	0.136	0.095	11.95	182.305	9.844	2.022
1590052	127.881	19.375	0.159	0.092	136.07	156.75	0.852	1.599
1591848	130.69	19.426	0.271	0.084	52.63	131.649	4.574	2.181
1598330	130.759	19.595	0.187	0.163	166.13	149.185	2.542	1.067
1599370	243.782	19.623	0.181	0.136	112.92	133.659	0.119	0.732
1604354	176.307	19.756	0.231	0.165	8.78	115.617	3.033	2.271
1610778	174.372	19.938	0.197	0.108	6.6	140.641	3.357	2.111
1613555	176.228	20.017	0.204	0.138	103.98	103.497	0.54	0.443
1616588	176.134	20.107	0.215	0.16	6.35	102.708	4.967	1.945
1621866	133.791	20.262	0.208	0.105	28.07	131.721	4.286	1.877
1646009	187.728	21.248	0.224	0.071	12.37	116.563	3.026	1.572
1659660	155.642	21.907	0.18	0.156	63.99	170.792	11.67	2.076
1674543	125.596	22.697	0.182	0.132	145.54	30.272	0.047	0.078
1674903	146.283	22.718	0.182	0.09	163.81	104.333	0.272	0.801
1677461	199.954	22.867	0.265	0.174	126.3	99.902	1.16	3.402
1681191	178.577	23.086	0.279	0.164	1.22	113.728	1.664	2.19
1687257	233.704	23.43	0.146	0.074	66.3	160.822	2.489	2.356
1689905	233.973	23.582	0.286	0.127	152.11	76.208	0.348	0.386
1699572	202.819	24.091	0.239	0.082	129.7	153.17	1.723	1.09
1700434	241.345	24.131	0.281	0.12	172.39	137.487	0.214	2.116
1701575	170.593	24.184	0.224	0.095	153.05	121.703	0.6	0.863
1702940	215.878	24.247	0.204	0.144	26.55	63.318	0.134	0.082
1708077	170.697	24.472	0.153	0.119	161.91	116.622	0.833	0.798
1709120	217.842	24.513	0.148	0.083	10.19	96.024	2.647	0.553
1714418	164.921	24.714	0.247	0.131	120.0	136.374	4.52	3.452
1718741	129.693	24.871	0.177	0.085	148.6	121.959	0.959	0.915
1723421	182.034	25.033	0.324	0.094	142.39	98.463	0.4	1.765
1726694	202.934	25.14	0.226	0.106	40.06	161.601	1.603	1.94
1730304	181.924	25.254	0.204	0.11	42.13	96.96	0.328	0.216
1730676	182.123	25.266	0.237	0.12	18.87	103.802	0.6	0.956
1750402	129.458	25.801	0.155	0.126	12.0	112.306	5.433	1.124
1753373	216.848	25.878	0.222	0.154	122.12	58.496	0.125	0.188
1769507	237.525	26.264	0.239	0.079	94.89	169.666	1.718	2.758
1771065	210.846	26.305	0.205	0.147	16.19	121.973	5.286	2.41
1797404	214.294	27.089	0.144	0.11	37.85	157.271	1.387	1.455
1799933	251.879	27.172	0.234	0.093	36.18	182.929	2.778	2.466
1812234	204.765	27.579	0.162	0.12	158.38	153.725	1.755	1.471
1812806	204.787	27.598	0.315	0.148	45.89	149.349	1.559	2.298
1815631	254.383	27.701	0.186	0.112	132.77	153.077	1.867	1.706
1817480	134.397	27.768	0.173	0.151	106.63	33.659	0.06	0.074
1820473	198.216	27.88	0.329	0.161	141.36	93.353	1.287	1.546

1826835	179.323	28.119	0.173	0.08	103.63	95.936	0.186	0.413
1826860	181.447	28.12	0.132	0.104	37.92	125.137	0.676	0.81
1832533	122.803	28.323	0.206	0.071	116.81	148.054	3.014	2.313
1835201	211.58	28.419	0.229	0.087	1.9	161.537	2.488	2.257
1839666	167.574	28.571	0.233	0.136	139.52	130.691	1.546	1.951
1840966	167.874	28.617	0.149	0.11	139.24	116.272	0.605	0.666
1841559	211.804	28.637	0.262	0.158	54.12	77.407	0.364	0.577
1841722	167.881	28.643	0.281	0.104	45.98	119.362	0.64	1.146
1842563	167.837	28.672	0.243	0.127	61.01	140.511	1.838	1.357
1847597	167.887	28.84	0.143	0.089	21.32	124.71	0.303	0.517
1864481	118.59	29.382	0.208	0.081	135.97	148.287	2.529	1.835
1901761	138.852	30.388	0.132	0.091	88.36	99.545	1.54	0.74
1901903	205.307	30.391	0.201	0.127	82.15	162.658	0.87	1.014
1906186	197.409	30.498	0.298	0.092	27.57	104.676	2.757	1.248
1913925	140.983	30.691	0.288	0.095	89.47	97.51	1.074	1.427
1937801	199.976	31.235	0.393	0.103	171.24	79.337	0.325	0.594
1954123	200.646	31.581	0.251	0.132	5.05	172.335	3.378	4.042
1957505	200.541	31.651	0.177	0.126	120.5	152.01	1.379	1.075
1960810	200.803	31.719	0.239	0.144	78.55	170.19	1.899	2.768
1963697	113.409	31.773	0.135	0.077	48.07	108.785	1.352	0.965
1974798	201.409	31.994	0.158	0.091	29.85	104.721	0.838	0.779
2006860	249.766	32.657	0.231	0.1	48.75	134.265	3.223	2.131
2015911	150.502	32.882	0.218	0.144	167.89	90.648	0.162	0.235
2034956	186.932	33.58	0.171	0.113	172.96	96.515	0.282	0.395
2037375	184.945	33.707	0.338	0.081	164.31	93.663	0.403	0.752
2038066	202.49	33.746	0.204	0.135	88.82	147.417	1.158	1.338
2040636	202.782	33.896	0.127	0.108	11.37	104.409	0.185	0.347
2056268	251.656	34.897	0.245	0.179	40.47	155.516	2.516	1.781
2059143	244.385	35.084	0.235	0.121	25.99	126.692	0.591	0.522
2059469	253.125	35.104	0.245	0.131	107.35	137.059	2.309	1.603
2060285	244.463	35.157	0.387	0.125	58.13	130.353	2.069	2.587
2067180	218.476	35.609	0.235	0.066	44.13	145.425	1.921	1.375
2080337	183.6	36.421	0.199	0.129	98.02	175.548	3.244	2.789
2108252	119.79	37.737	0.155	0.107	150.02	175.832	1.329	1.337
2112124	133.827	37.886	0.203	0.165	6.56	184.326	2.774	4.276
2115390	166.186	38.005	0.186	0.155	149.06	125.248	0.598	1.068
2128678	215.786	38.495	0.186	0.136	94.85	181.565	1.257	1.442
2139492	122.141	38.915	0.255	0.193	79.5	163.117	2.579	7.468
2141849	122.084	39.024	0.223	0.162	105.64	96.653	3.133	3.044
2147249	247.549	39.298	0.195	0.093	108.28	131.258	2.508	1.5
2147674	246.13	39.322	0.243	0.137	132.57	130.88	2.42	1.059
2149476	118.869	39.42	0.152	0.101	36.42	83.455	0.262	0.251
2150101	246.477	39.457	0.185	0.135	92.59	185.18	2.531	2.031
2151781	246.366	39.552	0.3	0.218	13.85	124.749	1.962	1.213
2155004	134.748	39.749	0.242	0.139	11.66	102.702	0.546	0.849

2156773	122.245	39.858	0.347	0.124	91.24	88.75	0.395	0.978
2159648	160.106	40.042	0.157	0.073	12.29	102.191	0.143	0.547
2163128	248.399	40.258	0.191	0.103	85.29	119.182	3.66	1.262
2169301	247.46	40.676	0.187	0.119	139.45	125.435	0.364	0.822
2169778	247.658	40.709	0.336	0.151	78.43	114.076	1.528	0.366
2170424	247.022	40.755	0.213	0.113	103.72	123.049	0.595	0.993
2172609	247.239	40.899	0.237	0.159	55.06	145.196	1.35	1.679
2173570	166.056	40.959	0.178	0.117	139.19	140.263	2.21	1.842
2177729	50.721	41.23	0.477	0.19	123.26	99.301	5.359	5.983
2196443	251.347	42.314	0.372	0.135	146.44	137.605	2.311	2.584
2202201	182.08	42.6	0.124	0.098	153.17	185.435	1.283	1.265
2218009	200.864	43.324	0.212	0.135	23.43	118.59	1.779	0.832
2219223	178.196	43.374	0.157	0.135	1.35	177.263	2.08	1.69
2224292	178.245	43.586	0.229	0.158	115.64	178.706	6.078	3.459
2230193	155.975	43.831	0.188	0.108	102.61	172.73	1.339	2.129
2234990	156.206	44.035	0.216	0.09	78.69	182.028	2.285	2.217
2239251	138.963	44.214	0.161	0.128	144.31	134.797	0.631	0.966
2243479	139.193	44.398	0.238	0.195	76.31	136.372	1.465	4.112
2259999	166.363	45.158	0.199	0.138	62.42	134.31	4.975	2.677
2292803	171.019	47.127	0.193	0.111	172.65	141.264	2.21	1.571
2293506	182.509	47.168	0.223	0.109	164.47	129.574	1.424	1.463
2315116	204.513	48.33	0.191	0.132	135.98	120.633	0.497	0.642
2334797	173.507	49.148	0.164	0.122	71.91	129.813	0.712	0.508
2337352	173.703	49.242	0.177	0.14	77.85	124.368	0.299	0.549
2353412	176.563	49.787	0.144	0.09	38.95	134.214	0.197	0.762
2362862	117.862	50.103	0.239	0.117	11.98	159.026	3.276	3.607
2365456	131.016	50.186	0.166	0.145	87.0	175.398	7.188	3.755
2369301	117.738	50.314	0.262	0.107	178.06	103.096	0.546	0.722
2371733	117.886	50.395	0.158	0.112	136.95	85.396	0.504	0.535
2372133	117.907	50.407	0.245	0.166	109.77	99.541	4.052	2.422
2381875	236.269	50.781	0.167	0.121	125.91	148.358	1.264	1.487
2400647	123.906	51.816	0.199	0.083	120.49	131.193	1.17	0.958
2401428	213.964	51.857	0.233	0.077	114.64	185.355	3.643	3.406
2403489	123.801	51.957	0.218	0.069	160.87	157.812	0.53	1.581
2424915	243.126	52.835	0.174	0.133	128.2	155.336	1.943	1.055
2427312	158.55	52.926	0.164	0.092	113.23	102.319	0.098	0.546
2428287	211.781	52.964	0.165	0.135	63.55	181.207	3.868	2.715
2433795	152.56	53.177	0.297	0.194	178.62	139.381	1.536	3.331
2435590	211.477	53.243	0.24	0.086	28.7	169.193	3.044	2.758
2442196	220.16	53.478	0.177	0.155	144.12	156.568	2.474	1.175
2460982	212.502	54.141	0.176	0.084	8.54	173.868	1.562	3.265
2468371	137.629	54.395	0.177	0.137	5.66	56.728	0.172	0.142
2482715	214.057	54.861	0.164	0.147	61.41	171.231	2.446	2.433
2484220	173.408	54.908	0.209	0.091	78.34	115.59	1.936	1.078
2489542	177.747	55.07	0.276	0.13	84.3	82.093	0.586	0.752

2490520	234.036	55.099	0.205	0.179	123.71	162.075	3.055	1.642
2504852	129.195	55.515	0.186	0.148	133.11	183.87	2.637	3.539
2507519	128.886	55.59	0.275	0.12	6.59	105.122	0.342	0.747
2515705	128.76	55.828	0.195	0.158	92.83	156.365	1.621	2.34
2530333	228.549	56.241	0.2	0.166	39.31	183.769	2.159	1.838
2553307	227.135	56.97	0.314	0.159	107.23	127.677	0.802	0.849
2561952	258.221	57.282	0.155	0.08	107.41	118.794	0.753	0.824
2564113	258.503	57.374	0.2	0.161	9.06	132.788	1.423	5.62
2568088	258.711	57.57	0.303	0.213	88.14	115.466	2.215	1.598
2573071	129.541	57.973	0.169	0.113	177.67	185.371	4.803	3.135
2573118	129.925	57.977	0.179	0.084	51.23	173.89	1.486	1.428
2573317	129.398	57.995	0.216	0.129	152.65	185.315	3.264	2.432
2578440	172.403	58.415	0.296	0.111	118.75	173.051	3.94	3.817
2587126	161.481	59.154	0.263	0.12	23.21	183.306	3.029	3.972
2590098	162.024	59.408	0.155	0.108	111.36	119.199	0.212	0.553
2594887	260.497	59.843	0.21	0.079	98.11	119.131	2.239	1.166
2610933	204.504	61.038	0.222	0.119	164.14	174.081	1.46	1.707
2696510	183.138	67.206	0.3	0.157	61.88	135.21	0.919	0.673
2815856	130.234	57.956	0.372	0.243	95.26	72.822	1.041	0.799
2815946	166.623	52.313	0.182	0.122	112.16	93.613	0.384	0.526
2816037	196.915	53.84	0.355	0.14	15.09	126.836	0.364	0.85
2816038	196.785	53.962	0.154	0.12	165.27	123.999	1.653	1.26
3087388	161.764	48.827	0.198	0.13	168.8	112.866	4.137	1.546
3087596	243.965	46.558	0.17	0.101	35.26	127.725	1.892	1.368
3090713	137.286	14.643	0.184	0.151	109.99	52.824	0.064	0.083
3091743	227.241	7.62	0.218	0.183	54.68	134.28	2.054	1.545
3092484	134.815	0.392	0.281	0.162	154.95	46.685	0.131	0.154
3093154	321.133	-8.312	0.411	0.27	145.09	103.415	1.676	1.263
3094758	215.054	56.681	0.34	0.157	51.45	125.0	2.326	1.372
3103599	319.528	-7.716	0.212	0.133	85.36	35.654	0.034	0.048
3105149	51.404	-5.969	0.228	0.115	81.09	140.53	1.12	0.815
3111153	15.296	-0.34	0.134	0.119	172.0	174.812	1.884	1.333
3114447	19.73	0.331	0.179	0.126	151.85	167.965	3.417	3.064
3122018	239.595	2.718	0.187	0.09	169.15	102.171	1.513	0.843
3129621	253.502	39.897	0.257	0.172	135.97	162.067	1.556	1.206
3136991	260.983	59.68	0.108	0.08	4.04	129.47	0.505	0.559
3137618	255.03	61.287	0.29	0.142	173.69	118.59	3.883	2.418
3138214	216.783	63.053	0.22	0.124	52.08	152.271	0.817	0.974
3138244	215.941	63.117	0.148	0.093	69.41	152.297	0.773	1.099
3139240	255.416	64.376	0.222	0.157	89.21	144.132	0.873	1.17
3293339	187.027	1.574	0.214	0.097	147.89	135.497	0.882	1.409
3336099	19.958	0.706	0.349	0.062	125.02	183.614	1.602	2.566
3351621	122.062	39.935	0.229	0.141	142.2	165.135	1.904	2.259
3381209	141.203	52.302	0.126	0.108	96.63	150.073	5.59	1.635
3388144	247.567	40.683	0.19	0.162	132.08	128.06	0.208	0.694

3388203	246.645	40.914	0.105	0.076	9.49	117.755	0.335	0.549
3390074	127.34	38.193	0.183	0.146	28.71	165.265	12.85	3.921
3403715	152.806	53.516	0.2	0.144	56.99	140.049	3.364	2.394
3408298	160.542	58.661	0.166	0.144	6.46	132.33	1.119	0.817
3408440	162.718	57.585	0.413	0.113	29.81	113.994	1.529	2.563
3408576	161.115	58.903	0.346	0.262	62.26	132.299	1.232	1.989
3409128	169.688	57.825	0.248	0.092	131.22	183.471	3.832	4.079
3445966	121.366	24.795	0.336	0.089	114.82	185.106	2.732	4.054
3468182	161.511	53.124	0.182	0.074	163.3	184.551	1.677	1.464
3469445	164.947	8.646	0.164	0.147	155.33	147.696	2.12	1.216
3473037	173.329	55.081	0.185	0.118	59.45	82.313	0.097	0.244
3475599	178.61	56.956	0.105	0.08	167.79	174.981	0.465	1.399
3495293	239.806	27.661	0.527	0.154	176.47	139.696	3.071	2.55
3498944	246.441	39.288	0.205	0.138	123.94	152.564	3.993	2.521
3506408	247.155	39.445	0.21	0.09	78.66	143.17	0.377	1.222
3532807	149.75	13.052	0.39	0.124	12.02	145.836	6.687	4.466
3538304	160.411	40.043	0.143	0.079	153.26	180.017	1.979	1.401
3555994	202.312	11.6	0.225	0.085	47.12	96.821	0.575	0.598
3564057	227.665	33.614	0.129	0.071	26.11	181.806	3.443	1.949
3668209	57.89	-0.993	0.275	0.059	140.98	158.085	2.019	2.266
3737721	136.414	16.725	0.158	0.108	145.5	153.444	3.128	1.503
3753948	154.784	19.982	0.223	0.145	179.91	158.281	1.916	1.38
3761083	162.33	22.98	0.166	0.113	84.29	132.739	1.196	0.882
3790180	187.503	8.104	0.182	0.151	98.96	153.345	1.66	3.376
3800271	195.066	34.814	0.147	0.126	124.27	114.345	1.303	0.802
3845383	230.6	7.635	0.217	0.147	1.64	163.074	4.929	3.387
3848497	233.043	4.846	0.324	0.081	25.41	155.488	2.696	1.535
3862692	244.097	19.487	0.291	0.109	87.69	136.953	4.878	3.21
3862874	244.241	12.795	0.175	0.123	152.54	124.318	0.485	0.546

Master table of the properties of the star-forming sample from the `HECATE` catalogue. Column (1) gives the catalogue ID (PGC number) of each galaxy; Columns (2), and (3) the sky coordinates (RA and DEC); Columns (4), (5), and (6) the semi-major and semi-minor radius and the position angle of each object respectively; Column (7) gives the distances of the galaxies; Columns (8) and (9) give the star-formation rate and the stellar mass respectively.

Table 4.3: X-ray properties of the star-forming sample.

PGC (1)	Nobs (2)	OBSID (3)	Detector (4)	Exposure ks (5)	Coverage % (6)
1014	9	0028740101	M2	30.89	84.71
		0028740101	M1	30.90	85.59
		0028740101	PN	27.87	86.79
		0028740201	PN	30.41	59.07
		0028740201	M1	33.02	65.48
		0028740201	M2	33.02	67.90
		0655050101	M1	119.41	46.46
		0655050101	PN	112.55	77.87
		0655050101	M2	119.91	83.01
1142	3	0403760701	PN	30.31	79.34
		0403760701	M2	49.45	89.35
		0403760701	M1	47.36	93.94
2388	3	0203690101	PN	31.77	100.04
		0203690101	M1	39.09	84.01
		0203690101	M2	39.46	87.88
2758	6	0601010101	M1	31.44	88.47
		0601010101	M2	32.38	90.34
		0601010101	PN	22.32	90.77
		0728190101	M1	34.53	82.36
		0728190101	PN	26.09	90.97
		0728190101	M2	35.22	91.27
3238	15	0112800101	M1	43.79	88.63
		0112800101	M2	43.79	89.46
		0112800101	PN	39.95	89.82
		0112800201	M1	34.04	88.45
		0112800201	M2	34.04	89.73
		0112800201	PN	30.45	90.77
		0305860301	M1	36.49	81.66
		0305860301	PN	34.86	91.20
		0305860301	M2	36.49	91.31
		0305860401	M1	35.02	84.94
		0305860401	M2	34.98	89.83
		0305860401	PN	31.19	91.01
		0656780401	M1	16.09	72.66
		0656780401	M2	16.72	90.11
		0656780401	PN	12.76	91.85
4979	6	0721900501	PN	17.11	100.10
		0721900501	M1	18.71	96.55
		0721900501	M2	18.70	97.21
		0782010101	M1	69.52	92.19

		0782010101	PN	67.91	99.36
		0782010101	M2	69.49	99.96
5193	3	0025541601	M2	11.86	82.46
		0025541601	PN	9.99	89.66
		0025541601	M1	12.05	96.77
6972	9	0109980101	PN	20.00	100.52
		0109980101	M2	23.89	75.95
		0109980101	M1	23.89	80.20
		0504780101	M2	79.65	72.20
		0504780101	M1	67.70	89.72
		0504780101	PN	18.40	90.84
		0504780201	M2	39.39	65.20
		0504780201	M1	36.48	91.45
		0504780201	PN	26.27	92.29
11631	3	0201120101	M2	31.29	2.48
		0201120101	PN	16.60	84.48
		0201120101	M1	29.95	93.03
		0201120101	M1	29.95	100.05
		0201120101	PN	16.60	1.42
		0201120101	M2	31.29	81.41
12286	66	0106860101	PN	24.53	89.48
		0106860101	M2	2.34	93.34
		0106860101	M1	2.33	94.84
		0150280301	M2	10.71	88.37
		0150280301	PN	8.24	90.06
		0150280301	M1	10.61	90.46
		0150280401	M2	8.12	88.58
		0150280401	M1	7.50	90.25
		0150280401	PN	3.70	91.13
		0150280501	M2	9.19	88.25
		0150280501	M1	9.09	90.17
		0150280501	PN	4.94	91.21
		0150280601	M2	13.05	86.90
		0150280601	M1	13.10	90.27
		0150280601	PN	9.20	91.09
		0150281101	M2	7.94	87.07
		0150281101	M1	7.94	90.01
		0150281101	PN	5.54	91.29
		0205230201	M1	9.74	85.86
		0205230201	PN	0.70	89.86
		0205230201	M2	10.57	93.64
		0205230301	M1	11.67	84.78
		0205230301	PN	9.84	89.94
		0205230301	M2	11.67	92.82
		0205230401	M2	14.66	89.70

		0205230401	M1	14.71	91.95
		0205230401	PN	6.80	93.09
		0205230501	PN	14.06	90.44
		0205230501	M2	15.70	90.70
		0205230501	M1	15.69	91.79
		0205230601	M2	12.93	88.58
		0205230601	M1	12.82	89.92
		0205230601	PN	10.50	92.41
		0301860101	M2	21.57	86.02
		0301860101	M1	21.56	88.98
		0301860101	PN	19.84	89.02
		0405090101	PN	94.29	90.04
		0405090101	M2	114.24	94.06
		0405090101	M1	109.51	94.86
		0693850501	PN	105.08	89.62
		0693850501	M1	117.14	92.74
		0693850501	M2	118.82	92.99
		0693851201	PN	101.52	89.70
		0693851201	M1	124.61	91.26
		0693851201	M2	124.90	93.07
		0722650101	M1	29.74	75.21
		0722650101	PN	18.40	89.38
		0722650101	M2	30.26	90.76
		0742490101	M1	98.42	47.46
		0742490101	M2	101.60	88.55
		0742490101	PN	92.71	91.14
		0742590301	PN	60.02	89.82
		0742590301	M1	61.65	93.39
		0742590301	M2	61.62	93.71
		0764770101	M1	72.47	77.17
		0764770101	M2	72.67	89.56
		0764770101	PN	60.86	91.05
		0764770401	M1	26.34	68.63
		0764770401	M2	27.93	90.36
		0764770401	PN	19.53	90.62
		0782310101	M1	89.53	54.92
		0782310101	M2	89.51	89.55
		0782310101	PN	87.53	94.00
		0794580601	PN	31.52	90.39
		0794580601	M2	41.67	91.37
		0794580601	M1	40.00	92.34
12418	3	0781040101	M2	88.20	100.25
		0781040101	M1	88.24	100.25
		0781040101	PN	82.13	82.30
12486	3	0781040101	M1	88.24	89.30

		0781040101	PN	82.13	99.19
		0781040101	M2	88.20	99.49
12785	5	0103861001	PN	7.51	97.74
		0402110201	M2	21.47	90.45
		0402110201	M1	21.41	92.32
		0402110201	PN	19.04	98.68
		0760230401	PN	19.27	81.87
12803	8	0103861001	M1	9.13	3.69
		0103861001	PN	7.51	99.58
		0402110201	M1	21.41	100.14
		0402110201	PN	19.04	59.73
		0402110201	M2	21.47	92.76
		0760230401	M1	21.29	92.33
		0760230401	PN	19.27	99.72
		0760230401	M2	21.35	99.72
14236	3	0110980401	PN	32.50	84.55
		0110980401	M2	40.41	85.47
		0110980401	M1	40.36	99.34
15345	3	0112290801	M2	17.52	85.56
		0112290801	PN	13.52	89.83
		0112290801	M1	17.53	96.66
16282	3	0148650101	M1	50.70	100.05
		0148650101	M2	52.01	84.26
		0148650101	PN	43.68	87.59
21396	11	0150651101	PN	9.81	51.43
		0150651101	M1	5.27	88.78
		0150651101	M2	5.37	89.83
		0150651201	M2	7.43	89.05
		0150651201	M1	6.90	90.29
		0150651201	PN	2.14	92.15
		0164560901	M2	76.28	87.83
		0164560901	PN	58.11	90.48
		0164560901	M1	74.71	91.26
		0729560901	M1	3.27	70.96
		0729560901	M2	3.24	89.20
22805	3	0138951401	M2	6.96	97.79
		0138951401	M1	6.96	98.03
		0138951401	PN	5.34	99.77
23359	3	0108860501	PN	18.38	100.03
		0108860501	M1	21.50	58.89
		0108860501	M2	21.56	80.58
23504	3	0721900101	PN	9.62	82.28
		0721900101	M1	18.53	93.86
		0721900101	M2	18.65	99.95
23850	1	0502220201	PN	57.30	87.52

25363	3	0725290148	PN	2.75	90.84
		0725290148	M1	2.75	94.26
		0725290148	M2	2.75	99.77
25470	3	0745010301	M2	34.45	88.84
		0745010301	M1	33.44	94.98
		0745010301	PN	29.73	96.95
27077	3	0556280301	PN	64.80	88.29
		0556280301	M1	72.68	91.32
		0556280301	M2	73.71	92.37
27658	3	0203270101	M1	48.49	91.82
		0203270101	PN	41.75	96.68
		0203270101	M2	48.53	99.97
28655	28	0112290201	PN	25.23	87.59
		0112290201	M2	29.90	93.02
		0112290201	M1	29.86	95.26
		0206080101	PN	66.36	88.64
		0206080101	M2	76.19	93.79
		0206080101	M1	74.93	93.92
		0560181301	PN	0.01	88.66
		0560181301	M2	4.03	93.83
		0560181301	M1	1.94	94.37
		0560590101	PN	26.60	88.68
		0560590101	M2	29.90	93.13
		0560590101	M1	29.85	96.40
		0560590201	PN	15.67	88.47
		0560590201	M2	21.99	93.71
		0560590201	M1	19.81	95.72
		0560590301	PN	16.25	87.63
		0560590301	M2	34.93	92.96
		0560590301	M1	28.62	93.17
		0657800101	M2	17.26	93.56
		0657800101	M1	11.91	95.49
		0657801901	PN	9.72	87.56
		0657801901	M2	11.44	92.91
		0657801901	M1	11.23	93.08
		0657802101	M2	18.04	92.38
		0657802101	M1	17.05	96.13
		0657802301	PN	9.60	87.83
		0657802301	M2	18.51	92.13
		0657802301	M1	16.38	95.99
28682	3	0404240301	M2	18.22	80.06
		0404240301	M1	18.22	90.12
		0404240301	PN	16.54	90.87
28990	6	0110930201	M1	8.44	65.10
		0110930201	PN	5.52	89.12

		0110930201	M2	8.23	93.70
		0147760101	M1	34.94	61.08
		0147760101	M2	36.03	65.17
		0147760101	PN	18.10	99.18
30087	3	0028740301	PN	22.27	87.32
		0028740301	M1	29.11	88.59
		0028740301	M2	29.43	90.10
		0723161001	PN	11.84	78.10
		0723161001	M2	16.32	99.91
		0723161001	M1	16.35	99.98
30948	2	0303720301	M2	73.84	100.07
		0303720301	M1	73.14	91.73
31856	3	0147630101	M2	24.26	100.16
		0147630101	PN	19.44	100.23
		0147630101	M1	24.05	94.72
32341	3	0652810201	M1	26.99	93.29
		0652810201	PN	24.04	98.35
		0652810201	M2	27.62	99.27
32434	3	0055990201	PN	14.06	100.11
		0055990201	M2	20.50	85.74
		0055990201	M1	20.23	99.72
32464	2	0781410201	PN	47.89	100.12
		0781410201	M1	51.00	28.08
32543	6	0781410101	M2	40.77	83.78
		0781410101	PN	37.32	89.18
		0781410101	M1	39.91	91.96
		0781410201	M2	50.94	83.41
		0781410201	PN	47.89	89.11
		0781410201	M1	51.00	91.81
32584	4	0781410101	M2	40.77	100.04
		0781410101	PN	37.32	100.14
		0781410201	PN	47.89	100.01
		0781410201	M2	50.94	99.84
32827	5	0606030101	M1	36.06	91.92
		0606030101	M2	36.16	97.68
		0606030101	PN	28.57	99.56
		0606030201	M2	23.74	100.05
		0606030201	M1	23.73	88.17
32907	17	0200530201	M1	22.77	100.01
		0200530201	M2	22.95	99.04
		0200530301	M2	18.40	100.01
		0200530301	PN	16.39	82.28
		0200530301	M1	18.39	91.08
		0200530401	PN	15.31	82.34
		0200530401	M1	17.91	90.72

		0200530401	M2	17.91	99.58
		0200530501	M2	24.22	91.93
		0200530501	PN	22.07	99.58
		0200530501	M1	24.11	99.58
		0200530701	M2	16.89	92.05
		0200530701	M1	16.62	99.83
		0200530701	PN	9.17	99.83
		0200530801	M2	14.87	91.93
		0200530801	PN	12.67	99.70
		0200530801	M1	14.86	99.70
33437	36	0099280201	M1	34.44	29.15
		0099280201	M2	34.58	34.25
		0099280301	M1	46.00	41.10
		0099280301	M2	46.11	47.00
		0099280401	M2	41.12	75.64
		0099280401	M1	40.49	80.30
		0136540101	M1	37.11	43.72
		0136540101	M2	37.06	65.14
		0150498701	M1	42.58	64.05
		0150498701	M2	43.26	66.16
		0158970101	M1	25.24	62.23
		0158970101	M2	26.66	88.68
		0158971201	M1	42.73	43.07
		0158971201	M2	45.28	63.10
		0158971301	M1	59.60	51.15
		0158971301	M2	59.71	57.13
		0162960101	M1	16.77	70.03
		0162960101	M2	20.04	80.67
		0302180101	M2	41.33	52.90
		0502030101	M1	17.29	34.10
		0502030101	M2	18.92	61.36
		0510610201	M1	17.26	39.28
		0510610201	M2	17.95	67.33
		0560983301	M1	11.11	57.78
		0560983301	M2	11.12	85.33
		0560983301	PN	9.17	89.70
		0658800801	M2	8.60	65.80
		0658800801	M1	6.98	66.09
		0658802301	M1	28.05	50.42
		0658802301	M2	28.01	81.90
		0670920301	M1	14.45	27.25
		0670920301	M2	14.39	49.04
		0670920401	M1	16.20	31.41
		0670920401	M2	16.30	52.61
		0670920501	M1	16.41	33.96

		0670920501	M2	16.35	56.25
33500	2	0099280201	M2	34.58	100.01
		0099280201	M1	34.44	95.67
34257	3	0761950101	M1	28.04	81.09
		0761950101	PN	26.42	94.02
		0761950101	M2	28.02	97.51
34612	3	0082140301	PN	28.89	81.03
		0082140301	M2	32.92	91.76
		0082140301	M1	32.90	98.62
34692	3	0503600401	M2	21.18	100.08
		0503600401	PN	15.12	64.93
		0503600401	M1	20.73	86.01
34767	12	0762610401	PN	7.04	84.51
		0762610401	M2	8.62	88.43
		0762610401	M1	8.65	93.13
		0762610501	PN	21.04	84.61
		0762610501	M2	22.62	88.50
		0762610501	M1	22.65	93.41
		0762610701	PN	7.04	84.52
		0762610701	M2	8.62	88.65
		0762610701	M1	8.65	93.40
		0762610801	PN	7.04	84.38
		0762610801	M2	8.62	88.50
		0762610801	M1	8.65	93.19
34963	3	0504101301	M2	22.46	99.48
		0504101301	PN	17.83	99.87
		0504101301	M1	21.73	99.87
35321	6	0112810101	M2	20.97	85.29
		0112810101	PN	16.01	86.29
		0112810101	M1	21.03	96.61
		0679381101	M2	10.18	83.93
		0679381101	M1	9.03	93.69
		0679381101	PN	7.40	94.87
35762	3	0149900201	M2	18.17	97.77
		0149900201	PN	16.54	98.06
		0149900201	M1	18.16	98.97
35838	15	0741140201	PN	17.74	100.27
		0741140201	M2	23.92	100.27
		0741140201	M1	23.59	88.58
		0741140301	M1	21.65	90.24
		0741140301	M2	21.62	99.67
		0741140301	PN	19.04	99.74
		0741140401	M2	36.60	100.12
		0741140401	PN	33.33	100.20
		0741140401	M1	36.64	86.99

		0741140501	M1	33.44	87.75
		0741140501	PN	31.83	99.44
		0741140501	M2	33.41	99.67
		0741140601	M1	23.65	91.82
		0741140601	M2	23.61	92.42
		0741140601	PN	22.04	99.52
35906	2	0601780401	M2	11.60	94.88
		0601780401	PN	10.00	99.72
36198	3	0303561801	M2	8.55	78.70
		0303561801	M1	8.24	88.86
		0303561801	PN	3.29	96.91
36349	3	0005210101	PN	24.65	100.14
		0005210101	M1	30.97	90.48
		0005210101	M2	30.88	99.72
36406	6	0005210101	M1	30.97	78.16
		0005210101	M2	30.88	90.13
		0005210101	PN	24.65	97.58
		0602200101	PN	20.74	90.34
		0602200101	M1	24.61	92.84
		0602200101	M2	24.57	99.87
36477	6	0005210101	M1	30.97	84.45
		0005210101	M2	30.88	96.96
		0005210101	PN	24.65	98.36
		0602200101	PN	20.74	100.01
		0602200101	M1	24.61	86.65
		0602200101	M2	24.57	90.12
37013	3	0049340301	M1	25.67	81.57
		0049340301	PN	23.32	94.01
		0049340301	M2	25.68	99.99
37282	3	0655380701	M2	11.02	81.96
		0655380701	M1	10.40	89.52
		0655380701	PN	2.87	93.97
37692	6	0744040301	PN	20.64	100.02
		0744040301	M2	23.33	91.32
		0744040301	M1	23.33	96.47
		0744040401	M2	22.62	92.52
		0744040401	M1	22.63	96.65
		0744040401	PN	20.63	99.66
37747	6	0744040301	M1	23.33	96.03
		0744040301	M2	23.33	99.29
		0744040301	PN	20.64	99.91
		0744040401	PN	20.63	100.19
		0744040401	M2	22.62	100.19
		0744040401	M1	22.63	93.80
37976	8	0555060301	PN	8.72	100.12

		0555060301	M1	23.01	92.23
		0555060301	M2	23.58	99.44
		0555060401	PN	13.65	11.29
		0555060401	M1	19.55	96.49
		0555060501	PN	13.20	73.40
		0555060501	M2	22.20	84.35
		0555060501	M1	20.28	85.71
38163	5	0112271001	M1	8.60	100.18
		0112271001	M2	8.67	95.11
		0112271101	M2	6.06	92.49
		0112271101	M1	6.05	99.58
		0112271101	PN	4.08	99.88
38672	2	0601780801	PN	18.80	85.09
		0601780801	M2	22.67	91.82
39152	30	0112610101	PN	52.40	81.09
		0112610101	M2	54.24	92.00
		0112610101	M1	54.43	98.35
		0502050101	M2	51.71	100.20
		0502050101	PN	47.36	78.58
		0502050101	M1	50.98	86.23
		0502050201	M2	37.39	100.08
		0502050201	PN	26.60	76.66
		0502050201	M1	36.13	93.84
		0745110101	PN	83.08	78.54
		0745110101	M2	85.62	89.64
		0745110101	M1	77.66	99.96
		0745110201	PN	95.06	78.07
		0745110201	M2	102.40	87.76
		0745110201	M1	101.85	99.88
		0745110301	PN	65.47	78.34
		0745110301	M2	91.34	94.59
		0745110301	M1	89.19	99.92
		0745110401	PN	92.88	79.01
		0745110401	M2	95.54	95.96
		0745110401	M1	95.27	100.00
		0745110501	PN	54.68	79.05
		0745110501	M2	56.61	96.23
		0745110501	M1	56.65	99.72
		0745110601	M1	93.95	100.08
		0745110601	PN	91.77	80.19
		0745110601	M2	93.91	98.27
		0745110701	PN	95.60	80.58
		0745110701	M2	97.55	96.27
		0745110701	M1	97.22	99.65
39225	3	0035940201	PN	5.03	86.40

		0035940201	M2	1.71	89.73
		0035940201	M1	2.39	96.84
39422	8	0105070201	M2	5.61	84.44
		0105070201	M1	5.30	92.32
		0553880201	PN	27.46	88.74
		0553880201	M1	32.97	90.20
		0553880201	M2	33.87	92.68
		0553880301	PN	40.67	88.70
		0553880301	M1	44.69	89.80
		0553880301	M2	45.26	92.62
39578	3	0147610101	PN	14.13	87.87
		0147610101	M2	19.72	89.94
		0147610101	M1	20.10	97.20
39783	3	0782530201	M2	6.62	80.08
		0782530201	M1	6.65	90.47
		0782530201	PN	5.04	93.73
39922	3	0205360101	PN	21.07	36.77
		0205360101	M2	28.39	97.52
		0205360101	M1	27.30	98.07
39950	3	0306060101	PN	79.40	72.06
		0306060101	M1	88.10	89.13
		0306060101	M2	88.50	95.75
40001	3	0205360101	PN	21.07	86.66
		0205360101	M2	28.39	91.79
		0205360101	M1	27.30	96.23
40425	15	0201670101	PN	17.70	100.15
		0201670101	M2	21.21	100.15
		0201670101	M1	20.90	86.25
		0651910401	M2	36.45	85.62
		0651910401	M1	36.29	98.68
		0651910401	PN	31.81	99.79
		0651910501	M2	31.00	90.87
		0651910501	M1	30.85	99.68
		0651910501	PN	28.14	99.84
		0651910601	PN	25.84	100.10
		0651910601	M2	32.60	90.66
		0651910601	M1	30.94	99.73
		0651910701	M1	30.33	95.06
		0651910701	M2	31.37	96.59
		0651910701	PN	27.10	100.00
40562	6	0108260201	M2	81.90	100.04
		0108260201	PN	54.79	100.12
		0108260201	M1	80.95	93.40
		0673310101	PN	37.19	74.09
		0673310101	M1	39.31	94.36

		0673310101	M2	39.93	96.21
40644	3	0108260201	M1	80.95	86.61
		0108260201	PN	54.79	99.71
		0108260201	M2	81.90	99.80
40705	3	0110930701	M2	11.67	100.09
		0110930701	PN	8.19	62.05
		0110930701	M1	11.67	91.76
40809	3	0651790101	PN	3.00	85.18
		0651790101	M1	16.72	91.40
		0651790101	M2	20.21	92.04
40962	3	0550540101	PN	71.50	100.31
		0550540101	M2	75.02	71.22
		0550540101	M1	74.57	78.90
41107	2	0722670201	M2	70.71	85.63
		0722670201	PN	60.05	99.98
41189	15	0112550601	M1	15.14	93.59
		0112550601	PN	12.41	99.60
		0112550601	M2	15.14	99.70
		0200130101	PN	80.52	86.28
		0200130101	M2	84.31	96.48
		0200130101	M1	83.85	98.55
		0722670601	PN	11.13	86.13
		0722670601	M2	25.93	99.03
		0722670601	M1	23.73	99.75
		0761630101	M2	107.26	87.96
		0761630101	PN	92.80	94.07
		0761630101	M1	101.97	94.17
		0761630201	M2	99.98	87.72
		0761630201	M1	97.20	93.59
		0761630201	PN	85.89	93.88
41566	3	0203170301	PN	76.07	100.35
		0203170301	M2	87.91	88.13
		0203170301	M1	87.59	90.52
41729	3	0722960101	PN	49.70	33.14
		0722960101	M1	52.49	90.31
		0722960101	M2	52.50	99.90
41763	3	0404120101	PN	30.04	80.87
		0404120101	M1	31.61	82.54
		0404120101	M2	31.62	96.48
41823	3	0551450301	M2	19.49	87.53
		0551450301	PN	5.63	91.11
		0551450301	M1	17.91	96.42
41857	3	0722960101	M2	52.50	77.33
		0722960101	PN	49.70	77.82
		0722960101	M1	52.49	99.98

41912	3	0403100101	M1	71.47	58.38
		0403100101	PN	63.76	88.17
		0403100101	M2	72.78	93.06
41967	3	0651740301	M2	4.96	78.67
		0651740301	PN	4.53	97.74
		0651740301	M1	4.91	99.84
42408	3	0721910301	M2	6.10	86.58
		0721910301	PN	0.20	93.57
		0721910301	M1	5.72	95.10
42637	3	0110900201	PN	41.96	90.33
		0110900201	M2	50.04	92.08
		0110900201	M1	49.72	94.68
42699	6	0202730301	M1	38.41	79.46
		0202730301	PN	33.89	87.57
		0202730301	M2	38.58	99.85
		0504240101	M1	86.36	79.13
		0504240101	PN	76.49	88.69
		0504240101	M2	89.36	99.68
42727	3	0202180201	PN	63.78	75.17
		0202180201	M2	78.67	92.00
		0202180201	M1	78.30	99.94
42816	6	0021540201	PN	47.74	86.93
		0021540201	M2	51.34	99.42
		0021540201	M1	51.34	99.80
		0502160101	PN	70.70	87.00
		0502160101	M2	75.50	99.33
		0502160101	M1	74.93	99.51
42999	3	0110980201	M2	57.81	100.02
		0110980201	M1	57.81	100.07
		0110980201	PN	54.43	87.76
43511	3	0008220201	PN	37.34	100.15
		0008220201	M1	39.74	100.15
		0008220201	M2	39.74	94.83
43843	6	0305360501	M1	15.32	67.67
		0305360501	M2	15.68	90.41
		0305360501	PN	13.68	91.35
		0305361501	M1	18.67	60.32
		0305361501	PN	17.04	73.34
		0305361501	M2	18.67	99.85
44418	2	0094383201	M2	5.96	98.29
		0094383201	M1	5.96	99.55
44536	9	0141150101	M2	27.97	86.48
		0141150101	PN	14.63	88.44
		0141150101	M1	27.97	99.91
		0141150401	PN	4.72	86.28

		0141150401	M2	9.85	88.26
		0141150401	M1	9.53	99.88
		0141150501	M2	10.71	86.32
		0141150501	PN	2.20	89.93
		0141150501	M1	10.71	98.72
44968	3	0124710801	M1	27.22	90.46
		0124710801	PN	22.15	99.97
		0124710801	M2	27.28	99.97
45700	3	0020540401	M2	49.17	84.69
		0020540401	M1	49.17	98.97
		0020540401	PN	46.95	99.41
47333	3	0305361601	M1	31.56	91.23
		0305361601	PN	29.92	99.08
		0305361601	M2	31.57	99.69
47337	3	0041180801	PN	17.43	100.01
		0041180801	M2	17.77	84.99
		0041180801	M1	17.82	99.75
47368	27	0142770101	PN	17.05	84.87
		0142770101	M2	18.67	89.37
		0142770101	M1	18.67	96.88
		0142770301	M2	7.34	86.88
		0142770301	PN	4.48	90.97
		0142770301	M1	7.19	97.19
		0150650301	M2	8.33	86.67
		0150650301	PN	6.05	89.42
		0150650301	M1	8.27	96.54
		0405690101	PN	1.94	84.62
		0405690101	M2	5.90	89.02
		0405690101	M1	5.93	96.53
		0405690201	PN	35.37	84.86
		0405690201	M2	44.99	86.41
		0405690201	M1	44.83	96.91
		0405690501	PN	25.17	84.43
		0405690501	M2	32.26	89.75
		0405690501	M1	31.43	96.69
		0693850701	M2	16.62	87.80
		0693850701	PN	12.04	88.65
		0693850701	M1	16.56	96.99
		0693851401	M2	16.62	87.45
		0693851401	PN	15.04	89.55
		0693851401	M1	16.57	96.90
		0741960101	PN	21.34	88.81
		0741960101	M2	22.92	89.42
		0741960101	M1	22.95	92.64
47503	3	0112240301	PN	27.40	100.26

		0112240301	M2	33.06	100.26
		0112240301	M1	33.07	77.67
48240	3	0152940101	M1	49.97	92.41
		0152940101	PN	39.03	99.89
		0152940101	M2	49.92	99.89
49221	3	0147540101	M1	23.02	83.92
		0147540101	M2	23.18	99.67
		0147540101	PN	21.61	99.88
49468	5	0204410201	M2	1.40	80.88
		0204410201	M1	1.40	97.38
		0404240101	M2	16.28	81.54
		0404240101	PN	13.30	90.01
		0404240101	M1	15.96	97.80
49921	6	0098010101	M1	34.21	100.39
		0098010101	M2	34.02	78.57
		0098010101	PN	29.88	96.68
		0551830101	M2	79.97	85.24
		0551830101	PN	60.89	99.86
		0551830101	M1	77.46	99.86
50063	9	0104260101	M1	40.50	89.67
		0104260101	M2	41.02	91.52
		0104260101	PN	29.06	91.80
		0164560701	PN	23.50	83.78
		0164560701	M1	26.94	87.95
		0164560701	M2	27.25	90.61
		0212480201	M1	27.99	88.42
		0212480201	M2	29.36	89.06
		0212480201	PN	18.97	92.09
50810	3	0103660101	PN	24.63	77.61
		0103660101	M1	34.62	86.79
		0103660101	M2	34.51	93.12
50881	3	0145480101	M1	21.17	87.75
		0145480101	M2	21.27	90.63
		0145480101	PN	15.28	99.70
50886	3	0103660101	M2	34.51	99.71
		0103660101	PN	24.63	99.93
		0103660101	M1	34.62	99.93
50944	3	0148620101	PN	14.97	99.90
		0148620101	M1	21.40	99.90
		0148620101	M2	22.08	99.90
51210	3	0762640101	M2	37.62	88.16
		0762640101	M1	37.63	88.29
		0762640101	PN	36.03	90.77
51353	3	0651740801	M2	9.12	78.70
		0651740801	M1	9.12	89.32

		0651740801	PN	6.23	94.29
51485	2	0744240101	PN	82.52	76.13
		0744240101	M2	84.49	99.75
51791	3	0501540201	PN	14.62	77.91
		0501540201	M2	16.57	99.77
		0501540201	M1	16.56	99.97
52112	6	0305920401	M2	24.38	78.50
		0305920401	M1	23.89	89.16
		0305920401	PN	18.73	95.01
		0674810501	M2	13.22	79.46
		0674810501	M1	13.21	89.58
		0674810501	PN	11.63	96.18
52318	2	0111530101	M1	52.04	91.04
		0111530101	M2	52.04	91.11
52939	9	0057560301	PN	36.54	100.17
		0057560301	M2	39.06	91.54
		0057560301	M1	39.01	93.05
		0148520101	M1	25.27	94.37
		0148520101	M2	25.17	98.65
		0148520101	PN	21.85	99.64
		0148520301	M1	32.05	94.44
		0148520301	M2	32.13	98.26
		0148520301	PN	29.83	99.71
53231	3	0150350101	PN	24.30	83.84
		0150350101	M1	31.42	93.54
		0150350101	M2	31.30	99.59
53245	3	0150350101	PN	24.30	100.14
		0150350101	M1	31.42	100.14
		0150350101	M2	31.30	79.10
53559	3	0401270301	M1	11.01	100.32
		0401270301	PN	8.00	80.32
		0401270301	M2	11.69	99.50
53683	1	0302460101	PN	26.27	99.67
54032	3	0402781001	PN	16.29	100.30
		0402781001	M1	18.38	43.69
		0402781001	M2	18.39	70.47
54219	3	0744411101	M2	33.35	100.07
		0744411101	PN	12.80	79.93
		0744411101	M1	31.81	99.27
54470	21	0145190101	PN	15.17	87.19
		0145190101	M2	22.00	94.70
		0145190101	M1	21.53	96.38
		0145190201	PN	18.70	87.16
		0145190201	M2	32.20	94.58
		0145190201	M1	31.05	96.32

		0673920201	M2	16.95	93.20
		0673920201	PN	6.74	93.35
		0673920201	M1	16.22	96.20
		0673920301	M2	18.62	92.72
		0673920301	PN	15.44	93.65
		0673920301	M1	18.56	96.24
		0724810201	PN	24.43	83.29
		0724810201	M1	32.53	87.53
		0724810201	M2	34.37	93.37
		0724810401	PN	26.93	80.56
		0724810401	M1	35.15	88.69
		0724810401	M2	35.11	94.49
		0729561301	PN	42.03	87.64
		0729561301	M1	43.65	88.87
		0729561301	M2	43.62	90.93
54479	3	0744930401	M1	67.95	99.37
		0744930401	PN	60.34	99.69
		0744930401	M2	68.36	99.69
55616	3	0740620101	PN	4.38	100.09
		0740620101	M1	8.77	89.21
		0740620101	M2	9.09	89.67
55696	2	0745010101	M2	40.19	84.82
		0745010101	PN	34.72	99.62
55717	2	0740620301	PN	39.69	99.69
		0740620301	M2	48.45	99.97
55976	3	0655380901	M1	18.62	70.95
		0655380901	PN	16.43	74.07
		0655380901	M2	18.62	99.99
56536	3	0694440201	PN	30.75	100.48
		0694440201	M2	34.62	100.48
		0694440201	M1	34.61	83.71
57924	3	0164560801	M2	11.08	87.95
		0164560801	PN	5.19	93.31
		0164560801	M1	10.61	99.82
58090	3	0691010901	PN	18.03	99.09
		0691010901	M1	29.68	99.54
		0691010901	M2	30.37	99.77
58130	6	0505010501	M2	13.62	78.49
		0505010501	M1	13.62	89.25
		0505010501	PN	10.64	96.83
		0505011201	M2	17.42	78.49
		0505011201	PN	16.04	95.75
		0505011201	M1	17.25	99.87
58132	4	0691010101	PN	31.75	82.28
		0691010101	M2	42.17	92.20

		0691011001	PN	29.33	100.46
		0691011001	M2	30.09	92.07
58152	6	0691010101	PN	31.75	79.14
		0691010101	M1	40.29	90.89
		0691010101	M2	42.17	96.20
		0691011001	PN	29.33	82.77
		0691011001	M1	29.91	90.22
		0691011001	M2	30.09	91.50
58189	6	0691010101	M1	40.29	85.75
		0691010101	M2	42.17	99.38
		0691010101	PN	31.75	99.60
		0691011001	M2	30.09	78.86
		0691011001	M1	29.91	92.85
		0691011001	PN	29.33	99.89
58715	3	0723260201	M2	35.59	91.69
		0723260201	M1	35.56	92.94
		0723260201	PN	33.01	99.58
58813	3	0782530501	M2	6.62	81.89
		0782530501	M1	6.65	89.95
		0782530501	PN	5.04	94.72
59498	2	0305750701	M2	1.49	88.16
		0305750701	M1	1.22	98.32
61742	2	0602420301	M2	5.32	86.10
		0602420301	M1	2.86	98.43
65001	25	0200670101	M1	4.21	92.75
		0200670101	M2	4.31	93.07
		0200670301	PN	9.70	90.67
		0200670301	M1	12.14	92.80
		0200670301	M2	12.11	93.12
		0200670401	PN	3.50	90.69
		0200670401	M1	9.68	92.98
		0200670401	M2	10.10	93.14
		0401360201	M1	4.77	92.12
		0401360201	M2	5.30	92.92
		0401360301	PN	3.37	90.62
		0401360301	M1	6.37	92.47
		0401360301	M2	6.91	92.90
		0500730101	PN	23.61	90.44
		0500730101	M1	28.19	92.05
		0500730101	M2	29.29	92.67
		0500730201	M1	32.88	89.81
		0500730201	PN	31.32	90.41
		0500730201	M2	33.61	92.69
		0691570101	M1	112.95	79.20
		0691570101	M2	114.85	90.46

		0691570101	PN	99.43	90.86
		0794581201	M1	45.57	70.48
		0794581201	M2	46.65	88.64
		0794581201	PN	41.35	90.57
67045	5	0200230201	PN	7.32	87.58
		0200230201	M2	10.81	89.18
		0200230201	M1	10.75	96.31
		0503460101	M2	14.98	91.17
		0503460101	M1	14.40	95.59
71031	12	0112310201	M1	22.61	84.96
		0112310201	M2	22.61	92.56
		0112310201	PN	19.69	99.69
		0204610101	M1	77.97	83.34
		0204610101	PN	71.99	99.95
		0204610101	M2	78.44	99.95
		0405380701	M2	9.62	82.42
		0405380701	PN	3.00	88.91
		0405380701	M1	9.04	97.35
		0782720301	M1	99.52	83.22
		0782720301	M2	99.79	99.90
		0782720301	PN	65.51	99.93
71066	11	0112310201	M1	22.61	77.06
		0112310201	M2	22.61	97.54
		0204610101	PN	71.99	0.96
		0204610101	M1	77.97	82.05
		0204610101	M2	78.44	94.09
		0405380701	PN	3.00	84.46
		0405380701	M1	9.04	84.47
		0405380701	M2	9.62	86.95
		0782720301	PN	65.51	1.13
		0782720301	M1	99.52	67.04
		0782720301	M2	99.79	94.54
73854	3	0404410201	M2	52.08	100.27
		0404410201	M1	51.76	90.01
		0404410201	PN	48.22	95.43
73858	5	0404410101	PN	43.50	100.11
		0404410101	M2	46.54	98.91
		0404410201	PN	48.22	100.26
		0404410201	M1	51.76	69.14
		0404410201	M2	52.08	69.74
73862	3	0404410201	M1	51.76	82.40
		0404410201	PN	48.22	87.79
		0404410201	M2	52.08	88.32
73875	3	0404410201	PN	48.22	74.36
		0404410201	M2	52.08	99.66

		0404410201	M1	51.76	99.97
94158	3	0550270101	PN	7.89	95.81
		0550270101	M2	3.09	99.74
		0550270101	M1	3.09	99.96
140771	44	0603190101	M1	18.56	76.95
		0603190101	M2	18.62	84.80
		0603190101	PN	17.04	99.58
		0603190201	PN	18.03	100.00
		0603190201	M1	19.61	73.98
		0603190201	M2	19.62	88.62
		0603190301	PN	12.83	100.21
		0603190301	M1	13.62	66.76
		0603190301	M2	13.99	90.45
		0603190401	M1	1.72	60.96
		0603190401	PN	8.13	89.89
		0603190401	M2	1.92	91.87
		0603190501	M2	19.62	100.21
		0603190501	M1	19.61	58.91
		0603190501	PN	18.03	80.62
		0764800101	PN	33.48	80.55
		0764800101	M1	52.13	87.84
		0764800101	M2	55.73	99.72
		0764800201	M2	41.53	100.00
		0764800201	M1	42.25	85.86
		0764800201	PN	27.94	92.86
		0764800301	M2	58.23	100.14
		0764800301	PN	32.16	87.06
		0764800301	M1	57.58	89.18
		0764800401	PN	20.39	84.87
		0764800401	M1	23.78	91.02
		0764800401	M2	23.97	99.93
		0764800501	M2	61.61	100.14
		0764800501	PN	54.32	77.79
		0764800501	M1	61.65	91.44
		0764800601	PN	54.00	77.02
		0764800601	M1	56.44	91.66
		0764800601	M2	56.48	99.51
		0764800801	PN	31.60	78.43
		0764800801	M2	54.14	78.57
		0764800801	M1	49.10	88.33
		0764800901	M2	51.62	73.27
		0764800901	M1	51.63	73.76
		0764800901	PN	43.73	95.05
		0770180101	PN	39.13	100.21
		0770180101	M1	55.23	73.83

		0770180101	M2	55.22	75.18
		0770180201	PN	56.44	100.36
		0770180201	M2	58.62	90.53
165662	3	0201902001	M1	27.96	100.24
		0201902001	PN	24.24	100.31
		0201902001	M2	28.06	81.58
200253	3	0103260801	PN	71.17	95.29
		0103260801	M1	12.49	99.44
		0103260801	M2	80.33	99.44
1126633	3	0200480401	PN	13.04	100.07
		0200480401	M2	16.67	72.18
		0200480401	M1	16.51	85.31
1154498	3	0651740901	M1	5.57	90.65
		0651740901	PN	2.13	97.99
		0651740901	M2	6.10	99.87
1160119	3	0724440401	PN	17.45	77.75
		0724440401	M1	20.00	99.71
		0724440401	M2	20.89	99.93
1168578	3	0400570301	PN	18.06	75.63
		0400570301	M1	24.98	86.16
		0400570301	M2	25.82	91.61
1284684	2	0744411201	PN	23.73	100.15
		0744411201	M2	31.05	100.15
1412010	3	0723161001	M1	16.35	54.07
		0723161001	M2	16.32	69.82
		0723161001	PN	11.84	99.74
1509913	1	0502091601	M2	87.12	100.19
1527695	4	0722570301	PN	18.73	100.01
		0722570301	M2	21.75	99.79
		0722570501	M2	62.36	99.34
		0722570501	PN	34.34	99.42
1531425	3	0740620301	PN	39.69	83.69
		0740620301	M2	48.45	83.84
		0740620301	M1	47.63	92.02
1573473	3	0761510201	M1	25.08	84.50
		0761510201	PN	22.44	99.37
		0761510201	M2	25.26	99.77
1616588	3	0602200101	M2	24.57	100.18
		0602200101	M1	24.61	87.51
		0602200101	PN	20.74	88.03
1646009	3	0112650201	PN	19.96	74.69
		0112650201	M1	24.21	82.19
		0112650201	M2	24.21	98.91
1681191	2	0502690601	M2	45.08	100.24
		0502690601	PN	27.70	100.32

1750402	3	0025540301	PN	5.90	78.54
		0025540301	M2	11.96	82.28
		0025540301	M1	11.91	88.45
1817480	3	0210280101	M1	97.35	29.44
		0210280101	M2	100.57	98.47
		0210280101	PN	75.04	99.83
2141849	3	0138951401	M2	6.96	93.94
		0138951401	PN	5.34	99.96
		0138951401	M1	6.96	99.96
2156773	3	0553790101	M1	11.56	100.22
		0553790101	PN	10.03	95.99
		0553790101	M2	11.62	99.32
2177729	3	0673020201	M1	27.61	100.17
		0673020201	PN	23.80	77.15
		0673020201	M2	27.77	99.61
2468371	3	0200960101	M1	70.19	97.40
		0200960101	M2	72.75	99.66
		0200960101	PN	58.29	99.74
2568088	6	0741580101	M2	12.22	71.65
		0741580101	M1	12.24	83.11
		0741580101	PN	10.53	99.81
		0764910201	M2	30.00	100.30
		0764910201	M1	33.29	92.64
		0764910201	PN	32.63	99.47
2816038	3	0109462201	PN	5.00	100.02
		0109462201	M2	7.60	100.02
		0109462201	M1	7.59	85.60
3094758	3	0762640101	PN	36.03	100.28
		0762640101	M2	37.62	100.28
		0762640101	M1	37.63	91.17
3105149	3	0760230401	M2	21.35	100.03
		0760230401	M1	21.29	38.96
		0760230401	PN	19.27	96.10
3122018	3	0402780501	M1	16.74	82.40
		0402780501	M2	16.75	86.35
		0402780501	PN	14.46	95.92
3390074	1	0554540201	PN	47.17	93.55
3408576	3	0554121001	M1	13.61	78.11
		0554121001	PN	12.03	79.62
		0554121001	M2	13.62	91.72
3532807	3	0504100201	PN	20.04	100.01
		0504100201	M1	21.60	91.23
		0504100201	M2	21.61	96.77
3737721	3	0670880501	M2	60.59	30.19
		0670880501	PN	53.58	57.48

		0670880501	M1	59.69	95.09
3845383	6	0109930101	M2	47.48	100.04
		0109930101	PN	35.41	100.18
		0109930101	M1	46.93	92.13
		0723801501	PN	111.59	78.17
		0723801501	M1	117.97	84.15
		0723801501	M2	118.01	84.52

Table of X-ray properties of the star forming galaxies. Column (1) gives the catalogue ID (PGC number) of each galaxy; Column (2) gives the total number of observations (Nobs) for the different combinations OBSIDs and detectors; Column (3) gives the observation ID of *XMM-Newton* and Column (4) the corresponding detector (EPIC M1, M2, or pn); Column (5) gives the exposure time of each observation, and Column (6) the angular extent of the galaxy covered in each observation.

Table 4.4: Count-rate to flux conversion and count-rates for the star-forming sample.

PGC (1)	OBSID (2)	Det (3)	fbroad 10^{-11} $erg/s/cm^2$ (4)	fhard 10^{-11} $erg/s/cm^2$ (5)	cr2 cnts/s (6)	cr_bkg2 cnts/s (7)	cr3 cnts/s (8)	cr_bkg3 cnts/s (9)	cr4 cnts/s (10)	cr_bkg4 cnts/s (11)
1014	0028740101	M2	1.52	3.76	112.82	52.70	155.43	74.64	86.51	53.66
1014	0028740101	PN	0.51	1.46	533.95	284.94	474.98	228.45	321.87	233.38
1014	0028740201	M1	2.00	5.02	92.75	37.04	141.37	58.70	68.15	32.94
1014	0028740201	M2	2.39	5.95	113.14	44.11	161.68	68.80	82.30	40.86
1014	0028740201	PN	0.72	2.09	470.34	200.49	375.40	192.54	222.09	129.61
1014	0655050101	M2	1.75	4.27	96.11	46.90	180.31	108.98	104.50	74.07
1014	0655050101	M1	1.84	4.59	61.87	26.16	112.34	69.54	67.54	48.06
1014	0655050101	PN	0.60	1.75	443.49	206.39	432.89	249.51	337.62	268.33
1014	2008740101	M1	1.52	3.80	109.46	56.27	159.12	78.43	94.51	59.64
1142	0403760701	M1	1.19	2.88	1.50	1.42	3.22	2.80	3.01	2.78
1142	0403760701	M2	1.30	3.14	1.30	1.14	2.68	2.51	2.62	2.30
1142	0403760701	PN	0.38	1.05	5.50	2.17	4.65	3.50	3.50	3.88
2388	0203690101	M2	1.28	3.16	5.16	1.42	7.92	3.02	4.91	2.59
2388	0203690101	M1	1.36	3.40	5.01	1.45	6.41	3.29	4.36	2.47
2388	0203690101	PN	0.40	1.14	28.10	7.54	20.75	7.19	15.11	9.60
2758	0601010101	M2	1.29	3.09	85.64	53.97	170.40	143.17	126.62	114.07
2758	0601010101	M1	1.37	3.36	88.96	59.86	172.67	147.18	139.96	128.81
2758	0601010101	PN	0.44	1.26	422.10	235.10	409.03	320.34	404.05	364.44
2758	0728190101	M2	1.22	2.92	140.74	57.39	224.04	105.86	149.20	94.35
2758	0728190101	M1	1.80	4.41	137.15	63.75	217.05	119.91	157.50	111.07
2758	0728190101	PN	0.41	1.18	774.26	343.65	767.94	409.84	635.94	493.46
3238	0112800101	M2	1.30	3.14	121.08	86.44	162.34	129.81	90.42	76.67
3238	0112800101	M1	1.30	3.18	114.58	81.58	159.12	126.47	93.63	79.15
3238	0112800201	M2	1.30	3.14	116.33	95.93	166.93	146.79	126.23	115.89
3238	0112800201	M1	1.31	3.19	110.88	88.22	160.92	139.63	124.10	114.17
3238	0112800201	PN	0.46	1.26	465.61	371.32	359.88	301.10	364.11	328.31
3238	0305860301	M2	1.37	3.27	134.05	98.75	228.07	195.16	124.07	113.56
3238	0305860301	M1	1.48	3.62	114.28	83.34	197.47	167.23	111.73	100.00
3238	0305860301	PN	0.47	1.29	495.40	346.13	407.71	327.45	355.37	327.27
3238	0305860401	M2	1.46	3.49	129.70	101.23	228.32	205.52	156.08	145.01
3238	0305860401	M1	1.64	4.01	128.43	97.69	222.25	198.88	167.80	155.67
3238	0305860401	PN	0.51	1.41	647.14	505.38	556.66	478.02	583.02	546.44
3238	0656780401	M2	1.33	3.16	130.53	117.19	262.87	255.79	180.62	176.32
3238	0656780401	M1	1.71	4.15	109.78	87.42	217.85	194.86	150.62	141.95
3238	0656780401	PN	0.47	1.28	566.92	459.36	496.76	420.15	483.97	446.77
4979	0721900501	M2	1.08	2.57	1.96	1.32	3.98	3.09	2.45	1.79
4979	0721900501	M1	1.09	2.64	2.35	1.43	4.20	3.52	3.49	2.08
4979	0721900501	PN	0.44	1.21	11.88	7.66	11.76	7.46	9.24	7.97

4979	0782010101	M1	1.26	3.05	1.95	1.39	4.79	3.84	2.79	2.45
4979	0782010101	M2	1.26	3.00	1.60	1.29	5.24	4.14	2.99	2.67
4979	0782010101	PN	0.44	1.23	9.27	6.88	11.16	8.19	10.53	9.15
5193	0025541601	M2	1.01	2.43	8.83	2.52	8.99	6.37	6.79	3.91
5193	0025541601	PN	0.35	0.96	35.78	11.86	29.53	11.78	24.55	12.05
5193	0025541601	M1	0.99	2.39	10.51	2.84	13.24	4.99	8.22	5.26
6972	0109980101	M2	1.29	3.14	8.95	6.63	12.63	12.00	5.02	4.27
6972	0109980101	M1	1.44	3.57	10.42	7.36	15.22	13.42	4.87	4.88
6972	0109980101	PN	0.41	1.14	56.16	41.13	51.48	44.22	18.09	15.25
6972	0504780101	M1	1.46	3.58	12.54	8.49	19.38	16.85	10.44	9.15
6972	0504780101	M2	1.83	4.43	8.36	6.42	15.68	13.31	7.40	7.05
6972	0504780101	PN	0.47	1.28	49.10	38.10	46.48	45.38	24.44	22.51
6972	0504780201	M1	1.46	3.58	11.41	8.19	17.31	15.28	8.35	7.10
6972	0504780201	M2	1.85	4.46	7.68	5.97	12.32	11.12	5.77	5.05
6972	0504780201	PN	0.47	1.28	48.37	36.47	47.98	44.68	24.09	21.71
11631	0201120101	PN	1.06	3.24	11.79	5.32	11.46	7.27	16.03	12.23
11631	0201120101	M1	3.58	9.12	2.60	1.93	4.23	3.80	4.42	3.64
12286	0106860101	M2	1.10	2.63	145.76	58.07	218.98	79.91	139.18	74.79
12286	0106860101	M1	1.10	2.67	169.71	60.87	268.57	80.57	168.03	74.51
12286	0106860101	PN	0.41	1.11	710.45	241.60	723.72	200.87	458.68	244.85
12286	0150280301	M1	1.52	3.73	123.05	75.37	209.66	110.87	122.28	80.87
12286	0150280301	M2	1.54	3.75	140.24	70.16	267.53	117.54	144.36	79.47
12286	0150280301	PN	0.56	1.58	1009.03	311.76	1284.37	334.69	623.59	207.22
12286	0150280401	M1	1.52	3.73	158.30	90.99	283.69	147.02	214.57	151.79
12286	0150280401	M2	1.54	3.75	205.96	101.84	387.66	150.99	256.21	154.04
12286	0150280401	PN	0.56	1.57	959.02	363.05	1218.79	288.19	607.63	228.76
12286	0150280501	M1	1.52	3.72	196.16	94.65	363.14	145.26	255.34	163.78
12286	0150280501	M2	1.54	3.75	151.64	92.51	273.38	144.06	208.38	150.75
12286	0150280501	PN	0.56	1.57	1046.22	526.32	1286.24	623.51	1072.60	837.12
12286	0150280601	M1	1.49	3.65	221.39	96.89	387.90	148.74	244.17	135.19
12286	0150280601	M2	1.54	3.74	191.25	81.20	350.49	137.16	207.36	117.00
12286	0150281101	M1	1.47	3.61	211.78	72.66	405.91	115.22	222.07	94.49
12286	0150281101	M2	1.54	3.74	188.51	75.59	359.94	119.56	197.96	92.70
12286	0150281101	PN	0.54	1.53	860.86	313.27	1082.87	336.25	722.51	409.52
12286	0205230201	M2	1.28	3.09	288.61	167.70	490.54	253.61	410.19	307.82
12286	0205230201	M1	1.30	3.19	211.07	132.73	319.65	201.21	298.18	243.01
12286	0205230201	PN	0.46	1.29	1353.41	1039.49	1739.38	1152.44	1658.26	1508.42
12286	0205230301	M2	1.27	3.07	214.77	52.49	478.63	102.23	227.93	58.06
12286	0205230301	M1	1.29	3.16	199.94	52.78	435.24	87.06	218.32	55.10
12286	0205230301	PN	0.46	1.30	890.71	279.79	1132.46	262.19	572.54	178.43
12286	0205230401	M2	1.31	3.17	247.66	128.44	365.86	174.50	216.26	164.92
12286	0205230401	M1	1.39	3.42	250.17	132.81	397.11	195.67	282.01	224.91
12286	0205230401	PN	0.46	1.28	1100.49	606.03	1138.45	637.15	818.76	681.97
12286	0205230501	M2	1.50	3.64	178.56	67.54	327.93	91.17	166.48	61.79
12286	0205230501	M1	1.54	3.79	170.51	65.57	335.91	108.60	177.32	75.15

12286	0205230501	PN	0.55	1.56	538.33	223.88	551.78	205.28	340.82	196.90
12286	0205230601	M1	1.40	3.46	167.58	66.85	292.32	112.46	167.53	80.88
12286	0205230601	M2	1.50	3.65	156.69	64.09	286.51	103.09	165.97	81.48
12286	0205230601	PN	18.11	50.90	836.13	306.35	858.94	303.91	581.18	318.72
12286	0301860101	M1	1.38	3.36	143.70	61.20	295.20	117.30	155.28	65.50
12286	0301860101	M2	1.43	3.42	153.75	60.24	324.32	121.26	162.72	64.77
12286	0405090101	M2	1.11	2.62	151.90	57.36	273.95	108.40	170.71	90.41
12286	0405090101	M1	1.11	2.68	155.30	51.39	272.57	99.49	170.33	82.77
12286	0405090101	PN	0.41	1.12	665.74	245.59	668.37	194.74	422.36	202.16
12286	0693850501	M2	1.12	2.64	156.57	52.37	277.67	92.86	155.74	64.87
12286	0693850501	M1	1.13	2.71	140.29	60.61	245.63	97.58	145.36	70.02
12286	0693850501	PN	0.41	1.13	702.84	213.15	727.22	197.33	436.42	198.53
12286	0693851201	M2	1.12	2.65	158.61	49.41	281.42	93.78	154.57	64.37
12286	0693851201	M1	1.13	2.72	168.13	65.69	291.13	101.63	174.44	81.61
12286	0693851201	PN	0.41	1.13	705.31	244.44	742.98	231.64	478.11	247.57
12286	0722650101	M2	1.31	3.12	165.09	70.58	283.73	106.22	182.22	98.55
12286	0722650101	M1	1.35	3.28	143.21	68.36	226.72	97.32	151.40	85.25
12286	0722650101	PN	0.45	1.24	738.83	301.40	747.02	243.76	487.17	255.86
12286	0742490101	M2	1.41	3.36	119.19	54.79	196.65	80.82	114.24	59.05
12286	0742490101	M1	2.47	5.98	62.11	27.73	91.36	41.95	52.18	30.83
12286	0742490101	PN	0.49	1.35	658.23	231.97	657.89	190.50	410.76	196.76
12286	0742590301	M2	1.12	2.63	177.50	38.26	389.41	86.64	197.41	45.95
12286	0742590301	M1	1.12	2.70	192.79	48.36	423.89	88.60	216.39	48.93
12286	0742590301	PN	0.41	1.13	902.15	213.93	1148.33	235.75	568.92	149.20
12286	0764770101	M2	1.56	3.75	129.52	60.05	249.32	119.20	150.41	87.52
12286	0764770101	M1	1.73	4.25	129.48	64.22	237.91	112.08	153.57	93.74
12286	0764770101	PN	0.56	1.59	481.50	292.86	463.32	273.63	374.72	292.69
12286	0764770401	M2	1.42	3.40	270.46	118.16	639.03	159.58	427.64	157.32
12286	0764770401	M1	1.71	4.20	222.13	78.64	547.93	139.24	379.14	127.19
12286	0764770401	PN	0.46	1.30	1110.04	304.03	1708.08	330.07	1045.33	312.19
12286	0782310101	M2	1.25	2.95	93.53	52.78	185.30	101.48	98.56	59.12
12286	0782310101	M1	2.14	5.18	123.66	32.10	229.70	63.66	114.67	34.41
12286	0782310101	PN	0.44	1.21	791.02	273.33	1002.47	245.15	553.86	224.51
12286	0794580601	M2	1.13	2.66	97.23	50.16	190.55	105.10	117.24	76.93
12286	0794580601	M1	1.14	2.75	117.23	55.92	229.02	108.48	138.74	77.76
12286	0794580601	PN	0.41	1.12	649.36	248.98	734.78	230.67	447.66	223.94
12418	0781040101	PN	1.12	3.25	5.36	3.72	5.22	5.05	5.85	5.64
12418	0781040101	M2	2.89	7.29	1.17	1.05	3.08	3.31	2.31	2.06
12418	0781040101	M1	3.00	7.45	1.66	1.38	3.79	3.24	3.40	2.68
12486	0781040101	M2	1.25	2.97	1.00	0.81	2.59	1.94	0.96	1.04
12486	0781040101	M1	1.29	3.08	0.93	0.93	2.19	1.88	1.43	1.22
12486	0781040101	PN	0.52	1.39	3.96	3.16	5.29	4.10	4.26	3.96
12785	0103861001	PN	0.40	1.11	20.46	6.73	10.94	4.44	4.59	3.53
12785	0402110201	M1	1.17	2.84	4.40	1.67	3.88	2.12	2.03	1.21
12785	0402110201	M2	1.18	2.83	3.40	1.35	2.98	2.08	1.61	1.15

12785	0402110201	PN	0.77	2.22	19.71	7.17	8.61	3.43	4.28	3.62
12785	0760230401	PN	0.42	1.16	21.58	6.35	9.85	4.38	5.44	4.56
14236	0110980401	M2	1.03	2.46	16.16	3.38	25.06	5.83	14.90	5.83
14236	0110980401	PN	0.36	0.97	74.47	13.21	67.69	11.81	39.94	13.75
14236	0110980401	M1	0.98	2.36	17.16	3.67	28.53	6.03	19.61	6.44
15345	0112290801	M1	1.10	2.41	28.48	6.98	45.06	9.99	14.15	7.65
15345	0112290801	M2	1.14	2.45	26.66	6.13	37.21	8.48	13.85	6.45
15345	0112290801	PN	0.42	0.97	123.88	17.20	103.87	18.58	38.50	16.20
16282	0148650101	M1	1.05	2.55	4.93	1.69	4.46	3.17	3.27	2.75
16282	0148650101	M2	1.06	2.56	4.17	1.61	3.89	2.73	3.06	2.56
16282	0148650101	PN	0.31	0.89	18.78	4.54	7.49	3.70	4.76	4.33
21396	0150651101	M2	1.25	3.02	300.19	270.98	445.69	366.49	470.23	424.36
21396	0150651101	M1	1.26	3.08	304.19	276.56	477.92	395.98	526.42	479.24
21396	0150651101	PN	0.44	1.22	308.48	1189.61	185.86	505.74	849.86	780.56
21396	0150651201	M2	1.23	2.96	262.40	214.98	454.28	348.36	451.86	394.61
21396	0150651201	M1	1.26	3.07	233.60	172.39	442.13	306.25	491.45	422.42
21396	0150651201	PN	0.45	1.24	932.69	684.69	1083.52	853.03	1293.97	1164.53
21396	0164560901	M2	1.35	3.23	162.51	113.31	331.25	224.13	260.90	198.12
21396	0164560901	M1	1.37	3.31	162.21	113.30	328.85	232.98	284.85	226.57
21396	0164560901	PN	0.48	1.32	576.23	348.06	649.49	323.19	511.12	341.36
22805	0138951401	PN	1.05	3.08	14.12	4.16	7.81	5.50	8.97	6.27
22805	0138951401	M1	2.36	5.88	2.85	1.32	2.87	2.26	3.26	2.05
22805	0138951401	M2	2.67	6.94	3.24	2.47	5.32	3.70	3.63	2.04
23359	0108860501	PN	1.04	3.26	6.35	5.59	7.88	5.98	4.98	5.03
23359	0108860501	M1	3.56	9.20	0.91	0.82	1.95	1.22	2.34	1.21
23359	0108860501	M2	3.68	9.70	1.20	1.17	2.81	1.88	2.33	1.32
23504	0721900101	PN	1.97	5.84	9.75	7.66	11.58	8.87	11.51	10.56
23504	0721900101	M2	2.48	6.29	2.35	1.84	4.21	3.66	3.89	2.94
23504	0721900101	M1	2.74	6.87	2.82	2.90	5.33	4.71	3.90	3.95
23850	0502220201	PN	1.22	3.98	9.43	6.78	12.33	10.21	13.11	12.83
25363	0725290148	M1	2.07	5.22	1.37	0.93	4.82	2.55	0.00	1.34
25363	0725290148	M2	2.36	6.16	0.75	0.65	2.96	2.16	1.53	0.99
25363	0725290148	PN	0.67	1.94	7.49	6.19	6.57	5.57	9.30	5.92
25470	0745010301	M1	1.10	2.68	1.64	0.82	2.35	1.82	1.32	1.39
25470	0745010301	M2	1.11	2.67	1.15	0.81	2.20	1.45	1.28	1.13
25470	0745010301	PN	0.32	0.89	7.80	4.48	6.96	5.07	6.17	5.15
27077	0556280301	M1	1.08	2.66	86.25	25.09	109.33	64.93	64.76	47.65
27077	0556280301	M2	1.08	2.60	81.20	27.49	105.93	63.24	58.25	41.91
27077	0556280301	PN	0.38	1.06	383.07	151.62	237.55	114.44	169.04	128.50
27658	0203270101	M1	1.63	4.16	0.97	0.81	1.23	1.56	1.53	1.30
27658	0203270101	M2	1.78	4.52	1.05	0.81	1.38	1.74	1.21	1.46
27658	0203270101	PN	0.50	1.46	4.41	3.73	4.37	3.96	4.77	4.25
28655	0112290201	M1	1.08	2.59	994.91	160.62	1174.81	102.90	651.11	65.59
28655	0112290201	M2	1.08	2.57	901.04	172.92	1039.35	89.28	555.99	58.06
28655	0112290201	PN	0.42	1.13	4019.63	1397.27	3061.94	614.41	1649.06	362.05

28655	0206080101	M2	1.08	2.56	894.72	154.59	1070.13	107.33	467.40	62.59
28655	0206080101	M1	1.08	2.60	918.17	153.64	1111.33	96.43	479.57	62.84
28655	0206080101	PN	0.41	1.11	4029.98	638.47	3156.74	255.29	1295.22	162.89
28655	0560181301	M1	1.08	2.59	1099.46	270.41	1468.89	395.76	983.93	351.05
28655	0560181301	M2	1.08	2.55	1004.68	248.00	1333.40	327.35	854.71	274.28
28655	0560590101	M1	1.08	2.60	970.38	209.22	1606.62	125.90	1342.86	77.07
28655	0560590101	M2	1.09	2.56	809.17	183.27	1287.44	121.83	1108.35	73.33
28655	0560590101	PN	0.41	1.11	3991.78	1222.38	4392.95	602.73	3616.71	399.82
28655	0560590201	M1	1.08	2.60	990.66	162.13	1575.34	143.28	1124.69	110.41
28655	0560590201	M2	1.09	2.57	895.32	174.77	1405.99	173.47	1041.52	121.91
28655	0560590201	PN	0.41	1.11	4025.32	1788.20	4259.71	825.78	2925.99	402.11
28655	0560590301	M1	1.08	2.60	975.52	151.43	1415.17	156.58	845.87	124.63
28655	0560590301	M2	1.09	2.56	876.38	167.30	1270.19	168.23	774.37	144.02
28655	0560590301	PN	0.42	1.13	3975.09	1469.68	3657.18	683.60	1998.86	327.18
28655	0657800101	M1	1.09	2.61	1090.55	360.84	1374.92	370.34	850.94	390.14
28655	0657801901	M1	1.09	2.60	951.21	173.75	1133.88	96.82	456.54	50.30
28655	0657801901	M2	1.09	2.56	859.96	182.08	995.77	104.53	384.03	56.95
28655	0657801901	PN	0.42	1.12	3941.35	1612.13	2889.44	687.58	1117.90	240.67
28655	0657802101	M1	1.08	2.59	969.05	163.61	1174.79	136.87	547.51	84.22
28655	0657802101	M2	1.10	2.58	783.87	171.97	928.90	116.84	448.99	83.96
28655	0657802301	M1	1.08	2.58	991.03	180.11	1253.35	171.64	687.30	138.35
28655	0657802301	M2	1.09	2.55	756.69	190.35	980.98	176.21	560.64	135.81
28655	0657802301	PN	0.42	1.13	3871.90	1592.74	3204.06	737.82	1571.51	255.82
28682	0404240301	M1	1.19	2.87	2.35	0.38	3.31	1.90	1.17	1.10
28682	0404240301	PN	0.32	0.90	11.67	2.54	9.06	2.92	6.50	4.00
28990	0110930201	M1	1.32	3.34	2.32	1.08	4.97	1.67	2.96	0.88
28990	0110930201	M2	1.32	3.29	3.01	1.92	6.16	2.08	3.85	1.22
28990	0110930201	PN	0.49	1.41	13.83	8.00	17.50	4.96	9.75	3.50
28990	0147760101	M2	2.29	5.64	2.59	1.21	2.81	2.02	2.72	2.28
28990	0147760101	PN	0.48	1.42	16.32	8.99	18.51	10.12	16.83	13.21
28990	0147760101	M1	5.10	13.53	1.30	1.15	2.44	1.90	2.37	2.29
30087	0028740301	M2	1.27	3.14	54.39	44.31	84.15	78.30	97.85	96.85
30087	0028740301	M1	1.30	3.25	51.02	41.61	79.38	71.81	90.79	86.61
30087	0028740301	PN	0.48	1.39	168.91	120.97	145.36	115.81	148.46	134.26
31856	0147630101	M1	3.11	7.97	2.82	1.46	3.03	2.93	2.79	2.40
31856	0147630101	M2	3.33	8.83	2.54	1.24	4.14	3.63	3.29	2.30
31856	0147630101	PN	0.99	3.12	11.57	5.12	7.59	6.31	8.61	8.05
32341	0652810201	M1	1.33	3.31	0.86	0.65	3.13	1.92	1.89	1.43
32341	0652810201	PN	0.41	1.16	7.48	3.56	5.99	4.30	5.10	5.03
32434	0055990201	PN	0.29	0.81	54.13	14.90	36.55	14.93	26.08	16.17
32434	0055990201	M1	0.95	2.34	12.19	2.95	14.24	3.74	8.98	5.67
32434	0055990201	M2	0.96	2.33	10.65	3.01	12.70	4.38	8.59	6.46
32464	0781410201	PN	1.05	3.46	5.34	4.64	9.17	6.68	7.70	7.34
32464	0781410201	M1	3.82	10.15	0.39	0.27	0.52	0.93	0.81	0.58
32543	0781410101	M2	1.07	2.55	2.94	0.94	5.95	2.43	4.58	1.82

32543	0781410101	M1	1.11	2.68	3.60	1.13	5.71	2.90	4.53	2.07
32543	0781410101	PN	0.32	0.89	16.01	4.36	17.53	4.74	13.44	5.57
32543	0781410201	M2	1.07	2.55	3.04	0.74	6.40	1.96	4.42	1.21
32543	0781410201	M1	1.11	2.68	2.82	1.12	5.13	2.14	4.36	1.41
32543	0781410201	PN	0.32	0.89	16.76	4.31	18.57	4.94	15.64	5.39
32584	0781410101	M2	1.64	4.03	4.47	2.01	6.90	4.89	4.45	3.58
32584	0781410101	PN	0.52	1.50	18.59	9.17	18.29	11.07	12.38	10.52
32584	0781410201	M2	1.64	4.03	3.23	1.92	6.38	4.42	3.92	2.92
32584	0781410201	PN	0.52	1.50	21.96	9.04	15.11	9.63	12.66	10.20
32827	0606030101	M2	3.19	8.53	2.26	1.90	4.82	4.78	3.93	3.16
32827	0606030101	M1	3.23	8.49	3.07	2.31	6.65	4.88	5.86	4.23
32827	0606030101	PN	0.89	2.86	11.30	8.17	15.72	10.98	14.90	11.09
32827	0606030201	M1	2.37	6.22	3.68	3.07	3.37	2.19	2.22	1.59
32827	0606030201	M2	2.51	6.72	1.79	0.96	4.70	3.18	1.52	1.79
32907	0200530201	M1	1.98	5.01	1.60	1.11	3.01	2.25	1.71	1.39
32907	0200530301	M1	1.61	4.07	1.89	1.00	3.16	2.06	1.50	1.16
32907	0200530301	M2	1.76	4.41	1.01	1.01	2.63	2.47	2.23	1.59
32907	0200530301	PN	0.53	1.50	7.69	3.66	4.89	3.12	3.47	3.29
32907	0200530401	M1	1.61	4.08	1.51	1.08	4.05	2.03	1.55	1.21
32907	0200530401	M2	1.76	4.42	2.06	1.01	3.44	2.56	2.38	1.85
32907	0200530401	PN	0.53	1.50	5.38	3.21	7.28	3.13	3.71	3.09
32907	0200530501	M2	1.85	4.54	1.48	0.95	3.34	2.25	1.66	1.61
32907	0200530501	M1	2.00	5.07	2.02	1.03	2.63	2.80	2.44	1.75
32907	0200530501	PN	0.58	1.66	7.42	4.14	9.37	4.76	5.67	4.88
32907	0200530701	M2	1.85	4.55	2.43	1.44	3.94	3.24	2.26	2.50
32907	0200530701	M1	2.00	5.08	2.26	1.66	4.75	3.92	4.37	3.18
32907	0200530701	PN	0.58	1.67	8.75	6.16	9.04	7.17	10.94	9.28
32907	0200530801	M2	1.86	4.56	1.79	0.81	5.09	2.92	2.22	1.45
32907	0200530801	M1	2.01	5.09	1.65	1.10	4.21	2.50	1.92	1.64
32907	0200530801	PN	0.58	1.67	7.74	4.89	7.90	5.59	7.16	6.02
33437	0099280201	M1	20.54	57.03	0.57	0.38	0.57	0.74	0.76	0.56
33437	0099280201	M2	9.99	26.48	0.43	0.59	1.47	0.96	0.88	0.78
33437	0099280301	M2	2.43	5.88	2.44	1.83	4.32	2.94	2.49	2.04
33437	0099280301	M1	5.21	13.71	1.37	0.96	1.74	1.67	1.53	1.36
33437	0136540101	M2	1.36	3.33	2.50	2.08	3.81	3.05	2.24	1.81
33437	0136540101	M1	1.45	3.61	1.22	1.41	2.32	2.06	1.23	1.24
33437	0150498701	M2	1.55	3.81	5.41	3.32	8.21	5.37	3.72	3.81
33437	0150498701	M1	1.60	4.01	2.59	1.94	4.43	3.65	3.36	2.81
33437	0158970101	M1	1.30	3.25	2.62	1.80	2.64	2.58	2.14	1.63
33437	0158970101	M2	1.33	3.25	2.96	2.26	5.09	3.64	3.16	2.68
33437	0158971201	M1	1.59	3.95	2.59	2.15	4.54	4.17	4.19	3.43
33437	0158971301	M1	2.33	5.28	1.48	1.27	2.78	2.69	2.67	2.07
33437	0162960101	M1	1.63	4.05	1.00	1.12	2.69	2.10	1.70	1.69
33437	0162960101	M2	1.67	3.77	2.52	2.13	4.10	3.47	2.57	2.42
33437	0502030101	M2	1.40	3.41	4.33	3.29	5.15	5.28	4.37	3.84

33437	0502030101	M1	1.70	4.25	2.70	1.94	3.43	2.76	2.85	2.26
33437	0510610201	M2	1.38	3.34	1.72	1.86	2.67	2.65	2.71	1.85
33437	0510610201	M1	1.47	3.65	1.57	1.25	1.73	1.70	1.97	1.42
33437	0560983301	M1	1.46	3.37	2.52	2.13	1.96	2.49	1.28	0.98
33437	0560983301	M2	1.50	3.37	0.94	1.70	4.34	3.18	1.80	1.90
33437	0560983301	PN	0.50	1.25	16.02	16.53	11.22	12.76	6.10	6.80
33437	0658800801	M1	47.38	118.33	2.13	0.81	1.72	1.57	1.52	1.30
33437	0658802301	M2	1.51	3.37	2.22	1.31	3.14	2.59	1.97	1.43
33437	0670920301	M2	1.99	4.77	1.87	1.70	3.28	2.76	2.08	1.72
33437	0670920301	M1	3.65	9.44	1.77	1.35	1.79	1.48	1.08	0.70
33437	0670920401	M1	2.31	5.78	1.29	1.03	1.85	1.40	1.04	0.71
33437	0670920501	M1	1.83	4.53	1.80	1.34	2.43	1.92	1.18	1.13
33500	0099280201	M1	2.15	5.47	1.98	1.59	2.54	2.34	2.79	2.24
33500	0099280201	M2	2.35	6.27	1.64	1.38	2.91	2.31	3.30	2.59
34257	0761950101	M2	2.42	6.05	15.43	7.48	18.04	13.20	11.87	7.61
34257	0761950101	M1	2.53	6.46	15.72	7.21	18.85	12.82	10.30	6.84
34257	0761950101	PN	0.82	2.45	69.55	22.65	38.46	19.56	32.53	22.53
34612	0082140301	M1	1.01	2.47	20.01	7.47	26.25	10.12	14.55	5.74
34612	0082140301	M2	1.02	2.46	18.01	7.98	21.93	9.43	13.68	5.61
34612	0082140301	PN	0.36	1.01	80.62	32.38	56.12	18.03	36.99	16.30
34692	0503600401	M1	2.14	5.45	2.74	2.09	4.97	4.91	3.51	3.06
34692	0503600401	M2	2.27	5.99	2.30	2.14	4.45	4.40	4.06	3.10
34692	0503600401	PN	0.77	2.28	8.10	3.65	10.40	6.29	5.07	4.57
34767	0762610401	M2	1.01	2.42	19.76	4.87	26.21	10.01	18.39	5.96
34767	0762610401	PN	0.38	1.08	107.20	27.53	95.10	28.67	61.27	31.93
34767	0762610401	M1	0.98	2.42	23.81	5.90	32.23	18.11	21.16	12.42
34767	0762610501	M2	1.00	2.40	22.54	3.33	37.49	8.45	23.72	5.19
34767	0762610501	PN	0.37	1.07	117.53	19.33	103.31	17.34	62.73	16.88
34767	0762610501	M1	0.99	2.42	25.68	2.74	40.26	10.37	24.56	7.51
34767	0762610701	M2	1.01	2.41	18.36	4.53	26.51	8.92	15.54	6.06
34767	0762610701	PN	0.38	1.08	97.73	20.41	69.16	17.13	46.04	18.63
34767	0762610701	M1	0.99	2.42	21.87	4.62	33.76	11.15	20.32	7.35
34767	0762610801	M2	1.01	2.41	19.73	5.75	24.72	9.34	15.36	7.25
34767	0762610801	PN	0.38	1.08	93.09	23.05	71.29	22.40	56.90	26.19
34767	0762610801	M1	0.99	2.42	21.97	5.80	31.95	12.34	18.85	6.60
34963	0504101301	M2	1.22	2.98	0.45	0.77	2.30	1.86	1.14	1.37
34963	0504101301	M1	1.26	3.11	0.57	0.80	2.17	2.11	1.50	1.65
34963	0504101301	PN	0.52	1.49	5.46	5.12	5.96	5.78	8.45	7.41
35321	0112810101	PN	0.35	1.00	343.87	23.69	219.68	10.49	81.36	8.80
35321	0112810101	M1	0.95	2.36	81.88	2.77	88.04	3.97	35.68	2.33
35321	0112810101	M2	0.98	2.40	76.52	3.14	73.11	3.22	29.78	2.17
35321	0679381101	PN	0.31	0.89	369.68	23.52	230.77	14.52	82.17	12.02
35321	0679381101	M1	0.95	2.34	79.20	2.65	82.34	5.31	32.71	4.36
35321	0679381101	M2	0.99	2.39	67.99	5.31	67.38	7.44	30.72	6.96
35762	0149900201	M1	1.76	4.47	1.74	1.32	2.29	2.02	1.12	1.08

35762	0149900201	M2	1.96	4.97	2.23	1.47	2.22	2.55	1.67	1.14
35762	0149900201	PN	0.55	1.59	9.90	7.27	6.89	5.85	4.75	3.33
35838	0741140201	M1	1.80	4.60	1.55	1.74	1.69	1.70	0.95	1.46
35838	0741140201	M2	2.00	5.10	1.69	1.05	1.67	1.73	2.69	1.88
35838	0741140201	PN	0.56	1.63	4.21	2.90	6.23	3.69	5.32	4.44
35838	0741140301	M1	1.80	4.59	1.61	1.74	1.86	1.38	2.45	1.13
35838	0741140301	M2	2.00	5.10	0.67	0.58	1.43	1.35	1.92	1.24
35838	0741140301	PN	0.56	1.63	6.91	5.57	7.99	6.94	9.41	8.12
35838	0741140401	M1	1.82	4.64	1.10	0.54	2.12	1.22	1.43	1.03
35838	0741140401	M2	2.03	5.19	0.65	0.70	2.53	1.72	1.83	1.13
35838	0741140401	PN	0.57	1.65	4.09	2.97	5.62	3.41	3.65	4.07
35838	0741140501	M1	1.82	4.65	0.76	0.47	1.72	1.03	1.08	0.73
35838	0741140501	M2	2.03	5.18	1.55	0.59	1.88	1.35	1.31	0.96
35838	0741140501	PN	0.57	1.65	4.28	2.51	4.10	2.51	3.07	2.53
35838	0741140601	M1	1.84	4.68	1.14	0.54	2.07	1.14	0.65	0.76
35838	0741140601	M2	2.03	5.19	0.94	0.48	2.43	1.40	1.05	0.82
35838	0741140601	PN	0.57	1.66	4.14	2.52	5.38	2.80	4.14	2.64
35906	0601780401	M2	1.90	4.73	1.40	0.74	3.11	2.29	0.97	1.28
35906	0601780401	PN	0.61	1.78	5.03	3.31	5.62	3.28	6.02	4.40
36349	005210101	M2	3.31	8.81	2.91	1.65	3.79	3.64	3.30	2.98
36349	005210101	M1	3.35	8.66	2.66	1.98	3.76	3.11	4.21	3.10
36349	005210101	PN	0.91	2.87	10.46	6.85	9.23	7.11	11.30	9.58
36406	005210101	M2	1.20	2.96	4.07	2.18	4.74	3.66	3.62	2.33
36406	005210101	M1	1.24	3.03	3.53	1.89	4.05	2.95	2.62	1.99
36406	005210101	PN	0.36	0.99	18.22	9.85	16.07	9.77	9.90	7.05
36406	0602200101	M1	2.04	5.19	3.29	2.33	6.70	4.97	2.99	2.87
36406	0602200101	M2	2.14	5.57	3.33	2.38	7.66	5.56	3.71	2.96
36406	0602200101	PN	0.64	1.87	18.33	9.71	16.26	12.03	12.24	9.16
36477	005210101	M2	1.84	4.70	3.99	3.79	8.48	6.48	5.21	4.74
36477	005210101	M1	1.87	4.78	3.77	3.19	6.45	5.79	4.20	3.91
36477	005210101	PN	0.56	1.65	14.96	14.98	19.31	16.16	12.93	11.54
36477	0602200101	M1	1.55	3.92	2.93	2.84	6.59	6.29	4.34	3.60
36477	0602200101	M2	1.77	4.42	3.28	2.96	7.51	6.55	3.78	3.70
36477	0602200101	PN	0.48	1.38	15.90	13.91	16.77	16.20	13.51	11.72
37013	0049340301	M2	1.18	2.91	1.04	0.66	1.55	1.13	1.00	0.67
37013	0049340301	M1	1.24	3.11	1.28	0.59	1.18	0.95	1.14	0.60
37013	0049340301	PN	0.37	1.04	7.48	3.18	3.23	1.93	2.62	2.10
37692	0744040301	M2	2.14	5.36	1.92	2.21	5.51	4.75	3.91	2.98
37692	0744040301	M1	2.30	5.85	4.39	3.44	9.59	6.17	4.87	4.04
37692	0744040301	PN	0.64	1.89	22.27	15.01	14.22	13.42	15.74	14.29
37692	0744040401	M2	2.12	5.31	4.08	2.64	6.28	4.34	3.71	2.55
37692	0744040401	M1	2.29	5.82	4.03	3.14	6.57	5.91	3.70	3.40
37692	0744040401	PN	0.63	1.88	23.63	15.94	21.32	11.74	13.59	12.23
37976	0555060301	M2	3.16	8.38	7.18	5.34	12.16	7.66	9.70	8.13
37976	0555060301	M1	3.29	8.72	5.43	4.70	12.27	8.40	11.56	7.90

37976	0555060301	PN	0.93	3.00	20.17	14.95	26.44	16.55	29.07	19.36
37976	0555060401	M1	2.46	6.52	7.35	3.89	6.25	5.54	5.48	5.03
37976	0555060501	M1	2.59	6.88	2.63	2.62	6.76	4.72	5.56	5.65
37976	0555060501	M2	2.83	7.50	3.46	2.89	8.23	5.79	8.09	6.77
37976	0555060501	PN	0.88	2.75	5.90	3.15	6.28	4.25	6.78	5.00
38672	0601780801	M2	1.65	4.06	1.37	0.87	3.81	2.57	2.72	2.01
38672	0601780801	PN	0.54	1.57	5.03	3.49	5.36	4.58	6.67	4.48
39152	0112610101	M1	2.90	7.33	5.94	1.88	12.51	4.33	6.42	3.85
39152	0112610101	M2	2.90	7.50	6.24	1.78	10.58	4.09	5.58	3.34
39152	0112610101	PN	0.89	2.66	15.61	6.45	15.76	7.05	13.29	8.89
39152	0502050101	M1	2.11	5.35	2.65	2.32	5.11	5.15	5.26	4.06
39152	0502050101	M2	2.12	5.50	2.52	2.26	6.34	5.58	4.09	4.08
39152	0502050101	PN	0.68	1.99	5.59	3.87	8.26	5.33	6.99	5.70
39152	0502050201	M1	2.04	5.19	4.50	3.19	5.68	5.65	5.07	4.00
39152	0502050201	M2	2.12	5.51	2.33	1.94	6.43	5.52	5.47	4.75
39152	0502050201	PN	0.69	2.03	6.10	4.55	6.70	5.87	8.26	6.51
39152	0745110101	PN	1.44	4.25	14.60	5.66	12.93	6.28	11.05	6.67
39152	0745110101	M1	2.84	7.15	3.67	1.57	6.23	3.86	3.83	2.87
39152	0745110101	M2	3.26	8.32	3.50	1.32	6.12	3.23	3.48	2.20
39152	0745110201	PN	2.16	6.33	11.34	6.01	10.76	6.75	10.65	8.19
39152	0745110201	M1	2.86	7.20	3.32	2.02	6.25	4.45	4.34	3.78
39152	0745110201	M2	2.91	7.43	2.78	1.59	5.78	4.04	3.60	2.67
39152	0745110301	PN	1.86	5.47	10.95	6.73	12.07	6.99	9.55	8.12
39152	0745110301	M1	2.86	7.20	4.22	2.79	7.26	5.37	6.20	6.01
39152	0745110301	M2	2.88	7.35	2.92	2.15	6.45	4.54	5.25	4.04
39152	0745110401	PN	1.47	4.35	9.67	5.47	9.82	5.88	8.08	5.76
39152	0745110401	M1	2.86	7.21	3.22	1.95	5.73	4.22	3.73	2.85
39152	0745110401	M2	2.87	7.32	2.59	1.41	5.22	3.52	3.63	2.54
39152	0745110501	PN	1.42	4.20	12.48	6.20	9.10	5.64	7.14	5.18
39152	0745110501	M1	2.86	7.20	3.20	1.89	5.56	4.13	4.30	2.76
39152	0745110501	M2	2.86	7.31	3.55	1.52	6.87	3.43	3.01	2.13
39152	0745110601	PN	1.11	3.27	10.16	5.98	8.70	6.19	9.10	6.83
39152	0745110601	M2	2.86	7.30	2.24	1.27	6.12	3.61	3.24	2.51
39152	0745110601	M1	2.87	7.22	3.33	2.10	5.69	3.96	3.74	2.94
39152	0745110701	PN	1.01	2.99	7.31	5.13	8.00	5.56	6.47	5.51
39152	0745110701	M2	2.84	7.25	2.80	1.48	5.52	3.53	2.44	2.38
39152	0745110701	M1	2.85	7.18	2.67	1.65	5.00	3.93	3.36	2.87
39225	0035940201	M1	1.01	2.47	29.30	23.49	66.75	55.20	36.21	32.41
39225	0035940201	M2	1.02	2.46	32.42	22.64	46.31	37.83	36.21	31.78
39225	0035940201	PN	0.38	1.05	159.44	77.96	132.26	106.54	125.93	109.91
39422	0105070201	M1	1.85	4.62	237.10	233.34	392.35	388.08	628.63	635.00
39422	0553880201	M2	1.15	2.79	41.24	39.73	115.95	113.19	90.07	87.49
39422	0553880201	M1	1.24	3.08	34.90	33.78	108.15	105.72	80.25	78.87
39422	0553880201	PN	0.41	1.17	171.26	152.84	212.75	198.02	254.68	245.52
39422	0553880301	M2	1.15	2.80	42.60	40.73	114.61	110.57	77.00	74.21

39422	0553880301	M1	1.25	3.10	46.13	43.53	117.88	113.04	85.92	83.42
39422	0553880301	PN	0.41	1.17	216.88	195.65	267.15	248.55	286.75	278.25
39578	0147610101	PN	0.36	0.99	247.22	88.39	144.86	80.40	106.57	79.22
39578	0147610101	M1	0.99	2.41	61.63	23.57	60.50	30.97	48.71	36.04
39578	0147610101	M2	1.00	2.41	55.30	20.37	54.97	31.24	40.30	31.01
39922	0205360101	M1	2.12	5.36	4.54	3.64	6.42	5.72	5.84	5.67
39922	0205360101	M2	2.35	6.18	5.43	3.89	5.56	5.90	7.26	6.73
39922	0205360101	PN	6.09	17.80	4.09	3.44	4.64	3.42	4.76	4.28
39950	0306060101	M2	1.07	2.56	5.68	3.15	8.10	4.71	4.91	3.62
39950	0306060101	M1	1.09	2.64	5.96	2.61	8.19	4.83	5.05	3.59
39950	0306060101	PN	0.60	1.69	15.47	7.98	12.22	7.28	8.76	7.11
40001	0205360101	M1	1.03	2.50	84.89	33.35	71.10	52.51	50.60	46.47
40001	0205360101	M2	1.03	2.47	76.67	32.37	67.63	49.53	50.38	49.91
40001	0205360101	PN	0.39	1.09	328.96	115.87	147.43	105.36	108.60	99.62
40425	0201670101	M2	1.60	3.99	1.22	1.08	2.46	2.48	2.36	2.11
40425	0201670101	M1	1.78	4.53	1.91	1.24	2.48	2.26	1.56	1.74
40425	0201670101	PN	0.47	1.35	3.98	4.01	5.54	4.07	5.31	4.51
40425	0651910401	M1	1.95	4.98	0.84	1.15	2.99	3.09	3.04	2.52
40425	0651910401	M2	2.36	5.89	0.73	0.81	2.72	2.91	2.22	2.11
40425	0651910401	PN	0.58	1.68	5.93	4.98	6.01	5.70	7.48	6.72
40425	0651910501	M1	1.95	4.97	1.06	1.28	2.85	3.27	1.95	2.38
40425	0651910501	M2	1.97	4.92	1.39	0.91	2.52	2.60	2.04	2.03
40425	0651910501	PN	0.57	1.68	6.23	5.30	5.93	5.30	7.62	6.81
40425	0651910601	M1	1.95	4.98	1.79	1.58	3.75	4.15	4.01	3.68
40425	0651910601	M2	1.97	4.92	1.29	1.53	3.93	4.02	2.71	3.23
40425	0651910601	PN	0.57	1.68	4.71	5.30	6.79	6.42	7.13	7.22
40425	0651910701	M1	1.98	5.06	1.77	1.94	5.38	4.61	4.43	4.23
40425	0651910701	M2	2.00	5.00	2.07	1.71	4.13	4.20	3.54	3.51
40425	0651910701	PN	0.58	1.68	5.63	4.82	6.47	5.66	6.18	6.46
40562	0108260201	M2	2.19	5.13	5.31	4.50	9.14	8.43	4.35	4.02
40562	0108260201	M1	2.37	5.55	5.12	4.73	9.68	8.62	4.73	4.10
40562	0108260201	PN	0.67	1.92	32.62	26.79	28.29	25.13	13.71	11.63
40562	0673310101	M2	2.38	6.05	7.67	5.92	13.56	11.87	6.93	6.54
40562	0673310101	M1	2.46	6.27	7.14	7.27	13.83	13.82	8.57	8.90
40562	0673310101	PN	0.81	2.37	25.82	20.98	25.28	23.40	18.49	17.09
40644	0108260201	M1	2.16	5.01	10.26	5.96	13.00	11.13	6.94	6.19
40644	0108260201	M2	2.18	5.00	10.45	6.92	17.01	12.37	9.04	7.97
40644	0108260201	PN	0.58	1.69	59.07	40.58	42.65	34.86	23.84	20.17
40705	0110930701	M1	1.98	4.98	7.82	8.40	16.13	12.15	9.40	5.53
40705	0110930701	M2	2.12	5.50	13.65	9.74	19.87	15.33	9.93	5.63
40705	0110930701	PN	0.74	2.19	30.91	23.29	34.14	24.77	24.99	15.69
40809	0651790101	M1	1.02	2.49	9.44	5.64	12.31	10.36	12.63	11.92
40809	0651790101	M2	1.08	2.60	8.56	6.11	12.71	11.18	12.48	11.92
40809	0651790101	PN	0.37	1.05	26.95	13.28	16.11	12.57	15.56	12.42
40962	0550540101	PN	1.02	3.34	14.31	11.54	18.25	14.53	12.37	11.44

40962	0550540101	M1	3.38	8.93	3.36	2.15	7.02	4.94	3.24	2.89
40962	0550540101	M2	3.62	9.57	1.76	2.00	5.99	4.46	3.30	2.44
41107	0722670201	M2	2.12	5.27	2.31	2.08	4.35	3.58	2.05	1.65
41107	0722670201	PN	0.62	1.80	11.70	11.80	13.54	11.26	8.04	7.36
41189	0112550601	M2	1.93	4.94	4.32	3.49	9.18	6.50	3.60	3.10
41189	0112550601	M1	2.15	5.54	5.08	3.05	6.86	5.14	2.37	2.04
41189	0112550601	PN	0.66	1.96	20.85	12.99	15.33	13.47	9.24	7.37
41189	0200130101	M1	2.13	5.45	4.71	2.74	5.69	5.20	2.97	2.32
41189	0200130101	M2	2.48	6.59	5.30	3.11	7.66	5.98	3.66	2.59
41189	0200130101	PN	0.67	2.00	22.66	13.45	18.24	12.66	7.74	5.96
41189	0722670601	M2	2.92	7.55	6.75	4.62	11.23	8.47	5.71	6.48
41189	0722670601	M1	3.02	7.66	5.63	4.11	9.50	8.85	10.77	7.92
41189	0722670601	PN	0.89	2.72	20.99	15.27	18.68	18.50	17.68	16.14
41189	0761630101	M1	1.18	2.94	4.36	2.93	6.25	5.40	3.12	2.55
41189	0761630101	M2	1.25	3.06	4.49	3.01	6.35	5.29	3.10	2.70
41189	0761630101	PN	0.36	1.04	20.60	12.16	15.19	12.00	8.33	6.27
41189	0761630201	M1	1.18	2.93	4.68	2.92	6.30	5.26	3.05	2.50
41189	0761630201	M2	1.25	3.06	3.95	2.66	5.92	5.04	3.29	2.75
41189	0761630201	PN	0.36	1.04	20.60	11.96	15.78	11.79	7.69	6.34
41566	0203170301	M1	1.89	4.80	1.13	1.02	1.85	1.77	1.49	1.41
41566	0203170301	M2	2.19	5.57	1.10	0.99	1.60	1.74	1.61	1.27
41566	0203170301	PN	0.60	1.75	5.50	5.22	4.08	3.92	4.84	4.73
41763	0404120101	M1	1.21	3.01	2.49	1.51	4.52	2.99	1.82	1.71
41763	0404120101	M2	1.29	3.14	3.09	2.37	4.96	4.14	2.59	2.10
41763	0404120101	PN	0.72	2.05	10.84	7.33	7.70	6.88	6.28	5.54
41823	0551450301	M1	1.00	2.44	44.54	20.12	55.45	30.92	40.60	31.32
41823	0551450301	M2	1.02	2.44	36.67	17.38	47.56	28.66	34.28	26.74
41823	0551450301	PN	0.40	1.13	175.84	77.39	129.30	73.30	119.91	97.49
41857	0722960101	M2	1.91	4.72	1.47	0.57	1.41	1.13	0.97	0.74
41857	0722960101	M1	1.93	4.95	1.89	0.81	2.56	1.56	1.29	1.18
41857	0722960101	PN	0.74	2.20	6.88	2.90	3.67	2.60	3.68	3.10
41912	0403100101	M2	1.32	3.23	1.31	0.93	2.30	2.03	1.85	1.63
41912	0403100101	M1	1.33	3.34	1.04	0.73	1.86	1.34	1.14	0.87
41912	0403100101	PN	0.45	1.28	3.72	3.48	4.53	3.09	4.08	3.44
41967	0651740301	M1	1.09	2.66	2.50	0.96	2.49	1.93	0.83	0.74
41967	0651740301	M2	1.10	2.64	2.47	0.77	1.03	1.29	2.47	0.92
41967	0651740301	PN	0.32	0.91	12.81	4.78	3.58	2.81	4.36	4.24
42637	0110900201	M2	1.10	2.67	66.69	26.03	68.13	27.39	44.34	21.16
42637	0110900201	M1	1.11	2.73	69.82	28.65	72.35	26.28	51.38	21.44
42637	0110900201	PN	-0.05	-0.12	283.02	108.13	173.60	54.20	111.06	47.97
42727	0202180201	M1	1.76	4.51	3.75	1.50	5.35	3.07	3.99	2.77
42727	0202180201	M2	1.79	4.49	3.29	1.19	5.04	2.46	3.09	1.89
42727	0202180201	PN	0.63	1.87	7.92	3.56	6.71	3.78	5.48	4.42
42816	0021540201	M2	1.01	2.45	25.67	7.05	22.43	9.49	8.00	5.19
42816	0021540201	M1	1.04	2.56	23.81	7.58	21.98	9.93	8.60	4.71

42816	0021540201	PN	0.41	1.14	87.54	53.04	48.27	25.17	20.89	14.47
42816	0502160101	M2	1.02	2.45	24.48	8.04	25.35	11.97	9.97	5.38
42816	0502160101	M1	1.04	2.57	24.10	7.31	24.08	11.89	10.40	6.11
42816	0502160101	PN	0.41	1.15	91.48	25.10	54.30	22.56	25.14	16.36
42999	0110980201	M2	1.56	3.86	2.84	1.76	3.56	2.53	2.70	1.80
42999	0110980201	M1	1.67	4.26	2.43	1.89	3.45	2.43	2.46	1.83
42999	0110980201	PN	0.50	1.46	11.14	6.69	8.00	4.12	6.59	4.72
43511	008220201	PN	1.18	3.36	4.47	3.10	4.27	3.47	4.92	3.92
43511	008220201	M1	3.44	8.37	0.96	0.61	1.56	1.61	1.57	1.19
43511	008220201	M2	3.78	9.33	1.23	0.58	2.21	1.72	2.04	1.17
43843	0305360501	M2	1.40	3.47	0.61	0.78	2.19	1.99	1.86	1.58
43843	0305360501	M1	1.45	3.70	0.78	0.45	1.66	1.29	1.33	1.05
43843	0305360501	PN	0.43	1.24	3.52	2.54	4.54	2.60	4.16	2.65
43843	0305361501	M2	1.42	3.55	0.75	0.63	2.25	1.50	1.07	0.92
43843	0305361501	M1	1.46	3.73	0.60	0.49	0.98	1.06	0.61	0.60
43843	0305361501	PN	1.85	5.50	3.73	1.99	2.38	2.08	2.48	1.94
44418	0094383201	M2	2.25	5.87	1.36	0.64	2.33	1.55	2.08	1.13
44418	0094383201	M1	2.42	6.12	2.63	1.49	2.57	1.52	0.40	0.92
44536	0141150101	M2	1.00	2.42	12.29	2.76	16.96	4.15	6.96	2.84
44536	0141150101	PN	0.34	0.96	72.76	12.05	57.18	8.95	24.59	8.47
44536	0141150101	M1	0.98	2.37	16.67	3.43	22.93	4.09	10.27	2.89
44536	0141150401	M2	1.01	2.43	11.65	3.88	15.40	5.79	9.84	6.01
44536	0141150401	PN	0.34	0.94	66.57	13.62	46.35	10.15	22.27	7.26
44536	0141150401	M1	0.98	2.38	16.25	4.39	20.76	6.30	11.72	5.82
44536	0141150501	M2	1.00	2.42	12.33	4.95	21.41	9.42	14.48	9.45
44536	0141150501	PN	0.34	0.96	77.33	43.90	75.84	55.90	55.85	59.91
44536	0141150501	M1	0.98	2.37	17.57	6.61	22.44	11.00	19.79	13.14
44968	0124710801	M1	1.88	4.82	1.63	0.95	2.22	1.75	1.60	1.29
44968	0124710801	M2	1.97	5.14	1.26	1.33	2.11	2.05	1.44	1.53
44968	0124710801	PN	0.58	1.70	8.25	5.04	4.69	4.53	4.42	4.34
45700	0020540401	M2	1.49	3.73	0.80	0.77	2.06	1.28	0.96	0.89
45700	0020540401	M1	1.65	4.23	1.58	1.02	1.87	1.52	1.56	1.13
45700	0020540401	PN	0.47	1.39	5.10	4.47	4.23	3.42	4.16	2.91
47337	0041180801	M2	1.08	2.60	3.44	3.16	3.04	3.07	1.84	1.56
47337	0041180801	M1	1.12	2.73	4.35	3.43	2.55	3.57	1.84	1.51
47337	0041180801	PN	0.33	0.92	17.58	12.48	9.85	9.03	5.15	6.18
47368	0142770101	M2	1.01	2.44	64.90	4.71	80.26	10.91	37.81	6.61
47368	0142770101	PN	0.34	0.96	270.59	28.57	227.00	24.37	106.51	22.18
47368	0142770101	M1	0.99	2.41	63.09	5.01	84.28	9.92	40.66	6.86
47368	0142770301	PN	0.36	0.99	408.56	37.07	316.15	31.68	136.99	30.54
47368	0142770301	M1	0.98	2.38	92.28	8.21	116.00	14.74	58.49	11.80
47368	0142770301	M2	0.99	2.38	78.28	7.57	96.98	17.36	42.60	11.90
47368	0150650301	PN	0.36	1.01	463.22	47.05	399.53	44.66	154.44	46.51
47368	0150650301	M1	0.97	2.37	105.94	8.09	137.20	13.24	53.97	13.00
47368	0150650301	M2	0.98	2.38	89.49	7.37	115.85	15.18	51.77	9.54

47368	0405690101	M2	1.01	2.42	117.84	9.66	166.45	20.93	65.59	17.85
47368	0405690101	PN	0.37	1.04	578.38	37.30	466.15	34.75	166.95	28.01
47368	0405690101	M1	0.99	2.41	126.50	10.88	181.45	20.93	69.67	20.98
47368	0405690201	M2	1.02	2.43	94.92	7.56	135.97	16.11	55.09	12.48
47368	0405690201	PN	0.37	1.04	469.46	35.05	409.96	38.85	155.20	39.33
47368	0405690201	M1	0.99	2.41	100.27	9.09	149.44	18.03	60.45	15.80
47368	0405690501	M2	1.02	2.42	74.29	7.04	106.76	16.20	49.06	12.19
47368	0405690501	PN	0.37	1.04	344.41	27.20	283.55	28.06	120.60	27.42
47368	0405690501	M1	0.99	2.42	79.19	8.16	106.37	16.49	51.09	14.01
47368	0693850701	M2	1.01	2.40	54.36	4.58	75.21	12.34	37.57	9.53
47368	0693850701	PN	0.35	0.98	295.50	35.76	235.56	39.47	123.48	38.19
47368	0693850701	M1	0.99	2.39	53.30	5.87	74.11	14.37	44.07	14.97
47368	0693851401	M2	1.01	2.39	48.05	4.55	72.39	9.69	33.79	7.36
47368	0693851401	PN	0.36	0.99	268.97	27.59	217.44	27.48	116.96	27.30
47368	0693851401	M1	0.99	2.39	59.45	4.23	81.30	12.81	41.67	9.74
47368	0741960101	M2	1.02	2.42	51.04	5.48	72.08	10.28	38.70	7.26
47368	0741960101	PN	0.34	0.94	252.65	26.55	206.55	23.34	97.62	19.55
47368	0741960101	M1	0.99	2.41	38.21	4.13	52.79	8.64	29.92	7.75
47503	0112240301	M2	1.22	2.98	3.54	2.99	4.24	4.64	2.42	2.84
47503	0112240301	M1	1.28	3.12	1.93	2.16	3.38	3.61	1.82	2.18
47503	0112240301	PN	0.36	0.99	13.31	10.98	9.36	11.55	6.99	6.90
48240	0152940101	M2	1.86	4.66	2.39	1.53	2.96	2.46	2.44	2.45
48240	0152940101	M1	2.01	5.14	2.18	1.61	2.53	2.44	2.81	2.51
48240	0152940101	PN	0.58	1.69	9.41	6.04	7.28	6.03	8.74	7.41
49221	0147540101	M2	1.92	4.92	1.89	1.09	3.72	1.84	1.86	1.52
49221	0147540101	M1	2.04	5.21	1.80	1.09	3.11	1.58	1.73	1.28
49221	0147540101	PN	0.59	1.72	8.44	4.63	5.77	3.65	5.59	4.75
49468	0204410201	M2	1.01	2.42	6.00	3.97	9.62	5.32	12.07	5.88
49468	0204410201	M1	0.98	2.36	6.81	3.47	12.31	6.79	11.04	6.76
49468	0404240101	M2	1.01	2.41	3.11	1.69	7.36	3.07	5.62	1.57
49468	0404240101	PN	0.35	0.96	10.11	7.88	9.77	7.62	10.19	7.50
49468	0404240101	M1	0.97	2.37	3.16	1.96	8.56	3.29	5.48	3.01
49921	0098010101	M1	1.69	4.35	2.05	1.33	2.90	1.84	2.33	1.81
49921	0098010101	M2	1.96	5.03	1.55	1.10	1.66	1.54	1.33	1.58
49921	0098010101	PN	0.53	1.55	6.22	5.66	4.36	4.13	4.80	4.46
49921	0551830101	M1	1.73	4.43	1.82	1.26	2.60	2.62	2.51	2.33
49921	0551830101	M2	2.01	5.10	1.19	1.25	2.73	2.42	1.76	1.77
49921	0551830101	PN	0.54	1.57	7.07	5.53	5.90	5.39	6.40	6.26
50063	0104260101	M2	1.53	3.76	495.39	419.63	775.33	680.17	751.37	698.57
50063	0104260101	M1	1.55	3.86	480.51	409.33	784.10	689.71	773.16	727.52
50063	0104260101	PN	0.53	1.54	2215.03	1860.48	2235.56	1941.91	2499.23	2358.93
50063	0164560701	M2	1.55	3.80	416.37	356.62	635.97	554.03	446.33	406.50
50063	0164560701	M1	1.56	3.88	410.81	355.38	630.70	565.71	436.89	411.50
50063	0164560701	PN	0.57	1.65	1814.20	1497.75	1391.39	1152.46	1280.44	1184.97
50063	0212480201	M1	1.61	4.03	429.24	362.38	724.14	640.44	683.52	641.18

50063	0212480201	M2	1.62	3.99	465.52	398.67	757.77	670.11	695.58	651.66
50063	0212480201	PN	0.54	1.58	1740.68	1381.30	1492.48	1219.67	1674.42	1579.69
50810	0103660101	M2	1.53	3.84	1.32	0.86	2.06	1.57	1.76	1.20
50810	0103660101	M1	1.83	4.71	1.42	0.79	1.79	1.77	1.68	1.56
50810	0103660101	PN	0.55	1.63	5.71	2.75	4.19	2.50	3.47	2.70
50881	0145480101	M2	1.43	3.47	1.26	1.37	1.91	1.80	1.56	1.51
50881	0145480101	M1	1.61	4.01	1.02	1.07	2.20	1.66	1.56	1.75
50881	0145480101	PN	0.56	1.56	5.94	5.50	3.57	3.52	6.39	4.43
50944	0148620101	M1	2.69	6.83	4.34	2.43	7.69	3.90	5.90	4.19
50944	0148620101	M2	2.98	7.96	4.48	1.90	5.97	4.28	5.54	3.82
50944	0148620101	PN	0.82	2.48	19.72	7.32	17.60	7.26	11.98	8.28
51210	0762640101	M1	1.05	2.58	5.52	4.19	10.80	8.86	6.74	5.33
51210	0762640101	M2	1.11	2.67	5.29	4.33	8.70	8.02	5.45	5.28
51210	0762640101	PN	0.36	1.04	23.82	15.78	21.70	12.18	19.93	12.32
51353	0651740801	M2	1.10	2.63	2.69	1.02	3.82	1.88	1.91	1.27
51353	0651740801	M1	1.17	2.84	3.25	1.16	3.80	2.08	2.36	1.62
51353	0651740801	PN	0.32	0.91	17.20	5.05	10.25	4.70	6.34	4.99
51485	0744240101	PN	10.59	33.27	5.29	4.00	4.22	2.95	4.64	3.75
51485	0744240101	M2	3.15	8.27	1.89	1.10	2.89	2.69	1.76	1.54
51791	0501540201	PN	2.42	7.13	7.39	3.99	5.55	4.77	7.96	5.66
51791	0501540201	M1	2.77	7.04	1.94	1.19	4.58	3.49	4.07	2.48
51791	0501540201	M2	2.79	7.21	1.88	1.21	4.79	3.55	2.37	2.76
52112	0305920401	M2	1.11	2.65	9.05	1.15	10.89	1.43	5.70	1.34
52112	0305920401	M1	1.16	2.80	6.82	1.31	8.10	2.02	5.58	1.47
52112	0305920401	PN	0.33	0.91	42.08	6.20	33.17	4.26	15.18	4.14
52112	0674810501	M2	1.12	2.65	8.03	0.62	9.27	1.44	5.34	0.64
52112	0674810501	M1	1.17	2.80	6.39	1.15	7.70	1.89	4.00	0.88
52112	0674810501	PN	0.33	0.91	47.43	5.30	33.16	4.01	16.33	3.52
52318	0111530101	M1	2.09	4.95	1.65	0.47	1.90	1.08	1.09	0.71
52318	0111530101	M2	2.25	5.30	1.19	0.52	1.65	1.10	1.51	0.81
53231	0150350101	PN	1.14	3.38	14.33	12.63	11.05	10.12	9.64	9.75
53231	0150350101	M1	1.14	2.81	3.67	2.56	4.53	3.95	3.22	3.43
53231	0150350101	M2	1.17	2.86	3.83	2.83	4.80	4.02	3.03	3.86
53245	0150350101	M2	1.16	2.84	0.77	1.16	1.62	1.43	1.10	1.39
53245	0150350101	M1	1.20	2.93	1.75	1.67	2.07	2.04	2.77	2.09
53245	0150350101	PN	0.36	0.99	10.00	8.70	7.33	6.71	8.32	6.94
53559	0401270301	PN	1.18	3.62	11.31	9.51	14.30	11.49	17.81	14.54
53559	0401270301	M2	2.82	7.40	3.57	2.13	6.01	3.88	3.36	4.32
53559	0401270301	M1	2.98	7.65	3.44	2.49	7.31	4.79	5.71	4.03
53683	0302460101	PN	1.54	4.95	14.15	11.03	11.51	9.32	13.43	10.60
54032	0402781001	PN	0.41	1.13	12.56	6.87	7.37	4.20	7.90	4.64
54032	0402781001	M1	4.27	10.88	0.72	0.56	1.08	0.90	0.58	0.54
54032	0402781001	M2	4.44	11.09	1.43	0.97	1.49	1.41	1.10	0.77
54219	0744411101	M1	1.93	4.86	3.81	3.68	5.01	5.28	5.47	5.68
54219	0744411101	M2	2.21	5.60	3.39	2.87	4.88	4.13	4.62	4.16

54219	0744411101	PN	0.68	1.93	9.62	9.26	9.52	8.14	8.80	8.51
54470	0145190101	M1	1.04	2.55	18.19	16.90	34.77	30.34	40.07	39.34
54470	0145190101	M2	1.05	2.57	19.41	17.27	33.81	28.55	36.86	34.36
54470	0145190101	PN	0.34	0.96	51.50	38.24	64.38	50.85	70.56	58.91
54470	0145190201	M1	1.03	2.55	16.76	14.05	30.91	25.78	36.68	35.15
54470	0145190201	M2	1.06	2.58	15.53	14.27	34.44	27.41	38.06	36.45
54470	0145190201	PN	0.34	0.96	51.93	42.05	64.03	47.01	71.43	63.93
54470	0673920201	M2	1.06	2.55	24.18	22.56	41.65	34.31	42.84	39.38
54470	0673920201	M1	1.07	2.65	26.54	24.41	52.70	44.49	59.91	54.90
54470	0673920201	PN	0.37	1.05	89.56	71.88	103.18	86.16	105.45	98.44
54470	0673920301	M2	1.06	2.55	14.55	14.02	25.33	21.15	18.24	14.99
54470	0673920301	M1	1.09	2.69	18.34	16.33	30.59	24.63	23.09	19.28
54470	0673920301	PN	0.37	1.05	81.07	69.06	78.32	59.84	78.21	60.94
54470	0724810201	M2	1.10	2.65	17.82	16.67	32.02	28.56	29.38	27.30
54470	0724810201	M1	1.10	2.71	18.57	16.40	34.09	28.76	33.10	31.24
54470	0724810201	PN	0.41	1.16	64.94	54.62	68.52	60.56	71.03	69.55
54470	0724810401	M2	1.09	2.64	13.55	11.79	26.91	20.44	22.36	18.23
54470	0724810401	M1	1.10	2.72	16.73	14.27	30.59	24.73	26.68	25.58
54470	0724810401	PN	0.42	1.19	85.01	76.39	97.76	87.58	115.90	107.93
54470	0729561301	M1	1.06	2.61	10.62	7.74	22.57	13.40	16.70	8.20
54470	0729561301	M2	1.06	2.56	9.67	6.96	22.12	13.03	14.66	7.28
54470	0729561301	PN	0.37	1.05	45.19	27.44	47.94	23.20	40.26	23.07
54479	0744930401	M2	1.22	2.92	2.23	2.13	2.85	2.71	1.51	1.46
54479	0744930401	M1	1.24	3.01	3.13	2.63	3.45	3.04	1.90	1.68
54479	0744930401	PN	0.41	1.13	13.29	11.14	9.56	7.80	6.38	5.59
55616	0740620101	M2	1.11	2.64	3.93	0.86	6.85	1.93	5.50	1.84
55616	0740620101	M1	1.13	2.75	3.82	1.14	6.48	1.83	3.94	1.97
55616	0740620101	PN	0.32	0.90	20.14	4.54	16.18	2.30	10.90	4.72
55696	0745010101	M2	1.86	4.58	2.07	1.83	2.64	1.94	2.10	1.81
55696	0745010101	PN	0.52	1.47	9.04	8.00	4.67	3.66	4.13	3.77
55976	0655380901	M1	1.51	3.71	0.61	1.03	2.55	1.41	1.25	0.82
55976	0655380901	M2	1.53	3.65	1.84	1.33	3.51	2.20	0.77	1.25
55976	0655380901	PN	1.85	5.11	6.09	4.93	3.67	2.75	3.53	3.14
56536	0694440201	M2	2.05	5.17	1.98	1.44	2.95	2.77	1.83	1.58
56536	0694440201	M1	2.05	5.14	2.33	1.35	2.45	2.35	2.51	1.90
56536	0694440201	PN	0.63	1.79	8.79	5.71	8.06	4.86	6.19	4.63
57924	0164560801	M1	1.01	2.38	13.04	11.37	15.61	14.53	15.92	17.79
57924	0164560801	M2	1.02	2.38	9.72	9.64	12.49	13.67	16.47	14.95
57924	0164560801	PN	0.35	0.91	45.13	44.58	53.97	50.21	68.45	64.26
58090	0691010901	M2	1.30	3.16	1.92	1.73	2.71	2.58	3.01	2.56
58090	0691010901	M1	1.37	3.42	2.57	2.19	4.57	3.82	4.69	3.96
58090	0691010901	PN	0.42	1.21	10.86	9.59	12.47	11.00	13.09	12.32
58130	0505010501	M2	1.11	2.66	0.60	0.38	2.03	1.10	1.06	0.69
58130	0505010501	M1	1.15	2.78	1.27	0.45	2.02	1.28	1.35	0.88
58130	0505010501	PN	0.32	0.90	4.71	2.26	5.13	2.64	4.27	3.41

58130	0505011201	M1	1.11	2.68	1.06	0.54	2.67	1.53	1.60	1.22
58130	0505011201	M2	1.11	2.66	1.00	0.41	2.35	1.34	1.12	0.85
58130	0505011201	PN	0.32	0.91	6.46	2.86	5.88	3.16	5.39	3.60
58132	0691010101	M2	1.35	3.28	2.02	1.31	4.41	2.38	2.36	2.04
58132	0691010101	PN	0.44	1.27	9.37	4.70	7.41	4.99	5.66	4.98
58132	0691011001	M2	1.35	3.28	2.30	0.94	2.52	1.65	1.46	1.13
58132	0691011001	PN	0.43	1.23	9.89	5.53	8.80	5.21	5.28	4.83
58152	0691010101	M2	1.14	2.78	1.43	1.06	2.44	1.99	2.98	1.83
58152	0691010101	M1	1.14	2.80	1.40	1.15	2.56	2.11	3.11	2.04
58152	0691010101	PN	0.56	1.57	4.67	3.47	4.81	3.35	6.47	3.63
58152	0691011001	M2	1.14	2.78	1.13	0.71	2.08	1.34	2.49	0.90
58152	0691011001	M1	1.15	2.82	1.12	0.66	2.46	1.33	2.43	0.91
58152	0691011001	PN	0.39	1.09	4.47	3.61	5.13	3.28	7.62	3.35
58189	0691010101	M2	2.24	5.83	1.91	1.45	3.07	3.00	1.76	2.51
58189	0691010101	M1	2.50	6.37	1.57	1.47	2.51	2.80	2.08	2.58
58189	0691010101	PN	0.69	2.06	8.01	5.69	8.31	6.66	7.20	6.30
58189	0691011001	M1	2.18	5.51	1.35	1.31	2.84	2.42	1.83	1.61
58189	0691011001	M2	2.39	6.25	0.93	0.70	1.44	1.84	1.00	1.08
58189	0691011001	PN	0.66	1.95	6.89	5.47	6.10	5.52	5.59	5.36
58715	0723260201	M1	1.16	2.86	0.71	0.60	1.90	1.32	1.07	0.83
58715	0723260201	M2	1.19	2.93	0.90	0.72	1.44	1.38	0.74	0.86
58715	0723260201	PN	0.35	0.99	4.17	3.42	4.01	3.15	3.86	3.42
58813	0782530501	M2	1.12	2.63	1.86	0.72	2.93	1.95	1.70	1.21
58813	0782530501	M1	1.15	2.74	2.14	0.92	3.07	2.32	1.99	1.25
58813	0782530501	PN	0.33	0.90	13.08	5.66	6.86	3.96	7.09	4.41
61742	0602420301	M2	0.98	2.30	21.56	14.79	31.86	24.86	27.63	27.07
61742	0602420301	M1	0.98	2.36	35.49	23.18	45.20	37.83	49.30	46.54
65001	0200670301	M2	1.24	2.72	141.31	74.29	217.09	133.60	113.94	83.00
65001	0200670301	M1	1.25	2.78	147.89	80.46	217.04	136.85	129.21	93.71
65001	0200670301	PN	0.48	1.15	651.22	317.52	597.29	389.42	448.80	364.35
65001	0200670401	M2	1.24	2.73	218.38	188.12	349.88	306.16	345.42	331.72
65001	0200670401	M1	1.25	2.79	216.61	168.99	352.50	269.27	348.26	333.96
65001	0200670401	PN	0.48	1.15	1307.32	1164.16	1550.61	1409.80	1720.03	1695.05
65001	0401360301	M2	1.24	2.73	202.55	161.39	329.25	252.97	256.55	237.03
65001	0401360301	M1	1.25	2.79	205.05	172.36	305.16	250.18	248.98	234.69
65001	0401360301	PN	0.49	1.15	744.95	506.31	779.47	560.91	661.82	603.60
65001	0500730101	M2	1.24	2.73	143.16	79.11	235.22	165.16	142.62	117.45
65001	0500730101	M1	1.25	2.78	147.52	88.29	240.53	158.01	141.92	114.88
65001	0500730101	PN	0.48	1.15	578.15	296.81	517.75	300.57	355.37	284.95
65001	0500730201	M2	1.25	2.73	146.44	75.46	252.96	150.22	130.99	90.27
65001	0500730201	M1	1.26	2.80	144.18	78.87	250.79	143.59	123.20	87.50
65001	0500730201	PN	0.49	1.15	574.56	281.23	537.62	251.12	326.17	232.57
65001	0691570101	M2	1.26	2.76	145.45	72.80	229.21	122.53	135.07	94.48
65001	0691570101	M1	1.51	3.36	134.32	91.83	209.37	119.89	126.49	89.87
65001	0691570101	PN	0.49	1.15	647.83	255.18	569.41	226.14	310.77	187.62

65001	0794581201	M2	1.39	3.03	157.33	87.54	258.32	150.21	141.16	98.53
65001	0794581201	M1	1.70	3.80	118.17	72.72	194.96	131.71	107.39	81.52
65001	0794581201	PN	0.51	1.23	698.04	388.26	647.19	328.87	404.77	286.55
67045	0200230201	M2	1.01	2.44	9.32	5.57	14.94	11.88	10.63	8.12
67045	0200230201	PN	0.36	1.01	51.70	42.57	41.03	37.42	44.48	37.26
67045	0200230201	M1	1.00	2.45	10.81	9.06	16.73	9.74	13.37	11.06
67045	0503460101	M2	1.02	2.46	21.17	14.62	45.04	28.10	39.07	24.28
67045	0503460101	M1	1.00	2.45	24.32	16.65	45.88	31.56	41.75	30.76
71031	0112310201	M2	1.60	4.00	14.19	3.01	18.29	5.06	9.44	3.13
71031	0112310201	M1	1.64	4.16	12.76	2.91	16.53	5.77	8.00	3.21
71031	0112310201	PN	0.54	1.56	61.61	16.69	54.32	16.45	28.60	15.56
71031	0204610101	M2	1.59	3.94	11.79	4.98	15.08	7.75	10.80	5.79
71031	0204610101	M1	1.62	4.09	10.56	4.16	12.59	8.18	7.82	5.35
71031	0204610101	PN	0.53	1.53	53.41	17.43	39.51	16.34	27.99	14.82
71031	0405380701	PN	0.33	0.94	78.58	18.79	58.99	18.18	32.79	14.05
71031	0405380701	M1	0.95	2.34	17.02	5.12	25.80	7.80	12.56	6.27
71031	0405380701	M2	0.99	2.39	13.02	2.73	20.68	5.94	10.06	5.58
71031	0782720301	M1	1.61	4.04	11.50	5.54	14.35	8.00	9.92	6.53
71031	0782720301	M2	1.61	3.96	11.70	4.06	15.38	9.45	9.98	5.82
71031	0782720301	PN	0.53	1.53	57.56	21.92	44.09	21.05	34.26	22.44
71066	0112310201	M2	2.35	5.95	11.81	9.06	20.62	12.83	11.79	8.20
71066	0112310201	M1	2.40	6.16	8.95	6.41	17.19	12.73	13.35	8.02
71066	0112310201	PN	2.77	8.15	4.94	3.90	5.17	3.86	2.79	3.54
71066	0204610101	PN	2.35	6.92	6.94	6.04	6.99	5.93	5.88	5.61
71066	0204610101	M2	2.41	6.06	9.65	6.30	22.57	14.09	16.39	9.60
71066	0204610101	M1	2.50	6.39	7.84	5.22	12.55	10.49	9.57	8.22
71066	0405380701	M1	1.16	2.90	9.46	7.09	19.04	13.27	17.80	12.94
71066	0405380701	M2	1.22	3.00	9.52	7.92	21.57	18.68	17.98	14.03
71066	0405380701	PN	0.38	1.10	48.04	27.42	51.72	31.93	45.33	31.07
71066	0782720301	M2	2.42	6.03	13.56	6.94	23.73	15.07	15.63	12.50
71066	0782720301	M1	2.69	6.84	9.04	5.63	16.23	12.76	12.22	10.33
71066	0782720301	PN	-0.29	-0.87	0.39	0.32	0.42	0.38	0.51	0.46
73858	0404410101	M2	1.54	3.80	3.11	3.09	6.22	6.01	2.96	2.79
73858	0404410101	PN	0.50	1.43	17.98	15.34	16.46	15.19	7.72	7.24
73858	0404410201	M2	1.72	4.16	1.93	2.45	4.95	4.59	1.91	2.05
73858	0404410201	M1	1.93	4.85	2.69	2.41	4.45	4.15	1.80	1.95
73858	0404410201	PN	0.41	1.16	16.64	15.12	17.16	15.86	7.98	7.84
73862	0404410201	M1	1.30	3.22	3.08	2.75	5.39	4.70	2.23	2.20
73862	0404410201	M2	1.38	3.35	3.16	2.79	5.63	5.37	2.66	2.52
73862	0404410201	PN	0.40	1.12	15.51	12.78	15.47	13.32	6.62	6.87
140771	0603190101	M2	1.34	3.29	0.57	0.42	1.87	1.46	1.18	1.02
140771	0603190101	M1	1.44	3.64	0.37	0.43	1.62	1.67	1.10	0.95
140771	0603190101	PN	0.41	1.16	3.47	2.53	4.09	3.00	4.26	3.62
140771	0603190201	M2	1.34	3.29	0.95	0.53	2.45	1.66	0.96	0.92
140771	0603190201	M1	1.49	3.77	0.48	0.41	2.37	1.59	1.18	0.86

140771	0603190201	PN	0.41	1.16	3.97	2.16	4.40	3.06	3.41	2.89
140771	0603190301	M2	1.34	3.28	0.76	0.65	2.66	2.06	1.15	1.34
140771	0603190301	M1	1.46	3.69	0.40	0.45	1.39	1.46	1.00	0.98
140771	0603190301	PN	0.40	1.16	3.93	3.02	4.67	3.91	5.82	4.51
140771	0603190401	M2	1.36	3.33	2.14	0.96	4.26	2.55	1.76	1.96
140771	0603190401	M1	1.39	3.51	1.11	0.76	1.87	1.65	1.30	1.47
140771	0603190401	PN	0.43	1.22	4.19	3.13	6.99	4.46	5.77	5.11
140771	0603190501	M2	1.38	3.39	0.90	0.65	2.48	1.95	1.68	0.97
140771	0603190501	M1	1.42	3.58	0.34	0.33	0.90	1.13	0.86	0.71
140771	0603190501	PN	0.59	1.68	3.24	2.04	3.18	2.41	3.26	2.50
140771	0764800101	M2	1.62	3.96	1.27	1.52	2.31	2.62	3.06	2.85
140771	0764800101	M1	1.73	4.36	2.27	1.68	3.56	2.72	3.00	3.16
140771	0764800101	PN	0.51	1.49	3.76	3.64	4.20	3.92	5.60	5.05
140771	0764800201	M2	1.62	3.95	1.23	1.11	2.23	2.11	2.49	2.07
140771	0764800201	M1	2.16	5.56	2.01	1.37	2.87	2.51	2.55	2.59
140771	0764800201	PN	0.51	1.48	5.24	4.14	5.05	4.63	7.31	6.25
140771	0764800301	M2	1.59	3.89	1.56	1.33	2.63	2.34	1.95	2.30
140771	0764800301	M1	1.69	4.27	1.78	1.80	3.12	3.05	3.41	3.33
140771	0764800301	PN	0.51	1.48	5.47	5.28	6.37	5.43	7.86	7.05
140771	0764800401	M2	1.58	3.87	0.83	0.76	1.55	1.29	1.40	1.01
140771	0764800401	M1	1.69	4.27	0.85	0.70	1.80	1.56	1.29	1.19
140771	0764800401	PN	0.51	1.48	4.40	3.53	3.99	2.80	3.50	3.34
140771	0764800501	M2	1.55	3.78	0.62	0.55	2.03	1.36	1.21	1.03
140771	0764800501	M1	1.73	4.36	0.84	0.78	1.90	1.54	1.75	1.39
140771	0764800501	PN	0.62	1.79	5.09	3.72	5.44	4.21	6.34	5.09
140771	0764800601	M2	1.54	3.76	0.73	0.50	1.63	1.25	1.15	0.87
140771	0764800601	M1	1.68	4.25	0.73	0.60	1.95	1.34	1.42	0.86
140771	0764800601	PN	0.88	2.54	2.87	2.77	2.86	2.43	3.50	2.84
140771	0764800801	M2	1.53	3.73	0.78	0.90	1.66	1.77	1.88	1.84
140771	0764800801	M1	1.65	4.17	1.14	1.11	2.87	2.23	2.81	2.92
140771	0764800801	PN	0.57	1.64	4.15	2.95	4.14	3.31	5.44	4.66
140771	0764800901	M1	1.82	4.55	1.13	0.72	1.75	1.39	1.68	1.16
140771	0764800901	M2	2.03	4.90	0.43	0.58	1.19	1.18	1.01	0.87
140771	0764800901	PN	0.48	1.39	6.61	6.36	7.91	7.30	10.49	10.09
140771	0770180101	M1	2.86	7.24	1.03	0.98	1.47	1.78	1.98	1.79
140771	0770180101	M2	3.84	9.97	0.68	0.71	1.29	1.34	1.14	1.10
140771	0770180101	PN	0.48	1.37	4.95	4.51	5.26	4.69	7.34	6.52
140771	0770180201	M2	1.40	3.40	1.09	0.58	1.33	1.12	1.08	0.76
140771	0770180201	PN	0.48	1.38	3.91	3.34	3.88	3.44	4.04	4.06
200253	0103260801	M2	1.15	2.78	2.07	0.82	2.32	1.42	1.86	1.20
200253	0103260801	M1	1.21	2.94	1.93	0.75	2.10	1.48	1.94	1.68
200253	0103260801	PN	0.36	1.00	8.04	3.09	5.36	2.45	4.07	3.34
1154498	0651740901	M1	1.32	3.27	1.88	1.48	4.83	3.31	4.15	3.15
1154498	0651740901	M2	1.35	3.28	3.20	1.77	3.38	3.62	2.55	3.28
1154498	0651740901	PN	0.41	1.16	4.92	6.54	13.23	5.66	14.63	7.92

1160119	0724440401	PN	2.47	7.17	6.51	6.84	5.40	5.61	5.40	6.44
1160119	0724440401	M1	2.76	6.95	3.09	1.92	4.80	2.68	4.13	2.96
1160119	0724440401	M2	2.80	7.13	2.60	1.64	2.97	2.60	1.85	1.99
1284684	0744411201	M2	3.05	7.90	1.58	1.82	2.24	2.58	2.49	1.86
1284684	0744411201	PN	0.84	2.49	9.44	7.20	6.81	4.23	4.26	4.50
1412010	0723161001	M2	1.93	4.67	0.96	0.69	2.09	1.48	1.72	1.10
1412010	0723161001	M1	3.11	7.60	0.51	0.60	0.94	0.99	1.15	0.96
1412010	0723161001	PN	0.47	1.33	4.47	4.32	9.11	5.58	8.18	6.52
1527695	0722570301	M2	2.07	5.30	1.40	0.96	1.05	2.08	2.17	1.64
1527695	0722570301	PN	0.57	1.68	4.33	3.19	1.62	3.04	4.64	3.05
1527695	0722570501	M2	2.08	5.34	2.34	2.05	3.57	2.91	3.04	3.17
1527695	0722570501	PN	0.57	1.69	4.17	4.16	5.02	4.80	6.19	5.97
1531425	0740620301	PN	1.00	3.15	13.73	8.62	11.01	6.00	8.10	6.65
1531425	0740620301	M2	3.25	8.54	3.84	2.14	5.24	3.01	3.07	2.22
1531425	0740620301	M1	3.37	8.74	4.51	2.45	4.93	3.33	2.62	2.94
1573473	0761510201	M2	1.74	4.36	1.55	0.77	2.76	2.01	1.46	1.33
1573473	0761510201	M1	1.74	4.44	1.65	0.74	2.93	1.82	0.89	1.22
1573473	0761510201	PN	0.52	1.50	7.78	3.35	4.49	3.08	4.61	3.12
1616588	0602200101	M1	2.92	7.45	3.99	2.30	6.23	5.24	3.82	3.15
1616588	0602200101	PN	3.02	9.52	10.91	9.59	11.90	11.80	9.26	9.41
1616588	0602200101	M2	3.08	8.12	2.96	2.16	6.27	6.21	3.84	3.20
1681191	0502690601	M2	1.96	5.00	1.66	1.45	2.92	2.81	2.25	2.41
1681191	0502690601	PN	0.61	1.81	3.88	3.30	4.32	4.05	5.56	4.99
1750402	0025540301	M1	1.54	3.87	0.47	0.88	2.74	1.47	1.31	0.82
1750402	0025540301	M2	1.76	4.38	0.52	0.47	1.83	1.24	1.09	0.98
1750402	0025540301	PN	0.60	1.69	4.41	2.33	3.57	2.13	7.07	3.40
1817480	0210280101	M2	1.62	4.05	2.29	1.86	3.56	2.93	2.73	2.67
1817480	0210280101	PN	0.50	1.46	5.29	2.62	5.78	3.00	4.94	3.55
1817480	0210280101	M1	8.30	23.20	0.85	0.54	1.17	1.02	0.95	1.02
2141849	0138951401	M2	1.83	4.49	2.55	0.89	1.29	1.37	0.77	0.79
2141849	0138951401	M1	1.87	4.66	2.07	0.68	1.79	1.43	0.54	0.83
2141849	0138951401	PN	0.56	1.59	12.36	3.06	7.66	2.65	4.09	2.55
2156773	0553790101	M2	1.18	2.81	0.48	0.52	2.37	1.56	1.62	1.02
2156773	0553790101	M1	1.20	2.89	0.39	0.67	1.76	1.70	1.48	1.07
2156773	0553790101	PN	0.36	0.97	1.91	1.85	3.30	2.97	4.31	3.05
2177729	0673020201	M2	1.23	2.78	3.67	1.89	9.21	4.63	4.86	3.13
2177729	0673020201	M1	1.29	2.93	5.15	2.75	10.50	5.93	6.78	4.46
2177729	0673020201	PN	0.99	2.53	19.43	8.44	23.15	11.61	13.41	9.32
2468371	0200960101	M2	1.70	4.17	2.05	1.50	2.74	2.70	2.78	2.46
2468371	0200960101	M1	1.81	4.58	2.02	1.78	4.06	2.87	3.52	2.63
2468371	0200960101	PN	0.53	1.53	4.16	2.37	3.27	2.76	3.91	3.09
2568088	0741580101	PN	1.03	3.02	9.27	6.27	10.28	6.72	5.56	4.12
2568088	0741580101	M1	2.61	6.60	1.01	1.18	3.35	2.37	2.86	1.74
2568088	0741580101	M2	7.05	18.99	1.59	0.97	2.56	2.28	0.63	0.88
2568088	0764910201	M2	2.03	5.07	2.00	1.45	4.49	3.06	2.13	2.24

2568088	0764910201	M1	2.18	5.59	2.42	1.65	4.05	3.19	3.26	2.65
2568088	0764910201	PN	0.61	1.80	12.38	6.93	11.64	8.57	8.23	7.88
3094758	0762640101	M1	1.33	3.32	0.60	0.53	1.26	1.14	1.09	0.94
3094758	0762640101	M2	1.34	3.29	0.83	0.50	1.49	1.44	1.10	0.81
3094758	0762640101	PN	0.40	1.14	3.34	2.83	2.94	2.53	2.35	2.75
3105149	0760230401	M2	2.03	5.05	2.01	1.00	3.51	1.43	1.47	1.29
3105149	0760230401	M1	2.97	7.33	1.46	0.71	1.73	0.94	1.13	0.71
3105149	0760230401	PN	0.64	1.81	9.01	5.07	10.35	4.25	5.70	4.92
3122018	0402780501	M2	2.61	6.53	1.45	1.39	3.71	2.38	1.62	1.42
3122018	0402780501	M1	3.67	9.10	1.94	1.58	2.73	2.43	1.58	1.76
3122018	0402780501	PN	0.72	2.03	8.93	9.40	8.88	7.19	10.76	9.28
3390074	0554540201	PN	1.17	3.90	4.25	3.19	6.75	5.65	9.11	6.95
3408576	0554121001	M1	2.31	5.93	1.17	0.67	1.99	2.03	2.33	1.61
3408576	0554121001	M2	2.42	6.28	1.26	0.90	2.96	2.93	3.06	1.87
3408576	0554121001	PN	3.29	10.11	3.75	2.76	5.32	3.71	4.70	4.19
3737721	0670880501	M1	2.41	6.08	1.70	0.89	2.65	2.25	2.60	1.99
3737721	0670880501	M2	37.10	94.41	0.38	0.22	0.52	0.67	0.54	0.50
3737721	0670880501	PN	0.98	2.83	2.66	1.81	2.99	2.45	3.64	2.88
3845383	0109930101	M2	2.00	5.06	4.77	4.33	6.62	5.28	5.75	5.37
3845383	0109930101	M1	2.16	5.56	3.95	3.46	5.27	4.69	6.08	4.39
3845383	0109930101	PN	0.61	1.79	16.85	12.98	13.61	10.04	8.15	6.64
3845383	0723801501	M1	1.72	4.36	2.97	2.06	4.08	2.76	1.87	1.37
3845383	0723801501	M2	1.87	4.67	2.50	1.97	3.78	2.78	1.92	1.36
3845383	0723801501	PN	2.31	6.88	11.00	9.85	9.10	6.68	5.94	4.64

Table of count-rates and conversion to flux values for the star-forming sample. Column (1) gives the catalogue ID (PGC number) of each galaxy; Column (2) gives the observation ID of *XMM-Newton* and ; Column (3) the corresponding detector (EPIC M1, M2, or pn); Columns (4) and (5) give the count-rate to flux conversions for the broad and hard band respectively; Columns (6)-(11) give the source and background count-rates for the 2, 3, and 4 *XMM-Newton* bands.

Table 4.5: Spectral fitting parameters of the star-forming sample.

PGC (1)	$N_H$gal 10^{22}cm^{-2} (2)	N_H 10^{22}cm^{-2} (3)	Γ (4)	kT1 keV (5)	kT2 keV (6)	χ^2 (dof) (7)
2388	0.0195	$0.0005 \leq +0.0454$	$2.20^{+0.28}_{-0.13}$	-	-	95.93 (93)
4979	0.0318	$0.0005 \leq +0.0355$	$1.68^{+0.21}_{-0.11}$	-	-	127.73 (110)
5193	0.0316	$0.0001 \leq +0.0605$	$1.76^{+0.35}_{-0.15}$	-	-	81.22 (59)
6972	0.0560	$0.1015^{+0.0332}_{-0.0313}$	$2.51^{+0.17}_{-0.16}$	-	-	402.58 (326)
12486	0.0628	$0.1788 \leq +0.3714$	$1.95^{+1.09}_{-0.75}$	-	-	15.92 (13)
12785	0.0423	$0.3180^{+0.2525}_{-0.1819}$	$4.77^{+1.75}_{-1.26}$	-	-	34.44 (28)
14236	0.0560	$0.0738^{+0.0252}_{-0.0242}$	$1.88^{+0.10}_{-0.10}$	-	-	340.39 (259)
15345	0.2200	$0.5552^{+0.1229}_{-0.0753}$	$2.28^{+0.58}_{-0.40}$	$0.27^{+0.02}_{-0.05}$	-	161.52 (147)
16282	0.0097	$0.3848^{+0.1173}_{-0.1649}$	$2.08^{+0.97}_{-0.78}$	$0.18^{+0.03}_{-0.03}$	-	77.51 (80)
25470	0.0283	$0.1823 \leq +0.6053$	$3.15^{+4.25}_{-1.62}$	-	-	11.63 (8)
28682	0.0181	$0.0240 \leq +0.1222$	$1.83^{+0.74}_{-0.34}$	-	-	22.38 (16)
28990	0.0092	$0.0028 \leq +0.3280$	$1.35^{+1.91}_{-0.53}$	-	-	1.82 (7)
32434	0.0197	$0.1190^{+0.0583}_{-0.0512}$	$2.75^{+0.37}_{-0.32}$	-	-	166.14 (137)
32543	0.0200	$0.0511^{+0.0266}_{-0.0254}$	$1.52^{+0.10}_{-0.10}$	-	-	301.52 (287)
32584	0.0196	$0.0821^{+0.0795}_{-0.0675}$	$2.34^{+0.49}_{-0.40}$	-	-	114.29 (88)
32827	0.0053	$0.0186 \leq +0.3963$	$0.87^{+1.02}_{-0.49}$	-	-	1.48 (6)
32907	0.0278	$0.1914 \leq +0.4750$	$2.48^{+2.39}_{-1.12}$	-	-	6.45 (6)
34257	0.0175	$0.0663 \leq +0.0991$	$2.65^{+0.70}_{-0.51}$	-	-	140.08 (89)
34767	0.0110	$0.0012 \leq +0.0116$	$1.59^{+0.09}_{-0.03}$	-	-	930.43 (901)
36406	0.0153	$0.0381 \leq +0.0923$	$2.10^{+0.54}_{-0.34}$	-	-	43.47 (43)
36477	0.0155	$0.0619 \leq +0.3722$	$1.55^{+1.09}_{-0.59}$	-	-	2.71 (6)
37692	0.0119	$0.0478 \leq +1.1582$	$2.46^{+2.05}_{-0.91}$	-	-	9.87 (8)
39152	0.0273	$0.0005 \leq +0.0121$	$2.02^{+0.12}_{-0.07}$	-	-	520.39 (463)
39950	0.0251	$0.0192 \leq +0.0502$	$2.20^{+0.30}_{-0.19}$	-	-	144.92 (144)
40562	0.0273	$0.5367^{+0.2242}_{-0.3603}$	$-1.00 \leq +1.19$	$0.16^{+0.05}_{-0.04}$	$1.37^{+0.31}_{-0.19}$	48.87 (48)
40809	0.0154	$0.5063 \leq +0.2600$	$1.27 \leq +2.27$	$0.10 \leq +0.12$	$0.54^{+0.52}_{-0.38}$	11.10 (14)
40962	0.0278	$0.5115 \leq +1.5834$	$3.62^{+1.0}_{-2.31}$	-	-	0.13 (5)
41107	0.0162	$0.0714 \leq +0.3815$	$2.21^{+1.79}_{-0.71}$	-	-	7.87 (5)
41189	0.0158	$0.0307 \leq +0.0476$	$2.25^{+0.29}_{-0.24}$	-	-	226.91 (199)
42727	0.0134	$0.1473 \leq +0.2056$	$2.27^{+0.31}_{-3.37}$	$0.19 \leq +0.21$	$0.68 \leq 1.0$	40.28 (45)
42816	0.0206	$0.0147 \leq +0.0322$	$2.10^{+0.34}_{-0.39}$	$0.20 \leq 1.0$	$0.90^{+0.09}_{-0.06}$	771.98 (622)
42999	0.0173	$0.0008 \leq +0.0401$	$1.71^{+0.25}_{-0.21}$	-	-	24.72 (42)

44536	0.0109	$0.0947^{+0.0244}_{-0.0234}$	$2.34^{+0.13}_{-0.12}$	-	-	343.28 (380)
45700	0.0123	$0.1465 \leq +1.1847$	$3.09^{+1.00}_{-1.53}$	-	-	8.32 (6)
47368	0.0175	$0.0807^{+0.0046}_{-0.0046}$	$2.33^{+0.02}_{-0.02}$	-	-	5914.47 (7073)
48240	0.0210	$0.0016 \leq +0.5069$	$2.09^{+3.78}_{-0.74}$	-	-	1.84 (6)
49468	0.0204	$0.1303 \leq +0.2141$	$1.32^{+0.49}_{-0.43}$	-	-	25.08 (16)
50944	0.0099	$0.0022 \leq +0.1474$	$1.96^{+0.94}_{-0.33}$	-	-	3.24 (9)
51210	0.0141	$0.0187 \leq +0.0686$	$1.53^{+0.26}_{-0.18}$	-	-	85.94 (120)
52112	0.0243	$0.0010 \leq +0.0084$	$2.06^{+0.05}_{-0.09}$	-	-	236.05 (257)
53231	0.0350	$0.0020 \leq +0.6644$	$2.47^{+5.07}_{-0.74}$	-	-	2.67 (6)
54479	0.0273	$0.1651 \leq +0.2509$	$3.14^{+1.65}_{-1.04}$	-	-	27.75 (27)
55616	0.0135	$0.0000 \leq +0.0686$	$1.60^{+0.40}_{-0.17}$	-	-	11.19 (13)
56536	0.0375	$0.0001 \leq +0.2116$	$1.84^{+1.16}_{-0.41}$	-	-	5.25 (8)
58130	0.0143	$0.0010 \leq +0.1447$	$2.67^{+1.32}_{-0.58}$	-	-	6.05 (7)
58132	0.0084	$0.2011^{+0.1933}_{-0.1432}$	$2.94^{+1.18}_{-0.83}$	-	-	40.95 (29)
58152	0.0085	$1.2463^{+0.6211}_{-0.6523}$	$1.15^{+0.62}_{-0.47}$	$0.06^{+0.05}_{-0.01}$	$0.01 \leq +0.2$	51.81 (31)
67045	0.0220	$0.0107 \leq +0.0990$	$1.71^{+0.46}_{-0.23}$	-	-	46.98 (58)
71031	0.0140	$0.0287^{+0.0193}_{-0.0186}$	$2.03^{+0.10}_{-0.10}$	-	-	785.51 (714)
71066	0.0141	$0.0341 \leq +0.0510$	$1.50^{+0.19}_{-0.17}$	-	-	197.81 (203)
140771	0.0225	$0.0000 \leq +0.1640$	$0.94^{+0.60}_{-0.51}$	-	-	8.80 (7)
200253	0.0294	$0.1689^{+0.1702}_{-0.1211}$	$3.08^{+1.14}_{-0.76}$	-	-	70.80 (39)
1531425	0.0289	$0.0017 \leq +0.1234$	$2.11^{+0.76}_{-0.40}$	-	-	15.38 (11)
1817480	0.0248	$0.0877 \leq +0.1561$	$2.08^{+0.80}_{-0.55}$	-	-	23.14 (26)
2177729	0.1460	$0.0004 \leq +0.0550$	$2.22^{+0.26}_{-0.16}$	-	-	35.42 (67)
2468371	0.0192	$0.0007 \leq +0.1802$	$2.01^{+1.34}_{-0.64}$	-	-	5.09 (7)
3845383	0.0274	$0.0653 \leq +0.0740$	$1.85^{+0.31}_{-0.27}$	-	-	84.54 (72)

Column (1): source catalogue identification ID (PGC); Column (2): line-of-sight hydrogen column density ($N_H gal$); Column (3): intrinsic absorption (N_H); Column (4): photon index Γ; Columns (5) and (6): thermal plasma model temperatures (kT1, kT2); Column (7): χ^2 of the spectral fit and corresponding degrees of freedom (d.o.f)

Table 4.6: Luminosities of the detected galaxies in the star-forming sample.

PGC	$\mathrm{L_x}(0.5-8.0\,\mathrm{keV})$	$\mathrm{L_x}(2-10\,\mathrm{keV})$
	10^{39} erg s^{-1}	10^{39} erg s^{-1}
1014	1.33 ± 0.01	0.62 ± 0.02
1142	5.23 ± 2.67	5.32 ± 4.11
2388	$28.01^{+3.78}_{-3.21}$	$14.33^{+3.92}_{-3.16}$
2758	4.52 ± 0.04	2.22 ± 0.06
3238	0.45 ± 0.01	0.18 ± 0.01
4979	$2.62^{+1.18}_{-0.72}$	$2.02^{+1.52}_{-0.86}$
5193	$18.92^{+7.18}_{-4.70}$	$14.15^{+7.80}_{-5.34}$
6972	$8.46^{+3.68}_{-2.54}$	$4.10^{+3.95}_{-2.03}$
11631	96.43 ± 7.63	77.36 ± 14.37
11650	0.37 ± 2.53	1.00 ± 6.20
12286	20.41 ± 0.08	11.20 ± 0.11
12418	49.85 ± 8.27	50.60 ± 10.25
12486	$22.79^{+13.84}_{-8.25}$	$17.41^{+16.42}_{-8.25}$
12785	$66.76^{+13.28}_{-14.86}$	$6.44^{+5.07}_{-2.75}$
12803	54.86 ± 6.85	7.18 ± 9.94
14236	$14.25^{+1.29}_{-1.07}$	$10.67^{+1.27}_{-1.19}$
15345	$0.31^{+0.26}_{-0.15}$	$0.26^{+0.28}_{-0.14}$
16282	$0.07^{+0.48}_{-0.06}$	$0.05^{+0.57}_{-0.05}$
21396	3.51 ± 0.03	2.32 ± 0.04
22805	46.02 ± 5.38	31.90 ± 9.96
23359	27.87 ± 4.24	39.86 ± 7.77
23504	8.76 ± 4.72	10.50 ± 7.11
23850	26.15 ± 2.81	4.74 ± 5.73
25363	23.14 ± 12.28	37.11 ± 23.03
25470	$18.33^{+9.12}_{-5.15}$	$5.82^{+7.44}_{-3.24}$
27077	12.57 ± 0.10	3.95 ± 0.14
27658	29.24 ± 10.56	32.61 ± 17.52
28655	39.36 ± 0.03	26.27 ± 0.04
28682	$2.47^{+0.73}_{-0.56}$	$1.68^{+0.99}_{-0.57}$
28990	$4.07^{+4.37}_{-1.73}$	$3.62^{+4.64}_{-2.01}$
30087	8.46 ± 0.44	3.94 ± 0.76
30948	14.72 ± 24.64	4.50 ± 37.53
31856	287.29 ± 25.56	214.63 ± 64.68
32341	27.22 ± 4.03	15.92 ± 12.49
32434	$8.65^{+1.17}_{-0.91}$	$3.40^{+1.07}_{-0.78}$
32464	2.72 ± 0.37	0.93 ± 0.74

32543	$3.69^{+1.01}_{-0.76}$	$3.27^{+1.28}_{-0.99}$
32584	$4.65^{+1.16}_{-0.92}$	$2.42^{+1.11}_{-0.77}$
32827	$108.82^{+108.35}_{-53.36}$	$125.20^{+151.83}_{-67.15}$
32907	$28.29^{+21.00}_{-9.82}$	$15.34^{+18.67}_{-8.53}$
33437	64.95 ± 18.59	29.02 ± 24.57
33500	51.62 ± 11.72	62.22 ± 19.68
34257	$1.24^{+0.35}_{-0.24}$	$0.48^{+0.31}_{-0.19}$
34612	5.75 ± 0.18	3.44 ± 0.22
34692	1.40 ± 0.59	2.57 ± 1.07
34767	$22.97^{+1.98}_{-1.88}$	$18.10^{+2.39}_{-2.11}$
34963	10.16 ± 8.17	19.26 ± 14.91
35321	470.99 ± 3.12	173.39 ± 3.27
35762	37.76 ± 7.66	38.07 ± 13.63
35838	17.32 ± 1.09	17.68 ± 2.46
35906	92.96 ± 18.35	77.29 ± 39.75
36198	5.12 ± 12.01	3.73 ± 20.60
36349	63.43 ± 5.96	61.69 ± 12.33
36406	$61.12^{+14.88}_{-11.78}$	$35.30^{+15.10}_{-11.04}$
36477	$100.77^{+76.60}_{-42.21}$	$87.46^{+92.58}_{-45.39}$
37013	13.87 ± 1.67	8.04 ± 3.36
37282	20.05 ± 7.31	11.24 ± 14.92
37692	$1.74^{+1.39}_{-0.63}$	$0.73^{+1.55}_{-0.46}$
37747	5.28 ± 11.06	0.07 ± 16.21
37976	55.04 ± 2.96	62.86 ± 5.78
38163	48.51 ± 19.34	29.08 ± 31.18
38672	85.98 ± 21.07	61.42 ± 36.48
39152	$10.09^{+5.41}_{-2.88}$	$6.15^{+6.78}_{-3.06}$
39225	0.39 ± 0.03	0.14 ± 0.05
39422	0.33 ± 0.03	0.19 ± 0.04
39578	18.07 ± 0.38	6.01 ± 0.53
39783	7.36 ± 12.43	7.91 ± 20.52
39922	5.23 ± 1.59	3.64 ± 3.01
39950	$3.03^{+0.55}_{-0.47}$	$1.60^{+0.60}_{-0.43}$
40001	16.14 ± 0.31	1.77 ± 0.46
40425	0.31 ± 0.07	0.43 ± 0.13
40562	$1.92^{+1.33}_{-1.31}$	$3.67^{+2.60}_{-2.43}$
40644	5.21 ± 0.18	1.60 ± 0.22
40705	6.36 ± 0.76	6.18 ± 0.93
40809	$2.19^{+1.12}_{-0.89}$	$3.98^{+45.52}_{-6.21}$

40962	$17.01^{+32.16}_{-8.98}$	$6.18^{+32.55}_{-4.93}$
41107	$36.15^{+24.71}_{-12.58}$	$20.92^{+27.62}_{-11.84}$
41189	$1.73^{+0.57}_{-0.37}$	$0.87^{+0.61}_{-0.32}$
41566	19.33 ± 8.77	53.17 ± 19.40
41729	1.42 ± 0.29	0.16 ± 0.37
41763	0.75 ± 0.15	0.33 ± 0.22
41823	14.97 ± 0.52	5.55 ± 0.74
41857	126.16 ± 14.24	33.47 ± 21.78
41912	11.41 ± 1.73	7.72 ± 2.49
41967	31.10 ± 7.98	39.32 ± 28.64
42408	0.13 ± 0.14	0.16 ± 0.22
42637	7.55 ± 0.11	4.47 ± 0.13
42699	0.32 ± 0.11	0.10 ± 0.28
42727	$56.46^{+25.94}_{-16.30}$	$47.77^{+83.48}_{-30.00}$
42816	$2.80^{+2.73}_{-2.29}$	$2.89^{+4.15}_{-2.17}$
42999	$1.19^{+0.87}_{-0.43}$	$0.86^{+0.97}_{-0.48}$
43511	2.82 ± 0.28	2.94 ± 0.50
43843	28.48 ± 5.68	25.58 ± 10.91
44418	60.62 ± 27.94	61.26 ± 50.77
44536	$2.65^{+0.72}_{-0.55}$	$1.39^{+0.82}_{-0.51}$
44968	26.40 ± 5.11	14.81 ± 13.83
45700	$4.43^{+2.85}_{-1.67}$	$1.24^{+2.55}_{-0.80}$
47333	18.75 ± 6.10	4.28 ± 12.27
47337	4.68 ± 7.57	8.07 ± 9.49
47368	$4.27^{+0.15}_{-0.16}$	$2.23^{+0.14}_{-0.15}$
47503	2.01 ± 11.56	2.26 ± 15.49
48240	$18.78^{+16.14}_{-6.81}$	$10.46^{+21.71}_{-6.81}$
49221	4.98 ± 0.47	1.82 ± 0.79
49468	$8.88^{+8.97}_{-4.25}$	$8.65^{+11.57}_{-4.94}$
49921	49.97 ± 7.67	30.73 ± 13.96
50063	31.46 ± 0.36	15.75 ± 0.56
50810	48.62 ± 11.48	45.20 ± 21.96
50881	36.92 ± 16.15	82.78 ± 27.37
50886	19.95 ± 19.49	19.42 ± 38.09
50944	$47.77^{+17.42}_{-11.82}$	$28.96^{+20.86}_{-11.88}$
51210	$1.16^{+0.32}_{-0.21}$	$0.98^{+0.34}_{-0.25}$
51353	110.68 ± 12.82	33.01 ± 22.06
51485	22.44 ± 4.23	10.65 ± 5.76
51791	167.62 ± 30.98	197.86 ± 58.88

52112	$354.47^{+52.00}_{-46.94}$	$202.69^{+61.84}_{-47.74}$
52318	122.03 ± 10.91	80.56 ± 16.95
52939	13.13 ± 7.68	11.70 ± 17.68
53231	$3.20^{+2.28}_{-1.32}$	$1.26^{+2.73}_{-0.87}$
53245	16.26 ± 5.57	24.70 ± 9.27
53559	228.21 ± 42.18	190.36 ± 79.09
53683	5.75 ± 0.58	6.42 ± 1.08
54032	119.01 ± 13.23	88.12 ± 19.46
54219	111.61 ± 38.63	75.72 ± 58.71
54470	4.97 ± 0.13	4.63 ± 0.20
54479	$43.76^{+12.36}_{-8.36}$	$13.57^{+10.57}_{-5.37}$
55616	$3.62^{+1.41}_{-0.93}$	$2.91^{+1.77}_{-1.09}$
55696	56.61 ± 13.66	30.86 ± 20.64
55717	22.63 ± 14.51	11.91 ± 11.21
55976	6.81 ± 3.16	6.25 ± 5.20
56536	$69.24^{+36.58}_{-22.76}$	$48.19^{+48.86}_{-24.04}$
57924	1.31 ± 1.12	1.83 ± 1.44
58090	37.70 ± 10.73	36.79 ± 17.43
58130	$38.43^{+17.08}_{-11.89}$	$11.96^{+17.98}_{-7.10}$
58132	$45.50^{+21.25}_{-11.71}$	$17.78^{+20.70}_{-9.31}$
58152	$148.97^{+398.09}_{-114.43}$	$195.37^{+889.54}_{-172.52}$
58189	60.74 ± 8.38	34.79 ± 15.32
58715	21.09 ± 6.08	13.05 ± 9.83
58813	41.45 ± 7.70	23.44 ± 13.05
59498	70.27 ± 39.21	13.41 ± 56.74
61742	7.71 ± 2.15	2.22 ± 4.34
65001	15.94 ± 0.06	5.79 ± 0.07
67045	$2.50^{+0.98}_{-0.72}$	$1.87^{+1.25}_{-0.75}$
71031	$20.06^{+2.36}_{-2.08}$	$12.14^{+2.41}_{-2.13}$
71066	$10.57^{+12.36}_{-5.34}$	$9.24^{+16.99}_{-6.12}$
73854	28.47 ± 12.16	4.27 ± 15.36
73858	65.33 ± 12.28	22.75 ± 18.00
73862	$59.49^{+35.75}_{-20.88}$	$29.41^{+41.30}_{-15.96}$
73875	8.25 ± 18.22	12.78 ± 23.35
94158	17.29 ± 228.17	107.65 ± 358.31
140771	$50.05^{+58.70}_{-24.58}$	$58.45^{+91.58}_{-37.20}$
165662	24.69 ± 13.39	1.57 ± 19.01
200253	$67.39^{+17.65}_{-12.24}$	$22.67^{+18.23}_{-9.25}$
1126633	27.87 ± 12.61	10.95 ± 24.85

1154498	105.99 ± 32.07	146.05 ± 68.53
1160119	331.94 ± 45.55	219.26 ± 82.42
1168578	79.94 ± 40.84	34.29 ± 63.72
1284684	5.28 ± 42.95	178.56 ± 78.47
1412010	46.40 ± 12.18	40.54 ± 21.17
1509913	25.19 ± 10.96	9.57 ± 15.73
1527695	5.39 ± 2.78	20.68 ± 6.21
1531425	$140.41^{+63.54}_{-37.97}$	$75.94^{+73.81}_{-35.07}$
1573473	100.32 ± 10.61	57.45 ± 17.61
1616588	97.39 ± 16.39	61.14 ± 25.24
1646009	16.18 ± 7.59	1.50 ± 11.94
1681191	12.78 ± 5.67	15.12 ± 10.50
1750402	25.42 ± 12.72	23.03 ± 22.33
1817480	$2.47^{+0.97}_{-0.63}$	$1.55^{+1.07}_{-0.60}$
2141849	94.08 ± 11.12	25.89 ± 18.27
2156773	9.59 ± 4.68	12.20 ± 6.83
2177729	$100.10^{+30.99}_{-22.58}$	$61.77^{+34.07}_{-21.58}$
2468371	$4.31^{+3.55}_{-1.47}$	$2.61^{+4.14}_{-1.61}$
2568088	91.25 ± 7.79	70.18 ± 20.08
2816038	44.46 ± 18.73	36.62 ± 36.88
3094758	13.15 ± 6.18	14.34 ± 10.40
3105149	152.38 ± 12.28	28.89 ± 17.86
3122018	37.08 ± 11.34	31.17 ± 15.42
3390074	156.10 ± 16.21	260.75 ± 35.77
3408576	66.05 ± 23.89	122.89 ± 45.14
3532807	33.28 ± 14.49	23.90 ± 32.28
3737721	116.62 ± 19.33	98.34 ± 29.72
3845383	$190.02^{+45.05}_{-37.34}$	$135.87^{+52.90}_{-36.35}$

Table of luminosities for the star-forming galaxy sample. We include in this Table only the spectroscopic luminosities for galaxies with information on both spectroscopic and photometric luminosities. Column (1): source catalogue identification ID (PGC); Column (2): luminosity of the broad band (0.5-8 keV); Column (3): luminosity of the hard band (2-10 keV).

Table 4.7: Upper-limit luminosities of the very faint galaxies in the star-forming sample.

PGC (1)	$L_x(0.5-8.0\ \mathrm{keV})$ 10^{39} erg s^{-1} (2)	$L_x(2-10\ \mathrm{keV})$ 10^{39} erg s^{-1} (3)
2365	5.81	3.74
3781	4.49	19.73
4195	5.84	6.62
4371	20.84	44.89
4420	73.27	103.28
4465	14.87	20.28
4616	16.72	7.94
4734	4.95	10.95
4806	7.33	6.47
4916	8.98	16.99
5127	12.99	21.19
5189	21.08	48.38
5238	81.43	74.50
6029	4.65	6.85
6169	22.69	35.30
6630	6.87	14.71
8837	21.58	27.56
9623	4.65	7.62
9677	15.80	28.62
9680	46.08	40.95
11563	3.87	2.00
11650	32.97	29.26
12803	45.65	15.17
21838	55.38	69.96
21978	12.05	19.54
22645	5.51	6.81
22766	60.81	83.35
23146	2.94	2.89
24169	23.34	24.50
24660	16.48	17.85
25046	86.63	203.97
25056	17.39	25.94
25180	27.24	17.81
25447	88.38	135.27
25506	35.24	76.59
26471	7.84	7.57
26495	6.05	7.65
26510	22.89	47.08
26572	33.35	53.18
26628	32.80	39.23

26635	57.95	61.59
26897	29.71	25.79
27505	45.43	109.28
27731	26.25	31.38
27844	15.64	30.93
27988	167.90	337.65
28848	0.83	1.39
29233	4.79	8.51
29363	12.37	25.41
29711	26.48	33.13
30109	51.47	58.22
30327	18.70	19.82
30663	21.52	29.31
30948	37.43	29.94
31707	1.59	2.21
31839	5.05	6.13
31991	3.55	12.07
32215	12.92	22.82
32706	2.64	3.11
33428	22.16	24.06
33571	6.13	4.90
33887	46.94	67.37
33953	0.55	1.56
34462	114.70	187.18
34661	69.25	134.97
34667	10.66	22.87
34804	32.14	36.23
34896	26.55	32.58
34949	12.32	12.12
35544	90.06	96.40
35595	71.77	74.47
35609	24.46	14.22
35631	45.46	41.53
35678	0.79	1.43
36181	8.34	16.06
36198	22.24	14.12
36308	7.89	17.78
36323	7.57	16.69
36371	5.78	10.28
36388	17.49	12.72
36671	9.11	13.74
37173	69.65	106.63
37180	4.60	7.21
37282	27.33	30.13
37410	35.80	50.80

37466	2.84	4.07
37747	8.79	7.04
38138	51.60	22.55
38163	30.60	30.20
38250	4.72	9.01
38406	98.49	221.25
38507	0.39	0.34
38508	1.56	1.52
38569	65.17	68.21
38885	0.79	0.91
39280	13.12	15.20
39655	0.43	0.24
39783	8.24	8.49
39840	2.83	3.41
40157	0.70	1.17
40273	0.69	1.18
40307	34.23	47.22
40461	0.72	1.34
40827	39.66	67.40
41320	4.73	7.80
41639	2.85	4.24
41729	0.62	0.33
41936	0.25	0.57
41950	17.90	39.57
42362	14.40	39.46
42408	0.39	0.55
42561	166.70	164.12
42699	0.47	0.49
43270	42.62	58.19
44586	13.70	17.90
44646	12.60	16.96
45594	2.44	3.62
45659	16.22	21.19
46367	29.09	77.81
46616	40.09	53.84
46736	13.88	20.21
46851	7.85	12.98
46859	7.03	7.76
46963	11.11	35.38
47333	13.18	16.33
47357	9.10	9.29
47555	24.66	46.66
47569	19.79	19.52
48276	20.21	27.16
48673	26.58	21.13

49399	6.45	20.68
50505	2.25	6.15
50572	4.10	5.02
50581	0.60	0.65
50584	5.66	3.50
50792	32.36	26.28
50886	19.13	22.68
50952	12.16	7.46
50957	73.11	109.80
51319	3.99	7.01
51460	17.08	10.81
51643	2.67	6.60
51667	4.20	4.10
51793	20.81	31.10
52633	4.21	11.02
52939	16.74	8.77
53013	10.84	21.88
53561	27.47	32.84
53742	24.18	55.48
54189	48.10	76.49
54386	4.96	7.36
54871	62.57	114.09
54903	16.17	27.38
54942	137.37	73.70
55307	40.45	20.21
55599	7.01	13.51
55717	10.74	20.77
55732	49.20	57.77
55902	67.13	90.20
55929	8.69	9.15
55992	2.18	2.19
56370	53.64	71.81
56387	27.48	42.11
56558	25.55	63.11
56907	26.09	38.16
57924	2.06	1.63
58126	14.73	25.43
58173	8.86	13.83
58221	134.33	271.04
58299	60.65	100.58
58377	41.96	60.06
58379	33.79	42.19
59498	48.09	88.15
59714	61.34	51.28
59740	12.66	17.21

60162	24.19	36.34
73823	59.23	57.72
73836	27.87	36.69
73854	10.63	20.25
73875	19.65	20.31
73878	15.96	27.47
82353	43.73	77.76
82589	19.79	30.17
83462	23.85	38.33
84609	41.91	92.29
86372	97.06	115.27
86872	37.99	56.12
87110	31.42	73.57
91254	117.34	129.43
94158	10.47	37.88
97397	12.23	28.35
100271	2.61	2.41
101487	18.34	19.87
104424	3.70	3.91
104426	26.51	37.97
139806	14.01	20.42
140989	3.70	4.95
142890	21.21	24.49
144745	130.39	104.54
153343	32.65	86.07
160382	22.99	12.82
165113	13.08	12.84
165662	59.08	41.11
166830	64.04	43.65
166849	24.11	79.38
169478	6.65	8.27
169870	9.30	13.43
170401	71.44	69.33
173666	35.45	86.04
184842	3.27	3.76
200317	21.29	26.80
212739	34.87	71.55
212839	9.01	13.11
213686	35.41	26.61
213777	19.47	29.34
213880	6.14	12.86
213971	20.50	16.99
214216	4.43	5.84
214224	13.27	17.63
215038	6.66	8.23

993850	58.29	83.11
995501	72.48	124.24
999709	19.48	32.70
1002198	27.57	47.01
1035578	9.72	19.28
1126633	31.70	31.84
1127439	0.95	1.29
1127665	11.21	15.10
1131909	140.25	167.34
1132617	23.82	41.45
1141653	55.70	154.63
1143153	13.14	13.86
1143577	8.78	18.15
1146872	29.21	51.72
1150845	70.86	158.53
1151122	37.55	13.29
1151377	37.43	44.59
1151586	37.73	70.03
1153648	8.63	12.42
1154030	75.31	116.43
1154576	33.57	49.19
1156435	29.85	45.43
1157161	51.99	50.21
1157504	32.94	75.27
1157594	46.30	74.70
1159277	37.46	51.43
1159724	138.92	232.75
1160491	44.20	34.75
1160736	36.88	45.07
1161644	51.23	130.34
1161668	68.04	123.69
1164082	129.44	166.25
1164755	10.98	7.49
1166532	11.56	9.91
1166629	22.39	47.73
1168578	90.71	81.75
1176661	17.70	53.81
1179785	4.19	6.82
1180313	9.54	19.63
1186693	6.07	14.04
1199361	6.48	13.12
1211119	75.39	84.07
1234778	15.86	34.06
1242633	79.37	80.46
1254758	16.98	12.92

1258884	19.48	38.51
1259470	45.49	75.27
1265456	14.18	8.46
1265554	25.38	34.48
1266959	36.99	24.51
1267212	10.53	6.88
1267864	37.45	77.04
1273805	57.06	143.67
1284684	72.07	35.57
1290867	29.64	39.37
1293678	83.45	111.36
1294315	44.36	52.37
1297733	8.80	15.67
1307172	6.91	7.06
1320598	58.98	25.11
1355941	54.75	94.49
1357606	37.33	45.09
1385124	11.98	16.00
1390199	55.90	70.68
1399144	8.92	9.93
1402425	66.93	40.93
1420321	34.59	31.19
1425153	34.89	69.40
1427577	43.12	50.00
1444428	20.86	16.73
1445759	14.26	30.48
1455644	22.67	32.02
1461143	143.70	217.76
1479647	62.78	50.90
1487667	57.30	102.54
1488517	37.36	44.60
1490109	61.49	57.44
1490643	31.25	61.21
1490808	180.74	319.54
1495724	49.01	62.71
1509913	23.95	22.35
1509990	12.43	15.95
1538974	12.46	26.53
1554617	21.52	46.93
1558878	64.73	87.73
1559618	74.58	53.38
1560165	28.25	31.42
1561298	7.78	14.63
1582573	71.59	96.26
1584516	14.50	31.13

1590052	134.81	68.74
1591848	7.33	14.98
1598330	17.92	39.37
1599370	33.68	29.85
1604354	21.30	19.07
1610778	31.41	29.73
1613555	11.53	18.02
1621866	32.65	25.74
1646009	21.88	12.89
1659660	70.04	71.89
1674543	0.33	0.46
1674903	36.69	52.42
1677461	13.33	24.43
1687257	7.30	10.06
1689905	9.55	13.55
1699572	16.98	21.77
1700434	39.95	45.81
1701575	10.68	15.09
1702940	2.56	4.17
1708077	39.39	63.05
1709120	15.19	47.12
1714418	29.69	48.59
1718741	19.32	24.55
1723421	17.30	15.06
1726694	22.99	42.61
1730304	3.99	5.90
1730676	10.69	18.32
1753373	1.40	2.31
1769507	81.79	170.65
1771065	85.95	282.10
1797404	77.98	141.27
1799933	24.47	25.65
1812234	25.95	29.05
1812806	67.21	63.32
1815631	10.86	16.03
1820473	6.36	13.25
1826835	17.47	30.00
1826860	21.34	42.68
1832533	28.09	57.43
1835201	26.62	35.07
1839666	63.90	59.30
1840966	44.75	57.98
1841559	5.72	11.34
1841722	28.37	35.05
1842563	33.58	62.52

1847597	67.46	79.66
1864481	32.80	59.14
1901761	22.01	28.82
1901903	76.08	90.38
1906186	18.60	44.28
1913925	27.93	38.71
1937801	18.24	26.39
1954123	10.44	28.16
1957505	53.33	71.50
1960810	19.70	27.37
1963697	8.44	8.26
1974798	5.89	9.42
2006860	44.43	102.98
2015911	19.43	36.83
2034956	3.60	3.45
2037375	23.80	42.39
2038066	13.04	14.29
2040636	8.47	9.64
2056268	18.63	22.06
2059143	47.18	23.44
2059469	9.66	16.04
2060285	61.79	146.63
2067180	11.80	11.11
2080337	49.56	92.63
2108252	17.18	22.94
2112124	36.89	51.91
2115390	5.65	11.48
2128678	34.77	59.05
2139492	108.25	60.87
2147249	20.45	29.14
2147674	25.94	104.32
2149476	18.01	47.39
2150101	70.90	120.56
2151781	17.10	25.80
2155004	15.37	38.33
2159648	7.02	7.23
2163128	6.61	23.49
2169301	51.78	78.82
2169778	83.56	125.77
2170424	72.35	194.27
2172609	37.97	76.51
2173570	40.43	61.95
2196443	33.75	36.68
2202201	23.29	53.90
2218009	17.98	27.60

2219223	141.36	188.19
2224292	83.53	176.02
2230193	7.54	12.56
2234990	54.89	120.20
2239251	35.21	41.89
2243479	43.81	91.05
2259999	68.16	50.74
2292803	43.93	73.20
2293506	11.81	25.09
2315116	11.17	20.10
2334797	43.16	40.02
2337352	7.95	13.21
2353412	111.10	167.19
2362862	58.69	67.34
2365456	235.55	386.60
2369301	9.13	22.11
2371733	9.22	17.71
2372133	41.58	32.21
2381875	30.07	32.38
2400647	55.63	129.73
2401428	142.09	338.46
2403489	48.10	93.11
2424915	98.38	72.74
2427312	8.12	9.99
2428287	19.41	24.62
2433795	24.62	66.68
2435590	33.61	43.09
2442196	34.47	23.70
2460982	28.37	48.55
2482715	48.49	69.31
2484220	21.93	32.13
2489542	15.19	12.72
2490520	71.00	129.70
2504852	99.86	235.32
2507519	12.28	26.36
2515705	69.85	118.13
2530333	52.69	66.65
2553307	43.64	98.45
2561952	144.05	195.74
2564113	21.10	18.43
2573071	149.23	148.35
2573118	92.46	126.01
2573317	96.57	214.67
2578440	34.12	41.03
2587126	22.87	38.46

2590098	16.51	19.96
2594887	28.03	26.89
2610933	410.81	739.11
2696510	16.64	30.38
2815856	50.24	56.18
2815946	12.44	19.70
2816037	18.25	16.30
2816038	31.03	37.17
3087388	20.09	28.90
3087596	45.03	30.61
3090713	0.51	0.95
3091743	24.91	30.33
3092484	2.65	4.46
3093154	35.10	46.74
3103599	1.63	3.09
3111153	33.16	39.70
3114447	46.74	80.22
3129621	24.19	26.49
3136991	105.41	74.35
3137618	57.32	121.68
3138214	21.72	24.30
3138244	15.85	23.54
3139240	38.58	22.94
3293339	35.83	23.35
3336099	41.48	69.90
3351621	22.96	17.83
3381209	27.14	37.68
3388144	56.74	75.19
3388203	100.91	171.10
3403715	26.94	31.55
3408298	20.57	45.85
3408440	4.61	10.59
3409128	56.11	54.77
3445966	18.01	28.37
3468182	82.47	95.24
3469445	65.22	54.53
3473037	4.65	8.20
3475599	88.07	170.55
3495293	12.39	25.91
3498944	44.33	85.20
3506408	18.32	45.85
3532807	12.04	23.00
3538304	27.17	42.77
3555994	6.90	13.66
3564057	40.18	84.92

3668209	44.18	38.91
3753948	30.63	43.39
3761083	24.69	40.90
3790180	7.95	9.78
3800271	15.58	40.48
3848497	56.03	51.64
3862692	33.64	73.11
3862874	27.35	21.94

Table of upper-limits in the luminosities for the very faint galaxies in star-forming galaxy sample. Column (1): source catalogue identification ID (PGC); Column (2): luminosity in the broad band (0.5-8 keV); Column (3): luminosity in the hard band (2-10 keV).

5

Conclusions-Future

5.1 Conclusions

In this work we have performed analysis of *Chandra* data of three star-forming galaxies that host large number of ULXs. We have explored the validity of the scaling relations between the luminosity of the XRB population, the star-formation rate (SFR), and the stellar mass (M_*), for these extreme cases, in galaxy-wide, and at sub-galactic scales. Moreover, we extended these scaling relations to a sample of 650 galaxies observed with *XMM-Newton* , which is the largest and most representative X-ray sample of galaxies in the local Universe. In more detail:

We have analysed a 90 ks *Chandra* ACIS-S observation of the X-ray luminous interacting galaxy system Arp 299 (NGC 3690/IC 694). We have detected 25 discrete X-ray sources with luminosities above $\sim 4.0 \times 10^{38}$ erg s^{-1} covering the entire Ultra Luminous X-ray source (ULX) regime. Based on the hard X-ray spectra of the non-nuclear discrete sources identified in Arp 299, and their association with young, actively star-forming region of Arp 299 we identified them as HMXBs. We found in total 20 off-nuclear sources with luminosities above the ULX limit, 14 of which are point-like sources. We attribute the marginally significant deficit in the number of ULXs, with respect to the number expected from scaling relations of X-ray binaries with SFR to confusion effects. We found that the AGN in NGC 3690 contributes only 22% of the observed broad-band X-ray luminosity of Arp 299. Moreover, a plume of soft X-ray emission in the west of the galaxy indicates a large scale outflow. We showed that the correlation between X-ray luminosity and SFR holds for SFRs as high as in the case of Arp 299 i.e. 2-4 times higher SFRs than the most actively star-forming galaxies in their samples previously used.

In the case of NGC 3310 and NGC 2276, we have studied the discrete sources in deep *Chandra* observations. We identify 27 and 19 discrete sources, with luminosities above $1.0{\times}10^{38}$ erg s^{-1}, in each galaxy. Both galaxies have large numbers of ultra-luminous X-ray sources (ULXs; sources with $L(0.3 - 10.0 \text{ keV}) > 10^{39}$ erg s^{-1}), 14 for NGC 3310 concentrated on the circumnuclear star-forming ring and north spiral arm and 11 for NGC 2276 with the brighter ones on the west side of the galaxy which is compressed due to harassment by the intra-group medium it is moving into. We found for both galaxies that the ULX-hosting areas are located above the general L_X-SFR scaling relations while other areas either follow or fall below the scaling relations. This indicates that sub-galactic regions follow the galaxy-wide scaling relations but with much larger scatter resulting from the age (and possibly metallicity) of their local stellar populations in agreement with recent theoretical and observational results. Such differences in age could be the origin of the scatter we observe in the low SFR regime in the Lx-SFR scaling relations.

Finally, we analysed all star-forming galaxies within a radius of 200 Mpc observed with *XMM-Newton*. These galaxies are the result of cross-correlation between the *XMM-Newton* archive and the `HECATE` catalogue, the most complete galaxy catalogue ~165,000 galaxies) of the local Universe incorporating robust distances and stellar population parameters. We have analysed in total 2645 *XMM-Newton* observations including 3041 galaxies within a volume of 200 Mpc. We performed photometric analysis for all of them and spectroscopic analysis for 1713 galaxies where we identified 330 galaxies as AGN. We measured the correlation between X-ray luminosity, star-formation rate, and stellar mass for the 650 non-AGN galaxies that had SFR and M_* information from the `HECATE` catalogue. We found that the Lx-SFR scaling relation for the full sample of normal local galaxies is sub-linear and that this most likely is the result of contribution from ULX-hosting galaxies and/or LMXBs in the low SFR regime. We also found a very good agreement with previous works for the Lx/SFR-sSFR scaling relation, however we measure about two times larger intrinsic scatter. We attribute this increase of the scatter to the dramatic increase in the number of galaxies we observe, which accounts for all different conditions of star forming activity and metallicity variations in the local Universe.

In summary these studies agree in that:

1. General scaling relations hold in sub-galactic scales as well as in large diverse samples.

2. There is a significant degree of scatter in sub-galactic scales resulting from variations of the ages and possibly metallicities of the local stellar populations.

3. When considering large, diverse, samples of galaxies, we find that while the general Lx-SFR-M_* scaling relations hold, there is an increasing degree of intrinsic scatter. This scatter is interpreted as the result of variations of the stellar populations (e.g. metallicity, age).

5.2 Future work

With the analysis of the *XMM-Newton* sample we have available a wealth of photometric (3041 galaxies) and spectroscopic (1713 galaxies; 5800 spectra) data. Therefore, we plan to use these data in order to :

1. Study the thermal-gas component in the sample galaxies. We plan to measure the correlations between the hot-gas luminosity and temperature with the star-formation rate (SFR) and stellar mass (M_*) of the host galaxy. Since the luminosity of the hot diffuse gas is the result of the energy released from supernovae and massive star stellar winds on the interstellar medium (ISM), those correlations would provide a direct measurement of the thermalisation of the mechanical energy output from star-forming activity. Deriving these relations from a large, and as representative as possible, sample of galaxies, will provide a robust benchmark for comparison with models for stellar feedback to the ISM of galaxies in different stellar environments (e.g. Strickland *et al.* (2004)).

2. Provide an X-ray library of AGN in the local Universe and explore the connection with the starburst activity. Since the `HECATE` catalogue incorporates several different AGN indicators (optical spectra, IR colours, SED fitting), their comparison with the X-ray based AGN identification will provide a picture of the bias in AGN detections using different methods, a more complete picture of AGN demographics in the local Universe, and their interplay with star-forming activity. We also plan to perform more detailed spectral fits for the 330 AGN (e.g. with different Comptonisation models and torus models) and produce a library of all AGN X-ray spectra observed in the local Universe.

3. Use the `HECATE` catalogue with the *eROSITA* data. *eROSITA* will provide a complete unbiased sample of galaxies observed in the X-ray band. Using the `HECATE` catalogue together with the *eROSITA* all-sky survey data we can calculate the ultimate X-ray luminosity scaling relations for all galaxies in our local Universe. The large number of objects covered, will allow us to derive the scaling relations for galaxies of different types and metallicity, measure their dependence on these parameters an address the origin of the observed scatter.

References

Aird, J., Coil, A.L. & Georgakakis, A. (2017). X-rays across the galaxy population - I. Tracing the main sequence of star formation. *MNRAS*, **465**, 3390–3415. 8, 100

Alonso-Herrero, A., Rieke, G.H., Rieke, M.J. & Scoville, N.Z. (2000). Extreme Star Formation in the Interacting Galaxy Arp 299 (IC 694+NGC 3690). *ApJ*, **532**, 845–866. 12

Alonso-Herrero, A., Rieke, G.H., Colina, L., Pereira-Santaella, M., García-Marín, M., Smith, J.D.T., Brandl, B., Charmandaris, V. & Armus, L. (2009). The Extreme Star Formation Activity of Arp 299 Revealed by Spitzer IRS Spectral Mapping. *ApJ*, **697**, 660–675. 12, 13, 38, 39, 40, 43

Alonso-Herrero, A., Roche, P.F., Esquej, P., González-Martín, O., Pereira-Santaella, M., Ramos Almeida, C., Levenson, N.A., Packham, C., Asensio Ramos, A., Mason, R.E., Rodríguez Espinosa, J.M., Alvarez, C., Colina, L., Aretxaga, I., Díaz-Santos, T., Perlman, E. & Telesco, C.M. (2013). Uncovering the Deeply Embedded Active Galactic Nucleus Activity in the Nuclear Regions of the Interacting Galaxy Arp 299. *ApJl*, **779**, L14. 13, 36

Anastasopoulou, K., Zezas, A., Ballo, L. & Della Ceca, R. (2016). A deep Chandra observation of the interacting star-forming galaxy Arp 299. *MNRAS*, **460**, 3570–3586. 5, 51, 54, 60, 84, 90

Anastasopoulou, K., Zezas, A., Gkiokas, V. & Kovlakas, K. (2019). Do sub-galactic regions follow the galaxy-wide X-ray scaling relations? The example of NGC 3310 and NGC 2276. *MNRAS*, **483**, 711–733. 100, 119

Antoniou, V. & Zezas, A. (2016). Star formation history and X-ray binary populations: the case of the Large Magellanic Cloud. *MNRAS*, **459**, 528–553. 95

Antoniou, V., Zezas, A., Drake, J.J., Badenes, C., Hong, J. & Collaboration, S.X. (2018). The formation efficiency of different generations of HMXBs in the low metallicity environment of the SMC. In *American Astronomical Society Meeting Abstracts 231*, vol. 231 of *American Astronomical Society Meeting Abstracts*, 421.08. 95

Antoniou, V., Zezas, A., Drake, J.J., Badenes, C., Haberl, F., Wright, N.J., Hong, J., Stefano, R.D., Gaetz, T.J., Long, K.S., Plucinsky, P.P., Sasaki, M., Williams, B.F. & and, P.F.W. (2019). Deep chandra survey of the small magellanic cloud. III. formation efficiency of high-mass x-ray binaries. **887**, 20. 119

Arnaud, K.A. (1996). XSPEC: The First Ten Years. In G.H. Jacoby & J. Barnes, eds., *Astronomical Data Analysis Software and Systems V*, vol. 101 of *Astronomical Society of the Pacific Conference Series*, 17. 19, 60

Bachetti, M., Harrison, F.A., Walton, D.J., Grefenstette, B.W., Chakrabarty, D., Fuerst, F., Barret, D., Beloborodov, A., Boggs, S.E., Christensen, F.E., Craig, W.W., Fabian, A.C., Hailey, C.J., Hornschemeier, A., Kaspi, V., Kulkarni, S.R., Maccarone, T., Miller, J.M., Rana, V., Stern, D., Tendulkar, S.P., Tomsick, J., Webb, N.A. & Zhang, W.W. (2014). An ultraluminous X-ray source powered by an accreting neutron star. *Nature*, **514**, 202–204. 6

Baldi, A., Raymond, J.C., Fabbiano, G., Zezas, A., Rots, A.H., Schweizer, F., King, A.R. & Ponman, T.J. (2006a). Chemical Enrichment of the Complex Hot ISM of the Antennae Galaxies. I. Spatial and Spectral Analysis of the Diffuse X-Ray Emission. *ApJs*, **162**, 113–133. 44, 90

Baldi, A., Raymond, J.C., Fabbiano, G., Zezas, A., Rots, A.H., Schweizer, F., King, A.R. & Ponman, T.J. (2006b). Chemical Enrichment of the Complex Hot ISM of the Antennae Galaxies. II. Physical Properties of the Hot Gas and Supernova Feedback. *ApJ*, **636**, 158–171. 44

Ballo, L., Braito, V., Della Ceca, R., Maraschi, L., Tavecchio, F. & Dadina, M. (2004). Arp 299: A Second Merging System with Two Active Nuclei? *ApJ*, **600**, 634–639. 12, 13, 33, 35

Basu-Zych, A.R., Lehmer, B.D., Hornschemeier, A.E., Bouwens, R.J., Fragos, T., Oesch, P.A., Belczynski, K., Brandt, W.N., Kalogera, V., Luo, B., Miller, N., Mullaney, J.R., Tzanavaris, P., Xue, Y. & Zezas, A. (2013a). The X-Ray Star Formation Story as Told by Lyman Break Galaxies in the 4 Ms CDF-S. *ApJ*, **762**, 45. 8, 9, 10, 11, 42, 43, 46, 100, 119

Basu-Zych, A.R., Lehmer, B.D., Hornschemeier, A.E., Goncalves, T.S., Fragos, T., Heckman, T.M., Overzier, R.A., Ptak, A.F. & Schiminovich, D. (2013b). Evidence for Elevated X-Ray Emission in Local Lyman Break Galaxy Analogs. *ApJ*, **774**, 152. 8, 42, 43, 100

Boroson, B., Kim, D.W. & Fabbiano, G. (2011). Revisiting with Chandra the Scaling Relations of the X-ray Emission Components Binaries, Nuclei, and Hot Gas of Early-type Galaxies. *ApJ*, **729**, 12. 8, 99, 100

Brassington, N.J., Zezas, A., Ashby, M.L.N., Lanz, L., Smith, H.A., Willner, S.P. & Klein, C. (2015). The Spitzer Interacting Galaxies Survey: A Mid-infrared Atlas of Star Formation. *ApJs*, **218**, 6. 17, 38, 39

Brorby, M., Kaaret, P. & Prestwich, A. (2014). X-ray binary formation in low-metallicity blue compact dwarf galaxies. *MNRAS*, **441**, 2346–2353. 8, 42, 43, 94, 100, 119

C., H.J. (2007). *Measuring Detected Source Extent Using Mexican-Hat Optimization*. 25

Cappi, M., Persic, M., Bassani, L., Franceschini, A., Hunt, L.K., Molendi, S., Palazzi, E., Palumbo, G.G.C., Rephaeli, Y. & Salucci, P. (1999). Diffuse thermal emission from very hot gas in starburst galaxies. *A&A*, **350**, 777–790. 26

Carter, C., Karovska, M., Jerius, D., Glotfelty, K. & Beikman, S. (2003). ChaRT: The Chandra Ray Tracer. In H.E. Payne, R.I. Jedrzejewski & R.N. Hook, eds., *Astronomical Data Analysis Software and Systems XII*, vol. 295 of *Astronomical Society of the Pacific Conference Series*, 477. 25

Charmandaris, V., Stacey, G.J. & Gull, G. (2002). Resolving the Buried Starburst in Arp 299. *ApJ*, **571**, 282–287. 12

Collaboration, P. (2018). Planck 2018 results. VI. Cosmological parameters. *arXiv e-prints*, arXiv:1807.06209. 52

Corwin, J., Harold G., Buta, R.J. & de Vaucouleurs, G. (1994). Corrections and additions to the Third Reference Catalogue of Bright Galaxies. *AJ*, **108**, 2128–2144. 14, 26, 55

Davis, D.S., Keel, W.C., Mulchaey, J.S. & Henning, P.A. (1997). Gravitational Interactions in Poor Galaxy Groups. *AJ*, **114**, 613–625. 53

Davis, J.E., Bautz, M.W., Dewey, D., Heilmann, R.K., Houck, J.C., Huenemoerder, D.P., Marshall, H.L., Nowak, M.A., Schattenburg, M.L., Schulz, N.S. & Smith, R.a.K. (2012). Raytracing with MARX: x-ray observatory design, calibration, and support. In *procspie*, vol. 8443 of *Society of Photo-Optical Instrumentation Engineers (SPIE) Conference Series*, 84431A. 25

de Grijs, R., Anders, P., Bastian, N., Lynds, R., Lamers, H.J.G.L.M. & O'Neil, E.J. (2003a). Star cluster formation and evolution in nearby starburst galaxies - II. Initial conditions. *MNRAS*, **343**, 1285–1300. 52, 94, 95

de Grijs, R., Fritze-v. Alvensleben, U., Anders, P., Gallagher, J.S., Bastian, N., Taylor, V.A. & Windhorst, R.A. (2003b). Star cluster formation and evolution in nearby starburst galaxies - I. Systematic uncertainties. *MNRAS*, **342**, 259–273. 52, 94, 95

de Vaucouleurs, G., de Vaucouleurs, A., Corwin, J., Herold G., Buta, R.J., Paturel, G. & Fouque, P. (1991). *Third Reference Catalogue of Bright Galaxies*. 14, 26, 55

Della Ceca, R., Ballo, L., Tavecchio, F., Maraschi, L., Petrucci, P.O., Bassani, L., Cappi, M., Dadina, M., Franceschini, A., Malaguti, G., Palumbo, G.G.C. & Persic, M. (2002). An Enshrouded Active Galactic Nucleus in the Merging Starburst System Arp 299 Revealed by BeppoSAX. *ApJl*, **581**, L9–L13. 12, 33

Dimai, A., Migliardi, M. & Manzini, F. (2005). Supernova 2005dl in NGC 2276. *IAUcirc*, **8588**, 2. 53

Douna, V.M., Pellizza, L.J., Mirabel, I.F. & Pedrosa, S.E. (2015). Metallicity dependence of high-mass X-ray binary populations. *A&A*, **579**, A44. 5, 8, 43, 51, 94, 119

Elmegreen, D.M., Chromey, F.R., McGrath, E.J. & Ostenson, J.M. (2002). Circumnuclear Star Formation in the Spiral Galaxy NGC 3310. *AJ*, **123**, 1381–1388. 52, 95

Fabbiano, G. (1988). X-Ray Spectra and Large-Scale Features of Two Starburst Galaxies: NGC 253 and M82. *ApJ*, **330**, 672. 46

Fabbiano, G. (1989). X-rays from normal galaxies. *ARAA*, **27**, 87–138. 2, 6

Fabbiano, G. (1995). Normal galaxies and their X-ray binary populations. In *X-ray Binaries*, 390–418. 6

Fabbiano, G. (2003). X-ray Source Populations in Galaxies. *Chinese Journal of Astronomy and Astrophysics Supplement*, **3**, 193–201. 28, 46, 91, 99

Fabbiano, G. (2006). Populations of X-Ray Sources in Galaxies. *ARAA*, **44**, 323–366. 2

Fabbiano, G., Krauss, M., Zezas, A., Rots, A. & Neff, S. (2003). The Multicolored Hot Interstellar Medium of "the Antennae" Galaxies (NGC 4038/4039). *ApJ*, **598**, 272–287. 3, 44, 90

Fornasini, F.M., Civano, F., Fabbiano, G., Elvis, M., Marchesi, S., Miyaji, T. & Zezas, A. (2018). Low-luminosity AGN and X-Ray Binary Populations in COSMOS Star-forming Galaxies. *ApJ*, **865**, 43. 8, 100

Fornasini, F.M., Kriek, M., Sanders, R.L., Shivaei, I., Civano, F., Reddy, N.A., Shapley, A.E., Coil, A.L., Mobasher, B., Siana, B., Aird, J., Azadi, M., Freeman, W.R., Leung, G.C.K., Price, S.H., Fetherolf, T., Zick, T. & Barro, G. (2019). The MOSDEF Survey: The Metallicity Dependence of X-Ray Binary Populations at z$\sim$2. *ApJ*, **885**, 65. 8, 100

References

Fragos, T., Lehmer, B., Tremmel, M., Tzanavaris, P., Basu-Zych, A., Belczynski, K., Hornschemeier, A., Jenkins, L., Kalogera, V., Ptak, A. & Zezas, A. (2013). X-Ray Binary Evolution Across Cosmic Time. *ApJ*, **764**, 41. 8, 9, 94, 95, 100, 119

Freeman, P., Doe, S. & Siemiginowska, A. (2001). *Sherpa: a mission-independent data analysis application.* 14, 60, 107

Freeman, P.E., Kashyap, V., Rosner, R. & Lamb, D.Q. (2002). A Wavelet-Based Algorithm for the Spatial Analysis of Poisson Data. *ApJs*, **138**, 185–218. 55

Garmire, G.P. (1997). AXAF CCD Imaging Spectrometer (ACIS). In *American Astronomical Society Meeting Abstracts #190*, vol. 190 of *American Astronomical Society Meeting Abstracts*, 34.04. 13, 54

Gehrels, N. (1986). Confidence Limits for Small Numbers of Events in Astrophysical Data. *ApJ*, **303**, 336. 17, 60

Giacconi, R., Gursky, H., Paolini, F.R. & Rossi, B.B. (1962). Evidence for x Rays From Sources Outside the Solar System. *PhRvL*, **9**, 439–443. 2

Gilfanov, M. (2004). Low-mass X-ray binaries as a stellar mass indicator for the host galaxy. *MNRAS*, **349**, 146–168. 7, 92, 99

Gladstone, J.C., Roberts, T.P. & Done, C. (2009). The ultraluminous state. *MNRAS*, **397**, 1836–1851. 29, 81

Gregory, P.C. & Loredo, T.J. (1992). A New Method for the Detection of a Periodic Signal of Unknown Shape and Period. *ApJ*, **398**, 146. 24, 77

Grimm, H.J., Gilfanov, M. & Sunyaev, R. (2002). The Milky Way in X-rays for an outside observer. Log(N)-Log(S) and luminosity function of X-ray binaries from RXTE/ASM data. *A&A*, **391**, 923–944. 5

Grimm, H.J., Gilfanov, M. & Sunyaev, R. (2003). High-mass X-ray binaries as a star formation rate indicator in distant galaxies. *MNRAS*, **339**, 793–809. 7

Heckman, T.M., Armus, L., Weaver, K.A. & Wang, J. (1999). An X-Ray and Optical Investigation of the Starburst-driven Superwind in the Galaxy Merger ARP 299. *ApJ*, **517**, 130–147. 11, 12, 31

Helou, G., Khan, I.R., Malek, L. & Boehmer, L. (1988). IRAS Observations of Galaxies in the Virgo Cluster Area. *ApJs*, **68**, 151. 39

Hibbard, J.E. & Yun, M.S. (1999). A 180 Kiloparsec Tidal Tail in the Luminous Infrared Merger ARP 299. *AJ*, **118**, 162–185. 12

Ho, L.C., Filippenko, A.V., Sargent, W.L.W. & Peng, C.Y. (1997). A Search for "Dwarf" Seyfert Nuclei. IV. Nuclei with Broad Hα Emission. *ApJs*, **112**, 391–414. 52, 102

Hodge, P.W. & Kennicutt, J., R. C. (1983). An Atlas of H II regions in 125 galaxies. *AJ*, **88**, 296–328. 53

Huo, Z.Y., Xia, X.Y., Xue, S.J., Mao, S. & Deng, Z.G. (2004). Chandra Observations of Ultraluminous Infrared Galaxies: Extended Hot Gaseous Halos in Merging Galaxies. *ApJ*, **611**, 208–219. 44

Iskudaryan, S.G. & Shakhbazyan, R.K. (1967). A supernova in NGC 2276. *Astrophysics*. 53

IWASAWA, K., SANDERS, D.B., EVANS, A.S., TRENTHAM, N., MINIUTTI, G. & SPOON, H.W.W. (2005). Fe K emission in the ultraluminous infrared galaxy Arp 220. *MNRAS*, **357**, 565–571. 36

IWASAWA, K., SANDERS, D.B., EVANS, A.S., MAZZARELLA, J.M., ARMUS, L. & SURACE, J.A. (2009). High-Ionization Fe K Emission From Luminous Infrared Galaxies. *ApJl*, **695**, L103–L106. 13, 33, 36

KAARET, P., FENG, H. & ROBERTS, T.P. (2017). Ultraluminous X-Ray Sources. *ARAA*, **55**, 303–341. 6, 51

KANKARE, E., MATTILA, S., RYDER, S., FRASER, M., PASTORELLO, A., ELIAS-ROSA, N., ROMERO-CAÑIZALES, C., ALBERDI, A., HENTUNEN, V.P., HERRERO-ILLANA, R., KOTILAINEN, J., PÉREZ-TORRES, M.A. & VAISANEN, P. (2014). The nature of supernovae 2010O and 2010P in Arp 299 - I. Near-infrared and optical evolution. *MNRAS*, **440**, 1052–1066. 46

KENNICUTT, R.C. & EVANS, N.J. (2012). Star Formation in the Milky Way and Nearby Galaxies. *ARAA*, **50**, 531–608. 39, 95

KIM, D.W. & FABBIANO, G. (2010). X-ray Properties of Young Early-type Galaxies. I. X-ray Luminosity Function of Low-mass X-ray Binaries. *ApJ*, **721**, 1523–1530. 119

KIM, M., WILKES, B.J., KIM, D.W., GREEN, P.J., BARKHOUSE, W.A., LEE, M.G., SILVERMAN, J.D. & TANANBAUM, H.D. (2007). Chandra Multiwavelength Project X-Ray Point Source Number Counts and the Cosmic X-Ray Background. *ApJ*, **659**, 29–51. 72

KING, A.R. (2002). The brightest black holes. *MNRAS*, **335**, L13–L16. 6

KING, A.R. (2009). Masses, beaming and Eddington ratios in ultraluminous X-ray sources. *MNRAS*, **393**, L41–L44. 6, 51

KOUROUMPATZAKIS ET AL., K. (2019). *in prep.*. 100, 113, 117, 119

KOVLAKAS ET AL., K. (2019). *in prep.*. 101, 102

KUNTZ, K.D. & SNOWDEN, S.L. (2008). The X-Ray-Emitting Components toward l = 111°: The Local Hot Bubble and Beyond. *ApJ*, **674**, 209–219. 105

KUNTZ, K.D. & SNOWDEN, S.L. (2010). The Chandra M101 Megasecond: Diffuse Emission. *ApJs*, **188**, 46–74. 44, 90

LEHMER, B.D., ALEXANDER, D.M., BAUER, F.E., BRAND T, W.N., GOULDING, A.D., JENKINS, L.P., PTAK, A. & ROBERTS, T.P. (2010). A Chandra Perspective on Galaxy-wide X-ray Binary Emission and its Correlation with Star Formation Rate and Stellar Mass: New Results from Luminous Infrared Galaxies. *ApJ*, **724**, 559–571. 7, 9, 10, 11, 39, 53, 85, 89, 99, 100, 112, 118

LEHMER, B.D., BERKELEY, M., ZEZAS, A., ALEXAND ER, D.M., BASU-ZYCH, A., BAUER, F.E., BRANDT, W.N., FRAGOS, T., HORNSCHEMEIER, A.E., KALOGERA, V., PTAK, A., SIVAKOFF, G.R., TZANAVARIS, P. & YUKITA, M. (2014). The X-Ray Luminosity Functions of Field Low-mass X-Ray Binaries in Early-type Galaxies: Evidence for a Stellar Age Dependence. *ApJ*, **789**, 52. 7, 8, 39, 100, 119

LEHMER, B.D., TYLER, J.B., HORNSCHEMEIER, A.E., WIK, D.R., YUKITA, M., ANTONIOU, V., BOGGS, S., CHRISTENSEN, F.E., CRAIG, W.W., HAILEY, C.J., HARRISON, F.A., MACCARONE, T.J., PTAK, A., STERN, D., ZEZAS, A. & ZHANG, W.W. (2015). The 0.3-30 keV Spectra of Powerful Starburst Galaxies: NuSTAR and Chandra Observations of NGC 3256 and NGC 3310. *ApJ*, **806**, 126. 10, 51, 52

Lehmer, B.D., Basu-Zych, A.R., Mineo, S., Brand t, W.N., Eufrasio, R.T., Fragos, T., Hornschemeier, A.E., Luo, B., Xue, Y.Q., Bauer, F.E., Gilfanov, M., Ranalli, P., Schneider, D.P., Shemmer, O., Tozzi, P., Trump, J.R., Vignali, C., Wang, J.X., Yukita, M. & Zezas, A. (2016). The Evolution of Normal Galaxy X-Ray Emission through Cosmic History: Constraints from the 6 MS Chandra Deep Field-South. *ApJ*, **825**, 7. 8, 99, 100, 116, 118

Lehmer, B.D., Eufrasio, R.T., Markwardt, L., Zezas, A., Basu-Zych, A., Fragos, T., Hornschemeier, A.E., Ptak, A., Tzanavaris, P. & Yukita, M. (2017). On the Spatially Resolved Star Formation History in M51. II. X-Ray Binary Population Evolution. *ApJ*, **851**, 11. 95

Lehmer, B.D., Eufrasio, R.T., Tzanavaris, P., Basu-Zych, A., Fragos, T., Prestwich, A., Yukita, M., Zezas, A., Hornschemeier, A.E. & Ptak, A. (2019). X-Ray Binary Luminosity Function Scaling Relations for Local Galaxies Based on Subgalactic Modeling. *ApJS*, **243**, 3. 99, 115, 118, 119

Linden, T., Kalogera, V., Sepinsky, J.F., Prestwich, A., Zezas, A. & Gallagher, J.S. (2010). The Effect of Starburst Metallicity on Bright X-ray Binary Formation Pathways. *ApJ*, **725**, 1984–1994. 8, 42, 43, 94, 100

Lira, P., Ward, M., Zezas, A., Alonso-Herrero, A. & Ueno, S. (2002). Chandra observations of the luminous infrared galaxy NGC 3256. *MNRAS*, **330**, 259–278. 28, 46, 91

Luangtip, W., Roberts, T.P., Mineo, S., Lehmer, B.D., Alexander, D.M., Jackson, F.E., Goulding, A.D. & Fischer, J.L. (2015). A deficit of ultraluminous X-ray sources in luminous infrared galaxies. *MNRAS*, **446**, 470–492. 12, 42, 43

Lutz, D., Spoon, H.W.W., Rigopoulou, D., Moorwood, A.F.M. & Genzel, R. (1998). The Nature and Evolution of Ultraluminous Infrared Galaxies:A Mid-Infrared Spectroscopic Survey. *ApJl*, **505**, L103–L107. 40

Makarov, D., Prugniel, P., Terekhova, N., Courtois, H. & Vauglin, I. (2014). HyperLEDA. III. The catalogue of extragalactic distances. *A&A*, **570**, A13. 101

Makishima, K., Maejima, Y., Mitsuda, K., Bradt, H.V., Remillard, R.A., Tuohy, I.R., Hoshi, R. & Nakagawa, M. (1986). Simultaneous X-Ray and Optical Observations of GX 339-4 in an X-Ray High State. *ApJ*, **308**, 635. 29

Mapelli, M., Ripamonti, E., Zampieri, L., Colpi, M. & Bressan, A. (2010). Ultra-luminous X-ray sources and remnants of massive metal-poor stars. *MNRAS*, **408**, 234–253. 7, 8

Mapelli, M., Ripamonti, E., Zampieri, L. & Colpi, M. (2011). Remnants of massive metal-poor stars: Viable engines for ultra-luminous X-ray sources. *Astronomische Nachrichten*, **332**, 414. 42, 43

Maragkoudakis, A., Zezas, A., Ashby, M.L.N. & Willner, S.P. (2018). The Star Formation Reference Survey - II. Activity demographics and host-galaxy properties for infrared-selected galaxies. *MNRAS*, **475**, 1485–1507. 94, 95

Mezcua, M., Roberts, T.P., Lobanov, A.P. & Sutton, A.D. (2015). The powerful jet of an off-nuclear intermediate-mass black hole in the spiral galaxy NGC 2276. *MNRAS*, **448**, 1893–1899. 53, 59

Mineo, S., Gilfanov, M. & Sunyaev, R. (2012a). X- ray emission from star-forming galaxies - I. High-mass X-ray binaries. *MNRAS*, **419**, 2095–2115. 7, 10, 11, 40, 41, 42, 43, 46, 53, 84, 85, 86, 88, 92, 99, 100, 114, 116, 117, 118

Mineo, S., Gilfanov, M. & Sunyaev, R. (2012b). X-ray emission from star-forming galaxies - II. Hot interstellarmedium. *MNRAS*, **426**, 1870–1883. 44, 45, 90

Mineo, S., Rappaport, S., Steinhorn, B., Levine, A., Gilfanov, M. & Pooley, D. (2013). Spatially Resolved Star Formation Image and the Ultraluminous X-Ray Source Population in NGC 2207/IC 2163. *ApJ*, **771**, 133. 53

Mineo, S., Gilfanov, M., Lehmer, B.D., Morrison, G.E. & Sunyaev, R. (2014). X-ray emission from star-forming galaxies - III. Calibration of the L_X-SFR relation up to redshift $z \approx 1.3$. *MNRAS*, **437**, 1698–1707. 8, 10, 11, 46, 53, 92, 95, 100

Miralles-Caballero, D., Díaz, A.I., Rosales-Ortega, F.F., Pérez-Montero, E. & Sánchez, S.F. (2014a). Ionizing stellar population in the disc of NGC 3310 - I. The impact of a minor merger on galaxy evolution. *MNRAS*, **440**, 2265–2289. 52, 94

Miralles-Caballero, D., Rosales-Ortega, F.F., Díaz, A.I., Otí-Floranes, H., Pérez-Montero, E. & Sánchez, S.F. (2014b). Ionizing stellar population in the disc of NGC 3310 - II. The Wolf-Rayet population. *MNRAS*, **445**, 3803–3822. 53

Mitsuda, K., Inoue, H., Koyama, K., Makishima, K., Matsuoka, M., Ogawara, Y., Shibazaki, N., Suzuki, K., Tanaka, Y. & Hirano, T. (1984). Energy spectra of low-mass binary X-ray sources observed from Tenma. *PASJ*, **36**, 741–759. 29

Moran, E.C., Lehnert, M.D. & Helfand, D.J. (1999). X-Rays from NGC 3256: High-Energy Emission in Starburst Galaxies and Their Contribution to the Cosmic X-Ray Background. *ApJ*, **526**, 649–664. 26

Moustakas, J., Kennicutt, J., Robert C., Tremonti, C.A., Dale, D.A., Smith, J.D.T. & Calzetti, D. (2010). Optical Spectroscopy and Nebular Oxygen Abundances of the Spitzer/SINGS Galaxies. *ApJs*, **190**, 233–266. 95

Mukherjee, ., E. S, Walton, D.J., Bachetti, M., Harrison, F.A., Barret, D., Bellm, E., Boggs, S.E., Christensen, F.E., Craig, W.W., Fabian, A.C., Fuerst, F., Grefenstette, B.W., Hailey, C.J., Madsen, K.K., Middleton, M.J., Miller, J.M., Rana, V., Stern, D. & Zhang, W. (2015). A Hard X-Ray Study of the Ultraluminous X-Ray Source NGC 5204 X-1 with NuSTAR and XMM-Newton. *ApJ*, **808**, 64. 117

Narayan, R., Sadowski, A. & Soria, R. (2017). Spectra of black hole accretion models of ultraluminous X-ray sources. *MNRAS*, **469**, 2997–3014. 6

Park, T., Kashyap, V.L., Siemiginowska, A., van Dyk, D.A., Zezas, A., Heinke, C. & Wargelin, B.J. (2006). Bayesian Estimation of Hardness Ratios: Modeling and Computations. *ApJ*, **652**, 610–628. 20, 24, 62, 106

Pereira-Santaella, M., Alonso-Herrero, A., Santos-Lleo, M., Colina, L., Jiménez-Bailón, E., Longinotti, A.L., Rieke, G.H., Ward, M. & Esquej, P. (2011). The X-ray emission of local luminous infrared galaxies. *A&A*, **535**, A93. 26

Pérez-Torres, M.A., Alberdi, A., Romero-Cañizales, C. & Bondi, M. (2010). Serendipitous discovery of the long-sought active galactic nucleus in Arp 299-A. *A&A*, **519**, L5. 13, 35

Prestwich, A.H., Tsantaki, M., Zezas, A., Jackson, F., Roberts, T.P., Foltz, R., Linden, T. & Kalogera, V. (2013). Ultra-luminous X-Ray Sources in the Most Metal Poor Galaxies. *ApJ*, **769**, 92. 5, 42, 43, 51, 94

Ptak, A., Hornschemeier, A., Zezas, A., Lehmer, B., Yukita, M., Wik, D., Antoniou, V., Argo, M.K., Ballo, L., Bechtol, K., Boggs, S., Della Ceca, R., Christensen, F.E., Craig, W.W., Hailey, C.J., Harrison, F.A., Krivonos, R., Maccarone, T.J., Stern, D., Tatum, M., Venters, T. & Zhang, W.W. (2015). A Focused, Hard X-Ray Look at Arp 299 with NuSTAR. *ApJ*, **800**, 104. 12, 13, 33, 34, 36

Rana, V., Harrison, F.A., Bachetti, M., Walton, D.J., Furst, F., Barret, D., Miller, J.M., Fabian, A.C., Boggs, S.E., Christensen, F.C., Craig, W.W., Grefenstette, B.W., Hailey, C.J., Madsen, K.K., Ptak, A.F., Stern, D., Webb, N.A. & Zhang, W.W. (2015). The Broadband XMM-Newton and NuSTAR X-Ray Spectra of Two Ultraluminous X-Ray Sources in the Galaxy IC 342. *ApJ*, **799**, 121. 29, 81

Ranalli, P., Comastri, A. & Setti, G. (2003). The 2-10 keV luminosity as a Star Formation Rate indicator. *A&A*, **399**, 39–50. 6

Rasmussen, J., Ponman, T.J. & Mulchaey, J.S. (2006). Gas stripping in galaxy groups - the case of the starburst spiral NGC 2276. *MNRAS*, **370**, 453–467. 52, 53, 54, 79, 84, 94

Read, A.M. & Ponman, T.J. (2001). ROSAT PSPC observations of nearby spiral galaxies - II. Statistical properties. *MNRAS*, **328**, 127–138. 6

Relaño, M., Lisenfeld, U., Pérez-González, P.G., Vílchez, J.M. & Battaner, E. (2007). On the Metallicity Dependence of the 24 μm Luminosity as a Star Formation Tracer. *ApJl*, **667**, L141–L144. 43

Rieke, G.H., Alonso-Herrero, A., Weiner, B.J., Pérez-González, P.G., Blaylock, M., Donley, J.L. & Marcillac, D. (2009). Determining Star Formation Rates for Infrared Galaxies. *ApJ*, **692**, 556–573. 85

Sanders, D.B. & Mirabel, I.F. (1996). Luminous Infrared Galaxies. *ARAA*, **34**, 749. 11

She, R., Ho, L.C. & Feng, H. (2017). Chandra Survey of Nearby Galaxies: The Catalog. *ApJ*, **835**, 223. 102

Shipley, H.V., Papovich, C., Rieke, G.H., Brown, M.J.I. & Moustakas, J. (2016). A New Star Formation Rate Calibration from Polycyclic Aromatic Hydrocarbon Emission Features and Application to High-redshift Galaxies. *ApJ*, **818**, 60. 39

Smith, B.J., Swartz, D.A., Miller, O., Burleson, J.A., Nowak, M.A. & Struck, C. (2012). ChAInGeS: The Chandra Arp Interacting Galaxies Survey. *AJ*, **143**, 144. 12, 42

Stampoulis, V., van Dyk, D.A., Kashyap, V.L. & Zezas, A. (2019). Multidimensional data-driven classification of emission-line galaxies. *MNRAS*, **485**, 1085–1102. 102

Stevens, I.R., Read, A.M. & Bravo-Guerrero, J. (2003). First-look XMM-Newton EPIC observations of the prototypical starburst galaxy M82. *MNRAS*, **343**, L47–L52. 46

Strickland, D.K. & Heckman, T.M. (2009). Supernova Feedback Efficiency and Mass Loading in the Starburst and Galactic Superwind Exemplar M82. *ApJ*, **697**, 2030–2056. 36, 46

Strickland, D.K. & Stevens, I.R. (2000). Starburst-driven galactic winds - I. Energetics and intrinsic X-ray emission. *MNRAS*, **314**, 511–545. 29, 46

Strickland, D.K., Ponman, T.J. & Stevens, I.R. (1997). ROSAT observations of the galactic wind in M 82. *A&A*, **320**, 378–394. 46

STRICKLAND, D.K., HECKMAN, T.M., WEAVER, K.A., HOOPES, C.G. & DAHLEM, M. (2002). Chandra Observations of NGC 253. II. On the Origin of Diffuse X-Ray Emission in the Halos of Starburst Galaxies. *ApJ*, **568**, 689–716. 44

STRICKLAND, D.K., HECKMAN, T.M., COLBERT, E.J.M., HOOPES, C.G. & WEAVER, K.A. (2004). A High Spatial Resolution X-Ray and Hα Study of Hot Gas in the Halos of Star-forming Disk Galaxies. I. Spatial and Spectral Properties of the Diffuse X-Ray Emission. *ApJs*, **151**, 193–236. 44, 201

SWARTZ, D.A., SORIA, R., TENNANT, A.F. & YUKITA, M. (2011). A Complete Sample of Ultraluminous X-ray Source Host Galaxies. *ApJ*, **741**, 49. 5, 11, 12, 42, 46, 51, 117

TZANAVARIS, P. & GEORGANTOPOULOS, I. (2007). Searching for hidden AGN in nearby star-forming galaxies with Chandra. *A&A*, **468**, 129–137. 52, 61

TZANAVARIS, P., FRAGOS, T., TREMMEL, M., JENKINS, L., ZEZAS, A., LEHMER, B.D., HORNSCHEMEIER, A., KALOGERA, V., PTAK, A. & BASU-ZYCH, A.R. (2013). Modeling X-Ray Binary Evolution in Normal Galaxies: Insights from SINGS. *ApJ*, **774**, 136. 9

ULVESTAD, J.S. (2009). Radio Emission from Young Supernovae and Supernova Remnants in Arp 299. *AJ*, **138**, 1529–1538. 46

WANG, L.L., LUO, A.L., SHEN, S.Y., HOU, W., KONG, X., SONG, Y.H., ZHANG, J.N., WU, H., CAO, Z.H., HOU, Y.H., WANG, Y.F., ZHANG, Y. & ZHAO, Y.H. (2018). Spectral classification and composites of galaxies in LAMOST DR4. *MNRAS*, **474**, 1873–1885. 102

WATSON, M.G., STANGER, V. & GRIFFITHS, R.E. (1984). X-ray emission from M 82. *ApJ*, **286**, 144–158. 46

WEISSKOPF, M.C., TANANBAUM, H.D., VAN SPEYBROECK, L.P. & O'DELL, S.L. (2000). Chandra X-ray Observatory (CXO): overview. In Truemper, ed., *procspie*. 13, 54

WIKTOROWICZ, G., SOBOLEWSKA, M., SKADOWSKI, A. & BELCZYNSKI, K. (2015). Nature of the Extreme Ultraluminous X-Ray Sources. *ApJ*, **810**, 20. 6, 8, 100

WIKTOROWICZ, G., SOBOLEWSKA, M., LASOTA, J.P. & BELCZYNSKI, K. (2017). The Origin of the Ultraluminous X-Ray Sources. *ApJ*, **846**, 17. 6

WOLTER, A., PIZZOLATO, F., ROTA, S., MAPELLI, M. & RIPAMONTI, E. (2011). The population of ULXs in the spiral galaxy NGC 2276. *Astronomische Nachrichten*, **332**, 358. 10, 51, 53, 54, 79

WOLTER, A., ESPOSITO, P., MAPELLI, M., PIZZOLATO, F. & RIPAMONTI, E. (2015). NGC 2276: a remarkable galaxy with a large number of ultraluminous X-ray sources. *MNRAS*, **448**, 781–791. 10, 51, 53, 54, 72, 79

WU, H., CAO, C., HAO, C.N., LIU, F.S., WANG, J.L., XIA, X.Y., DENG, Z.G. & YOUNG, C.K.S. (2005). PAH and Mid-Infrared Luminosities as Measures of Star Formation Rate in Spitzer First Look Survey Galaxies. *ApJl*, **632**, L79–L82. 39

ZEZAS, A., WARD, M.J. & MURRAY, S.S. (2003). Chandra Observations of the X-Ray-luminous Star-forming Galaxy Merger Arp 299. *ApJl*, **594**, L31–L34. 12, 13, 16, 17, 24, 26, 33, 35

ZEZAS, A., FABBIANO, G., BALDI, A., SCHWEIZER, F., KING, A.R., PONMAN, T.J. & ROTS, A.H. (2006). Chandra Monitoring Observations of The Antennae Galaxies. I. Catalog of Source Properties. *ApJs*, **166**, 211–248. 54, 55

Zezas, A., Fabbiano, G., Baldi, A., Schweizer, F., King, A.R., Rots, A.H. & Ponman, T.J. (2007). Chandra Monitoring Observations of the Antennae Galaxies. II. X-Ray Luminosity Functions. *ApJ*, **661**, 135–148. 112

Zezas, A.L., Georgantopoulos, I. & Ward, M.J. (1998). ROSATASCA observations of X-ray luminous starburst galaxies: NGC 3310 and 3690. *MNRAS*, **301**, 915–925. 12, 26

Zhang, Z., Gilfanov, M. & Bogdan, A. (2012). Dependence of the low-mass X-ray binary population on stellar age. *A&A*, **546**, A36. 8

Zhu, Y.N., Wu, H., Li, H.N. & Cao, C. (2010). Stellar mass estimation based on IRAC photometry for Spitzer SWIRE-field galaxies. *Research in Astronomy and Astrophysics*, **10**, 329–347. 39, 85

Zombeck, M.V. (2006). *Handbook of Space Astronomy and Astrophysics*. 43

Declaration

I hereby declare that the work in this thesis is that of the candidate alone, except where indicated below.

Chapter 2: This Chapter is published in the Monthly Notices of the Royal Astronomical Society as: K. Anastasopoulou, A. Zezas, L. Ballo, R. Della Ceca, 2016, MNRAS, Vol. 460 3570-3586

Chapter 3: This Chapter is published in the Monthly Notices of the Royal Astronomical Society as: K. Anastasopoulou, A. Zezas, V. Gkiokas, K. Kovlakas, 2019, MNRAS, Vol. 483 711-733

Konstantina Anastasopoulou
December 2019